Low-temperature Isothermal Rankine cycle for Desalination

Opubo Ngoye Igobo

Doctor of Philosophy

Aston University

September 2015

Aston University

Low-temperature Isothermal Rankine cycle for Desalination

Opubo Ngoye Igobo

Doctor of Philosophy

2015

Abstract

In brackish groundwater desalination, high recovery ratio (of fresh water from saline feed) is desired to minimise concentrate reject. To this effect, previous studies have developed a batch reverse osmosis (RO) desalination system, DesaLink, which proposed to expand steam in a reciprocating piston cylinder and transmit the driving force through a linkage crank mechanism to pressurise batches of saline water (recirculating) in a water piston cylinder unto RO membranes. However, steam is largely disadvantaged at operation from low temperature (< 150^{o}C) thermal sources; and organic working fluids are more viable, though, the obtainable thermal cycle efficiencies are generally low with low temperatures. Consequently, this thesis proposed to investigate the use of organic working fluid Rankine cycle (ORC) with isothermal expansion, to drive the DesaLink machine, at improved thermal efficiency from low temperature thermal sources. Following a review of the methods of achieving isothermal expansion, 'liquid flooded expansion' and 'expansion chamber surface heating' were identified as potential alternative methods. Preliminary experimental comparative analysis of variants of the heated expansion chamber technique of effecting isothermal expansion favoured a heated plain wall technique, and as such was adopted for further optimisation and development. Further, an optimised isothermal ORC engine was built and tested at < 95^{o}C heat source temperature, with R245fa working fluid – which was selected from 16 working fluids that were analysed for isothermal operation. Upon satisfactory performance of the test engine, a larger (10 times) version was built and coupled to drive the DesaLink system. Operating the integrated ORC-RO DesaLink system, gave freshwater (approximately 500 ppm) production of about 12 litres per hour (from 4000 ppm feed water) at a recovery ratio of about 0.7 and specific energy consumption of 0.34 kWh/m^{3}; and at a thermal efficiency of 7.7%. Theoretical models characterising the operation and performance of the integrated system was developed and utilised to access the potential field performance of the system, when powered by two different thermal energy sources – solar and industrial bakery waste heat – as case studies.

Keywords: Reverse osmosis (RO), batch operation, desalination, quasi-isothermal, solar, waste heat recovery, organic Rankine cycle (ORC).

Acknowledgements

I would like to express my profound gratitude to my supervisor, Dr Philip Davies for his continuous support, guidance and outstanding supervision.

I would also like to thank all the administrative and technical staff for their various contributions in the course of the project. Thanks also to all my friends, colleagues and family for their support in making the journey a smooth one.

Finally, I sincerely acknowledge and appreciate the financial support (PhD scholarship) from the School of Engineering and Applied Science, Aston University.

Publications

Igobo O.N. and Davies P. A. Review of low-temperature vapour power cycle engines with quasi-isothermal expansion. *Energy*. 2014;70: 22-34.

Igobo O.N. and Davies P.A. A high-efficiency solar Rankine engine with isothermal expansion. *International Journal of Low-Carbon Technologies*. 2013;8(suppl 1):i27-i33.

Igobo O.N. Davies P.A. Low-temperature organic Rankine cycle engine with isothermal expansion for use in desalination. *Desalination and Water Treatment*. 2015;55(13):3694-703

Table of Contents

List of Figures

List of Tables

Nomenclature

A	Area (m^2)
AFR	Air to fuel ratio
$\mathcal{B}$	membrane salt permeability coefficient (m/s)
BR	Brackish water
C	Concentration (ppm)
C_p	Specific heat capacity at constant pressure (kJ/kg.K)
D	Diameter (m)
d	Diameter (m)
EES	Engineering equation Solver
ETC	Evacuated tube collector
F	Force (N)
FPC	Flat plate collector
α	Convective heat transfer coefficient (W/m^2K)
α_{ci}	Condensation heat transfer coefficient (W/m^2K)
HV	Heating value (MJ/m^3)
Imp	Intrinsic membrane permeability (m/s.pa)
k	Thermal conductivity (W/m.K)
L	Length (m)
m	Mass (kg)
$\acute{m}$	Mass flux ($kg/s.m^2$)
$M.A$	Mechanical advantage
Nu	Nusselt number
ORC	Organic Rankine cycle
P	Pressure (Pa)
Pr	Prandtle number
PR	Production rate
$\dot{Q}$	Heat flow rate (kW)
r	Recovery ratio
Re	Reynolds number
r_p	Pressure ratio

R	Resistance
RO	Reverse osmosis
s	Specific Entropy (kJ/kg K)
S	Piston stroke/displacement (m)
SAD	Surface area density (m^2/m^3)
SEC	Specific energy consumption (kWh/m^3)
SW	Sea water
T	Temperature (K)
TDS	Total dissolved salts (mg/l)
U	Overall heat transfer coefficient (W/m^2K)
V	Volume (m^3)
V	Velocity (m/s)
v	Specific volume (m^3/kg)
$\dot{V}$	Volumetric flow rate (m^3/s)
V_d	Dead volume (m^3)
V_{liq}	Volume of injected liquid (m^3)
W	Work done (kJ)
w	Specific work (kJ/kg)
x	Vapour quality
∅	Angular position of linkages (^{o})
ϒ	Aspect ratio
ɕ	Correction factor
Đ	Effective or hydraulic diameter (m)
ϵ	Emissivity of cylinder
ε	Effectiveness
Ɠ	Volume of gas released per unit mass of bakery dough (m^3/kg)
Ł	Crank length (m)
θ	Angular position of the crank (^{o})
η	Efficiency
ρ	Density (kg/m^3)
$\overline{\rho}$	Relative density
ƥ	porosity
ŧ	Thickness (m)

μ	Dynamic viscosity (kg/m.s)
$\mathfrak{v}$	Fractional volume
ω	Width (m)
γ	Isothermality

Subscripts

ad	Adiabatic
avg	Average
c	Condenser
cnt	Carnot
$evap$	Evaporation
f	Liquid fluid
$\mathfrak{f}$	Feed
$\mathfrak{f}g$	Flue gas
g	Gaseous fluid
h	High side or upper
HTF	Heat transfer fluid
i	Inside, inlet or input
ini	Initial
iso	Isothermal
k	Thermal conductivity
l	lower
$\mathfrak{l}$	Liquid
liq	Liquid
mem	Membrane
$mech$	Mechanical
o	Outside, outlet or output
p	Power piston cylinder
$\mathfrak{p}$	Permeate
pm	Pump
r	Refrigerant
reg	Regenerator
th	Thermal
sat	Saturated

v	Vapour
vap	Vapour
VE	Volumetric efficiency
ɯ	Wall
ɯ	Water
w	Water piston cylinder

Chapter 1 Introduction

Scarce energy and water resources, and climate change due to energy-related pollution are the key drivers for this research work; as such it is aimed at making advances in the efficient application of sustainable energy for water quality improvement. This thesis explores a new approach to the desalination of brackish groundwater using renewable or sustainable heat from a variety of sources. The goal is to convert low-grade heat sources into useful work coupled to a desalination process for effective recovery of freshwater from saline feedwater. This chapter begins by outlining the motivation behind the study and it goes on to outline the immediate context of the research advances described in the rest of the thesis. An unconventional thermal power cycle, the isothermal Rankine cycle, is introduced as it will form the basis for the rest of the thesis.

1.1 Global water and energy challenges

Energy and water are two of the most vital resources for the socio-economic development and sustenance of humanity on earth. However, despite progress towards the UN millennium development goal, about 768 million people in the world still lack access to improved (safe) drinking water, and over 2 billion people suffer inadequate supply [1]. Salinity in water resources (both surface/sea and ground water) contributes greatly to the fresh water shortfall, and also affects agricultural yields. Desalination of saline water to recover fresh water has been practiced for some decades, and is a well-established means of water supply in many countries [2], most notably Saudi Arabia, United Arab Emirates and Kuwait in the Middle East [3]. However, in Europe, Spain is a leading producer of the desalinated water, with about 8% of the worldwide desalination capacity [4]. The global capacity of desalination plants has been increasing steadily since the early 1970's, and was over 25 million m^3/day by the year 2000 [5], and is now over 74 million m^3/day [6]. Although seawater desalination projects seem to have attracted more attention, the number of brackish desalination projects is increasing at a more rapid rate. Brackish groundwater desalination is very crucial for regions with low precipitation, especially arid and semi-arid regions of the world. Desalination processes consume large amounts of energy; however the global energy supply is also faced with a number of challenges.

Virtually all work done by humans on the planet requires some form of energy, and in most cases involves the conversion of available form of energy into a desired form. Presently, fossil fuel is the primary source of energy on the planet, accounting for about 81% (Oil 31.5%, Gas 21.3%, and Coal 28.8%) of the global energy demand, with other sources including Nuclear and Renewables

accounting for the remaining fraction [7]. Humanity's strong dependence on fossil fuels for energy has eventually given rise to a global energy challenge which stands to threaten the future of the global energy supply. These challenges include: rising energy cost, increasing demand, energy security and concerns for climate change due to energy related pollutions. The average cost of oil is soaring yearly (except during the period of the recession in 2009, which saw a slight decrease for the first time in 3 decades, and the recent crash). Demand is also on the increase, according the IEA the global energy demand (which is presently about 500 EJ) could increase by more than 30% by the year 2035 [7]. Increase in demand alone does not make much impact, but the magnitude of the effect of the demand depends on the security of the supply. The Earth is said to have a finite quantity of fossil fuels which will eventually be depleted at some point; analysts have predicted a depletion time of about 35 to 110 years [8, 9]. Yet, about 1.6 billion people (a quarter of the world's population) have no access to electricity, and another 1 billion only have unreliable and intermittent supply [10].

1.2 Alternative energy source(s)

The energy challenges have fostered growing interest into sustainable alternatives or renewable energy sources such as: wind, solar, geothermal, biomass and waste heat [11]. Presently, renewable energy sources account for less than 15% of the global energy supply [12], of which biomass is a major contributor. However, solar has recorded the fastest growth, and the renewables have been projected to possibly become the world's second largest source of power generation by 2016 [13]. As a means of encouraging the exploitation of the renewable heat sources, 'heat policies' (including incentives, grants, tax benefits etc.) have been introduced in some countries [14, 15]. In the UK, 'renewable heat incentives' are provided as financial supports for the utilisation of renewable heat in heating buildings; while renewable electricity generation is encouraged through the 'renewable obligations' which requires electricity suppliers to source a portion of their electricity from renewable sources; and the 'feed-in-tariff' schemes which pays energy users for generating the electricity they use from renewable sources, and for any electricity exported back to the grid [16].

Studies have already shown that the renewable heat sources have the potential of meeting the global energy demand several times over [17, 18]. For instance, of these energy sources, biomass is an old and well-known energy source, it has the advantage of continuity over the intermittence of other energy sources like solar, but its wide spread adoption is inundated by the competitive demand for fertile land for farming food crops [19] and high replenishment time, however biomass from agricultural, industrial and municipal wastes are quite promising.

On the other hand, solar energy has the highest capacity [20]. It stands out as a potential solution for meeting the global energy demand, the annual fraction of the sun's energy striking the earth is about 3900000 EJ, but considering technical constraints (including conversion efficiencies), only about 1600 EJ can be harvested [17] which is still over 3 times the global energy need. Thus, the solar energy resource is evidently abundant and could meet the global energy demand, but its widespread adoption is not yet economically competitive. Nevertheless, it is viable and most suited for decentralized applications in remote or isolated regions of the world with high solar insolation.

Besides the natural renewable thermal sources, the potential of exploiting waste heat from existing thermal processes (including industrial processes and internal combustion engines) that would otherwise be wasted have also been considered promising [21]. This is achievable, as between 20 to 50% of the energy input to these processes are discharged (lost) as waste heat [22, 23]. For example, in the US industries, this equates to about 5 – 13 EJ of waste heat, according to the US Department of Energy (DOE) [24]. In the face of the global energy challenges, it can be agreed that waste heat recovery offers a viable means of reducing the effect of the energy challenges for industrial facilities by increasing the energy productivity.

In harnessing the thermal energy, external combustion heat cycle engines are generally employed to convert the thermal energy into useful mechanical work which can be used to drive electricity generators or other applications. A number of such large scale (>1 MW) thermal plants have been built and commercialised for electricity production, such as the solar thermal power plants in Spain [25] and USA [26], the waste heat recovery power plant built by Echogen [27], and the biomass fired power plants in Austria [28] and UK [29]. Medium scale power systems are also being developed, and small-scale (< 100 kW) applications are widely investigated by researchers [30, 31]; however, there is still a scarcity of engines, commercially, that readily convert low grade thermal sources into useful work for small scale applications (like desalination), partly due to the associated cost and low conversion efficiencies [31]. But since, globally, these alternative thermal sources are abundantly available in distributed form as low to medium grade heat, they are considered well suited for decentralized small-scale applications, thus where the cost of providing conventional energy supply is prohibitive, the renewable energy sources can be harvested to power desalination applications.

1.3 Renewable energy powered desalination

Over the years, there have been a number studies on alternative energy (especially solar) driven desalination technologies, as seen in reviews such as [32-34]. Reverse osmosis (RO) technique is

increasingly gaining popularity over thermal distillation technique, as it is considered more energy efficient, due to its relatively lower specific energy consumption (SEC) [35, 36]. RO desalination is a mechanical separation technique which involves the application of pressure to saline water against a semipermeable membrane, such that water is forced through the membrane as permeate, leaving behind the salt particles as concentrate. For most of the installed solar RO desalination plants, the energy required to produce the pressure is generated from solar photovoltaic (PV) array [37, 38] (whose electrical output is converted to mechanical energy); but cost and low efficiency of scale tend to be drawbacks of this technology.

Nevertheless, heat cycle engines can also be used to produce the required mechanical work directly (without the electrical to mechanical energy conversion process associated with the solar PV method, thus avoiding the inherent losses associated with the conversion process), or if necessary be further converted to generate electricity to drive the system. The heat engine allows the possibility of a variety of heat sources to be exploited. In a typical application (as depicted in Fig. 1.1a), the heat engine converts the thermal energy from the heat source into shaft work, to power a high pressure (HP) pump which continuously pressurises feed of saline water through the RO membrane.

The energy required to be delivered by the HP pump strongly depends on the characteristics/salinity of the feed water to be desalinated – the higher the salinity, the higher the pressure, and thus the higher the energy. – The salinity of water is usually expressed in terms of its total dissolved solids (TDS). The TDS include inorganic salts (principally calcium, magnesium, potassium, sodium etc.) and small amounts of other dissolved matter. Sea-water typically has a TDS of more than 25000 mg/L. Water is considered brackish when it's TDS concentration is between 1000 and 10,000 mg/L. According to the WHO, water is considered good for drinking at a TDS level of less than 600 mg/L [39].

Ideally, in the desalination of brackish groundwater, high recovery ratio would be preferred, so as to maximize fresh water output and minimize the volume of concentrated brine rejected, since the disposal could pose an environmental problem. However, high recovery ratio tends to require large energy inputs due to increase in osmotic pressure as a result of concentration increase with water removal at the RO module outlet, i.e. the concentration and thus the osmotic pressure increases from the inlet to outlet of the module. The conventional method of continuous flow (Figure 1.1a) operation suffers from this high energy requirement or otherwise low recovery ratio. One possible way to minimise this issue is to employ several RO stages in series, with intermediate pumps in place – multistage continuous operation (Figure 1.1b) – to supply appropriate pressure to each stage [40], however, this would require an infinite number of stages for the energy consumption to approximate the theoretical minimum. A potential solution to address this drawback is to have a

cyclic/batch operation, rather than continuous operation. Example of such cyclic RO desalination system is the "Closed Loop Desalination" (CLD) [41, 42] (Figure 1.1c). The concept of the cyclic CLD utilises: a recirculation pump to recycle the concentrate through the RO module so as to maintain fairly even concentration, HP pump with variable pressure according to the salinity of the concentrate, and a valve to enable the concentrate to be discharged at the end of the cycle – when the desalination reaches a desired recovery level. The energy saving profile is depicted in Figure 1.2.

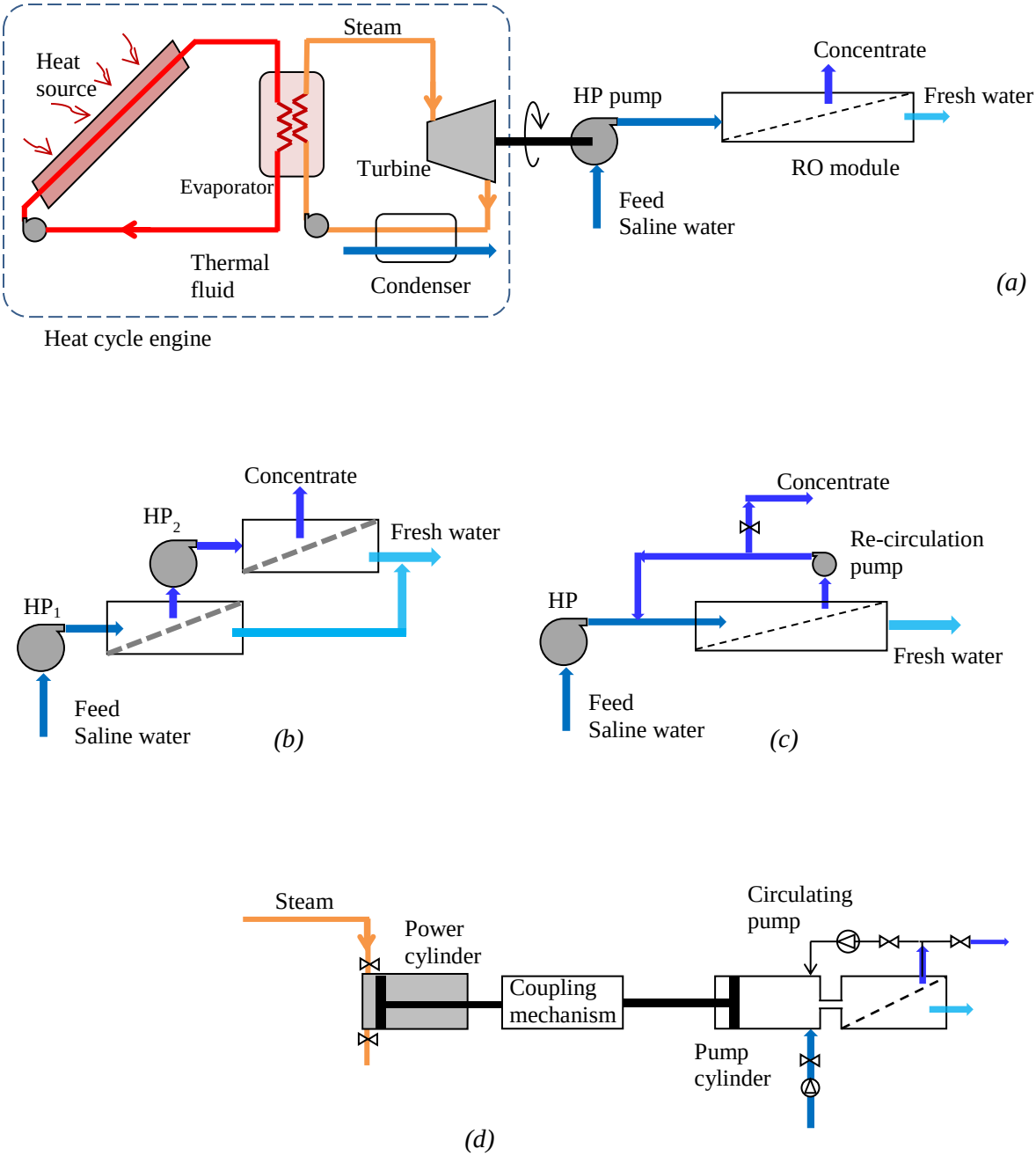

Figure 1.1: Different modes of operation in RO desalination: (a) Continuous (b) Multistage continuous (c) Closed-loop, and (d) Batch mode

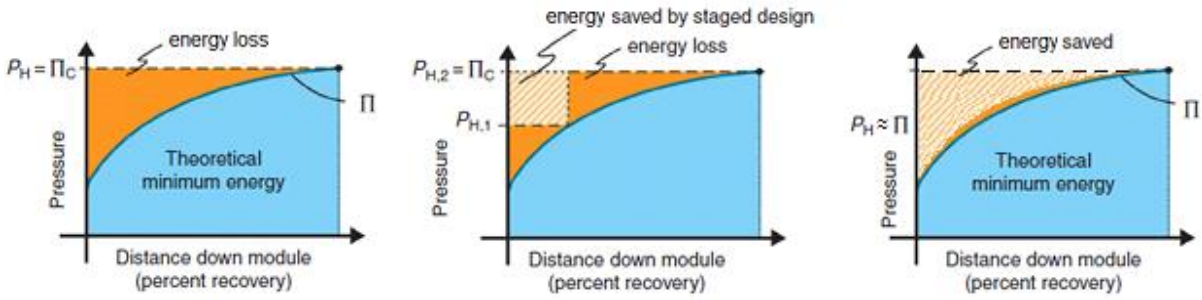

(a) Continuous (b) Multistage continuous (c) Cyclic/Batch

Figure 1.2: The energy consumption profile for continuous, multistage continuous [40] and batch operations. *For the continuous operation, the pump pressure is constantly supplied to equate the high osmotic pressure at the concentrated outlet*.

Another desalination system that uses cyclic operation is 'DesaLink', proposed by Davies [35]. Here, batches of a given volume of saline water are fed into a water pump cylinder, which pressurises the saline water (as it is recirculated) through the RO module (Fig. 1.1d). The driving force is provided by steam pressure in another cylinder (power cylinder), via a coupling mechanism. The coupling mechanism is made up of an arrangement of crank and linkages (Figure 1.3), in which the crank, *OP*, reciprocates about the fixed point *O*. This arrangement provides increasing mechanical advantage as the power piston advances, thus ideally balancing the forces of the declining pressure (of the expanding steam) in the power cylinder and the increasing saline water pressure in the pump cylinder.

In a nutshell, the operation of the cyclic/batch mode RO desalination can be distinguished from the continuous mode, in that, with the former, the pressurisation is halted at some time intervals during the operation, and the module is purged. This, together with the recirculation of the pressurised feed during operation helps maintain fairly uniform, relatively lower concentration through the system at each moment in time in the module, hence obviating the additional energy requirement due to concentration increase, as with the continuous operation [35]; and thus resulting in energy consumption that approaches the theoretical minimum (Fig 1.2c).

Qiu et al [43] described a prototype of the DesaLink machine that was tested with compressed air to simulate steam as the working fluid (Figure 1.4). At this time the machine was envisaged as a type of steam Rankine cycle driving the batch-RO process. However, there are several theoretical and practical disadvantages of using steam, in particular the high specific volume at low temperatures and the need for a pressure steam boiler.

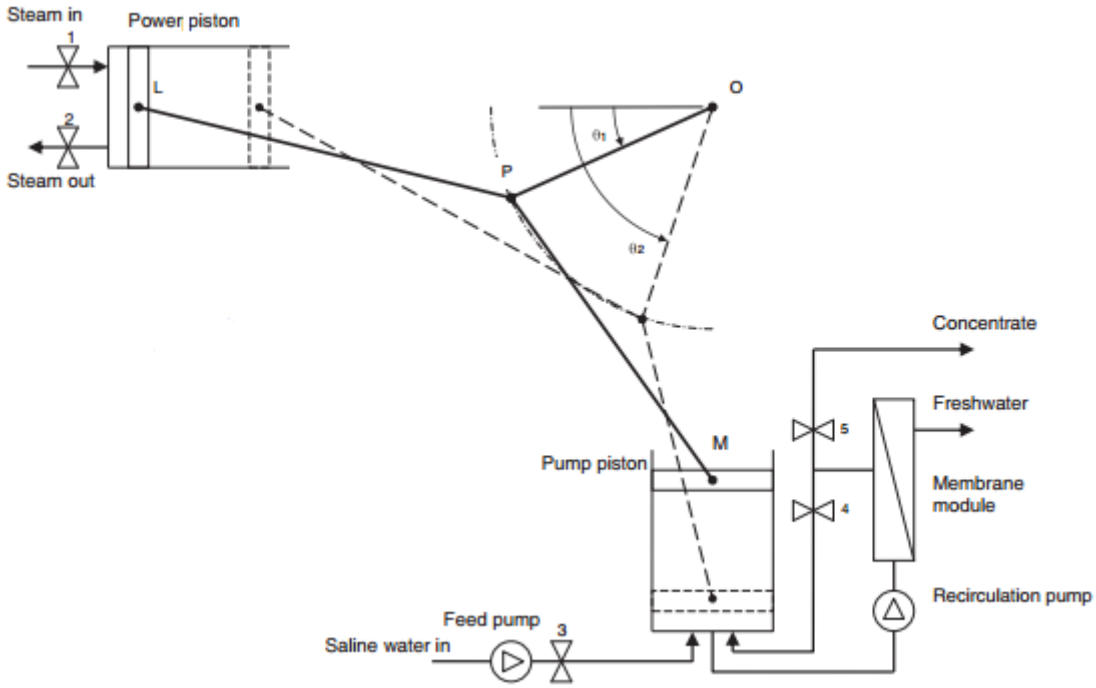

Figure 1.3: Schematic of DesaLink concept [35]. *The initial and final positions of the system are shown by bold and dashed lines respectively*.

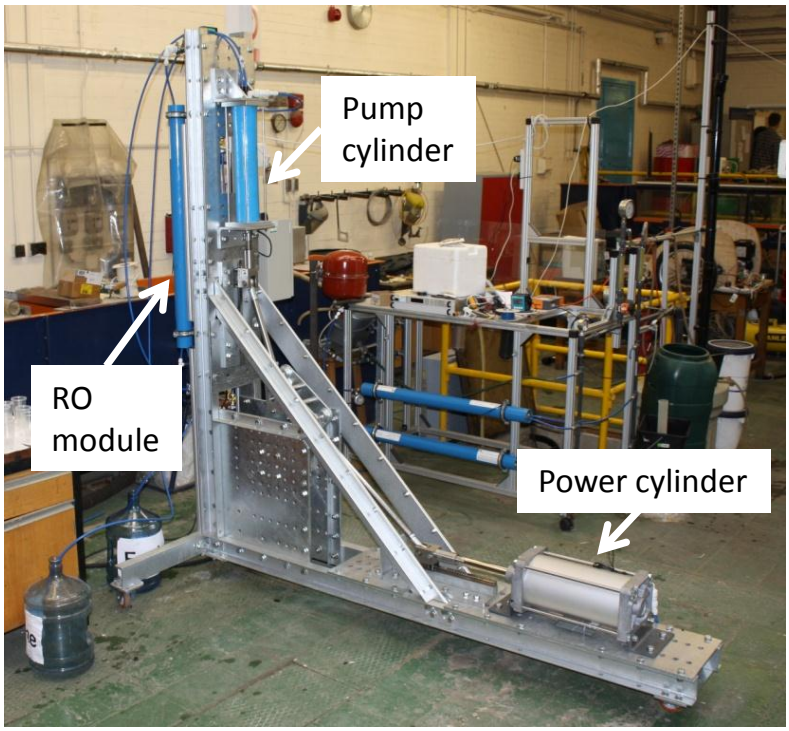

Figure 1.4: DesaLink batch RO desalination system [43]

In this current work the focus is moved from steam to alternative working fluids such as hydrocarbons. In this sense, the thesis is a study of the organic Rankine cycle (ORC) with specific characteristics as needed to drive the batch-RO process. Though the term ORC is adopted in this

thesis for convenience, it can be understood to encompass a range of low temperature Rankine cycle designs using working fluids which, though typically organic, could also include fluids such as ammonia, siloxanes or even water, as long as the design is intended for low temperature (typically < 200^{o}C) application. An evaluation of the working fluid options is within the scope of this study.

In seeking to optimise overall efficiency and recovery rate of the ORC-RO concept, this study makes use of unconventional version of the Rankine cycle, referred to as the *isothermal* Rankine cycle, indicating that the expansion stage of the cycle is carried out isothermally or nearly isothermally. This cycle was identified at an early stage of the study as having potential advantages (higher specific work output) over the conventional Rankine cycle using adiabatic expansion. Because of its importance to this whole thesis, the basic concept of the isothermal Rankine cycle is introduced next. A more quantitative description of the cycle is reserved for later chapters.

The isothermal Rankine cycle simply entails providing continuous heat supply to the working fluid during the expansion phase such that it expands at constant or near constant temperature. The version explored in this study proposes to provide sufficient heat to the expander such that it uses no separate boiler; instead the working fluid is heated in the expander. A schematic is depicted in Figure 1.5(a), while (b) shows the temperature-entropy (*T*-*s*) diagram for the cycle (assuming an ideal reversible cycle). On operation, a liquid working fluid is directly injected into the hot expansion chamber, where it vaporises and expands at constant temperature (T_h) whilst performing work against the piston. At the end of the expansion (assuming it was ideally expanded to same pressure level as the condenser), on the return stroke of the piston, the vapour exits via a regenerator (where its temperature is reduced) and is condensed back to liquid at temperature T_c in the condenser. Noting that the net work done of an ideal reversible cycle is equivalent to the enclosed area on a *T*-*s* diagram, it can easily be seen from Figure 1.5b that the isothermal cycle promises more work output than the conventional adiabatic cycle.

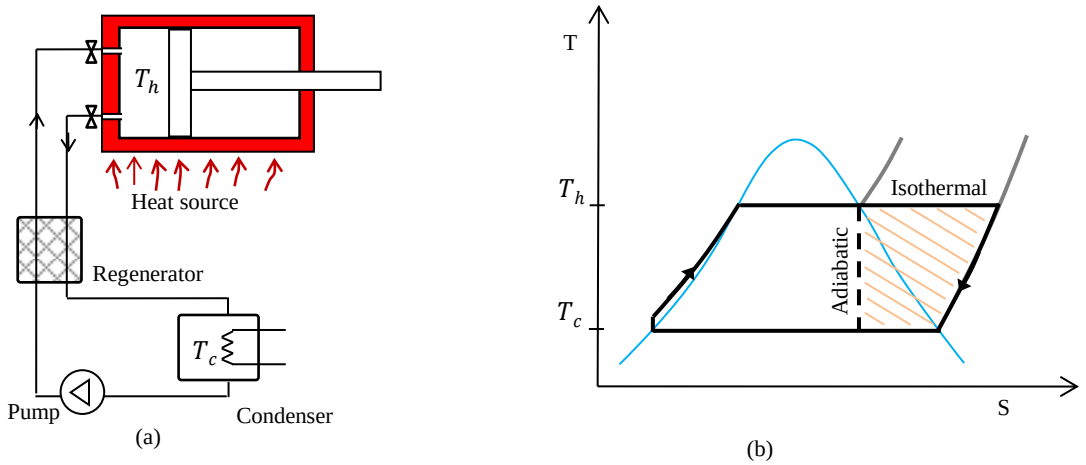

Figure 1.5: System schematic (a) and T-s diagram (b) of the isothermal Rankine cycle

Further advantages of the cycle are foreseen to be:

- High efficiency theoretically approaching that of the Carnot cycle, because heat is substantially added at the constant upper temperature (due to the use of the isothermal expansion) and rejected at the lower temperature
- High work ratio as in the conventional Rankine cycle, and distinct to gas power cycles such as the Brayton or conventional Stirling cycle which tend to have poor work ratio due to the absence of phase change in the working fluid
- Ability to use a wide range of working fluids (including both zeotropic and azeotropic fluids) and thus optimise the cycle for a broad range of design constraints
- Absence of any external boiler which may be onerous from health and safety and maintenance considerations

The broad aim of the thesis is therefore to investigate the feasibility of using the isothermal Rankine cycle to drive the batch-RO process, thus revealing the extent to which these potential advantages can be realized as well as identifying advantages of the approach. Specific aims and objectives will be identified once a literature survey has been conducted to provide further context to the work.

Chapter 2 Review of low temperature Rankine cycle RO desalination and of isothermal vapour power cycles

The isothermal Rankine cycle as mention in Chapter 1 has important novel aspects and its use to drive desalination is entirely new. However, the idea of using an isothermal expansion in a vapour power cycle is not without precedent. After reviewing the recent work on Rankine-cycle RO desalination, this chapter reviews various low-temperature vapour power cycle heat engines with quasi-isothermal expansion (the prefix is used to indicate that isothermal expansion may only be achieved in the ideal limit).The review covers the methods employed to realize the heat transfer. The heat engines take the form of Rankine cycle with continuous heat addition during the expansion process, or Stirling cycle with a condensable vapour as working fluid. Compared to more standard Stirling engines using gas, the specific work output is higher. Cryogenic heat engines based on the Rankine cycle have also been enhanced with quasi-isothermal expansion. Liquid flooded expansion and expander surface heating are the two main heat transfer methods employed. Liquid flooded expansion has been applied mainly in rotary expanders, including scroll turbines; whereas surface heating has been applied mainly in reciprocating expanders. Some of the material presented in this chapter has been published by the author in a review article in the journal 'Energy' [44].

2.1 Introduction

Heat cycle engines, as introduced earlier in chapter 1, can be employed to convert energy from a variety of thermal sources into mechanical energy to drive a number of systems including RO desalination. Generally in RO desalination systems, tremendous improvement in energy consumption reduction can be achieved with pressure exchange devices, which are employed to recover hydraulic energy from the fresh water output flow; this in addition with the recent advances in RO membrane technology (example in terms of increased productivity and higher salt rejection) have significantly bolstered the market share of the RO desalination [45]. However one particular benefit that could be realized in coupling a heat engine with a RO desalination system is that, the feed saline water provides a heat sink for the heat engine's condenser, while at the same time it is preheated to increase the RO membrane permeability, thus resulting in further reduction in energy consumption. Though, the practical application of the heat engines to RO desalination is still far from full commercialisation, research studies are albeit advancing in the literature [46, 47].

In this chapter, the state of the art in the use of low temperature heat cycle engine coupled to RO desalination will be reviewed. Thereafter, vapour power cycles will be reviewed with focus on the current methods of achieving efficiency improvements by means of isothermal expansion. Following the literature review, the aims and objectives of the thesis will be presented.

2.2 Rankine cycle RO desalination

Desalination by reverse osmosis is typically a filtration process across a semi-permeable membrane. The process works against the phenomenon of natural osmosis that would normally occur between two solutions of different concentrations separated by semi-permeable membrane, wherein solvent from the lower concentration naturally moves to high solute concentration, due to the chemical potentials of the solutions across the membrane. The minimum pressure difference (or pressure in the high concentration solution) that would be required to maintain equilibrium (such as to stop the movement of solvent across the membrane) is referred to as the osmotic pressure, P_{osm}, of the solution, and is directly proportional to the concentration of the solution. However, in reverse osmosis, external pressure (greater than the osmotic pressure) is applied to the high concentration solution to overcome the osmotic pressure, and force the solvent to flow in reverse – from the higher concentration, through the membrane, to the lower concentration. Thus in reverse osmosis desalination, external pressure is applied to a feed saline water (high concentration solution), such that fresh water (solvent) is passed, forced through RO membrane as permeate, while much highly concentrated solution is rejected as brine.

The amount of pressure energy required depends on the osmotic pressure of the feed saline water and the recovery ratio, *r*. The recovery ratio can be idealised as a ratio of the volume of achieved permeate to the volume of the feed saline water. The ideal minimum energy, *E*, required to produce a volume V_p of fresh water can be given by [35]:

$$E = P_{osm} V_p \frac{1}{r} \ln\left(\frac{1}{1-r}\right) \tag{2.1}$$

$$r = \frac{V_p}{V_f} = \frac{\dot{V}_p}{\dot{V}_f} \tag{2.2}$$

And the specific energy consumption *SEC* required for producing a unit volume of permeate can be expressed as:

$$SEC = \frac{E}{V_p} = P_{osm} \frac{1}{r} \ln\left(\frac{1}{1-r}\right) \tag{2.3}$$

Typical specific energy consumption values for sea water desalination is about 8 kWh/m^3 [48]; however, with the aid of pressure exchange energy recovery devices (which are employed to recover energy from the pressurised membrane reject flow stream, to augment in driving the feed flow), these values can be reduced to about 2.3 kWh/m^3 [48, 49].

The specific energy consumption can generally be adopted as a representative parameter in accessing the performance of desalination system, though, for solar thermal desalination systems, the ratio of the volumetric flow rate of desalted water to the aperture area of the solar collector can be considered as an appropriate representative parameter because it reflects the combined effects of the solar collector's efficiency, heat engine's thermal efficiency and specific energy consumption of the RO unit [50]. However, the specific energy consumption corresponding to thermal energy requirement can be influenced by the efficiency of the heat cycle engine employed to drive the RO process. Different heat cycle engine configurations have thus been studied for driving RO desalination systems.

El-Nashar and Husseiny [51] studied a brackish water RO desalination system driven by a dish Stirling cycle engine (and a diesel engine as backup). The Stirling cycle (using a gaseous working fluid) operates at high temperature and results in high performance. Another high temperature gas cycle design was proposed by Childs [52, 53]. The proposed RO desalination system features a reciprocating piston engine, coupled directly to hydraulic pistons, which are in turn connected to pump pistons, where the saline water is pressurised against the RO module. The hydraulic system was employed to absorb or provide power to the system (i.e. performing power compensating function). The proposed thermal engine design was a recuperated closed loop Brayton cycle (whose performance was predicted to approach that of the classic Stirling cycle); however the concept could potentially be applied with other heat cycle engines that use reciprocating pistons e.g. the classic steam engine.

A preliminary design of a solar thermal RO system driven by steam engine was presented by Bowman et al [54]. Line-focus tracking solar collectors were used to heat a high pressure liquid-vapour water storage tank. Steam from the heated water tank is fed to a reciprocating piston steam engine which directly drives the RO HP pump. Analysis of the system showed that 26 m^3 of freshwater per day (8.5 h) could be produced from 5400 ppm brackish water at a recovery rate of 75% [55]. A similar system was also presented by Attia [56], albeit, with no separate HP pump; instead it was proposed to have the saline water contained in one side of a rod-less piston cylinder and pressurised directly by the steam in the other side.

Water/steam as working fluid has also been studied in the more conventional Rankine cycle engine configuration. Nafey and Sharaf [57] modelled the performance of water as a working fluid

alongside three organic working fluids – butane, hexane and toluene – operating at temperatures of about 80, 130 and 300^{o}C respectively in a Rankine cycle RO system. The predicted SECs and efficiencies of the organic fluids were 6.8, 7.3 and 7.8 kWh/m^3 and 8.2, 15 and 25% respectively, while permeate outputs were respectively 166, 200 and 520 ltr/m^2/day. For the different temperatures considered, the thermal efficiency for water was predicted to be somewhat similar (or slightly higher) to those of the organic variants, however for the low temperature scenarios (80 to 100^{o}C), the evaporating pressures for water (0.6 bar) could be considered too low for practical utilisation, in comparison to the predicted 10 bar for Butane at same temperatures.

Studies have also investigated other organic fluids for RO desalination; Delgado-Torres et al. [58, 59] carried out a design study of solar thermal ORC-RO sea water desalination for a range of working temperatures and working fluids, and presented potential ORC efficiencies of 15 – 32%, with freshwater production range of 0.36 – 0.88 m^3/m^2 per day (8 h). A later study [50] analysed R245fa ORC for different solar thermal collector temperatures, and predicted efficiencies of 9 – 16% and fresh water outputs of 0.5 – 1.2 m^3/m^2/day from sea water; while for brackish water, with the same temperature range and ORC efficiencies, water output of 1.8 – 4.7 m^3/m^2/d was predicted. In a design study by Karellas et al [60], a water production of 47 m^3/h (at 15% recovery ratio) was projected with R134a ORC efficiency of 6.9% from operating temperature of 86 – 113^{o}C. Bruno et al [61] carried out a design study and presented ORC mechanical power capacity requirement of 11.7 kW for a desalting capacity of 15 m^3 per 7 h/d from 3,000 ppm brackish water. Manolakos et al. [62] reported an experimental R134a ORC-RO desalination system that produced 2.55 m^3 (per 9 hours) of fresh water from sea water, at a recovery ratio of 21%, and with a SEC of 2.3 kWh/m^3 (8.28 kJ/litre) and thermal cycle efficiency of 1.17%; although a system efficiency of 7% was initially predicted in the design study [48]. It was also proposed to cascade the R134a cycle with R245fa upper cycle for higher temperature and thus higher efficiency [63]. In an experimental study on Freon (R11) ORC driven brackish water desalination, Libert and Maurel [64] achieved thermal ORC efficiency of 2.2%, fresh water output of 130 ltr/m^2/day, mechanical SECs of respectively 1 kWh/m^3.

An overview of low temperature driven RO systems can be given as in Table 2.1, as can be observed from the presented studies, a good number of organic working fluids have been investigated (as an alternative to the conventional use of water as working fluid) for heat engine in driving RO desalination. The obtainable performance depends on the thermodynamic properties of the working fluid considered and the operating temperature. For example, in the ORC-RO desalination design study by Bruno et al [61], R218 was found to be the optimum choice, with efficiency of 7.81% (amongst R125, R32, R134a, R290) for FPC collector (< 90^{o}C); while R245 was optimal (amongst R218, R227, R134, R134a, RC318, R31, R1270) for ETC collector (<121^{o}C).

Table 2.1: Overview of low temperature (< 300^{o}C) heat engine driven RO systems

Reference (study type)	Feed water (ppm)	Collector type/ Temp. (^{o}C)	Working fluid	Cycle Efficiency (%)	SEC (kWh/m^3)	Freshwater production (ltr/m^2/day)	Recovery ratio
[57] (design)	SW 45,000	FPC / 80-100	Butane	8.2-8.1	6.85 [e]	166 [c]	0.3
			Water	8.9-10.1	7 [e]	188-192 [c]	
		CPC / 130-150	Hexane	14.5-13.9	7.3 [e]	200-230 [c]	
			water	17.7-13.4	7.4 [e]	220-280 [c]	
[50] (design)	SW 35,730	CPC / 82-100	R245fa	9.3-11.8		504-744 [c]	0.45
		FPC / 83-113		9.3-13.6		552-960 [c]	
		ETC / 124-148		13.5-16.1		984-1224 [c]	
	BW 5,331	CPC / 82-100		9.3-11.8		1782-2600	0.6
		FPC / 83-113		9.28-13.6		1920-3310	
		ETC / 124-148		13.5-16.1		3408-4752	
[60] (design)	SW	86-113	R134a	6.9	3.2-5.3	5.5 [f]	0.15
[61] (design)	SW 36,000	FPC / 87	Octaflouropropane	7.8		21-29 [d]	0.5
		ETC / 121	R245fa	13.2		42-53 [d]	
		PTC / 290	Isopentane	29.3		75-117 [d]	
	BW 3,000	FPC / 87	Octaflouropropane	7.8		58-96 [d]	0.75
		ETC / 121	R245fa	13.2		140-172 [d]	
		PTC / 290	Isopentane	29.3		170-220 [d]	

[62] (experimental)	SW 41,000	ETC / 75	R134a	0.73-1.17	2.3	80-140 [c]	0.18-0.2
[48] (design)	SW 42,700	ETC / 75	R134a	7	2.5 8.4 [e]	240 [c]	0.2
[64] (experimental)	BW 3,000	92	Freon (R11)	2.2	1	130	
[58, 59] (design)	SW 35,730	235	MM	15-26	1.8	47-90 [f]	0.49
		235-300	D4	15-27		45-90 [f]	
		244-300	Toluene	22-32		64-110 [f]	
[63] (design)	SW 42,710	137	R245 upper cycle R134 bottom cycle	11.8	2.5 9.75 [e]	100 [d]	0.2
[65] (experimental)	BW 2,000	FPC	R114		0.67		0.5
[66] (experimental)	SW 31,000	60	R134a	3.5-5	2 - 3	300 [g]	0.19

Note: SW = sea water; BW = Brackish water; FTC = flat plate collector; ETC = evacuated tube collector; CPC = compound parabolic collector; [c] = 24 hours day; [d] = 7 hr day; [f] = 1hr day; [g] = litre/hr; [e] = without pressure exchange energy recovery device

Besides the thermodynamic performance, environmental issues such as the global warming potential (GWP) and the ozone depletion potential (ODP) also influence choice of fluid. For example fluids containing chloroflourocarbons such as Freon have high ODP, as such would normally not be a good choice, while fluids such as Toluene have toxicity concerns.

In a nutshell, it can be seen that the practical performances of the reported experimental systems are in the range of 0.7 – 1 kWh/m^3 and 2 – 3 kWh/m^3 specific mechanical energy consumption for brackish water and sea water respectively, with thermal efficiencies often less than 5%. However, it can also be seen that the efficiency of the heat cycle engine is key in the overall performance of the desalination system; the higher the efficiency in thermal to mechanical energy conversion, the higher the volume of desalted water per unit thermal input. Hence for maximum utilization of available thermal energy, and maximizing water production, it would be expedient to adopt heat engines with high thermal efficiencies, or employ appropriate techniques of efficiency improvements. As mentioned in chapter 1, isothermal expansion of the working fluid in the heat engine, is one potential technique for achieving such improvement; the subsequent sections of this chapter will explore this technique in detail. It is hoped that this will aid this thesis to improve on the above performance figures.

2.3 Vapour power cycles with isothermal expansion

The previous section shows that RO desalination system could be driven by a wide array of thermal power cycle engines. The classical thermal power cycles using the concept of isothermal expansion are the Stirling and Ericsson cycles. These gas power cycles are noted for having the high theoretical efficiencies of the Carnot cycle – which is the maximum obtainable efficiency for given temperature limits [67]. On the other hand, for vapour power cycles (typically the Rankine cycle), the working fluid is a condensable vapour, and is intermittently vaporised and condensed; the expansion process is ideally adiabatic (i.e. the fluid expands without experiencing heat transfer during the process) and produces less work than its isothermal counterpart [68]. Nevertheless, in comparison to the gas compression work of the gas power cycles, less input work is required to pressurize the condensed liquid of the vapour power cycles, and the cycle pressure-volume characteristics exhibit higher net work output than the gas cycles [69]; thus the vapour cycle engines have higher specific work output. The vapour power cycles can also exhibit advantages over the gas cycle equivalents because the phase change allows smaller surface areas and temperature differences to drive the boiling/condensation required by the cycle. This inference arises from the higher heat transfer coefficients associated with phase change (by orders of magnitude) relative to that of forced convection for gas [70]. The smaller surface areas lead to compact heat exchangers

and engine size [71]; this together with the higher work output gives the vapour cycle engines higher power density; and the low temperature differences aid better performance (relative to the gas cycles) in low-grade heat applications. This has been demonstrated in a study that showed the Rankine cycle to be more efficient than Stirling cycle for temperature range of 150 – 300^{o}C [72].

In power plants operating on the Rankine cycle, reheating is a practical approach to improve the cycle efficiency and specific work output. As the number of stages of reheating increases, the expansion and reheat processes approximate an average isothermal process and the cycle efficiency increases [73]. But in the reheating process, the steam must be returned back to the boiler for each reheat, which, besides requiring many additional components, inevitably adds complexity to the plant layout and geometry, and results to heat and pressure losses [74]. Alternatively, the vapour cycle engine could be designed in such a way that (like the Stirling or Ericsson engines) heat is continuously transferred to the working fluid during the expansion process thus resulting in isothermal expansion, or more realistically, quasi-isothermal expansion – which may be somewhere between the adiabatic and ideal isothermal processes.

In the following sections, relevant research works with emphasis on low temperature vapour power cycles with quasi-isothermal expansion will be presented. Various methods employed to effect quasi-isothermal operation, including concepts, studies and results, will be reviewed to provide an insight into their practicality, system performance and energy efficiency. The first part (subsections 2.3.1 and 2.3.2) of the review presents the general theoretical advantage of quasi-isothermal expansion, including the various heat transfer methods used to achieve it. While the second part (subsections 2.3.3 - 2.3.5) covers the power cycles to which the methods are applied. For each power cycle, the theory and principle of operation is explained, and then specific studies are reviewed in which these cycles have been implemented. Figure 2.1 classifies the methods and vapour power cycles for quasi-isothermal operation according to the approach used in this review.

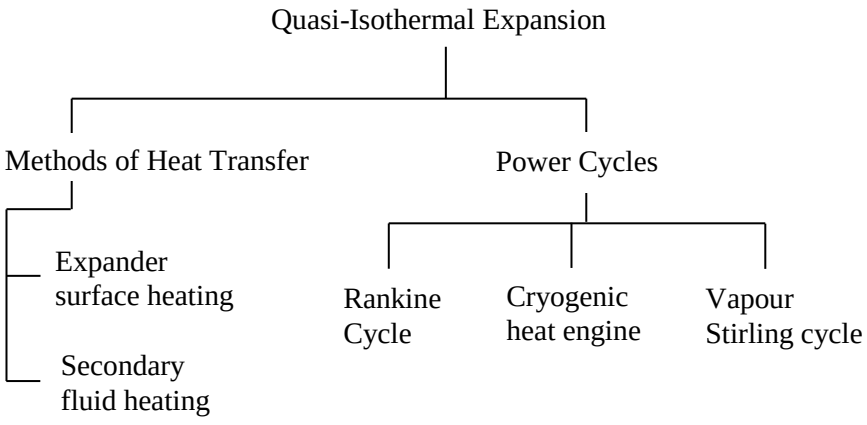

Figure 2.1: Overview of the review approach

2.3.1 Quasi-Isothermal expansion

The paths of both the isothermal and adiabatic expansion processes can be illustrated graphically on a pressure-volume (*P*-*v*) plane as shown in Figure 2.2, using the gas equation $P_1 v_1^n = P_2 v_2^n$. The expansion index *n* is equal to 1 and k for isothermal and adiabatic processes respectively [75], where k is the ratio of the specific heats (C_p/C_v) of the gas, and is always >1 [76]. For example, under some range of operating conditions, k is about 1.4 and 1.3 for nitrogen gas and steam respectively [77].

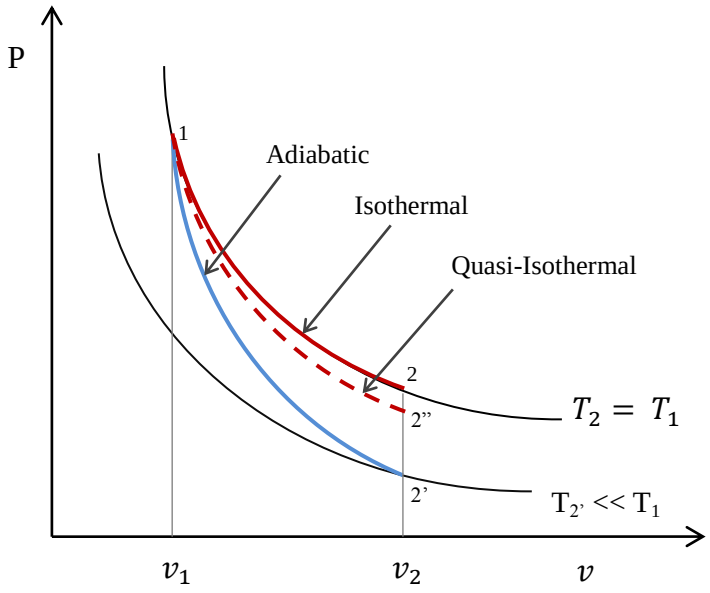

Figure 2.2: Graphical representation of isothermal and adiabatic expansion processes

The work output is simply the integral ($\int PdV$) between the two end states (1 and 2), as is represented by the area under the path curves. Hence, from the figure it can be seen that the area under the curve (i.e. the expansion work output) for the adiabatic expansion is less than that of an isothermal expansion having the same initial operating conditions. This can also be seen numerically from the integration of both curves from state 1 (start of expansion) to state 2 (end of expansion).

The work done by isothermal expansion can be given as [78]:

$$W_{iso} = \int PdV = P_1 v_1 \ln\left(\frac{P_1}{P_2}\right) \tag{2.4}$$

Similarly, the work done by adiabatic expansion can be expressed as:

$$W_{ad} = \int PdV = P_1 v_1 \frac{1 - \left(\frac{P_1}{P_2}\right)^{\frac{1-n}{n}}}{n-1} \tag{2.5}$$

Hence, from the above equations, the relative improvement of the isothermal expansion work over the adiabatic work can be expressed in terms of the expansion index and pressure ratio $r_p = P_1/P_2$ as:

$$Relative\ improvement = \frac{W_{iso}}{W_{ad}} - 1 = \left[\frac{(n-1)\ln(r_p)}{1 - (r_p)^{\frac{1-n}{n}}}\right] - 1 \tag{2.6}$$

For example, with $r_p = 7$ and n = 1.4, Eq. (2.6) shows that the isothermal expansion promises 83% more work than the adiabatic.

The expansion process of conventional vapour power cycles is generally assumed adiabatic, and as such is subject to this reduced work output [68]. The adiabatic expansion process is also characterised by drop in temperature from T_1 to T_2'. Hence, modifying an adiabatic expansion to an isothermal one would ideally require the addition of heat to the expanding fluid to maintain its temperature constant.

In reality, when the heat absorbed by the vapour is not sufficient to maintain isothermal expansion, the result is termed quasi-isothermal expansion. In this case, the heat absorbed shifts the expansion process from adiabatic behaviour towards the ideal isothermal behaviour. Consequently, the work output will be more than the adiabatic work, but less than the isothermal work available, in proportion to the extent to which the expansion approaches the isothermal case. This extent has been termed isothermality, γ, defined as the ratio of actual work output to the ideal isothermal work [79].

$$\gamma = \frac{W_{ac}}{W_{iso}} \tag{2.7}$$

Thus it determines the work output as a fraction of the isothermal work available. On the other hand, for rotary expanders some authors have described the extent of isothermal behaviour as the ratio of discharge temperature to supply temperature [80].

2.3.2 Methods of effecting quasi-isothermal expansion

Over the years, a number of methods have been developed, by which a vapour power cycle's working fluid can continuously gain heat during the expansion process to effect quasi-isothermal

expansion; often times this result in variants of the traditional power cycles. The identified methods can be generally grouped on the basis of the means of heat transfer as: secondary fluid heating and expander surface heating. The methods and the power cycles (including the variants) to which it is applied are shown in Table 2.2.

Table 2.2: Heating methods and the applicable power cycles for quasi-isothermal operation, with relevant examples from the literature

Methods / Applications	Secondary fluid heating	Expander surface heating
Rankine cycle engine (sub section 2.3.3)	Theoretical study of liquid flooded scroll turbine, using various fluids [81] Experimental study of the effect of flooding liquid quantity in scroll turbine [82]	Theoretical study of surface heated scroll turbine [83] Experimental study of surface heated reciprocating cylinder [84]
Cryogenic engine (sub section 2.3.4)	Experimental studies of evaporating cryogenic liquid in water [85, 86]	Theoretical studies of surface heated reciprocating cylinder [85, 87]
Stirling cycle engine (sub section 2.3.5)		Theoretical studies of controlled evaporation in Stirling engine [88, 89] Experimental study of vapour Stirling engine [89]

2.3.2.1 Expander surface heating

A simple approach to achieve heat transfer to the working fluid during the expansion process is to provide a means of heating the expander sufficiently above the fluid temperature; such that during the expansion process, heat could be effectively transferred from the surface of the expansion chamber to the fluid, as illustrated in Figure 2.3a. This is quite popular for reciprocating expanders as found in conventional Stirling engines, and steam-jacketed steam engines. The extent of

isothermal operation achievable here will depend on the rate of heat transfer, which is a function of the overall heat transfer coefficient and temperature differential between the engine wall and the fluid, and the surface area of the wall exposed to the fluid [90]. As such, geometries giving high surface to volume ratios such as tubes and fins are generally utilised to increase the total heat transfer area, as found in conventional Stirling engines [91].

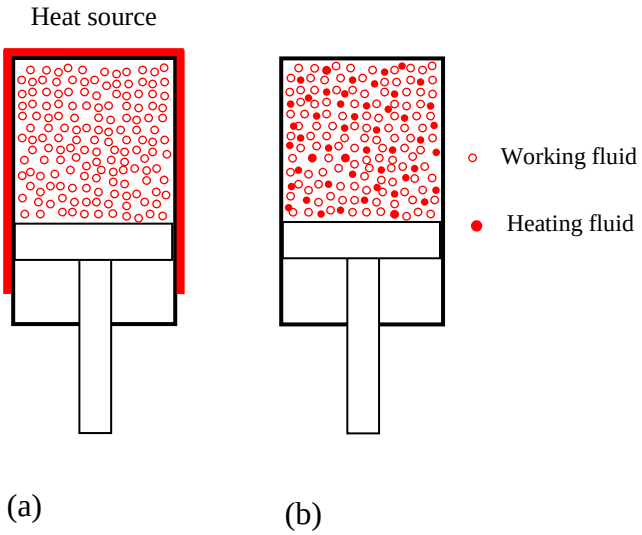

Figure 2.3: The two main means of heat transfer used to achieve isothermal expansion: (a) expander surface heating; (b) secondary fluid heating system

2.3.2.2 Secondary fluid heating

The heat transfer required to effect quasi-isothermal expansion could be provided by means of a secondary fluid which co-exists with the working fluid in the expander during the expansion process (Figure 2.3b). In this case, the secondary fluid – which will ideally be of a high thermal content – is dispersed into the working fluid such that during the expansion process, the temperature dropped by the expanding working fluid is quickly recovered from the secondary fluid. The heating fluid could ideally be a vapour – as with direct steam injection; or more practically, a liquid – as with liquid flooded expansion.

The concept of achieving isothermal expansion by direct steam injection entails injecting small amount of relatively very high temperature steam (secondary fluid) into the expanding steam [92]. The secondary steam transfers heat to the working steam by virtue of its higher temperature thermal content, as such requires the secondary steam to be continuously injected with appropriate amount and temperature in such a way as to keep the expansion temperature constant.

On the other hand, the liquid flooded expansion process involves literally flooding a screw or scroll machine with a large quantity of liquid simultaneously as the working fluid passes through the device, such that the liquid provides a medium of heat exchange with the working fluid whilst in transit through the device. Unlike with steam injection, the secondary fluid is normally different from the working fluid, and is immiscible with it. This concept can ideally be applied to compression and expansion processes (its application to expansion processes will be covered in sub section 2.3.3). Over the last two decades, there have been a significant number of studies on the application of liquid flooding to compressors. Researchers have studied oil-flooding in screw compressors [93] and scroll compressors [94] primarily to improve sealing and lubrication, but without much emphasis on heat transfer [95]. In recent years, conventional screw [96] and scroll [97] compressors have been effectively used in reverse as expanders (with minor modifications), thus widening the scope for liquid-flooded expansion. The combinations of the different working fluids and flooding liquid considered in the literature are shown in Table 2.3.

Table 2.3: Combinations of different working fluids and flooding liquid

Working fluid	Flooding liquid	Expansion device	Ref.	Study type
Ammonia (R717) Carbon dioxide (R744) R410A Isobutane (R600a) n-pentane R245fa	Water	Scroll	[81]	T
	Zerol 60			
R245fa	Compressor oil	Scroll	[82]	Ex
Liquid air	Water	Reciprocating cylinder	[85, 86]	Ex

T – Theoretical; Ex – Experimental

The concept of flooded expansion (and compression) was studied by Hugenroth [98] in a liquid flooded Ericson cycle cooler, which used liquid flooding of both the compressor and the expander (to achieve nearly isothermal compression and expansion) to overcome the practical difficulties of achieving isothermal conditions in the basic reverse Ericson cycle. In a later experimental work [99], off-the-shelf automotive scrolls were used as the compressor and expander, nitrogen as the working fluid and alkyl-benzene as the flooding liquid. The performance of the off-the-shelf scroll machine was not sufficient to achieve high cycle efficiency. For increasing operating pressure ratios, the expander adiabatic efficiency was reported first to increase and then to decrease. This

effect was partly attributed to the limitation of the expander not being designed for liquid flooded operation

To optimize the design of the compressor and the expander, Bell et al. [100] developed comprehensive models of both machines. Validation of the models and optimization of the design were also carried out [101]. The model developed was an extension of earlier models that were developed by Halm [102], and Chen et al [103] for scroll compressors without liquid flooding. The important contribution of the work was said to be the treatment of a mixture of gas and large fraction of oil. Also, Lemort et al. [104] further studied the performance of liquid flooded expansion using scroll expander and developed a detailed model of the flooded scroll expander, to facilitate predictions of the performance over a wide range of operating conditions and design changes. The model was able to predict the shaft power to about 6.7% maximum deviation from measured experimental value.

2.3.2.3 Summary of methods of effecting quasi-isothermal expansion

In summary, quasi-isothermal expansion has been identified as a realistic alternative to adiabatic expansion to improve the work output of vapour power cycle engines. This can be achieved by further heat addition to the working fluid during the expansion process. The heat can be transferred by means of heating the expander external surface, or by means of a secondary heating (flooding) fluid. The expander surface heating is found to be more popular with reciprocating engines, whereas the secondary fluid heating is more popular with rotary engines.

2.3.3 Quasi-isothermal Rankine cycle engines

The quasi-isothermal Rankine cycle is simply a Rankine cycle whose working fluid gains significant amount of heat during the expansion process of the cycle, such that it is somewhere between adiabatic and isothermal, but its reference limit is ideally isothermal, as depicted on the temperature entropy (T-s) diagrams in Figure 2.4. Figure 2.4a shows a case where the expansion starts from a super-heated state [105]; while in Figure 2.4b, the expansion starts from a saturated state [106]. As a result of the heat addition during the expansion process, the spent vapour becomes significantly superheated at the end of expansion, thus necessitating regeneration (utilising the heat available at the end of expansion to preheat the feed working fluid) to improve the thermal efficiency. Studies have shown that the efficiency of the ideal cycle (with isothermal expansion and regeneration) can be up to 93% of the efficiency of a Carnot cycle operating with the same temperatures limits [92]. Where isothermal expansion is not fully achieved, the resulting quasi-

isothermal cycle's performance will depend on the quantity of heat successfully absorbed during expansion, which of course is dependent on the heat transfer technique employed.

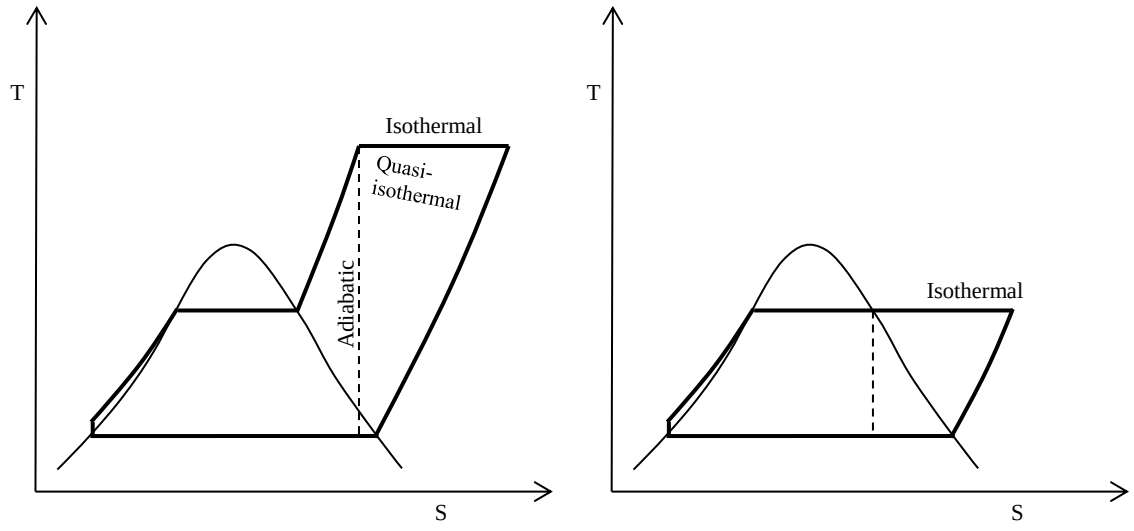

(a) (b)

Figure 2.4: T-s diagrams of Rankine cycle with isothermal expansion , (a) starting from superheated state [92]; (b) starting from saturated state [106].

Using the thermodynamic cycles of Figure 2.4, researchers have proposed and studied different versions of the quasi-isothermal Rankine cycle using different modes of heat transfer. Thus, both liquid flooded and external heated surface machines have been reported. These implementations will now be reviewed.

2.3.3.1 Liquid-flooded Rankine cycle

The idea of liquid flooded expansion can be applied to Rankine cycle, as patented by Woodland [107]. A schematic of the system is depicted in Figure 2.5. The working fluid and the flooding liquid are both pressurised and heated to the required high side pressure and temperature (via separate pumps and heat exchangers). The fluids are then mixed and fed to the expander where they flow together to do work. During the expansion process, temperature drop of the working fluid (vapour) is inhibited by heat gain from the liquid (because the liquid has a relatively higher heat capacity), thus resulting in a near isothermal expansion. At the end of expansion, the superheated working fluid is then separated from the liquid and passed through a regenerator (before being condensed) to preheat the condensed fluid pumped for the next cycle, as the flooding liquid is simultaneously re-pressurized and heated back to the high side conditions.

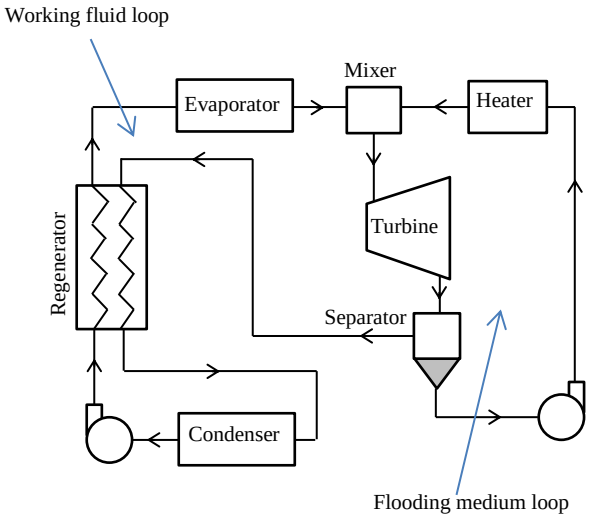

Figure 2.5: Schematic of the liquid flooded ORC [81]

Woodland [81] also carried out theoretical study of the application of liquid flooding to organic Rankine cycle (ORC) with regeneration, for different working fluids (ammonia, carbon dioxide, R410a and dry fluids such as isobutane, n-pentane and R245fa). The analysis showed that, working fluids ammonia and R410a exhibited higher performance improvement due to the flooded expansion. For ammonia, the addition of the liquid flooding offered about 20% more improvement in thermal efficiency. A later study [108] that featured water as a working fluid in the liquid flooded ORC, showed a relative improvement of 10% due to the flooded expansion; the improvement increased with the source temperature. In contrast, the improvement for the dry fluids was significantly less (only about 5%), and approaches zero at higher (>250^{o}C) operating temperatures. Higher work output was expected from the more isothermal flooded expansion than from ordinary expansion process. However, for these dry fluids, the improvement in work output is not high enough to significantly outweigh the additional energy inputs (pump work and heat input) required for the flooding process.

Lemort et al. [82] developed a prototype of a flooded Rankine cycle engine with a hermetic scroll expander and R245fa working fluid. The study was focused on investigating the impact of flooding oil quantity on the expander performance. For operating pressure ratio of 4.2 bar, supply temperature of 92^{o}C and oil mass fraction of 0.023 – 0.1, the results showed that the expander overall isentropic effectiveness (ratio of the measured power output to the ideal expander power) decreased with increasing oil quantity. Further investigation was recommended to ascertain with certainty the underlying reason; nevertheless, increase of supply pressure drops (at the expander inlet) and viscous losses were mentioned as likely reasons for the decrease in performance. This is in agreement with the results of a previous study on the performance of liquid flooded expansion

using scroll expander [104]. For a given pressure level, in the experiment, the measured power output reportedly decreased with the oil flow rate as a result of increasing pressure drops due of the oil suction process at the expander inlet. The study also analysed the variation of exhaust temperature with oil fraction for different operating speeds. As would be expected, the result further showed that the expansion tends to approach isothermal behaviour for higher oil fractions. The range of isothermal expansion (in this case defined as the ratio of discharge temperature to supply temperature) achieved was about 0.93 to 0.99 for oil fractions of 0.2 to 0.8 respectively. This shows that, although the liquid flooding facilitated sufficient heat transfer, such that isothermal behaviour is approached, there are practical challenges in translating it to net performance improvement. Another practical issue worth noting is that the separation of the refrigerant from the oil in the oil separator is not generally perfect, as such some amount of refrigerant usually remain entrained in the oil [99]. This entrainment may pose a durability issue in the long run, as higher oil flow rate will result to larger amount of refrigerant entrained, thus it can result in the need for frequent servicing, as has been observed with oil flooded compressor [109].

For the purpose of increasing the efficiency of a trans-critical CO_2 Rankine cycle thermo-electric energy storage (TEES) system, Kim et al. [110] proposed the application of a variant of the liquid flooded concept to achieve isothermal expansion (and compression) for the discharging (and charging) process of the TEES system. The discharging process is basically the retrieval of mechanical-electrical energy from the stored thermal energy by means of a heat engine (Rankine cycle, in this case). Figure 2.6 depicts the discharging process of the proposed isothermal TEES system.

The system is somewhat like a double cylinder engine. On operation, pressurised CO_2 is heated in the evaporator and fed via valve ‘A’ into the first cylinder which is initially filled with hot liquid. The vapour then exerts pressure and expands against the hot liquid (serving as a liquid piston) which flows through the 4-way valve and the hydraulic motor (wherein the flow and pressure of the liquid is converted into rotary work). During the expansion, the circulation pump continually sprays a portion of the hot liquid unto the expanding vapour, thus providing a means of heating the vapour to effect isothermal expansion. The expended liquid continuous in flow, through the heat exchanger in the hot storage tank and back through the 4-way valve into the second cylinder, thus exhausting the hot expanded vapour in the second cylinder via valve ‘D’ and the regenerator to the condenser. As the stroke ends, the 4-way valve switches to reverse the flow (between the two cylinders), without changing the hydraulic pump’s direction of rotation. An analysis of the system performance for the operating conditions of 160 bar and 122^{o}C showed that the isothermal expansion can result in a 46% increase in work output.

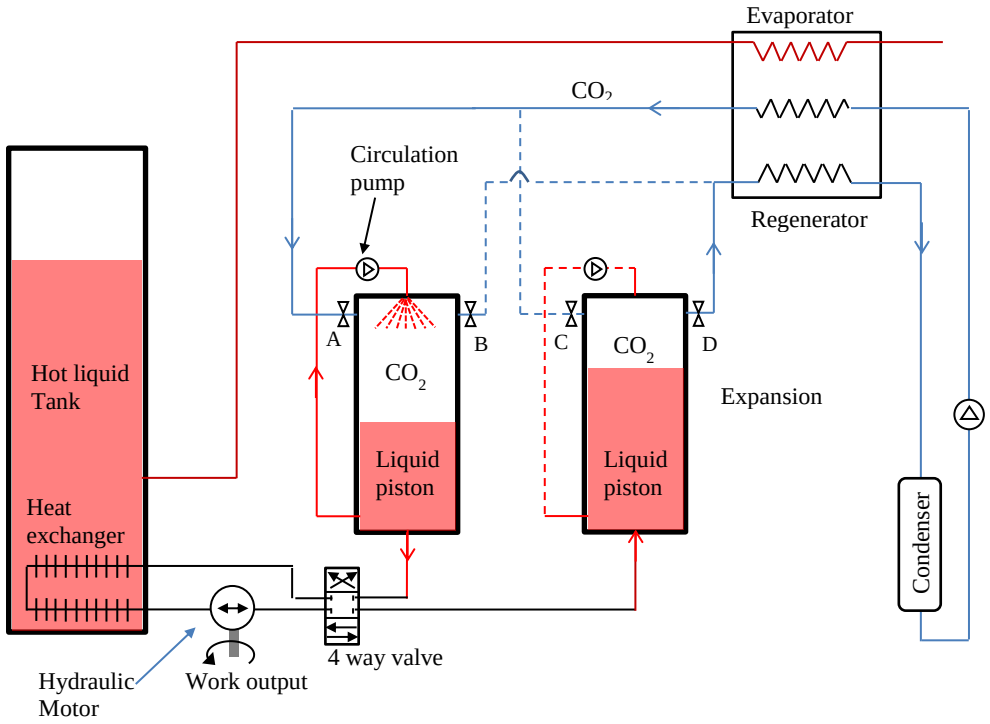

Figure 2.6: Isothermal thermo-electric energy storage (TEES) system [110]

2.3.3.2 Expander surface heated engines

The heating of expanders surfaces have been observed (in literature) mainly with positive displacements expanders including reciprocating piston cylinders, and scroll expanders; however the concept is ideally applicable to other expanders. For reciprocating piston cylinder engines, the steam jacketed steam engine is a classic approach to quasi-isothermal expansion. Nevertheless, certain features and observations are interesting in the modern context where steam or other (organic) working fluids may be used.

In steam engines, there tends to be heat transfer between the steam and the cylinder wall, in such a way that heat is rejected by the steam to the cylinder during the admission and early expansion process, while heat is transferred from the cylinder to the steam in the later part of the expansion and exhaust. This phenomenon is most pronounced for dry steam (relative to superheated steam) as the heat rejection and gain respectively leads to steam condensation on the cylinder wall and re-evaporation of some of the condensate during the rest of the expansion process thus leaving behind some amount of condensate-water in the cylinder. The condensation of steam in the cylinder results in a very rapid drop in maximum pressure and thus decrease in work output, which implies an increase in steam consumption (quantity of steam) required to achieve a given power output. This

consequently results to reduced efficiency, since not all the admitted steam is available to produce work for a given amount of heat energy input to generate the steam [111].

Besides the use of sufficiently superheated steam, or protecting the cylinder with lagging (insulation), steam jacketing the cylinder can be effectively utilised to mitigate the heat loss from the steam. Various experiments carried out by a number of researchers, as recorded by Clark [112] in the 1800*s*, have showed that the alternate condensation and re-evaporation in steam jacketed cylinders are much less than that in unprotected cylinder. The steam jacketed cylinders results to economy in the steam consumption and displayed a greater degree of efficiency than the cylinder with superheated steam, whilst both of them are clearly superior to an unprotected cylinder with saturated steam. The steam jackets have reportedly resulted to economy of 14 - 25% in steam consumption rate per power output, net specific work output increase of 42% (from 224 to 318 kJ/kg) and efficiency (in terms of the total heat passed into the cylinder and the work output) increase of 28% (from 8.65 to 11.05%). Further results showed that better performance was recorded for higher working pressures – this could be explained by the fact that heat transfer is facilitated by higher pressure. It was also demonstrated that by the utilisation of the steam jacket with high temperature, heat can be supplied (from the cylinder to the working steam) in quantity sufficient to prevent (or mitigate) the initial condensation in the cylinder and to re-evaporate the whole of such that may have been condensed.

On the other hand, though the reciprocating heat engine is already a matured technology, the scroll expander engine is a relatively compact device with few moving parts. Scroll expanders and compressors are widely used in refrigeration cycles and have become popular for use in small scale ORC heat engines [113]. Among these, scroll engines using isothermal expansion are an interesting option. Kim et.al. [83] proposed a scroll expander with external heating structure which included external fins attached on the scroll casing and a heating jacket (as depicted in Figure 2.7); such that heat could be effectively transferred from an external source, through the scroll casing into the scroll interior. In the expansion process of the system, the transfer of heat from the scroll interior to the working fluid will reduce the temperature drop that would have otherwise resulted, thus effecting a quasi-isothermal expansion, and consequently contributing to improvement in specific work and thermal efficiency. For air as the working fluid, the isothermal process can result in a potential 34% increase in the expansion work. The system was suggested to be applicable to Ericsson cycle, refrigeration cycle and Rankine cycle.

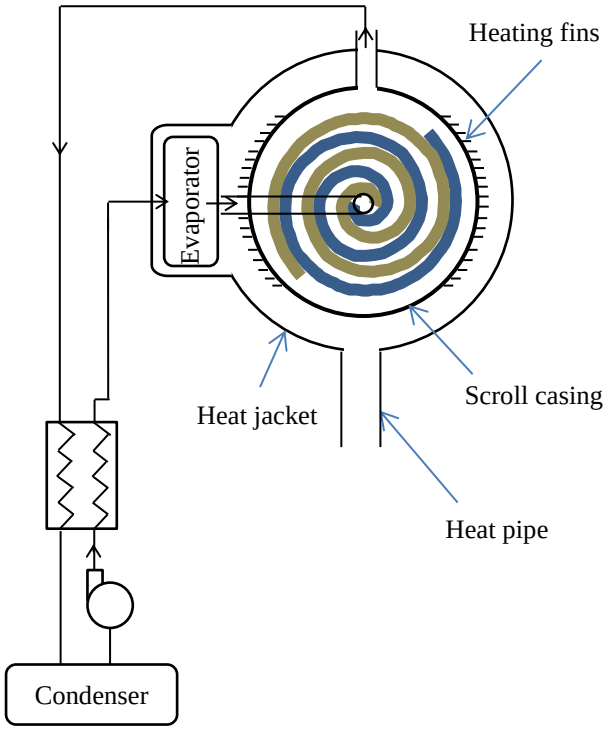

Figure 2.7: Schematic of the Rankine cycle with a heated scroll expander [83]

For use in Rankine cycle, they also highlighted the possibility of the system acting as an expander and partially as a boiler, such that a very wet vapour could be employed as the working fluid at the point of entry into the expander, since the scroll machines are noted for tolerating substantial quantities of liquid fraction. In that case, given that sufficient heat is available from the scroll, the liquid fraction will vaporise during the expansion process, thus tending to reduce the rate of fall in pressure that would have otherwise resulted, and permitting higher volumetric expansion ratio and thereby enhancing the extraction of more work.

2.3.3.3 Summary of quasi-isothermal Rankine cycle engine

To summarise with regard to the Rankine cycle engine and its implementation with quasi-isothermal expansion, the expander surface heating can achieve significant improvement in performance even though the expansion chamber surface area available for heat transfer may not be sufficient to approach the level of isothermal behaviour reported with the liquid flooding system. On the other hand, the liquid flooding may experience deteriorating performance in reality, mainly because, unlike the expander surface heating, the liquid flooding incurs additional pumping energy input (for the liquid loop) and increased suction pressure drop, which (together with other associated losses) can eventually outweigh the expected performance improvements. From the

perspective of technology availability, liquid flooding can be easily implemented, since its main components (scroll compressor, pump and heat exchanger) are readily commercially available. Nevertheless, it is a relatively new technology (that is yet to be fully developed), in comparison to steam jacketing, which can be regarded as a mature technology that has been proven effective and operational. However, for practical consideration for both technologies, proper insulation is recommended, to ensure that the heat loss (from the engine and piping) to the ambient is greatly minimised, so as not to result to a detrimental effect on the overall performance. In addition, further research work should be carried out on modelling of complex, unsteady multi-phase heat transfer with liquid flooding devices; and development of efficient separation mechanism for the flooding liquid separator.

2.3.4 Cryogenic heat engine

Cryogenic engines are another example where quasi-isothermal expansion is used. It is interesting to review the works in this area for possible application of similar features to heat powered engines working at higher temperatures. Cryogenic heat engines utilize the thermodynamic potential between the ambient atmosphere and a cryogenic fluid, which is generally regarded as an energy storage medium. The basic concept of the cryogenic heat engine is to utilize ambient heat from the atmosphere as heat source to heat a pressurised cryogenic fluid which can be used to drive a prime mover. This is in contrast with typical heat engines which utilize an energy source at temperature significantly above ambient and use the atmosphere as a heat sink [87]. As with conventional heat engines, the performance of the cryogenic engine is strongly dependent on the cryogenic working fluid employed. A study pointed out the benefits of using low-mass gases (like H_2, He, Ne, N_2, and air) in two-phase system, as having large maximum specific work values [114], with H_2 having the largest value. Other common cryogens are hydrocarbons, including liquefied natural gas (LNG), of which methane (CH_4) is noted for having high specific work output potential [115]. Nevertheless, liquid nitrogen and liquid air are considered most attractive because they are essentially inexhaustible resource (that can be effectively produced from air) with considerable safety and environmental benefits.

Standard thermodynamic power cycles can be employed to produce useful work from the cryogenic fluid. For instance, a cryogenic gas Stirling cycle could utilise seawater (ambient temperature) as the heat source to heat nitrogen gas in the expander, while liquefied natural gas (LNG) serves as the heat sink to cool the gas during compression [116]. Similarly, ambient evaporation of a cryogenic fluid and condensation by means of LNG as heat sink, can be employed for cryogenic Rankine cycle (Figure 2.8a); and multiple cryogenic cycles can be cascaded to yield better cold energy

recovery (Figure 2.8b and c) [117]. For these closed cycles, propane (C_3H_8) and ethane (C_2H_6) are commonly considered as the working fluids; nevertheless, other low boiling point substances can be employed. The cryogenic power cycle can also be used as the bottom cycle in combined (or hybrid) cycles with other relatively higher temperature power cycles [118]. However, the simplest and most applicable power cycle is the open system (direct expansion) Rankine cycle [119], where the spent exhaust gas is released into the atmosphere. In this case the principle of operation is similar to that of a typical open cycle steam engine.

A schematic of a typical cryogenic heat engine is depicted in Figure 2.9. The cryogenic liquid stored in a tank (which may be vacuum jacketed) is pumped to the required working pressure; the pressurised liquid is then vaporised and heated in an appropriate ambient heat exchanger system, and then fed to an expander, where it expands to do work. Since the rapid expansion process of the cryogenic fluid results in the temperature of the fluid always being less than ambient, the expander will be at a relatively higher temperature than the expanding fluid, thus during the expansion process, further heat may be transferred from the expander to the fluid, resulting to a possible quasi-isothermal expansion process [87]. The T-s diagram of the ideal cycle at critical pressure operation is shown in Figure 2.9b. Process 1-2 indicates the pumping process, process 2-3 is the heating process in the heat exchanger, and process 3-0 is the isothermal expansion. Process 0-4-1 is the condensation stage (for closed loop system), or the liquefaction process which takes place remotely in an air processing plant [120] (for open system).

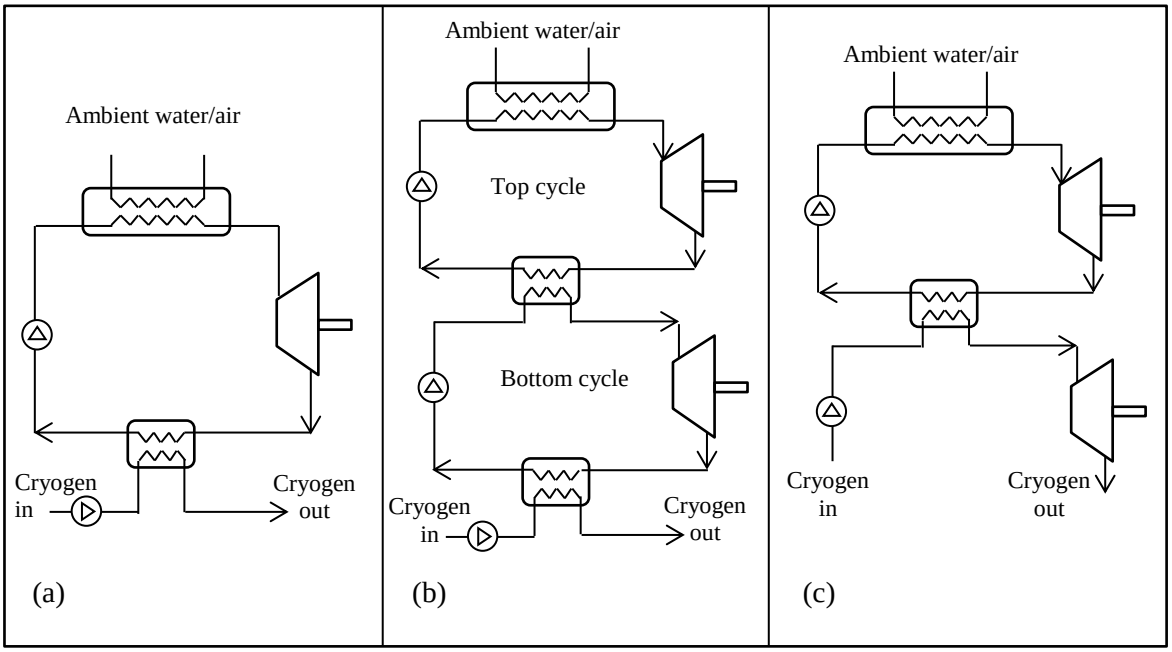

Figure 2.8: Schematic configurations of cryogenic Rankine cycles [115]: (a) Rankine cycle, (b) cascaded Rankine cycle, (c) combined closed-open cycle

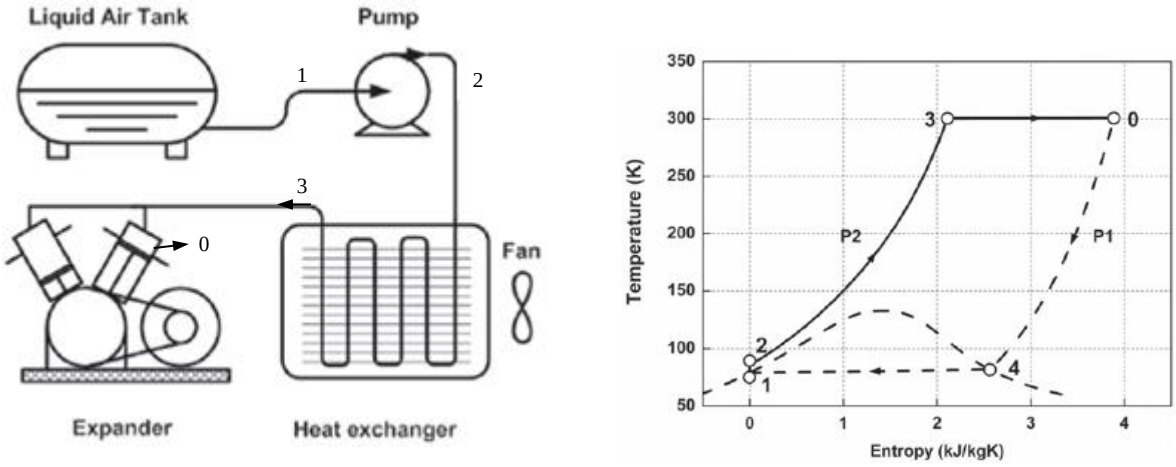

(a) (b)

Figure 2.9: Schematic (a) and T-s diagram (b) of a direct expansion (open system) Cryogenic heat engine [79]

2.3.4.1 Studies and performance

Over the years, there have been investigations on the application of cryogenic heat engine for power generation, and also as an automotive propulsion for non-polluting zero emission vehicles; concept and technical feasibility have been evaluated [121], flow simulations in the engine have been carried out [122], and demonstration models have been built to test its practicality [123]. Key for practical realisation of the engine is the heat exchanger. Considering the low temperature of the cryogenic fluid, it will be essential for the liquid to be vaporized without the accumulation of frost, so as to avoid deteriorating performance. William et al. [124] developed a frost free heat exchanger for using atmospheric air to vaporize and superheat relatively large quantities of liquid nitrogen without the adverse building up of frost. Amrit et al. [125] also developed a cryogenic heat exchanger and presented analytical model for turbulent flows.

Research work carried out at the University of Washington highlighted substantial benefits in the overall energy efficiency for isothermal expander over an adiabatic one, in liquid nitrogen cryogenic engines [126]. The study investigated the specific work output as a function of peak cycle pressure for adiabatic and isothermal expansions and showed that the isothermal work increases monotonically with increasing pressure, while that for the adiabatic process is found to be only weakly dependent on peak cycle pressure above 4 MPa. For pressure range of 10 to 300 bar at 300 K, the net specific work is 190 to 420 kJ/kg and 140 to 190 kJ/kg for isothermal and adiabatic conditions respectively.

Knowlen [127] studied the performance of two cryogens (namely CH_4 and C_2H_6) alongside N_2 for both isothermal and adiabatic expansion, and also showed that for all the working fluids, at a given injection pressure, the specific work obtainable from isothermal expansion exceeded that of the adiabatic expansion, with the difference greater as pressure is increased. The study also examined the use of N_2 as a heat sink for different closed loop CH_4 and C_2H_6 topping cycles, and found that for binary (N_2-CH_4) and ternary (N_2-CH_4-C_2H_6) cascaded cycles, specific energies in the range of 200-380 kJ/kg and 300-450 kJ/kg can be realized respectively, depending on the extent of isothermal operation achievable. Yuanwei et al. [128] proposed a Temperature - Energy level - Energy (T-Ω-H) diagram method for analysing the performance of two different configurations of three-loop cascaded cycles with seawater and LNG respectively as the heat source and heat sink. They claimed that the proposed method facilitates quick optimisation process on a base case design. A number of authors have also explored different closed cycles that use seawater and LNG respectively as the heat source and heat sink. Choi et al. [129] compared the performance of different configurations of two and three loop cascaded cycles and combined (closed-open) cycles in comparison with the conventional single closed or open cycles. The study showed that the cascaded cycles exhibited better performance than the conventional single closed or open cycles; it also showed that, C_3H_8-C_2H_6 cascaded cycle exhibited 51%, 49% and 89% more work output than C_2H_6-C_3H_8 cascade, C_3H_8 and C_2H_6 cycles respectively; while the C_3H_8 cycle gave 27% more work than C_2H_6. Liu and Guo [130] studied a variant of the cascaded cycle combined with vapour absorption process, the cycle employed a binary mixture of Tetrafluoromethane (CF_4) and C_3H_8 as the working fluid. The study showed that, the proposed cycle can achieve 206 kJ/kg specific work output, which is 63% higher than that of a C_3H_8 cycle (124 kJ/kg). In a study by Li et al. [119], an open cycle with two-stage expansion was shown to exhibit 326 kJ/kg work output. This compares reasonably with the performance reported for other two-loop cascaded cycles. Hence, although cascading closed cycles can significantly improve performance, it is also possible to achieve reasonable performance improvement with the relatively simpler open system, with the aid of multiple expansion stages.

In a bid to avoid drop in expander wall temperature, which could result to deteriorating performance, Knowlen [87] suggested the use of "warmant" anti-freeze liquid (as a heat transfer fluid) to be pumped through the wall, so as to maintain it at near ambient temperature. Also, a parametric analysis on engine (reciprocating expander) geometry showed that long strokes, small bore and low RPM enhances heat transfer during the expansion process. Nevertheless, the transferable heat will be limited by the expander's surface area exposed to the fluid, which will limit the degree of isothermal operation achieved. For standard engine (without modifications to cylinder piston geometry), isothermality is typically about 0.75 and can be improved further by enhancing

heat transfer during expansion. Further analysis showed that finned piston and cylinder head geometries (Figure 2.10) having high surface-to-volume ratios can be used to facilitate further heat transfer during the expansion, resulting in potential net work output of 0.85 of the ideal isothermal work.

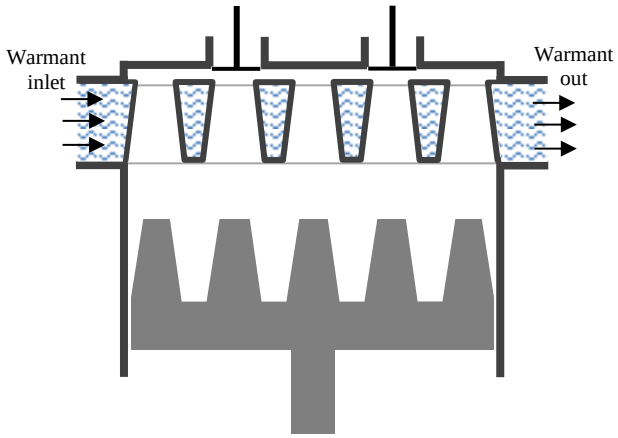

Figure 2.10: Conical finned piston and heater core cylinder head [87]

Liquid air and liquid nitrogen cryogens have also been studied. Liquid air has similar properties to those of liquid nitrogen since air is composed of 78% nitrogen. Chen et al. [79] studied the performance of a liquid air engine for a range of working conditions and reported that, for a properly designed and manufactured engine with operating conditions of 100 bar and 300 K, the practical (taking into account the losses associated with conventional engines) net work outputs of the liquid air engine for isothermalities of $\gamma = 0.90$ and 0.75 were respectively 200 kJ/kg and 150 kJ/kg, i.e. respectively about 122 and 66% higher than that for an adiabatic engine (about 90 kJ/kg). Given that the energy consumption for liquid air production is about 1080 kJ/kg [120], the efficiency of the cryogenic engine (in terms of energy in and energy out) for the above stated isothermalites will be about 18.5% and 13.9%, while that for the adiabatic condition will be 8.3%. However, Ameel et al. [131] indicated that the efficiency of the isothermal cycle can be improved by about 17%, if the liquefaction process is combined with the heat engine.

Dearman [85] developed a variant of the cryogenic engine, whereby the cryogenic liquid is directly injected into a heat exchange liquid (water) in a reciprocating expander, thus the heat exchange takes place inside the engine, consequently eliminating the need for the relatively complicated, heavier and expensive heat exchanger as required previously. The principle of operation is such that, when the piston is at the top of the cylinder, water is admitted into the cylinder dead space, and then a little amount of the cryogen is injected into the water. Since the water temperature (ambient)

is substantially higher than that of the cryogen, the cryogen rapidly vaporises, builds up pressure, becomes superheated and pushes the piston as it expands to do work. At the return stroke, the spent gaseous cryogen and the water are exhausted out. The water can be recovered, reheated and pumped back to the cylinder for another cycle [132].

Wen et al [86] studied the heat transfer behaviour between liquid nitrogen and water (as the heat transfer fluid) in Dearman's engine, and reported a much stronger heat transfer than that obtained from boiling on smooth surfaces and flow boiling through pipes, but comparable to that of rough surfaces and pipes with porous inserts. The pressure was seen to develop very rapidly (up to 500 kPa/s) and increased approximately linearly with the injection pressure; thus indicating that high pressure could be effectively developed to run the engine. Morse and Kytomaa [133] also carried out experimental study of the vaporisation of liquid nitrogen and LNG in water, and found that, the evaporation rate is significantly dependent on both the turbulence intensity of the water surface, and the thickness of the cryogenic liquid layer. However, vaporising LNG in water may require safety precautions against possible ignition of the vapour, as has been reported with incidents of LNG spills at sea [134].

2.3.4.2 Summary of cryogenic heat engine

In summary, the cryogenic engine provides an inherent means of effecting quasi-isothermal expansion with ambient temperature. The potential isothermal performance increases with increasing pressure and could be as much as twice that of the adiabatic case. Cascading multiple cycles would give better energy recovery than single closed or open cycles; however, the open cycle is the most applicable. For an operating pressure of 10 bar, the potential performance of the liquid nitrogen open cycle cryogenic engine can have an ideal efficiency of 19% and specific work of 200 kJ/kg; but this performance is quite low in comparison to the reported 318 kJ/kg specific work achieved for a real surface heated (steam jacketed) engine operated at 5 bar [112]. Furthermore, unlike the surface heated engine, although the cryogenic engine has the advantage of not losing heat to the ambient (since it can be at the same or even lower temperature potential with the ambient), it could suffer evaporative losses and safety (explosion) risks at the storage tank; as it slowly absorbs heat from the ambient, which could result to excessive pressure rise [135].

2.3.5 Vapour Stirling cycle engine

The idealised Stirling cycle is a classical implementation of isothermal expansion. Though ideally efficient, it suffers from low specific power output at moderate temperatures and pressures [136].

As a means of increasing the specific power output, the use of condensable working fluid has been investigated in prior arts – the vaporisation of liquid at the hot side of the Stirling engine followed by condensation at the cold side has been identified as a viable solution [88], the use of refrigerants as working fluid has also been considered [137]. Prior arts (including a number of patents) have investigated various means of employing vapour as the working fluid in the Stirling cycle engine (including liquid-piston variants).

The concept of liquid-piston Stirling (fluidyne) engine is to replace the conventional solid-pistons of Stirling engine with columns of liquid (typically water) in U-tubed cylinder. Unless the liquid in the expansion cylinder has a low vapour pressure at the operating temperature or is separated from the hot gas by some kind of insulating float (generally referred to as dry fluidyne), ample evaporation will take place from the liquid surface and wetted cylinder walls to effect a mixture of gas and vapour working fluid [138]. As such the fluidyne engine can provide both gas and vapour power cycles. One critical design parameter in the fluidyne engine is the frictional losses in the oscillating liquid columns [139]. Studies have shown large dry fluidynes to be quite successful, but on the other hand, small dry fluidynes (which generally suffer from the large transient heat-transfer and flow losses associated with small-diameter tubes) have been reported to be impractical in the absence of evaporation [138]. The evaporation tends to raise the pressure during the expansion phase and thus increases the indicated power in the fluidyne engine. Owing to the fact that the power output is available in the form of pulsating pressure/movement of liquid in a tube, the most obvious application was as a pumping engine [140]. However, a rotating shaft power output option has also been identified, via the use of hydraulic motor [141] or solid pistons [142]; with the former, as shown if Figure 2.11, the solid piston converts the pressure in the liquid piston into a force which can then be applied to a shaft, like conventional engines.

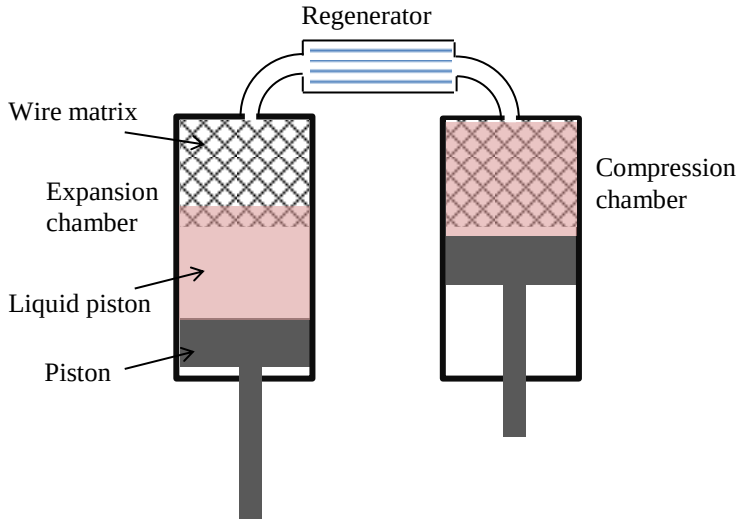

Figure 2.11: Liquid piston Stirling engine [142]

Since liquids can conform to irregular shapes, unlike solid-piston, liquid pistons have the advantage of possibly allowing the adoption of working chambers with very large surface area to volume ratios such as wire matrix, tube bundle, metal foam, etc. (Figure 2.11), to substantially improve heat transfer to the working fluid and consequently bring the working fluid behaviour into the nearly isothermal regime (which will result to improved power output and efficiency). However, the high area to volume ratio will result to smaller size of flow passages, increased flow restrictions and thus, increased viscous losses. As such the heat transfer area and the viscous frictional losses must be adjusted to maximize the efficiency of the liquid piston engine [143]. Besides the increased viscous losses, the liquid piston also suffers operating stroke and frequency limitations imposed by gravity-controlled oscillation and by surface instability at high frequency; and the need to keep a more or less constant orientation of the engine [142].

Various concepts involving the conventional solid-piston Stirling engines variants with modifications on operational configurations have also been recorded. Redderson [69] patented a vapour Stirling machine based on the alpha Stirling configuration. It featured heating and cooling chambers on the hot and cold cylinder tops respectively, and with a regenerator interconnecting the two chambers (Figure 2.12). But in contrast, the working fluid in the cooling chamber is substantially in the liquid phase as such resulting to a significantly larger swept volume ratio than a conventional Stirling engine. On operation, the upward motion of the cold cylinder piston pumps the fluid through the regenerator into the hot chamber where it gets completely vaporised and superheated and then expands to perform work against the hot piston while gaining further heat from the hot chamber, thus tending to approach isothermal expansion. At the end of expansion, the upward motion of the hot piston pushes the spent vapour through the regenerator and into the condenser where it condenses back to water. As a means of providing output control, a control cylinder is included at the cold section to vary the effective mass of the working fluid within the engine.

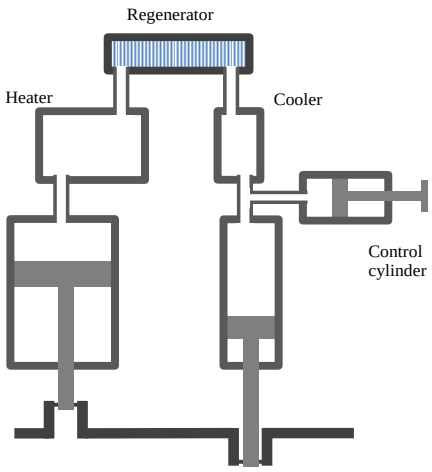

Figure 2.12: Vapour Stirling engine [69]

Davoud and Burke [144] patented a condensing vapour Stirling engine, in which at the end of expansion, a portion of the spent vapour is expelled (via a receiver cylinder) and condensed, while the remaining portion is compressed in the power cylinder, during which the weight equivalent of the condensed portion is pump and injected back into the cylinder as a fine spray of water. This was said to lower the entropy and enthalpy of the steam in the cylinder, and thus lower the compression work that would have been required. The compressed steam gets superheated in the heater tubes arrangement at the top dead centre of the cylinder, and then expands against the piston to do work. They later went further to patent a simpler version (with only one cylinder), in which bulk of the spent steam is expelled directly to the condenser. The condensed water is then pumped and injected into the cylinder top dead volume containing the heater tubes where it gets vaporised and superheated [145].

2.3.5.1 Studies and performance

West [88] developed a two-phase, two component working fluid system for an alpha Stirling engine configuration (Figure 2.13), in which, the working fluid consists of both a condensable vapour (steam) and permanent gas (air), such that the air is contained in the cold section, and prevented from passing into the hot section by means of controlled evaporation (i.e. steam pressure) in the hot section. Water injected into the evaporator vaporises into the hot cylinder where it expands to do work. The expended vapour then passes into the cold end where it condenses and is subsequently removed.

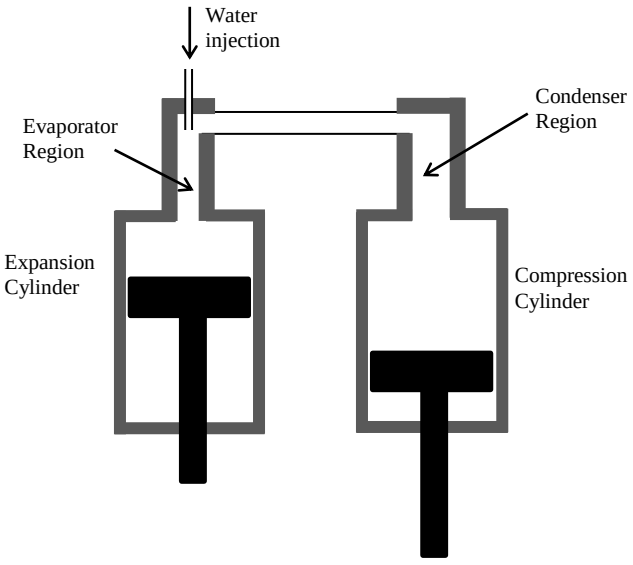

Figure 2.13: Basic layout of the two-phase, two-component Stirling engine [88]

The analysis showed that under moderate operating conditions the engine can achieve a cyclic power output at least five times greater than a conventional Stirling-cycle machine of similar dimensions, but at the expense of significantly lower ideal cycle efficiency. Nevertheless, by controlling the rate at which the liquid is evaporated into the expansion cylinder an indicated efficiency in the range of 3 to 9% at low temperatures (110°C to 130°C) may be achievable even without regeneration.

Isshiki et.al. [89], developed a steam Stirling engine which operates as a hybrid of Stirling and Rankine systems, such that the engine featured a power cylinder (with heating tube at the cylinder top), displacer cylinder and a regenerator in between, as with Stirling; but also has injection/exhaust port, thus spent steam could be ejected, condensed, pump and re-vaporised externally just like Rankine. On operation, when the power piston comes near its top dead centre, saturated steam from the external boiler injected into the displacer cylinder, passes through the regenerator and heater, and then expands into power cylinder at near constant high temperature. On the return stroke, the spent steam passes through the regenerator and is exhausted to a condenser where it gets condensed and then pumped back to the boiler. Experiments carried out on a mini scale prototype operated at 0.2 Mpa (gauge) and 250°C showed that output power of about 12 watt was achieved at 400 rpm. This is significantly higher (approximately five times) than the reported 2.6 watt achieved for a conventional gas Stirling engine operated at 320^{o}C [146].

2.3.5.2 Summary of vapour Stirling engines

In summary, the use of vapour as the working fluid in Stirling engines can result in power outputs about five times larger compared to conventional non-condensable gas working fluid. To facilitate more heat transfer to the fluid to approach a more isothermal behaviour, liquid pistons could be employed to allow the expansion space to be enhanced with high surface area geometries like wire matrices. However, it introduces practical issues that will need to be further investigated. As such it is recommended that further research be carried out on: modelling the behaviour of the oscillating liquid in liquid piston devices with particular attention to viscous forces and inertia effect of the liquid oscillation. Since the various technologies presented are still in the concept or early development stage, further experimental studies should be carried to give a better insight on their practical realisations; and optimization of the various full engine dynamics to maximize efficiency and power density for specific applications.

2.4 Review Summary

Heat cycle engines can be employed to convert low grade thermal energy into useful work to drive RO desalination systems. Here, the higher the thermal to mechanical energy conversion efficiency, the higher the desalinated water output per unit of thermal input, thus high thermal efficiency is desirable for improved heat utilisation and water production. For typical low temperature (<180^{o}C) Rankine cycle heat engine driven RO system, organic working fluids promises better performance than the conventional use of water as a working fluid. However, thermal efficiencies are generally low at the low operating temperatures.

As a means of improving the performance of the heat engines, relative to the traditional ideal adiabatic expansion, isothermal expansion (continuous heat addition to the working fluid during the expansion process) has been identified to improve the specific work output and cycle efficiency of the engines. Variants of vapour power cycle heat engines with such isothermal operation include Rankine cycle with continuous heat addition during the expansion process, Cryogenic heat engines, and Stirling cycle with a condensable vapour as working fluid. The vapour Stirling cycle exhibits higher specific work output compared to the traditional Stirling engines using gas.

Two main methods of effecting the quasi-isothermal expansion have been identified – liquid flooding and expander surface heating. In practical performance of the quasi-isothermal expansion, studies have showed that liquid flooded expansion approaches isothermal behaviour with increasing oil fraction; but at the expense of deteriorating overall performance, that was partly attributed to the resulting increased suction pressure drop and viscous losses. On the other hand, the expander surface heating has been shown to achieve significant improvement in performance (over 40% and 20% increase in specific work output and efficiency respectively). Here, a relatively slower operating speed is required to enable significant heat transfer during the expansion process as the cylinder wall surface area available for heat transfer limits the isothermal operation. However expander geometries with high surface-to-volume ratios (such as fins) could be employed to facilitate heat transfer and further improve performance, as has been demonstrated with cryogenic engine. Furthermore, much higher surface area to volume ratios (such as wire matrix) could be easily realized with the adoption of liquid pistons.

While the quasi-isothermal vapour power cycle engines have the potential to significantly improve performance, there are research areas to be further examined. This may require further research be carried out on: modelling of complex, unsteady multi-phase heat transfer with liquid flooding devices to predict performance and tailor to applications; modelling the behaviour of the oscillating liquid in liquid piston devices with particular attention to inertia and viscous losses; and the

investigation (selection) of other appropriate liquids and working fluids for a range of low temperature operations. Further experimental studies are also recommended to give better insights on the practical realisations and optimisations of the technologies presented.

This chapter concludes that while the traditional ORC-RO is promising in low temperature application, improvement in performance can be sought through the use of the new isothermal techniques. However, there are research areas that need further examination. The relevant research gaps that need addressing by this thesis can be briefed as part of the objectives of the aims of the thesis, as presented in the next section.

2.5 Aims and objectives of the thesis

In light of the foregoing, this thesis broadly sets out to make advances with regards to efficiency improvement in small scale thermal engine applications – particularly the use of low-temperature engines to drive RO desalination process to recover freshwater from saline groundwater. To achieve this, reviews of the state of the art in the use of low-temperature Rankine cycles coupled to desalination by Reverse Osmosis, and the current methods of achieving thermal efficiency improvements by isothermal expansion, have been carried out; consequently, the following objectives are considered.

- Develop theories to represent the operation of the isothermal Rankine cycle for use in desalination
- Evaluate experimentally and theoretically, alternative methods of achieving isothermal expansion
- Design and build test engine to ascertain the practicability – including selection and evaluation of an appropriate working fluid for isothermal operation and to meet technical and environmental constraints
- Optimise the engine for low temperature operation, in the context of specific case study applications
- And finally use the engine to drive a pre-built desalination system to produce fresh water.

2.6 Thesis outline and structure

The first chapter (**Chapter 1**) introduced the motivation and scope of the research work. The global energy challenges and the prevalent shortage of improved water situation were presented. Overviews of the potential measures to address the situation were also outlined.

This chapter (**Chapter 2**) have reviewed the use of low temperature heat cycle engine to drive RO desalination system. After highlighting the benefits of vapour power cycle with isothermal expansion over the more common adiabatic expansion, it proceeded to review various vapour power cycle heat engines with isothermal expansion, and the different methods employed to realize the isothermal heat transfer.

Chapter 3 describes the development and set-up of two preliminary experiments; aimed at analysing the practicality of two different concepts of the heat engine with isothermal expansion – expander surface heating and regenerative liquid flooded expander – and selecting the optimum design (in terms of practicality and performance) for further development.

Chapter 4 redesigns and optimises the selected concept for low temperature application. Here, various organic working fluids are screened for isothermal operation for maximum energy efficiency and engine size requirement; as a result, R245fa is found as one of the potential organic fluids. And a prototype isothermal ORC test engine is built for more detailed experimental analysis.

Chapter 5 describes the scaling up and integration of the isothermal ORC engine to drive a batch RO desalination machine (DesaLink), and the experimental results of the integrated system for various operating conditions.

Chapter 6 presents analytical models describing the systems cycle. Models of individual subsystems are first developed based on physical relations between input and output parameters, and then validated by experiments results. The full model that combines the individual models is thereafter developed within Engineering Equation Solver (EES) environment.

Chapter 7 presents case studies to provide insights on the potential on-site performance of the integrated system. Here, India and USA are considered for solar thermal and waste heat energy sources respectively.

Chapter 8 gives the conclusion of the thesis, including the research outcomes with particular reference to the original aims. The main contributions of the research and recommendations for potential further work are also outlined.

Chapter 3 Preliminary assessment of variants of isothermal Rankine cycle engine

This chapter analyses and compares experimentally two methods of effecting quasi-isothermal expansion in steam power cycle (surface heated expander and liquid piston regenerative expander) in terms of performance and practicality, with the aim of selecting the optimum variant for further development. A thermodynamic analysis of the isothermal cycle is introduced as a basis for theoretical development of these two variants and subsequent developments in the thesis. In preliminary experimental analysis, relatively higher efficiency was obtained from the surface heated variant in comparison to the regenerative (12% relative to 4.5%). The performance of the liquid piston variant was mired by practicality issues that would require further work to address; as such the surface heated variant was preferred. Some of the work presented in this chapter has been published by the author in the 'International journal of low-carbon technologies'[84].

3.1 Introduction

As reviewed in the previous chapter, the Rankine cycle heat engine is popular in converting thermal energy into mechanical power; and efforts to improve its performance have included heat addition during the expansion process, thus resulting in quasi-isothermal expansion – where the heat absorbed by the working fluid is not sufficient to maintain isothermal expansion. Amongst other factors, the heat transfer to the working fluid strongly depends on the geometry of the expansion chamber (i.e., the chambers' surface area available for heat transfer). Furthermore, the surface heated expander and the liquid piston regenerative expander were identified as promising means of effecting heat transfer to heat engine's working fluid during expansion. Standard reciprocating engines (without modifications to piston/cylinder wall) have limited surface area for heat transfer, on the other hand, modifications to the cylinder base and piston with fins can tend to potentially increase the surface area, however, this has practicality issues of the need to maintain alignment between mating surfaces.

Besides the practicality issues, the surface area-to-volume ratio obtainable from this (fin) modification could be considerably less when compared to porous materials (such as wire mesh, metal foam, metal wool etc). These high surface-to-volume ratio porous materials have been investigated by a number of researchers for various heat exchanger applications including

regenerators for Stirling cycle, thermal storage, and convective heat transfer enhancements [147, 148]. Prasad et al [149] experimentally investigated the heat transfer performance of wire mesh in solar packed bed air heater, and found that thermal efficiency enhancement of 75-90% can be obtained relative to conventional solar air heater. Abduljalil et al [150] carried out an experimental analysis to compare the performance of six different porous materials (steel scourers, steel wool, wire mesh screen and ceramic substrate) in regenerator application. The result showed that the steel wool and steel scourers performed poorly, relative to the ceramic substrate and the wire mesh. The poor performance of the wool and scourer was attributed to relatively higher friction pressure drop. A numerical study by Coasta et al [151] developed friction pressure drop correlation by characterising pressure drop phenomena in woven wire matrix. The developed correlation was able to predict pressure drop to less than 5% deviation from experimental data. An experimental study on packed spheres matrix, by Trevizoli et al [152], highlighted that average pressure drop exhibits parabolic increase with the operating frequency or superficial fluid velocity.

Considering the high heat transfer potential of the porous materials, the concept of employing them in the expansion chamber to expedite heat transfer to the working fluid during expansion is worth exploring. However, this will necessitate the adoption of a liquid piston (as noted in the previous chapter) to transmit the working fluid's pressure through the matrix unto a conventional solid piston where work can be extracted conventionally. Conversely, here, the liquid piston (besides being incompressible and immiscible with the working fluid) will essentially be a thermal fluid that will serve to heat the regenerator matrix. Although friction/viscous losses are expected as a result of the fluid flow restrictions through the matrix, this effect could be less daunting at low operating speeds, thus possibly better suited for slow speed applications.

In other to assess the practicality of this concept (regenerative expander) in comparison to the surface heated expander variant, this chapter will experimentally investigate the performance and practicability of both variants (for steam cycle) under similar operating conditions/parameters; and select the optimum for further development. Modelling of the general isothermal cycle will be presented to estimate the potential performance in terms of efficiency and work output. For the surface heated variant, standard piston cylinder geometry will be considered for the sake of simplicity; while for the liquid piston variant, various porous materials will be analysed to select a low cost material that can yield reasonable performance based on surface area-to-volume ratio.

3.2 Performance analysis of ideal isothermal expansion

The ideal isothermal (Rankine) cycle only differs from the classic Rankine cycle, mainly that, constant temperature is maintained during the expansion process in the former. The performance of the ideal/reversible isothermal cycle (the non-ideal practical issues will be considered in the next chapter) can be analysed with the aid of the T-s diagram (Figure 3.1) with reference to the numbered states (1-6). State 1-2: heat addition to the water, 2-3: water vaporizes and expands at constant temperature (full expansion is assumed here for the ideal cycle), 3-4: exhaust of spent vapor, 4-5: condensation, 5-6: condensate water pumped (pressurized) back to repeat the cycle (state 6=1).

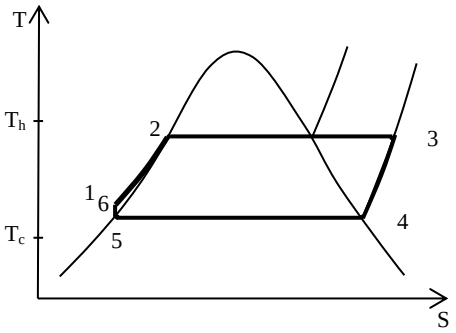

Figure 3.1: T-s diagram of the isothermal Rankine cycle

3.2.1 Cycle efficiency and work output

A general analysis of the ideal isothermal steam cycle can be carried out with the help of reasonable assumptions, namely:

(i) the heat capacity c_{pf} in the liquid phase is constant from state (6) to (2);

(ii) similarly the heat capacity c_{pg} in the vapour phase is constant from state (3) to (4); and

(iii) the work input to the pump is very small, so effectively the states (5) and (6) coincide on the T-s diagram.

(iv) a regenerator with 100% effectiveness is applied

(v) since full expansion is assumed for the ideal cycle, blow down is ignored

The efficiency, η, of the cycle is given in terms of the specific heat input or rejected between different stages of the cycle:

$$\eta = 1 - \frac{q_{out}}{q_{in}} \tag{3.1}$$

$$\eta = 1 - \frac{q_{out45}}{q_{in12} + q_{in23}} = 1 - \frac{q_{out45}}{(q_{in52} - q_{out34}) + q_{in23}} \tag{3.2}$$

From fundamental thermodynamic relations:

$$q_{in23} = T_h(s_3 - s_2) \tag{3.3}$$

Thus

$$\eta = 1 - \frac{h_{fg}}{(c_{pf} - c_{pg})(T_h - T_c) + T_h(s_3 - s_2)} \tag{3.4}$$

And using the general thermodynamic relations

$$s_3 - s_4 = c_{pg} ln\left(\frac{T_3}{T_4}\right) \tag{3.5}$$

$$s_2 - s_5 = c_{pf} ln\left(\frac{T_2}{T_5}\right) \tag{3.6}$$

With

$$s_3 - s_2 = (s_3 - s_4) + (s_4 - s_5) + (s_5 - s_2) \tag{3.7}$$

And

$$s_4 - s_5 = \frac{h_{fg}}{T_c} \tag{3.8}$$

Leads to

$$\eta = 1 - \frac{\left(\frac{T_c}{T_h}\right)}{1 - \varphi\left[\frac{T_c}{T_h} - 1 - ln\left(\frac{T_c}{T_h}\right)\right]} \tag{3.9}$$

Where,

$$\varphi = \frac{T_c(c_{pf} - c_{pg})}{h_{fg}} \tag{3.10}$$

In which h_{fg} is the latent heat at T_c. It can be seen that if $\varphi = 0$, the efficiency will equal the Carnot efficiency $\eta_{cnt} = 1 - T_c/T_h$. The value of φ will depend on the fluid properties and operating temperatures. In this paper we consider only steam though other working fluids are possible. For

example, for T_c = 50°C, we find that for a substantial range of temperatures c_{pf} = 4.2 kJ/kg K and c_{pg} = 2 kJ/kg K, thus φ = 0.3. The corresponding results for the cycle efficiency and, for comparison, the Carnot efficiency are shown in Table 3.1. It can be seen that the theoretical cycle efficiency is close to the Carnot value.

Table 3.1: Isothermal Rankine cycle efficiency

T_h (°C)	@ T_c = 50°C		@ T_c = 99°C	
	η	Carnot η_{cnt}	η	Carnot η_{cnt}
175	0.268	0.279	0.166	0.17
200	0.304	0.317	0.207	0.214
250	0.363	0.382	0.277	0.289
300	0.412	0.436	0.335	0.351
350	0.453	0.482	0.382	0.403

Isothermal Rankine cycle efficiency η, and Carnot efficiency η_{cnt}, for different T_h and T_c

However, the work output can be obtained from non-flow energy relations, as:

$$w_{out} = q_{in} - (u_3 - u_2) \tag{3.11}$$

And the work ratio r_w can be given as:

$$r_w = \frac{w_{out} - w_{in}}{w_{out}} \tag{3.12}$$

Where w_{in} is the pump work, which can be obtained in terms of the average specific volume, v_f, within the operating pressure range, as:

$$w_{in} = v_f(P_6 - P_5) \tag{3.13}$$

3.3 Surface heated expander

The surface heated expander is proposed to require no separate boiler; instead the working fluid is heated inside the power cylinder – provided sufficient heat is supplied. A schematic layout of the system is depicted in Figure 3.2. Operation may be described as follows. The power cylinder is heated externally by a heat transfer fluid (e.g. thermal oil) which is supplied from solar collectors or other heat source. Water injected into the cylinder evaporates on contact with the walls, thus expanding at constant temperature and performing work against the piston. Due to further heat transfer from the cylinder walls, the water vapour continues to expand at constant temperature until

the end of stroke. On the return stroke of the piston, the steam exits via a valve, and passes through a regenerative heat exchanger whereby its temperature is reduced to the temperature inside the condenser. Before being returned to the injector, the condensed water is pressurized by the feed pump and preheated in the heat exchanger.

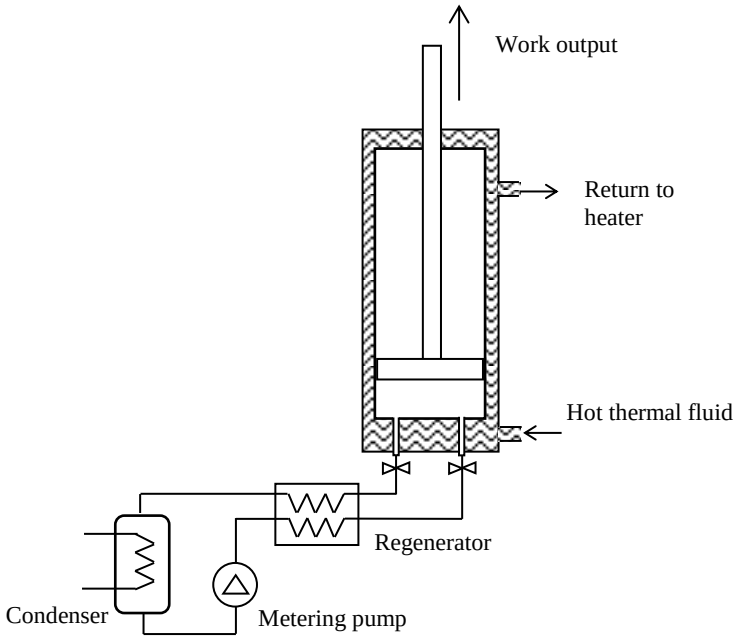

Figure 3.2: surface heated expander schematic

3.3.1 Rate of heat transfer

The performance of the proposed machine will depend on the rate of heat transfer from the heated cylinder wall to the working fluid; hence, to assess the feasibility of the cycle with regards heat transfer, calculations have been carried out of the rate of convective and radiative heat transfer as follows.

3.3.1.1 Convective heat transfer

The convective heat transfer between the cylinder wall and the steam can be given as:

$$\dot{Q} = \alpha\, A_{\text{ш}}\, (T_{\text{ш}} - T_g) \tag{3.14}$$

where α is the convective heat transfer coefficient, which will be calculated from the Nusselt number $Nu = \alpha D/k$. For gases, Nu can in turn be correlated to Reynolds number (Re) as

$$Nu = a\, Re^{b} \tag{3.15}$$

$$(10^3 \leq Re \geq 10^5)$$

Note that D is cylinder bore diameter, k is thermal conductivity of the gas, Re is Reynolds number defined as $Re = \rho V D/\mu$, where ρ = gas density, V = mean piston speed, μ = dynamic viscosity, a and b are correlation constants.

In the study of heat transfer in reciprocating internal combustion engines, Annand's correlation is one of the most widely used correlations [153, 154]; it suggests that the value of constant *a* varies from 0.25 to 0.8, and that it increases directly with increasing intensity of gas motion [155, 156]. Typical Annand recommended values of a and b are 0.4 and 0.7 respectively, but Whitehouse recommended values of a = 0.06 and b = 0.85 for a medium speed engine [157].

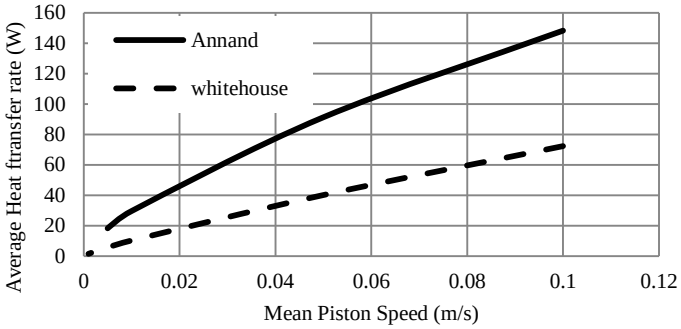

Figure 3.3: Average heat transfer rate variation with mean piston speed

In our study, the analysis of the heat transfer rate using Annand and Whitehouse correlations (Figure 3.3) shows that, the convective heat transfer approaches zero as the engine runs at very slow speed. As such, for a given slow piston speed (<0.01m/s), the resultant forced convective heat transfer alone cannot supply all the required heat to sustain isothermal expansion.

3.3.1.2 Radiative heat transfer

The radiative heat transfer between the cylinder wall and the steam can be computed from the grey body equation [111]

$$Q = \frac{\epsilon_{\text{ш}}\,\epsilon_g}{1-(1-\epsilon_{\text{ш}})(1-\epsilon_g)} A\sigma(T_{\text{ш}}^4 - T_g^4) \tag{3.16}$$

$$Q = \frac{\epsilon_{\text{ш}}\,\epsilon_g}{1-(1-\epsilon_{\text{ш}})(1-\epsilon_g)} A(q_{b\text{ш}} - q_{bg}) \tag{3.17}$$

Where, $\epsilon_{\text{ш}}$, $T_{\text{ш}}$ and ϵ_g, T_g are the emissivity and temperature of the cylinder wall and steam respectively, A is the heat transfer area (cylinder and piston surface area). The term σT^4 (Stefan-

Boltzmann law) is equal to the total energy emitted q_b per unit time, per unit area of a blackbody for all wavelengths.

The equation assumes non-selective (constant) emissivity and thus cannot be directly applied to obtain the energy transferred because the absorptivity and thus the emissivity of the steam varies with wavelength; therefore we can write ϵ_g as a function of wavelength as $\epsilon_{g\lambda}$. Hence, considering that, both the wall's emitted energy and the steam's absorbed energy vary with the wavelength of the radiation spectrum, it will be worthwhile to analyse these energies in their spectral components, to evaluate the energy transferred over the whole spectrum.

Consider the energy absorbed within an elemetal range of wavelengths (waveband) d_λ. The amount of energy dQ_λ absorbed per unit time within the waveband d_λ can be written as

$$dQ_\lambda = Q_\lambda \, d_\lambda \tag{3.18}$$

Thus, the total amount of energy absorbed by the steam can be written as

$$Q = \int Q_\lambda \, d_\lambda = \int_0^\infty \left[\frac{\epsilon_{\text{ш}} \epsilon_{g\lambda}}{1-(1-\epsilon_{\text{ш}})(1-\epsilon_{g\lambda})} \, A \, (q_{b\text{ш}\lambda} - q_{bg\lambda}) \right] d\lambda \tag{3.19}$$

To assess the rate of radiative heat transfer achievable in practice, we carried out an analysis of radiant heat transfer assuming that the cylinder wall is a grey surface with emissivity of 0.57 at a temperature of 250°C. The optical absorptivity of water vapour in the infra-red region was modelled using SpectralCalc® software. For example operating parameters of: piston area 0.035 m^2, stroke length 0.228 m, cylinder volume 0.008 m^3, and expanding steam pressure decreasing from 9 bar to 1.8 bar isothermally at 175^{o}C, it was found that the absorptivity and thus the absorptance (the absorptive power per unit area) decrease as the piston advances; but the increase in the surface area of heat transfer exposed to the steam (in relation to increase in length of stroke) results in a steep increase in the energy emission rate from the cylinder wall, and consequently results in a net increase in the energy absorption rate of the steam (Figure 3.4). For this example, the heat required to maintain isothermal expansion of the steam is 3 kJ, and it was deduced that radiant heat transfer alone could supply this required heat in 37 s.

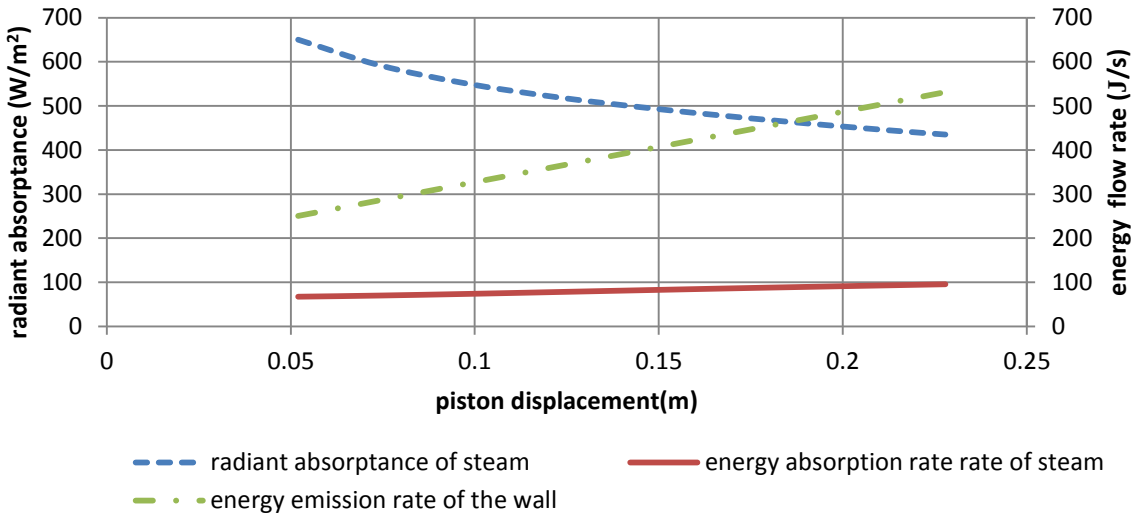

Figure 3.4: Variation of heat absorption with expansion

Parametric calculations carried out to analyse the effect of operating parameter variations on the heat transfer time is shown in Figure 3.5 for a cylinder diameter range of 1 to 200 mm with steam pressure decreasing from 9 to 1.8 bar. The analysis shows that there is a very strong positive correlation (R^2 = 0.996) between size and the radiative heat transfer time; the time required for isothermal expansion to be achieved reduces for smaller cylinders. This can be explained by the surface area available for the heat transfer. The surface area relative to the expansion volume i.e surface area-to-volume ratio ($SA{:}V$) can be shown to be obtained as:

$$SA{:}V = \frac{2D + 4L}{DL} \tag{3.20}$$

where, D and L are the cylinder/piston diameter and stroke length respectively. The surface area-to-volume ratio decreases with larger cylinder diameters (Figure 3.6); and for a given cylinder diameter, it can be seen to decrease sharply from the onset of the expansion stroke up till stroke length of about a quarter of the diameter, beyond which the decrease flattens.

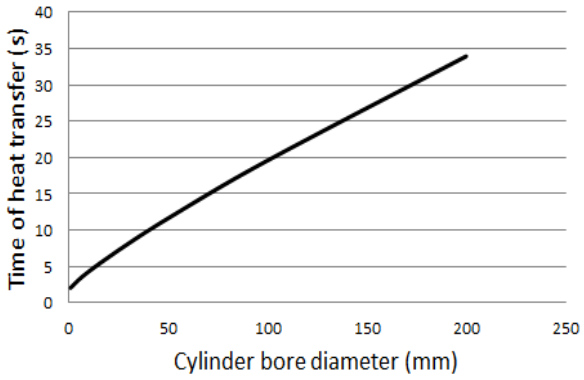

Figure 3.5: Effect of size variation on heat transfer time

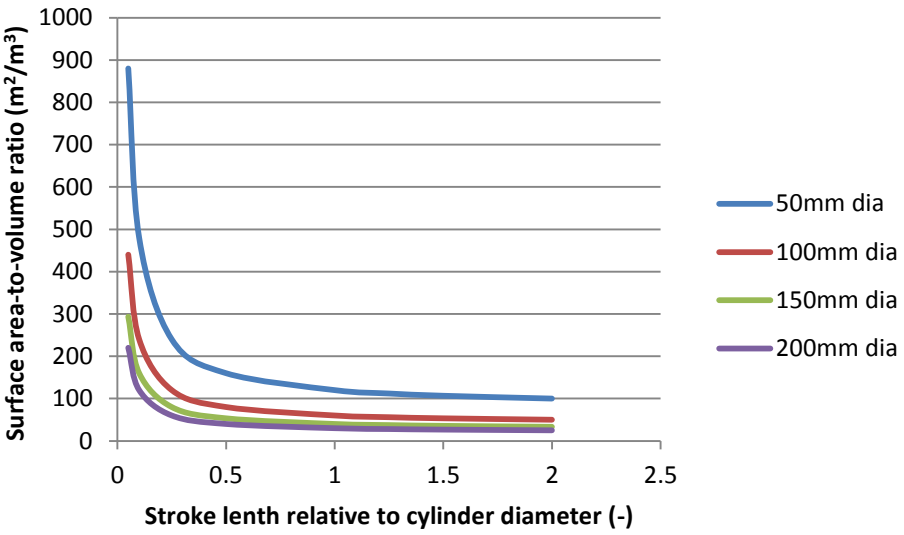

Figure 3.6: Surface area-to-volume ratio variation with stroke length

The heat transfer analysis shows that for very slow piston speed (<0.01 m/s) applications, radiation plays significantly a dominant role over convection in heat transfer to the steam. And the heat transfer rates suggest that it is feasible for the cycle to ideally achieve isothermal expansion. And this can be achieved faster for smaller cylinders.

3.3.2 Surface heated expander preliminary Experiment

To examine the feasibility of the proposed isothermal engine, a pilot experiment is carried out with the aim of accessing the piston output force achieved for different quantities of input water, and the corresponding work output and thermal efficiencies achieved in comparison to the ideal cycle.

The experimental set up included a power cylinder, which was adapted from an off-the shelf pneumatic cylinder (SMC95) with a 1 MPa rated maximum pressure. To simulate solar or other thermal power source, electrical heaters were used. The standard cylinder base was replaced with a bespoke aluminium base fitted with an injection nozzle, a pair of cartridge heaters, thermocouple (K type, accuracy ± 2.5^{o}C), and insulation pad; while the cylinder wall was equipped with trace heating tape and a thermocouple. The cylinder/piston seals were replaced with high temperature O-rings; Viton O-rings (rated 220^{o}C) were used for cost savings, although other higher temperature seals such as Kalrez (rated 300^{o}C) would have provided better tolerance. The assembly was insulated with Superwool insulation blanket. The temperature of the cylinder wall was controlled by means of PID temperature controller (XMT7100).

The pump was assembled from a double acting 10 mm bore cylinder (SMC-C85) configured as a metering piston pump by means of two reversed non-return valves connected at the outlet port. This

configuration employed standard parts to minimize build time and development cost. The choice of the piston pump enabled metering of very small volume of water (<3 mL), which could be driven mechanically or pneumatically. The test system parameters and operating conditions are listed in Table 3.2.

Table 3.2: System parameters for surface heated expander

Parameter	Value
Cylinder Bore	100 mm
Piston Stroke	100 mm
Wall temperature	250^{o}C
Heating power	300 W
Engine speed	150 mm/min

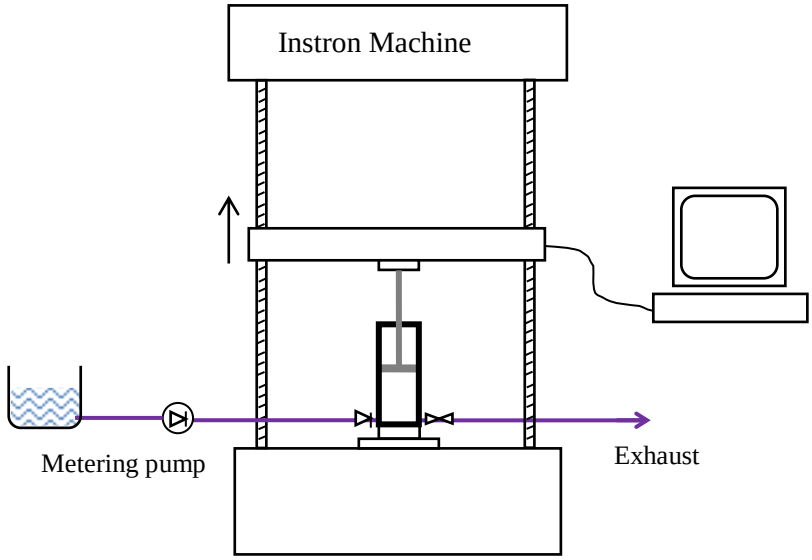

Figure 3.7: Schematic of experimental set-up for surface heated expander

3.3.2.1 Test procedure

The experimental set-up is depicted in Figure 3.7. The material testing machine (Instron® 5500R) was used to provide a means of variable resistance to motion (controlling the speed of expansion) and related data acquisition. On the start of operation, the metering pump injected the required volume of water into the heated cylinder. The water on vaporization into steam, expanded and pushed the piston against the load beam (incorporating a load cell) of the material testing machine; the resulting force (which is a measure of the steam pressure) and piston displacement were recorded in the computer as the load beam retreated. Values of the force (corresponding to the

cylinder pressure), piston displacement and steam temperature were collected at various operating parameters, for analysis.

3.3.2.2 Results

The performance indicators taken into account were the expander output (piston force), the work output, and the cycle efficiency.

The cycle efficiency η can be given as:

$$\eta = \frac{w_{out} - w_{in}}{q_{in}} \tag{3.21}$$

Where w_{in} is the pump work, which is a product of the driving pneumatic pressure and the swept volume, while w_{out} is the work done by the expander piston, and q_{in} is the heat input to the water and steam, which will be integrated approximately, using the trapezium rule as:

$$q_{in} = \frac{1}{2}(T + T')(s'_g - s_f) + \frac{1}{2}(T' + T'')(s''_g - s'_g) \tag{3.22}$$

Where, T' and s'_g are the temperature and specific entropy of steam corresponding to the pressure at the end of vaporization; while T'' and s''_g are obtained at the end of expansion.

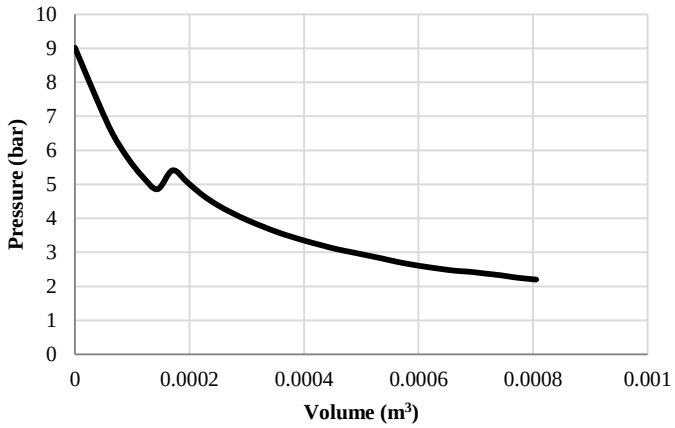

Figure 3.8: Pressure–volume (*p*-*V*) diagram of the surface heated expander

Figure 3.8 shows the pressure (abs) variation with volume of the steam from 0.8 mL injected water. The kink on the curve corresponds to the time it takes for the injected water to be completely vaporized. Thus, in the region to the left-side of the kink, the fluid is a liquid-gas mixture. As shown in Figure 3.9, output piston forces ranging from 4 kN to 13.2 kN were achieved for a corresponding

input water volume of 0.5 to 1.6 mL, giving a very strong positive correlation (R^2 = 0.99) between the output force and the injected water.

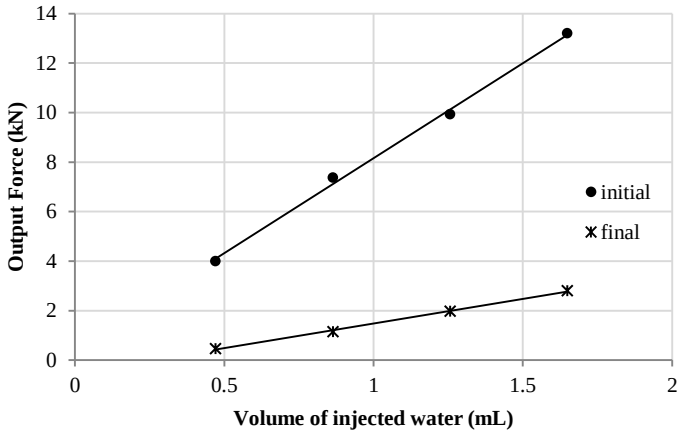

Figure 3.9: Output force vs. input water at the beginning and end of stroke

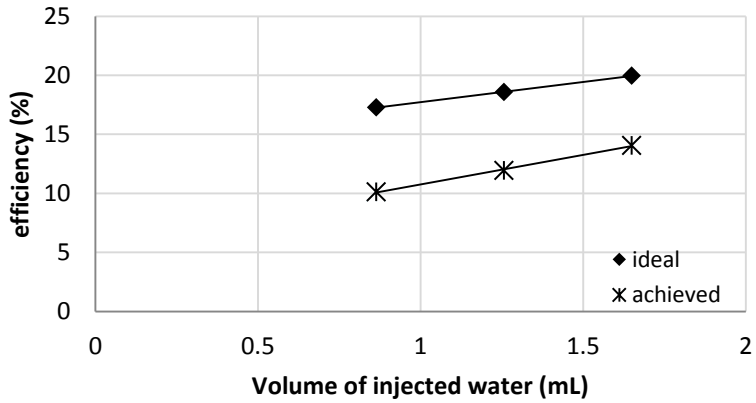

Figure 3.10: Cycle efficiency vs. input water

The cycle efficiency increases as the volume of injected water increases (Figure 3.10); for 0.5 – 1.6 mL of input water, efficiency range of 10 – 14 % was achieved, which is slightly over a half of the ideal cycle efficiency of 17% and Carnot efficiency of 18% (This is similar in performance to the reported efficiency ratio achieved by real Stirling engine [158, 159]). The less-than-ideal efficiency was attributed to non-isothermal operation. As the water vaporised and expanded as steam, its temperature dropped. This was due to the limited power of the electrical heaters, lack of thermal mass in the cylinder walls, insufficient surface area for heat transfer and heat losses in particular through the piston and rod. In future experiments, the use of thermal fluid to carry out the heating is expected to improve the situation by providing additional thermal mass and more uniform heating. Improved insulation is also expected to increase the cycle efficiency towards the ideal value.

Nevertheless, high work ratio is achieved – within the same operating parameters, the pump work was found to be between 0.4J to 1.5J, while the work output was correspondingly 255 J to 532 J,

thus achieving high work ratio of about 0.997, which is in perfect agreement with the expected theoretical value of >0.99.

3.4. Liquid flooded regenerative expander

The regenerative expander variant is analysed in this section. A schematic layout of the proposed regenerative Rankine cycle engine is depicted in Figure 3.11, while the stages of operation are shown in Figure 3.12. At the start of operation, stage 1, the regenerative chamber is initially filled with the hot thermal liquid, and a metered volume of the working fluid is directly injected (via valve *y*) into the hot liquid at the bottom of the chamber. The working fluid then ascend while vaporizing and expanding (stage 2), thus pressurizing and displacing the thermal liquid (from the regenerative chamber) to the power cylinder, thereby indirectly performing work against the piston. Due to further heat transfer from the regenerator packing material (matrix) and to a lesser extent the thermal fluid, the vapour continues to expand at constant temperature, thus achieving isothermal expansion. At the end of expansion, on the return stroke (stage 3), the vapour exhausts via valve *x*, as the thermal liquid is pushed back through the heater (where it gets reheated) into the regenerator, thus charging the matrix ready for the next cycle.

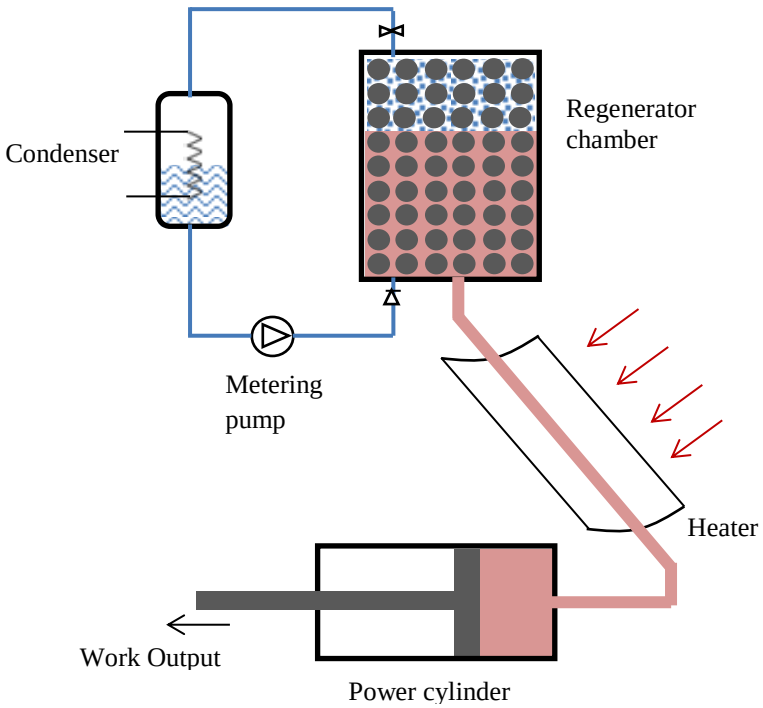

Figure 3.11: Schematic of liquid flooded regenerative expander Rankine cycle

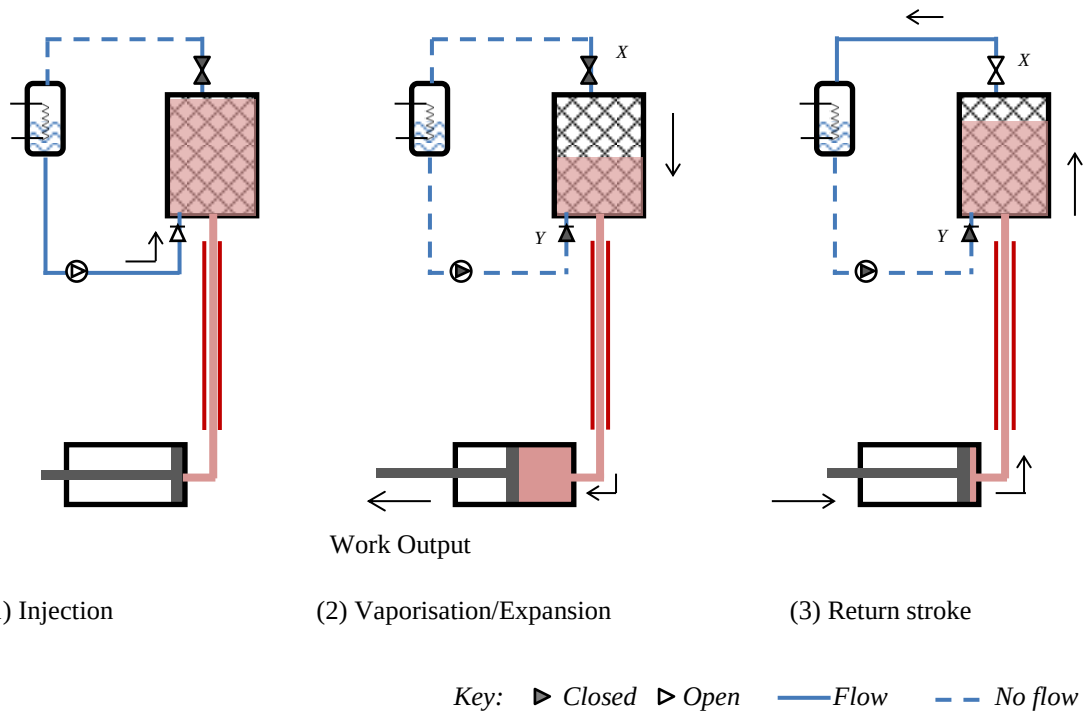

Figure 3.12: Stages of operation of the regenerative expander cycle

3.4.1 System analysis (matrix selection)

The performance of the system can greatly depend on the choice of the regenerator matrix. Stacked screens and packed spheres are the commonly used geometries [160]; however, metal foam and packed rods will also be considered for selection. Ideally, the matrix geometry will be selected to achieve a balance between heat transfer (a measure of surface area) and flow friction (a measure of porosity). For enhanced thermal transport and compactness of heat exchanger size, large surface area-to-volume ratio or surface area density (SAD) is desirable. Thus the surface area density and the porosity form the key geometric parameters for the matrix selection.

The porosity of the matrix is a measure of the void spaces of the matrix and can be expressed in terms of the void volume (V_v) and total volume (V_t), or in terms of the relative density ($\overline{\rho}$) of the matrix as:

$$Porosity\ (\mathfrak{p}) = \frac{V_v}{V_t} = 1 - \overline{\rho} \tag{3.23}$$

The relative density ($\overline{\rho}$) is the density of the matrix ρ relative to the density of the solid material ρ_s of the matrix – defined as: $\overline{\rho} \equiv \frac{\rho}{\rho_s}$

The surface area density (SAD) can be given as

$$SAD = \frac{surface\ area\ (A_s)}{total\ volume\ (V_t)} \tag{3.24}$$

However, the surface area density can also be defined in terms of the porosity and solid volume as

$$SAD = \frac{A_s(1 - \text{p})}{V_s} \tag{3.25}$$

These key parameters can be easily determined for matrixes with simple geometries such as uniform spheres and rods; however, complex geometries such as metal foam and wire mesh would require other geometric parameters to be defined.

Sphere matrix (equal size), can be packed orderly or randomly; for ordered packing – simple cubic (sc) – arrangement, the SAD can be shown to be

$$SAD = \pi/d \tag{3.26}$$

While, the porosity can be given as

$$\text{p} = 1 - \frac{\pi}{6} \tag{3.27}$$

This gives a maximum porosity of $\text{p} = 0.476$ for ordered arrangement. Other ordered arrangements such as body centred cubic (bcc) have porosity of 0.32 [161], whereas the least porosity is observed for face centred cubic / rhombohedral packing, where the porosity is 0.2595 [162, 163]. On the other hand, random arrangement is difficult to calculate but porosity range of $\text{p} = 0.36 - 0.42$ has been widely reported [162, 164].

Similarly, for closely packed **uniform rods**, the porosity of the rods matrix (for cubic packing arrangement) can be obtained as

$$\text{p} = 1 - \frac{\pi}{4} \tag{3.28}$$

This gives a porosity of 0.215; however, for equilateral ($diameter \approx length$) rods with random packing, porosity range of 0.25 – 0.46 can be obtained [162].

For **wire mesh matrix**, the relative density of a mesh screen can be obtained as [165].

$$\overline{\rho} \equiv \frac{\rho}{\rho_s} = \frac{\pi N d^2}{2\mathfrak{t}} \sqrt{1 + \left(\frac{1}{1 + \mathfrak{w}/d}\right)^2} \tag{3.29}$$

And the surface area density can be given as

$$SAD = \frac{\pi}{\mathfrak{o} + d} = \pi N \tag{3.30}$$

Where, N (mesh number) is the number of pores per unit length and is given as $N = 1/(d + \mathfrak{w})$; d is the wire diameter, $\mathfrak{o}$ is the aperture (width of pores), and $\mathfrak{t}$ is the screen layer thickness $\mathfrak{t} = 2d$.

For metal **foam matrix**, the relative density can be calculated as [166]

$$\overline{\rho} = \frac{(\sqrt{5} + 1)\pi}{4}\left(\frac{d}{a}\right)^2 - \frac{\pi}{2}\left(\frac{d}{a}\right)^3 \tag{3.31}$$

$$\frac{d}{a} \approx \sqrt{\frac{20}{(5\sqrt{5} + 3)\pi}}\,\overline{\rho}^{1/2} \tag{3.32}$$

Where d is the strut diameter, and a = 2 mm, 1 mm, and 0.5 mm for different pore densities (defined as pores per inch (PPI)) 10 PPI, 20 PPI and 40 PPI respectively.

And the surface area density can be obtained approximately as

$$SAD \approx \frac{5.97}{a}\overline{\rho}^{1/2} \tag{3.33}$$

Alternatively, the relative density could be specified by the manufacturer alongside the pore density; thus, the surface area density (or specific surface area in this case) can be more easily obtained from a readily available chart – e.g. from ERG Duocel® metal foams [167] – that gives the measured surface area density as a function of both the relative density and pore density.

A comparison of the performance of the matrixes in terms of geometric parameters can be shown for aluminium base material (although materials with better thermal conductivity e.g. copper would be desirable for a given geometry). The geometries considered for selection were: 1.5 mm spheres, 1.5 mm rods, 0.28 mm wire mesh with aperture 1.214 mm, and metal foam with pore sizes 40 PPI & 20 PPI.

Figure 3.13 shows that, as would be expected, the surface area density decreases with increase in porosity. 1.5 mm spheres matrix show the highest surface area density of 2964 m^2/m^3 (at a porosity

of 0.259). Increase in diameter adversely reduces the SAD. For porosities above 0.5, the wire mesh appears to have a very slightly higher SAD of 2103 m^2/m^3 (at a porosity of 0.85); nevertheless, the 1.5mm sphere and 40 PPI metal foam also have very close SAD's at porosities of 0.46 and 0.88 respectively.

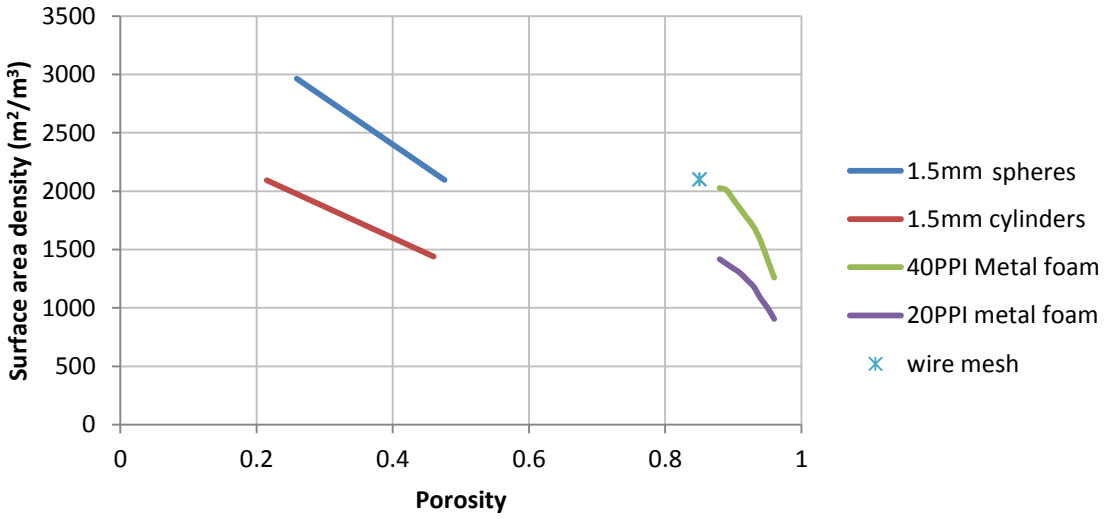

Figure 3.13: variation of surface area density with porosity

Unlike conventional regenerator applications where fluid *flows through* the regenerator, here the fluid *flows into* the regenerator; as such the void volume would be required to be at least equal to the stroke volume of the power cylinder, so as to be sufficient to contain the thermal fluid during the return stroke of the piston. The size of the regenerator matrix relative to the stroke volume is inversely proportional to the porosity, and is given in Figure 3.14.

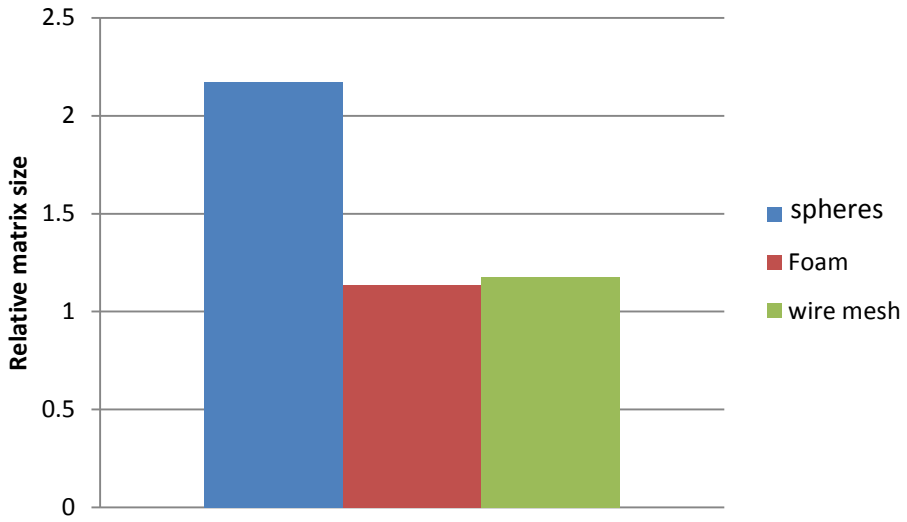

Figure 3.14: relative matrix sizes

The comparison shows that, although the 1.5 mm spheres, the wire mesh and the 40 PPI metal foam all have similar SADs (at porosities of 0.47, 0.85 and 0.88 respectively), the sphere would require a regenerator size of more than twice the volume of the power cylinder stroke. Whereas, the metal foam and the wire mesh would only require a regenerator size slightly (less than a fifth) more than the stroke volume. Additionally, wire mesh is more readily available and cheaper, and as such is selected over metal foam.

3.4.2 Liquid flooded regenerative expander experiment

Using wire mesh as the regenerator matrix, a preliminary experiment is carried out to access the performance – the pressure characteristics, work output and efficiency – and the practicality of the concept of the liquid flooded regenerative expander. The experimental set up is shown in Figure 3.15. The test engine was assembled as an open cycle; a condenser was not included, for simplicity. The regenerator cylinder was initially a glass pressure vessel so as to enable a visual insight of the fluid behaviour; but was afterwards replaced with flanged aluminium tube; while the regenerator matrix was made from a roll of aluminium woven wire mesh (1.31 mm aperture). The heat collector was made from a standard 2 inch aluminium pipe, fitted with double 360 W electric heating tapes and thermocouple (K type, accuracy ± 2.5^{o}C); temperature control was implemented by means of a PID temperature controller (XMT7100). The thermal fluid used was Globaltherm^{Tm} Syntec (thermo-physical properties attached in Appendix 1), because of its thermal/oxidation stability at high operating temperatures up to 350^{o}C. The pump was assembled from a double acting 10 mm bore cylinder (SMC-C85) configured as a metering piston pump by means of two reversed non-return valves connected at the outlet port. The power cylinder was a standard pneumatic cylinder (SMC95) but the seals were replaced with Viton O-rings for high temperature rating. Threaded rods with a beam assembly overhead the piston rod end were employed to provide a means of setting the desired stroke length. A displacement transducer – linear slide potentiometer (tolerance ± 20%) was affixed to the piston rod end to provide measurements of the piston stroke displacements. A needle flow control valve was employed to resist the fluid flow to the power cylinder, thus providing a means of an indirect load, to enable load pressure measurements to be taken. The pressure and displacement signals were acquired through LabVIEW® data acquisition system. The test system parameters and operating conditions are listed in
Table 3.3.

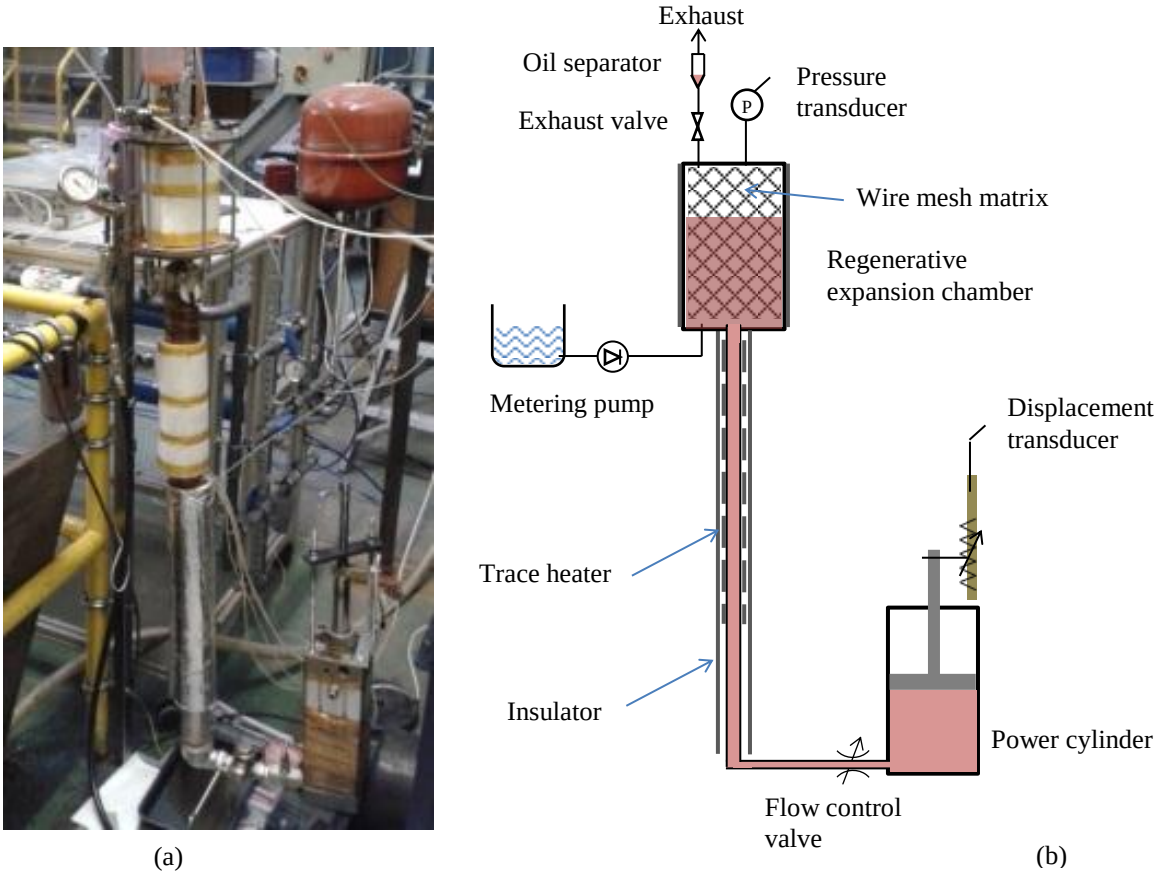

Figure 3.15: The experimental set up (a) and its schematic representation (b) of the liquid flooded regenerative expander

Table 3.3: Regenerative expander system parameters

Parameter	Value
Regenerator diameter	100 mm
height	300 mm
wire mesh matrix	
wire diameter	0.28 mm
aperture	1.31 mm
Heating pipe diameter	50.8 mm
length	2.5 m
temperature	250^{o}C
Thermal oil	
Thermal conductivity	0.102 w/(m.k)
Power cylinder diameter	100 mm
stroke	100 mm

3.4.2.1 Test procedure

The experimental procedure is as follows: at the initial stage of operation, when the heater is switched 'on', ample time can be allowed for the thermal oil and wire matrix mass in the regenerator to attain the pre-set temperature (250^{o}C); however, since heat is supplied to the regenerator from the bottom, via the thermal oil, the bottom region will absorb the heat first and naturally be conducted upwards. But heat transfer by conduction alone is quite a slow process, thus, to fasten the heating process, the heating is commenced from the full stroke position, i.e., the minimum oil level in the regenerator and maximum level of oil in the power cylinder. When the oil in the heating pipe gets heated to the desired temperature (250^{o}C), the piston is engaged on a return stroke, thereby displacing the hot oil into the regenerator. For this initial heating stage, compressed air is employed to move the oil back into the full stroke position. The forth and back sequence of the oil flow is repeated until the regenerator temperature stabilises. This forth and back sequence facilitates convective heat transfer and thus enables the regenerator to be heated more quickly. Upon attaining the set temperature in the regenerator, the metering pump then injected the required volume of water into the base of the regenerator, where it vaporises. The pressure and displacement data are then collected for analysis. A basic gravity based oil separator was affixed above the exhaust valve, to enable oil expelled alongside steam during exhaust to be seeped back into the regenerator. The oil is denser than water, as such settles at the bottom of the separator.

3.4.2.2 Results

Two different modes of injection process were tested in this experiment – in the first instance the water was directly injected into the hot oil, while in the second instance the water was injected through a spiral coiled copper tube (Ø 4 mm of 1 meter length) placed in the oil. For both instances, a metered volume (3.5 mL) of water was injected. When the water was directly injected into the thermal oil, the water vaporised very slowly, and large bubbles were formed in the oil. The pressure did not rise significantly, and as a result the piston could be barely moved (the pressure build-up wasn't enough to move the flow through the needle valve); whereas, injection through the copper tube resulted in a very rapid rate of vaporisation (Figure 3.16), as the water did vaporised in the tube. The performance variation can be attributed to the significantly higher thermal conductivity of the copper tube, and the overall heat transfer coefficient achieved from the liquid to metal contact, relative to that of the liquid to liquid interface.

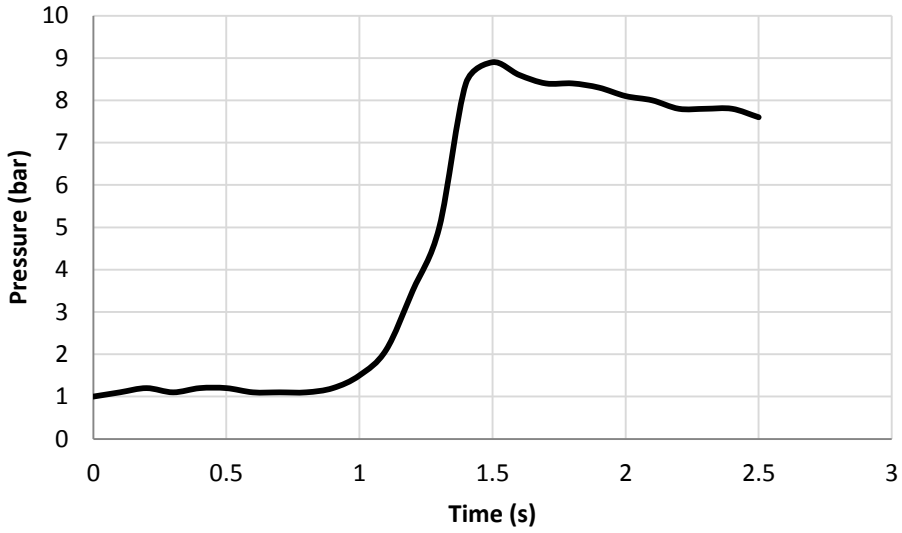

Figure 3.16: Pressure profile in the regenerator cylinder, showing rapid pressure rise upon injection at time 1 s.

As can be seen from the figure, the pressure in the regenerator cylinder is constant before water is injected, it then increases very rapidly (at a rate of about 14 bar/s) upon injection (this steep pressure rise corresponds to the vaporisation of the water), and the increase diminishes after some time elapsed (in fractions of seconds) towards the end of vaporisation. Afterwards, the pressure is seen to reduce slightly; ideally, a constant pressure would have been expected here (at the end of vaporisation), however, the observed drop in pressure can be partly attributed to fact that the vapour gets condensed at the top region of regenerator, due to the relatively lower temperature of the cover, and the significant heat loss to the surroundings.

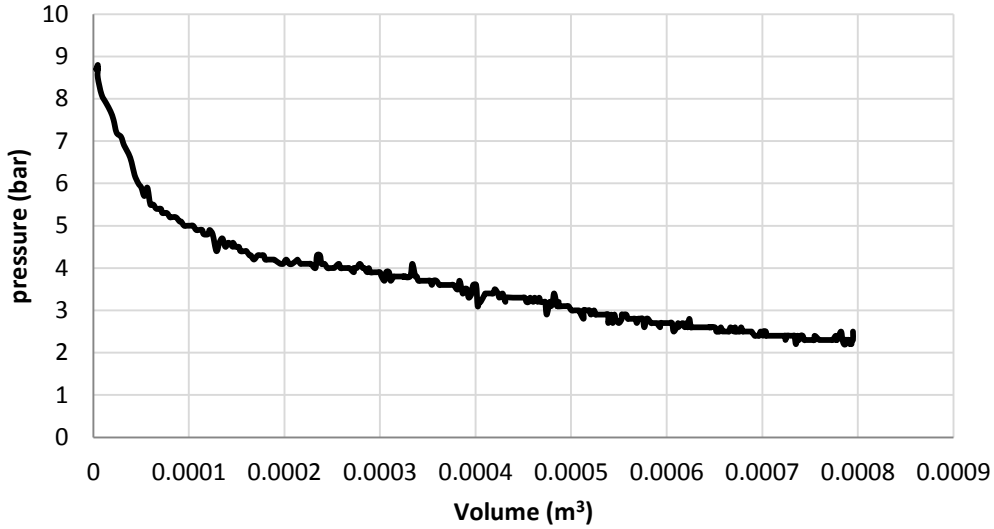

Figure 3.17: Pressure-volume (*p-V)* diagram of the regenerative expander

As shown in the *p-V* diagram (Figure 3.17), pressure of 8.7 bar at the start of expansion and 2.4 bar at the end of expansion was achieved for a 3.5 mL of injected water. The work output was 294 J and the thermal efficiency thus achieved was 4.5%. This is about a fifth of the Carnot efficiency (16%) obtainable for similar operating temperatures. However, this compares poorly against the reported performance of about a half of Carnot efficiency for conventional engines.

The poor performance can be attributed to the fact that, there was significant level of foaming of the oil especially towards the end of expansion and during exhaust (Figure 3.18), which consequently led to substantial amount of oil being expelled (into the separator) alongside the spent vapour during exhaust.

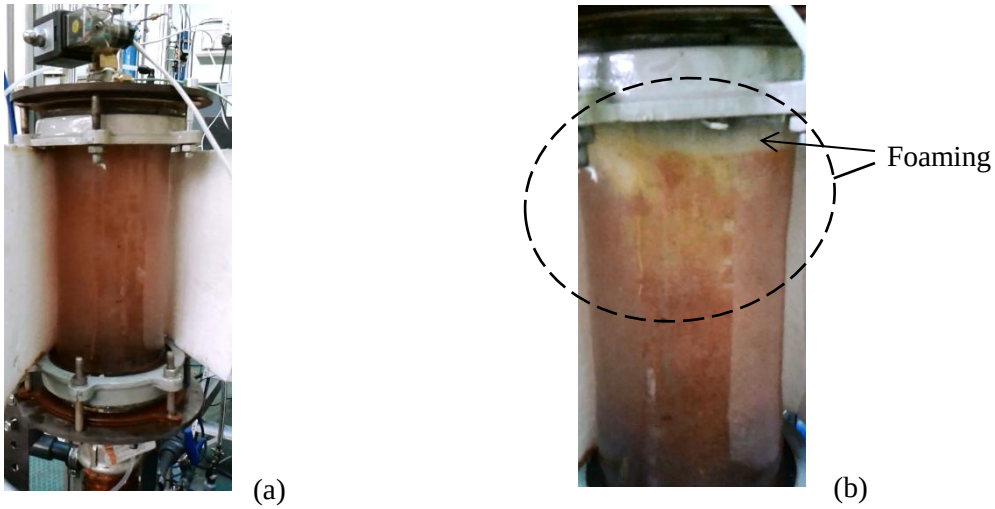

Figure 3.18: A typical foaming action of the thermal oil in the Liquid flooded expansion chamber, (a) minimal foaming at the early stage of operation, (b) substantial foaming at later stage

This foaming phenomenon hampers the returning of the oil (from the separator) into the cylinder, and hinders the filling of the cylinder during the return stroke; moreover, in the separator, the oil tends to quickly thicken and also entraps some water bubbles. The combination of these effects consequently reduced the effectiveness of the separator in returning the expelled oil back into the cylinder, thus reducing the oil level in the cylinder, and as a result creating undesired space (dead volume) that consequently lead to reduced pressure build-up upon the next cycle of injection, otherwise inevitably requiring increased amount of water input to achieve a desired pressure.

3.4.3 Summary of findings with regenerative liquid flooded expander

In a bid to expedite heat transfer to the working fluid during expansion, a heat power cycle engine with an auxiliary expansion chamber enhanced with high surface area density matrix has been

investigated. Preliminary experiment showed that efficiency of 4.5% was achieved for 3.6 mL of injected water. Despite the fact that rapid vaporisation and pressure build-up was achieved with the aid of spiral copper tube, the performance (efficiency) was mired by the vapour condensing whilst in the regenerator (partly as a result of poor insulation), oil foaming, and ineffectiveness of the oil separator employed. To address these issues, it is recommended that the system be re-designed to reduce foam formation; in this case, de-foamers or anti-foaming agents could be investigated for addition to the oil, to reduce/hinder the formation of foam or break away already formed foam. Other thermal fluids with minimal foaming characteristics and better thermal properties could also be investigated. The oil separator could be optimised for improved performance by employing some form of heating, to maintain low oil viscosity, and prevent entrapment of water bubbles. Furthermore, adequate insulation would also be required to minimise heat loss.

3.4 Discussion

The two variants (regenerative expander and surface heated expander) of the isothermal steam Rankine cycle were experimented with similar operating conditions/parameters (100 mm cylinder diameter, 100 mm stroke, and 250^{o}C heat source temperature). The regenerative expander investigated (with wire mesh matrix) had a surface area density of 2100 m^2/m^3 while that for the surface heated variant decreased from 440 to 60 m^2/m^3 as the stroke length increased from 5% of 100%. As such the regenerative variant clearly had much higher average surface area and thus higher potential of achieving very high heat transfer to maintain isothermal expansion. However, the experiment showed that it consumed 3.5 mL water input and delivered work output of 294 J, with a work ratio of 0.992 and thermal efficiency of 4.5%; whereas, the heated expander variant achieved a work output of 378 J, with a work ratio of 0.996 and thermal efficiency of 14% from 1.6 mL of injected water. Hence, relative to the regenerative expander, the surface heated variant delivered more work output from significantly less water input, and achieved about 3 times higher efficiency, despite the high heat transfer potential of the regenerative variant.

The poor performance of the regenerative variant is mainly attributed to reduced work output due to the dead volume caused by foaming of the oil and incomplete recovery of vented oil back from the oil separator; and furthermore, the phenomena of significant condensation. Consequently requiring more (than would normally be required) water input, in other to achieve a reasonable pressure level.

It is worth mentioning that, the surface heated expander also exhibited some level of dead volume (as a result of the clearance volume of the piston/cylinder base, and also the spaces at inlet and outlet ports) which must have reduced its performance to some extent. This however, appears to be

minimal relative to that exhibited by the regenerative expander. Attempts to address the practicality issues encountered with the regenerative expander will require significant amount of optimisation efforts, as such the surface heated expander is preferred for its impressive performance with simple practicality.

3.5 Chapter Summary

Surface heated expander and regenerative expander are considered as two variants of expander that could effect heat transfer to a working fluid during expansion. Both variants entailed injection of working fluid (water) into a heated expansion chamber, where it vaporises and perform work quasi-isothermally due to further heat addition from the chamber during expansion. The surface heated expander simply entailed heating the expander surface, while the regenerative variant employed a porous matrix (for increased heat transfer surface area) to be charged by a thermal oil (which also acted as liquid piston). The matrix selection process included packed spheres, packed rods, wire mesh and metal foam for consideration; however, wire mesh was favoured for its reasonable surface area density and porosity.

The two variants were evaluated experimentally for similar operating conditions – temperature and engine size – to enable direct comparison between their performances (in terms of thermal efficiency and work output in relation to the quantity of water input). The result showed that, although the regenerative expander markedly had higher surface area available for heat transfer, the achieved performance (4.5% efficiency and 293 J work output) was substantially poor, relative to that of the surface heated variant (14% efficiency and 378 J work output at 1.6 mL input water); therefore the surface heated variant was considered optimal.

The performance of the regenerative was mired by practicality issues such as foaming of the oil, inadequate oil separation, and vapour condensation in the expansion chamber. As such further work would be required to investigate anti-foaming agents and better thermal fluids. Nevertheless, both variants suffered significant heat loss to the ambient, as such adequate insulation is essential.

Chapter 4 R245fa ORC with isothermal expansion

This Chapter explores the isothermal expansion of organic Rankine cycle (ORC) working fluid to achieve improved efficiency; for the potential of driving a batch-RO desalination system, 'DesaLink'. Though water was convenient for initial experimentation, the organic fluid is advantageous with regard to power density and heat transfer properties. The previous chapter identified expander surface heating as the preferred method to achieve isothermal expansion. This chapter includes a more complete analysis of the isothermal Rankine cycle, taking into account effects of cut-off point and blow down which all tend to result in a less than ideal performance. Experimental investigations with R245fa working fluid have shown thermal efficiency of 8.8%. And it is predicted that scaling up the engine swept volume by a factor 10 could produce enough power to drive DesaLink. Some of the work of this chapter has been presented at the 'Desalination for the Environment Clean Water and Energy' conference and published in the 'Desalination and Water Treatment' journal [168].

4.1 Introduction

The proposed quasi-isothermal steam cycle (with surface heated expander and direct vapour generation in the expansion chamber) investigated in the previous chapter, was demonstrated to be practicable, with impressive performance in the small-scale low temperature applications (where conventional steam Rankine cycle, though matured in the large-scale medium to high grade heat operation, is generally reported inefficient, partly due to low heat extraction [169, 170]). However, when the temperature level of the available heat source is very low and not sufficient for the steam cycle, organic working fluid becomes an attractive alternative. Lately there has been a significant growth of interest in organic Rankine cycle (ORC).

Recent advances in organic working fluids (e.g. refrigerants, siloxanes and hydrocarbons) have expanded the scope for Rankine cycle use in small-scale medium (<400^{o}C) and low grade (<200^{o}C) temperature heat source applications. They overcome the limitations of water; this is owing to their lower boiling point and higher molecular weights. Studies have shown that for low temperature heat sources, the organic fluids achieve higher efficiencies compared to water [171]. However, the choice of the working fluid is quite critical; besides environmental issues, it entails a proper

matching of the thermodynamic properties of the fluid and the operating conditions, so as to ensure optimum performance whilst maintaining chemical stability on operation [172-174].

For low temperature heat sources, Quoilin et al. [175] evaluated various ORC thermodynamic cycles (at 120 – 189^{o}C) and reported that overall efficiencies of about 7 – 8% can be obtained. However, Declaye et al [97] experimented on a R245fa ORC system and reported a maximum cycle efficiency of 8.5% for evaporating temperature of 97.5^{o}C. On the other hand, Jradi [176] achieved a thermal efficiency of 5.7% for the HFE7000 working fluid at average evaporating temperature of 125^{o}C. Pei et al [177] developed and tested a small-scale ORC with R123 working fluid and achieved a thermal cycle efficiency of 6.8% at 101^{o}C evaporating temperature. Furthermore, Wang et al. [178] tested an ORC engine, operated between 70 and 80^{o}C and obtained a cycle efficiency of 3.6% for constant flow rate (0.97 ltr/h) of the working fluid; the efficiency reached a maximum of 6.2% at an increased flow rate of 2.275 ltr/h; hence indicating that the efficiency could be improved by regulating the flow rate.

Hence, while reasonable efficiencies can be obtained from the organic Rankine cycle, its performance is strongly dependent on the choice of working fluid and the operating conditions. Thus, in this chapter, the performance of ORC will be re-investigated for isothermal operation. To achieve this, the performance of the isothermal ORC engine will be modelled and various working fluids will be analysed to select the potential fluid(s); experimental work with a potential fluid will be carried out to ascertain its real performance. And finally, the feasibility of employing the isothermal ORC engine to drive a batch desalination system will be considered.

4.2. Description of the isothermal reciprocating heat engine

Figure 4.1 depicts the schematics of the isothermal reciprocating engine. The processes that occur within one cycle of operation in the cylinder, C, are as follows:

- Injection (C1-C2): During the injection process, the intake valve opens, and the metering pump injects a volume (with mass, m) of pressurized working fluid into the cylinder.
- Vaporization (C2-C3): The injected liquid is heated and vaporized by the hot cylinder wall to become dry saturated vapour, with pressure P_{C3}. In this process, the vapour performs some work, since the volume of the vapour is greater than that of the liquid.
- Expansion (C3-C4): The vapour expands and performs further work against the piston. Due to continuous heat transfer from the cylinder wall, the vapour is superheated, as the expansion proceeds isothermally to pressure P_{C4} at the end of stroke.

- Blow down (C4-C5): At the end of stroke, the exhaust valve is opened and some of the vapour blows down (through a regenerator, if employed) into the condenser and the vapour's pressure (P_{C4}) is reduced to the condenser Pressure (P_{C5}).
- Exhaust (C5-C1): On the return stroke, the piston displaces the remaining vapour through the regenerator (if employed) into the condenser, until piston gets back to the cylinder head, and then the valve is closed in preparation for the next cycle.

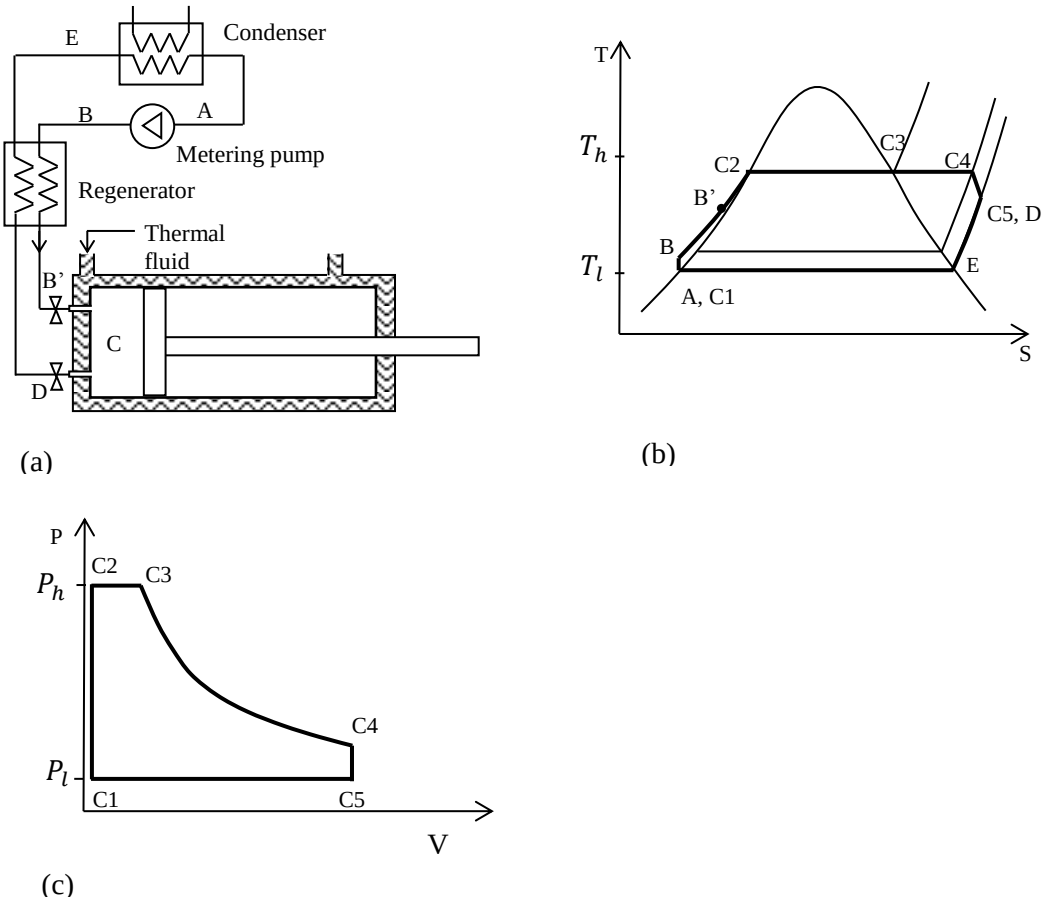

Figure 4.1: Detailed operation of the isothermal Rankine cycle: (a) the system schematic (b) T-s diagram showing states in the system at different positions in the system A – E and times C1 – C5 (c) P-V diagram showing states in the cylinder (position C) at different moments in time during the cycle (1 – 5)

4.2.1 System analysis

The working process of the processes within one cycle of operation could be modelled with a set of appropriate non-flow analyses. However, it can be assumed that the mass of fluid in the regenerator and condenser is much larger than in the cylinder, therefore the flows and pressure in the condenser

are effectively steady over time; thus flow analysis can be approximated here. The analysis is carried on the basis of mass '*m*' of working fluid corresponding to one cycle of the engine.

The work input by the pump in injecting the working fluid into the cylinder entails the work required to pressurize the liquid. Thus the pump work can be obtained as:

$$W_{AB} = mv_{fl}(P_h - P_l) \tag{4.1}$$

Where, P_h and P_l are the upper and lower pressures of the cycle corresponding to saturation temperatures T_h and T_l respectively; while v_{fl} is the specific volume of the saturated liquid at P_l.

The heat input required to heat and vaporize the fluid is given by:

$$Q_{BC3} = m[C_{pf}\,(T_h - T_l) + T_h(s_{C3} - s_{C2})] \approx m(h_{C3} - h_B) \tag{4.2}$$

The work output during the vaporization phase can be given as:

$$W_{C23} = mP_h(v_g - v_f) \tag{4.3}$$

The heat input required to achieve isothermal expansion of the superheated vapour can be given as:

$$Q_{C34} = m\,T_h(s_{C4} - s_{C3}) \tag{4.4}$$

And the expansion work output can be given as:

$$W_{C34} = Q_{C34} - m(u_{C4} - u_{C3}) \tag{4.5}$$

The work input during the return stroke to exhaust the vapour can be given as:

$$W_{C51} = P_l(V_{C5} - V_{C1}) \tag{4.6}$$

The net work output is:

$$W_{net} = W_{C23} + W_{C34} - W_{C51} - W_{AB} \tag{4.7}$$

Thermal efficiency can thus be given as:

$$\eta_{th} = \frac{W_{net}}{Q_{in}} = \frac{W_{C23} + W_{C34} - W_{C51} - W_{AB}}{(Q_{BC3} + Q_{C34})} \tag{4.8}$$

If a regenerator is utilized to preheat the liquid before injection, then the heat saved can be given as:

$$Q_{C4E} = m[C_{pg}\,(T_h - T_l)] \;\approx m[h_{C4} - h_E] \tag{4.9}$$

And the improved thermal efficiency becomes:

$$\eta_{th} = \frac{W_{C23} + W_{C34} - W_{C51} - W_{AB}}{(Q_{BC3} + Q_{C34} - Q_{C4E})} \tag{4.10}$$

4.2.2. Practical performance

For real engines, the expansion process of the working fluid may not absorb sufficient heat to maintain isothermal expansion. The extent of isothermal behaviour achieved can be termed isothermality, γ, defined as the ratio of the actual work to the isothermal work [79], as mentioned in Chapter 2,

$$\gamma = W_{ac}/W_{iso} \tag{4.11}$$

Also in order to account for friction losses (that inevitably exists between piston and cylinder walls) and other thermodynamic losses, the efficiency terms: engine efficiency, η_{en}, and pump efficiency, η_{pm}, can be taken into consideration. As such, the realistic net work of the cycle becomes:

$$W_{net} = \eta_{en}[W_{C23} + \gamma W_{C34} - W_{C51}] - W_{AB}/\eta_{pm} \tag{4.12}$$

Similarly, the realistic heat saved by the regenerator to preheat the feed liquid can be expressed in terms of the regenerator effectiveness, η_{re}, to account for thermodynamic losses.

Therefore, the realistic efficiency becomes:

$$\eta_{th} = \frac{\eta_{en}[W_{C23} + \gamma W_{C34} - W_{C51}] - W_{AB}/\eta_{pu}}{(Q_{BC3} + Q_{C34} - \eta_{re}Q_{C4E})} \tag{4.13}$$

4.2.3. Effect of dead volume on engine performance

With the aid of the pressure-specific volume (P-v) diagram in Figure 4.2, the operating maximum pressure achievable in the cylinder can be illustrated to depend on volume/mass of injected liquid, m, cylinder wall temperature, T_{w}, and cylinder dead volume V_d.

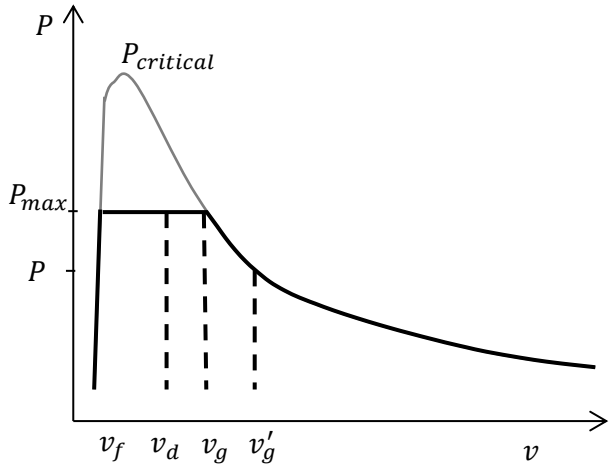

Figure 4.2: *P-v* diagram showing the effect of dead volume. *Large dead volumes move the operation starting point to the right, thus reducing the specific work (area under the curve) realisable.*

Ideally, the maximum pressure achievable corresponds to the saturation pressure at the wall temperature $\left(P_{max} = f(T_{\text{ш}})\right)$. And since the specific work transfer during the vaporization phase is given by $P_{max}(v_g - v_f)$, it can be seen that for a given desired max pressure, to completely extract this work, the specific dead volume v_d (ratio of the dead volume to mass of injected fluid) of the cylinder should be as little as the specific volume of the liquid v_f at the desired pressure. This implies that the dead volume should be equal to the volume of injected liquid. In reality, this may not be the case. If the dead volume is slightly greater than the liquid volume, $v_f < v_d < v_g$, the max pressure will still be maintained, but the vaporization work will be reduced to $P_{max}(v_g - v_d)$. If the dead volume is as large as the volume of the dry vapour, $v_d = v_g$, the fluid will be in the dry saturated vapour state, at the same max pressure, but no vaporization work can be extracted. Conversely, if $v_d > v_g$, the fluid will be in a saturated vapour state at a relatively lower pressure; and the pressure will no longer depend on $T_{\text{ш}}$, but rather on the specific dead volume $\left(ie., P = f(v_d)\right)$. In this case, no vaporization work is realized, and the achievable expansion work is relatively low since the pressure is reduced.

4.3. Organic working fluid comparison

The selection of working fluid for Rankine cycle is strongly correlated to the choice of the heat source, as the efficiency of the ORC varies considerably with the thermodynamic properties of the working fluid employed [179]. Hence, in order to compare a reasonable number of working fluids, a pre-screening is carried out based on the two main thermodynamic parameters i.e. the evaporating

and condensing temperature and pressure (depending on the available heat source and heat sink). The maximum evaporating temperature, T_{Evap}, is limited to 150°C, while the minimum condensing temperature, T_{Cond}, is 30°C. But if necessary, the minimum T_{Cond} is raised to correspond to a minimum vapour pressure slightly above atmospheric pressure 1 bar (the permissible minimum pressure desired to avoid air infiltration issues).

With aid of the models outlined in section 4.2, analysis of the working fluids has been carried out using Engineering Equation Solver (EES) [180]. The thermodynamic properties of the working fluids are computed directly in EES, using the built-in property functions. Given that a regenerator is employed, the regenerator effectiveness is assumed to be 0.8; the pump and engine efficiencies are also both taken to be 0.8.

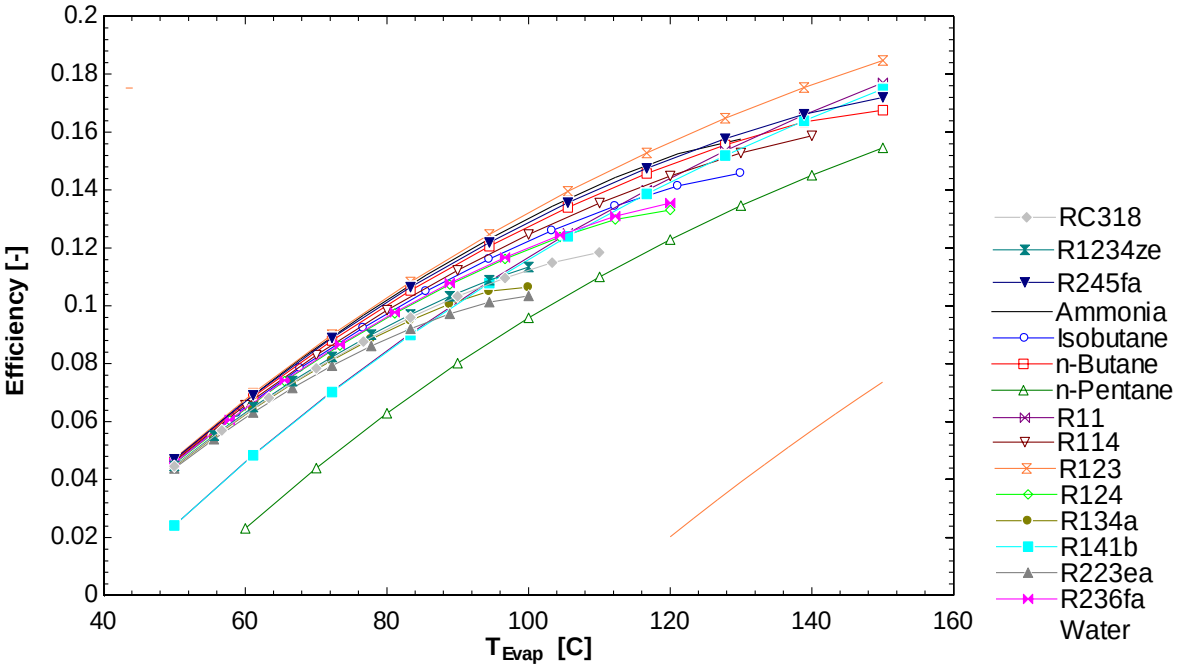

Figure 4.3: Variation of efficiency with temperature for different working fluids

Sixteen working fluids were considered, and the variation of the thermal efficiency with evaporating temperature for the different working fluids is shown in Figure 4.3. Generally, the efficiency increases sharply with temperature, but the increase diminishes as the temperature approaches the critical temperature of the fluid. As can be seen from the figure, most of the fluids show very similar efficiencies at lower temperatures (below 70°C). A comparison of the fluids parameters and performance at a reference evaporating temperature of 100°C is given in Table 4.1. The maximum efficiency limit for the temperatures – Carnot efficiency, η_{Cnt}, – is included for comparison.

Table 4.1: Comparison of working fluids parameters and performance for isothermal ORC

Substance	T_{Crit} [°C]	ρ [kg/m^3]	k [W/m.K]	T_{Cond} [°C]	T_{Evap} [°C]	P_{Cond} [bar]	P_{Evap} [bar]	E [kJ/m^3]	η_{Cnt} [%]	η_{th} [%]	V [$10^{-6}m^3$]
R11	198	7.915	0.0146	40	100	1.73	8.17	249	16.09	11.69	22.08
R114	145.7	14.33	0.0153	30	100	2.5	14.06	372	18.77	12.46	26.7
R123	183.7	5.53	0.0142	30	100	1.1	7.87	200	18.77	13.23	19.08
R124	122.3	20.74	0.0175	30	100	4.46	23.77	593	18.77	11.96	26.15
R245fa	154	7.87	0.0199	30	100	1.77	12.69	310	18.77	12.9	19.16
R134a	101	27.29	0.0194	30	100	7.71	39.75	854	18.77	10.64	26.92
R227ea	102.8	30.91	n.a	30	100	5.27	28.27	606	18.77	10.34	37.78
R236fa	124.9	16.45	0.0225	30	100	3.2	19.36	470	18.77	12.01	26.1
R1234ze	109.4	22.76	0.0128	30	100	5.80	30.27	709	18.77	11.33	28.04
nPentane	196.5	3.855	0.0221	50	100	1.6	5.9	194	13.41	9.58	33.42
nButane	152	5.542	0.0250	30	100	2.84	15.26	413	18.77	12.75	23.7
Iso-Butane	134.7	7.994	0.0257	30	100	4.05	19.84	528	18.77	12.25	27.88
HFE7000	164.6	7.96	n.a	40	100	1.20	6.62	186	16.09	11.15	31.2
R141b	204.2	5.14	0.0141	40	100	1.33	6.77	202	16.09	11.61	21.01
Water	374	0.743	0.029	110	150	1.43	4.76	169	9.46	7.37	4.61
RC318	115.2	24.85	0.0175	30	100	3.66	20.54	489	18.77	11.24	34.4
Ammonia	132.3	6.77	0.0345	30	100	11.67	62.57	1612	18.77	13.03	7.06

ρ and k are the density and thermal conductivity of the vapour at the end of expansion; E – Energy density – the amount of work output that can be obtained from a unit swept volume of engine size; V – liquid volume required for 1kJ of work output

The table indicates that R123 gives the highest efficiency, followed by: ammonia, R245fa, n-Butane, R114, isobutane and R236fa, which all have good efficiencies of >12%. Amongst these fluids, R236fa, R114, and isobutane have high vapour densities and thermal conductivities, and as such have better potential to absorb heat during expansion. On the other hand, in terms of engine size, high saturation pressures result to higher energy density and smaller engine swept volumes. As such, ammonia and R134a (both having the highest operating pressures) exhibit the largest energy density and thus would require the smallest engine volume for a given amount of work output. Although, the small engine volume is desirable, excessive high operating pressures may exceed material or safety limits. R245fa, R114, n-Butane, R236fa and isobutane have modest pressures and show more than 1.5 times better energy density than R123. Conversely, besides water and ammonia, R123 and R245fa show relatively better pump size – with regards the volume of liquid required to deliver a kJ of work.

However, it should be noted that some substance contribute to global warming (GWP) and ozone layer depletion (ODP), owing to these negative effects on the environment, less harmful substances are preferred. R11 and R114 (chlorofluorocarbons – CFCs) have high ODP and GWP and have already been banned under the Montreal protocol. R123 and R124 (hydrochlorofluorocarbons – HCFCs) are in commercial use at present but have already been scheduled for phase out, while no phase out date is set for R245fa, R236fa, (hydrofluorocarbons – HFCs). Water, ammonia and the alkanes are environmentally friendly; however, alkanes are flammable and as such poses safety concerns. On the other hand, ammonia and R123 are toxic, while R245fa and R236fa are non-flammable and non-toxic.

4.4. Isothermal ORC pilot experiment

A pilot isothermal ORC prototype engine was built (Figure 4.4), and using R245fa as the working fluid, an experiment was carried out to assess the piston output force, the work output and thermal efficiency in relation to the quantity of injected liquid, in comparison to the ideal cycle.

The set up of the test engine is quite similar to that in the previous chapter (section 3.3.21); however, here the power cylinder and the metering pump are assembled with a condenser unit (which was absent in the previous case) as a closed cycle on aluminium strut (Figure 4.4). The configuration of the power cylinder (including the heating system and injection mechanism) is same as in the previous chapter. The metering pump's configuration is also similar to that in the previous chapter; albeit with a larger cylinder bore diameter (25 mm bore), to meet the required metering capacity for the organic fluid. The condenser unit was fabricated as a water cooled counter-flow helical coiled copper tube in flanged aluminium tube housing, fitted with a thermocouple and

pressure gauge (accuracy class 2.5); and a liquid receiver affixed at the condenser exit. The cooling system was implemented by means of a 120 mm fan radiator (GTS120-LITE) and a 4 ltr/min circulating pump.

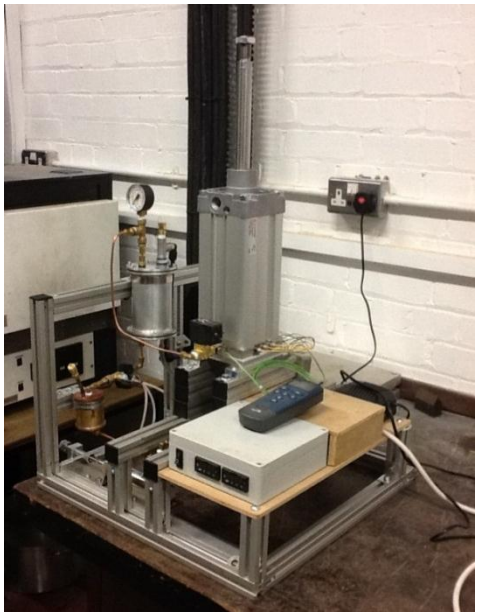

Figure 4.4: The isothermal ORC pilot prototype

Before the start of experimentation, the complete assembled system was pressure tested with compressed air to check for leakages; and then evacuated (using a vacuum pump) to remove air and moisture. After which the unit was charged with the R245fa fluid to the required condenser pressure. The system parameters and operating conditions are listed in table 4.2.

Table 4.2: System parameters for the isothermal ORC pilot prototype

Parameter	Value
Cylinder Bore	100 mm
Piston Stroke	100 mm
Wall temperature	90^{o}C
Heating power	300 W
Condenser temperature	30 ^{o}C
Condenser pressure (abs)	2 bar
Engine speed	<200 mm/min

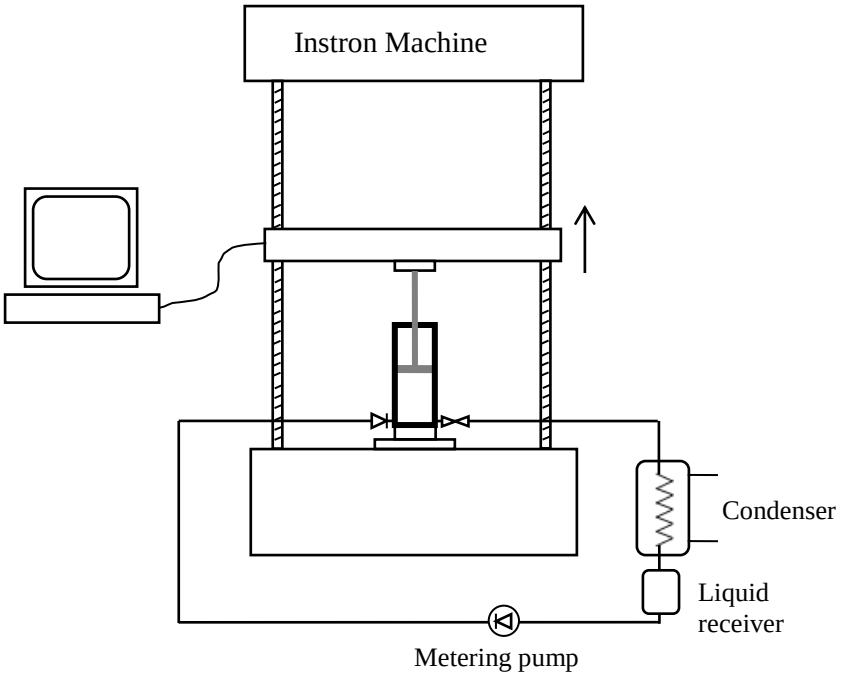

Figure 4.5: Schematic of the pilot isothermal ORC experimental set-up

4.4.2 Test procedure

Figure 4.5 shows schematically the experimental set-up. The Instron machine (material testing machine, Instron® 5500R) was employed to simulate a variable load with a controlled expansion speed. On operation, the metering pump injected the required volume of liquid into the heated cylinder. The resulting vapour expanded and pushed the piston against the load beam (incorporating a load cell) of the Instron machine; the resulting force (which is a measure of the vapour pressure) and piston displacement were recorded in the computer as the load beam retreated. Values of the force and piston displacement were collected at various operating parameters, for analysis.

4.4.3 Results

The results were taken, after heating the cylinder and making some runs to allow the system temperature to stabilize. The achieved p-V diagram (for 9.5 mL injected liquid and 50 mm/min piston speed) is shown in Figure 4.6. The vaporization phase is clearly shown as the plateau on the curve – evaporation pressure (abs) of 7.2 bar which corresponds to a saturation temperature of 76.3^{o}C. The pressure is dependent on the pump's driving pneumatic pressure (< 9 bar). The extent of isothermal expansion achieved is shown in Figure 4.7, for different piston speeds. On close inspection, it can be seen that the isothermality tends to slightly decrease with increase in speed. Nonetheless, isothermality of about 1 was achieved, i.e., the achieved expansion work equalled the expected isothermal work; thus implying that isothermal expansion was fully achieved.

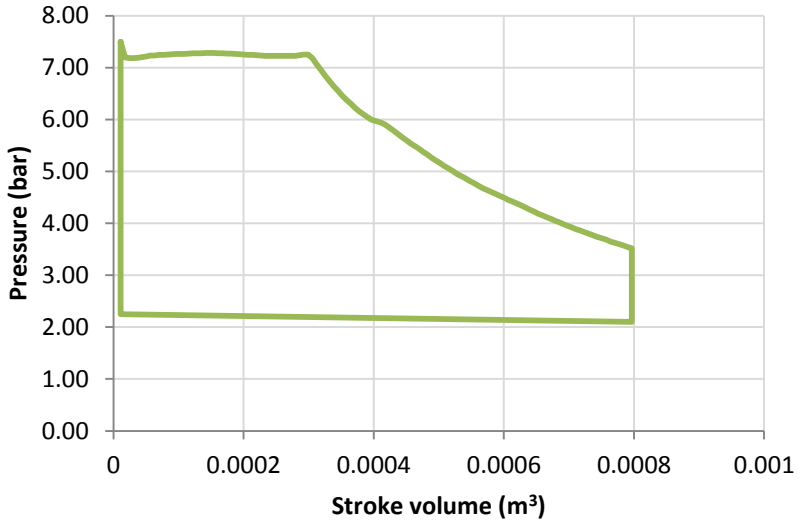

Figure 4.6: Experimental P-V diagram of the isothermal ORC pilot engine

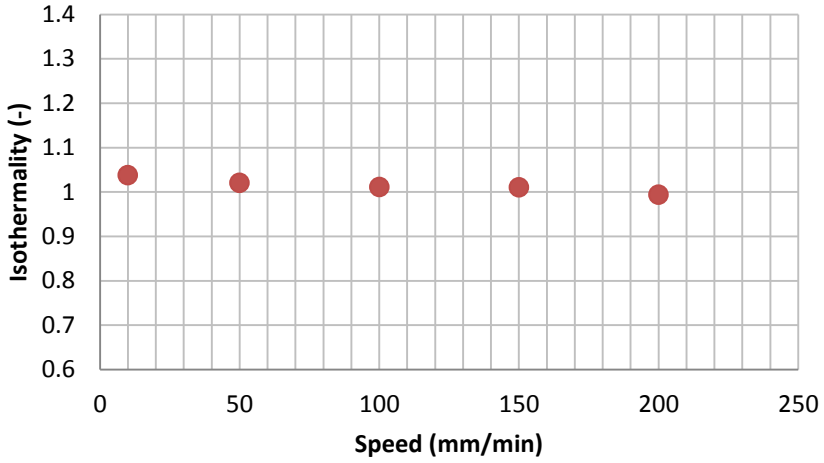

Figure 4.7: Variation of isothermality with piston speed

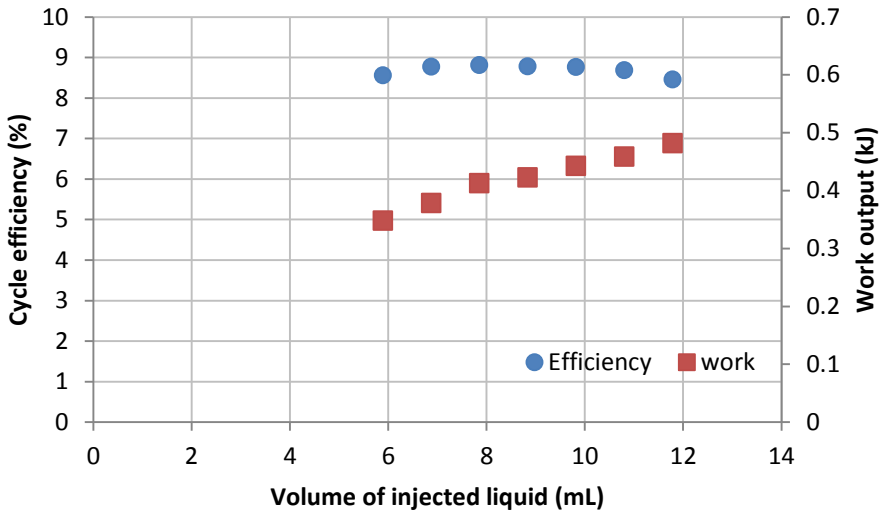

Figure 4.8: Cycle efficiency and work vs. input liquid

Figure 4.8 shows the variation of the cycle efficiency and work output achieved with the volume of injected liquid. As expected, the pressure at the end of stroke, and thus, the work output increases with increase in the quantity of injected liquid; 0.35 – 0.49 kJ of work was achieved for 6 – 12 mL of liquid input. However, the efficiency is seen to increase and then decrease slightly. High under-expansion losses (i.e., inadequate work extraction, due to the stroke length being too short relative to the increased pressure at the end of stroke) diminished the achieved performance as the liquid volume increases. Nevertheless, a maximum cycle efficiency of 8.8% was achieved (at 8 mL of input liquid), which closely matches the expected theoretical value of 9.2%, and is more than a half of the Carnot efficiency (14.4%) obtainable at the same evaporating and condensing temperatures. The achieved performance is better than the reported efficiency of about 5% for conventional ORC engines with same working fluid and at similar operating conditions [97, 181]. Nevertheless the performance can be further improved by increasing the stroke length to extract more work and/or employing a regenerator to save on the heat input.

4.5 Potential application to DesaLink

The results from the pilot isothermal ORC prototype showed promise for application to the DesaLink described in Chapter 1. The following calculations were carried out to assess compatibility for scale up. In DesaLink experiments, Qiu et al [43] showed that initial and final driving pressures of 9 and 1.78 bar at 3.2 kJ work was required (for a 200 mm bore power cylinder with 0.0072 m^3 stroke volume) to produce fresh water output of 2.4 litres per cycle at cycle time of 7.5 mins from 4000 ppm brackish water. In comparison, this study indicates good isothermality in the order of tens of seconds cycle time, and work output of 0.35-0.49 kJ for a 100 mm bore cylinder with 0.00078 m^3 stroke volume (about a tenth of that of DesaLink). This suggests that the isothermal ORC can be easily scaled-up (by a factor of ten) to drive DesaLink on a similar scale.

With the aid of the models outlined in section 4.2, using EES in modelling and computing state properties; assuming a condenser temperature of 30^{o}C and a corresponding pressure of 1.79 bar, the final pressure at stroke end is taken as 2.58 bar, while the starting pressure is 9.8 bar with a corresponding evaporating temperature of 88.8^{o}C. Consequently the required mass of fluid is obtained to be 0.095 kg, which corresponds to 72 mL of liquid. Thus, for one cycle of operation, 72 mL of R245fa will be required to produce 2.4 litres of fresh water. With regards to thermal requirements, 79 W of heat input will be needed to produce 19 litres of fresh water per hour.

4.6 Chapter Summary

ORC with isothermal expansion have been investigated for improved efficiency at low source temperatures. Various working fluids were analysed in terms of efficiency and engine size for temperatures below 150^{o}C. The analysis showed that R123 offers the highest cycle efficiency amongst the fluids studied, but suffers the disadvantage of large engine swept volume. Ammonia and R245fa also offer good efficiencies, with ammonia having the most compact engine size but with detrimental high operating pressures.

Experimental investigation with R245fa showed that isothermal expansion was achieved for operating speed < 200 mm/min. Although the work output increased steadily with increase in the volume of injected liquid, the efficiency was impaired as a result of under expansion losses; nevertheless efficiency of 8.8% was realized. Preliminary assessment of the engine's potential in application to desalination (DesaLink) indicated that, on a similar scale, the engine could produce sufficient power to drive DesaLink. This prompted further work to scale up and realise the isothermal ORC-RO concept, as will be described in the next chapter.

Chapter 5 Application to desalination

This chapter discusses the integration of the isothermal ORC to drive the batch desalination machine 'DesaLink'. A larger capacity ORC unit was built and coupled to the power unit of the DesaLink machine. Experimental results showed that, with 112 mL of R245fa injection, the ORC produced 2.3 litres of fresh water per cycle, from 4000 ppm saline feed water, at thermal or mechanical specific energy consumption (SEC) of 4.4 kWh/m^3 or 0.34 kWh/m^3 respectively, which is significantly lower (better) than those of conventional systems.

5.1 Introduction

Having achieved promising performance (in terms of work output and efficiency) from the isothermal ORC system in the previous chapter, this chapter investigates the performance of the isothermal ORC (when scaled up by 10 times increase in capacity, relative to the pilot prototype in the previous chapter) in RO desalination application (particularly the batch RO desalination system 'DesaLink'), in comparison with conventional ORC-RO systems. As mentioned in chapters 1 and 2, the performance of ORC-RO desalination can generally be assessed by the ORC thermal cycle efficiency, volume of fresh water output, the recovery ratio and the mechanical or thermal specific energy consumption (SEC). Practical studies on conventional low temperature ORC-RO systems (with energy recovery devices) have reported typical specific mechanical energy consumption of about 1 kWh/m^3 (3.6 kJ/litre) [64] and 2.3 kWh/m^3 (8.28 kJ/litre) [62] for brackish water and sea water respectively; however, the reported performance of the ORC engines at the low temperature operation is significantly low (often less than 5% efficiency).

Having gained an insight of the obtainable performance of the conventional ORC-RO desalination systems; this chapter will proceed with the description of the development and experimentation of an up-scaled isothermal ORC system in driving DesaLink, and the assessment of the energy and desalting performance of the integrated system. However, it is worth mentioning here that, this experiment is primarily aimed at establishing the feasibility of the integrated isothermal ORC DesaLink system, and as such will be limited to considering the desalination of only a typical brackish water salinity (4000 ppm), since the previous work by Qiu [182] had already extensively experimented DesaLink for a range of brackish water salinities (2000 – 4500 ppm).

5.2 The integrated isothermal ORC DesaLink test rig

A schematic of the quasi-isothermal ORC coupled to DesaLink is depicted in Figure 5.1. The DesaLink machine has a saline water feed line, a water cylinder, RO membrane, circulating pump, a triangular crank linkage mechanism, and a power cylinder – which provides the driving force. The initial DesaLink setup had a compressed air supply line (to the power cylinder) which provided the driving pressure. However, in this study, the rig has been modified such that the driving pressure is provided by the proposed isothermal ORC subunit attached to the power cylinder (Figure 5.2). On operation, liquid injected into the heated power cylinder vaporizes, expands and drives the triangular crank linkage mechanism, at increasing mechanical advantage, thus pressurizing a batch of saline water in the water pump cylinder through the RO module where the salt is trapped while fresh water is permeated out. To overcome the low side pressure of the ORC closed cycle, the other (piston rod) side of the power cylinder is connected to the condenser, to provide a back pressure, so as to facilitate the return stroke.

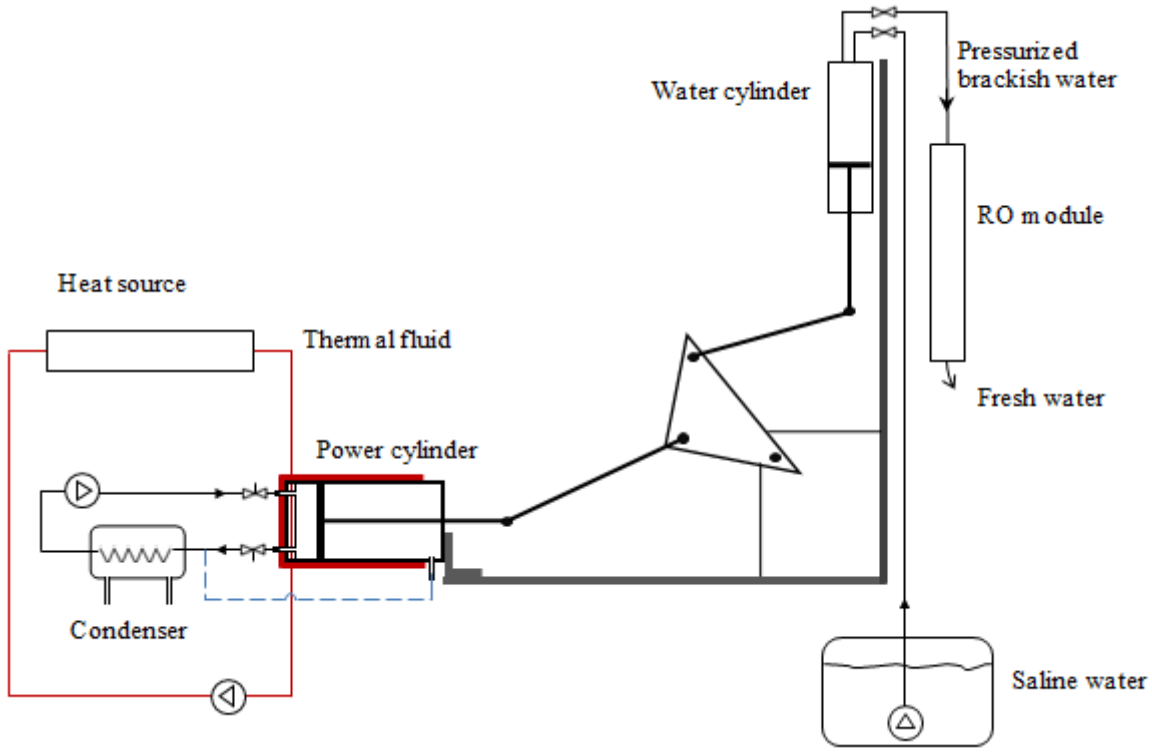

Figure 5.1: Schematics of the isothermal ORC DesaLink system

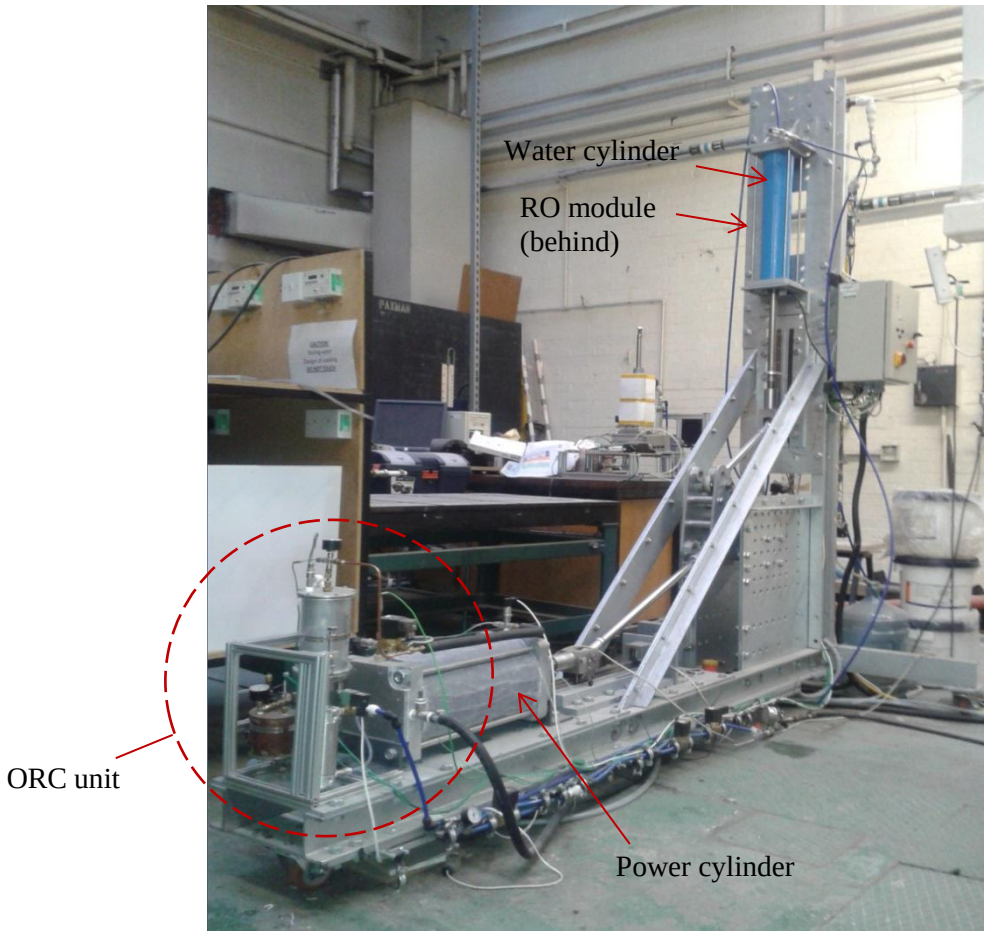

Figure 5.2: The DesaLink machine fitted with the isothermal ORC system

The batch operation process of the RO subunit can be explained with the Schematic of Figure 5.3. the operation starts with the refill phase (with valves 1 and 3 open, valves 2 and 4 closed), where, the feed pump feeds a batch of saline water through the membrane into the water pump cylinder, as the piston moves downward to accept the feed. Having filled both the pump cylinder and RO module with saline water, the pressurisation stage commences (with valves 2, and 3 open, while valves 1 and 4 closed) as the piston pressurises the saline water against the membrane; thus causing freshwater to permeate through the membrane. As freshwater permeates out, the concentration of the solution in the system increases gradually, however, with the aid of the re-circulation pump the concentrations at the inlet and the outlet of the module are kept nearly equal. After the water pump piston reaches the end of its stroke, only concentrated brine is left in the module. Thus, it is necessary to purge the module by introducing feed water (with valves 1 and 4 open, valves 2 and 3 closed). In the purging stage, the concentration at the outlet decreases towards the value at the inlet. After purging out the residual concentrate, the system reverts back to the refill status, for the feed pump to supply the next batch of saline water, and repeats the cycle of operation.

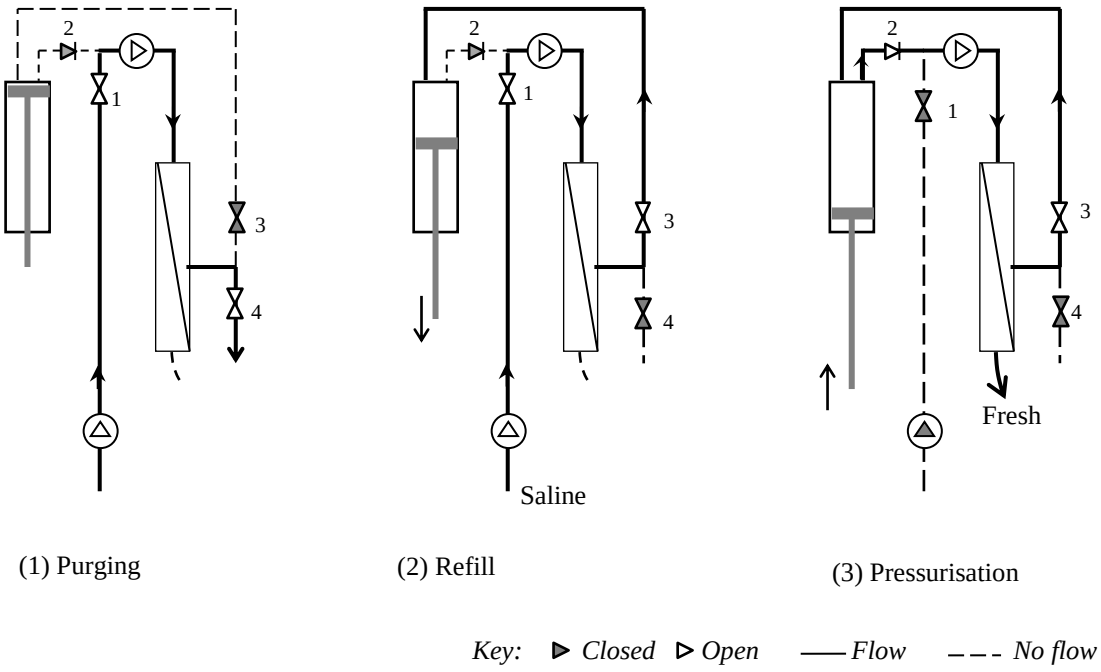

Figure 5.3: Stages of the batch operation of DesaLink

5.3 Details of the units of the test rig

The key components of the test rig can be grouped into RO subunit, ORC subunit, Instrumentation and Data acquisition.

5.3.1 RO sub-unit

For the RO subunit, the water pump cylinder was a 105 mm bore diameter glass reinforced fibre, GRF, pressure vessel, the recirculating pump was a Wilo, 3 m^3/h max flow volume pump, while the RO membrane was Dow FILMTEC^{TM} BW30-2540. The saline water feed line included a 200 ltr water barrel, 0.7 h.p submersible pump and cartridge filters.

5.3.2 ORC sub-unit

The ORC sub-unit included the power cylinder, condenser and the metering pump (Figure 5.4). The original cylinder base of the power cylinder was replaced with a bespoke fabricated cylinder base with integrated heat exchanger design (Figure 5.5). The new cylinder base was milled from solid aluminium block (engineering drawing attached in Appendix 4). The two sides of the cylinder base were designed to enhance heat transfer; the external side featured a fin design (fins with 2.5 mm thickness and 4 mm channel width), while the internal side employed parallel plate. The external side of the cylinder base serves as the heat collector i.e. to absorb heat from a thermal fluid, and

transfer the heat to the other (inner) side, where it heats up the cylinder. A copper plate attached to the inner face aids to provide increased surface area for heat transfer. Since the cylinder is mounted in horizontal orientation, this plate is essential to contain the injected liquid, to avoid the liquid flowing down (accumulating) to the bottom of the cylinder wall, and to spread the liquid and ensure sufficient surface area for heat transfer. The incorporation of the heat exchanger to the cylinder base provides the necessary heat during expansion to effect quasi-isothermal expansion.

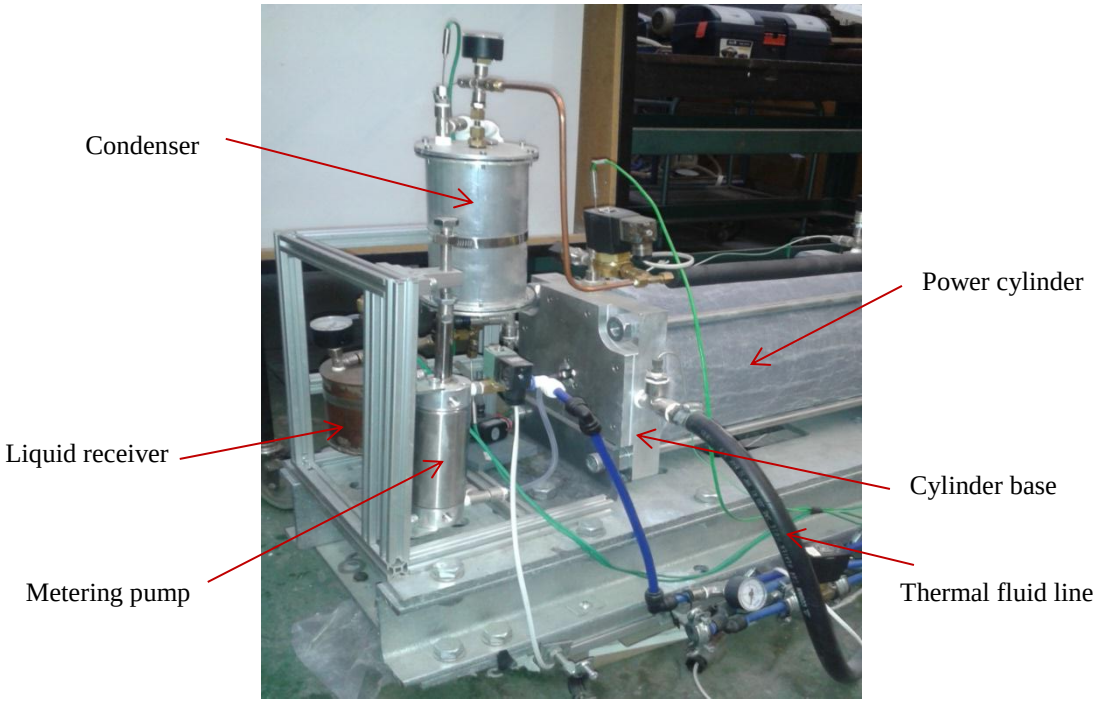

Figure 5.4: The ORC sub-unit of the DesaLink rig

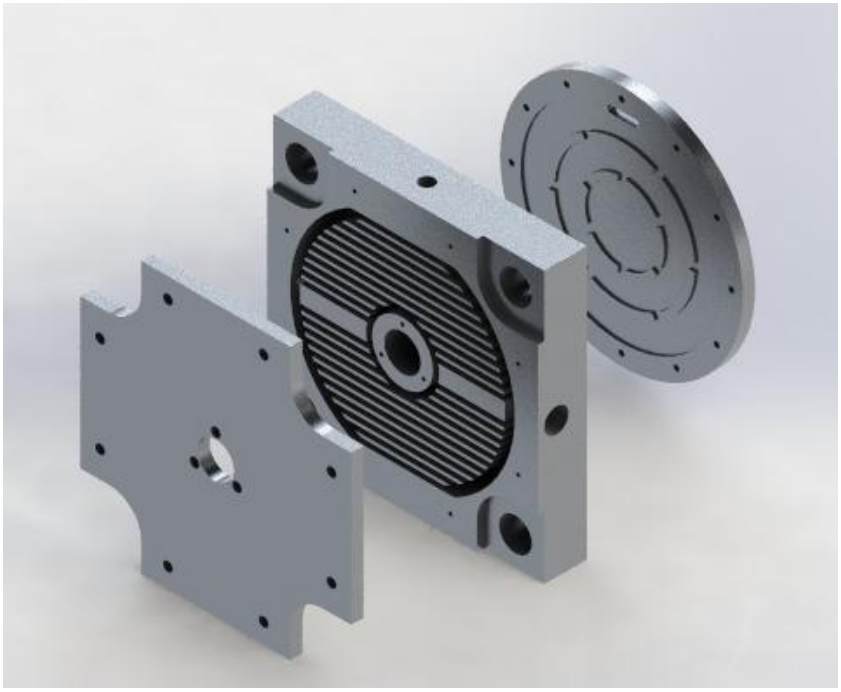

Figure 5.5: Exploded view of the finned cylinder base assembly

The thermal fluid employed (to be circulated through the finned cylinder base) was ethylene glycol and water mixture. A mixing ratio of 70% (glycol) was done to elevate the boiling point temperature to about 120^{o}C, as the heating temperature was desired to be maintained at about 100^{o}C. The thermal fluid circulation system included a 5 litre stainless steel kettle with 2 kW immersion heater, fitted with a thermocouple and temperature control unit; Grundfos 15-60 domestic circulating pump moves the thermal fluid through the system via a 5/8 diameter steam hose; and 2-30 ltr/min turbine flow meter (+/- 3% accuracy). The inlet and exit of the cylinder base were equipped with thermocouples.

On the other hand, the condenser was fabricated as a counter-flow double helix coil in tube heat exchanger. The helical coil was made from 6 mm diameter copper tube of 6.5 m length; the helix coil diameter of the outer coil was 80 mm with 9mm coil pitch and 16 turns; the inner helix also had same pitch and no of turns, but with a coil diameter 50 mm. The end of the coils were welded (silver brazed) to a common access port. The coil assembly was enclosed in a 100 mm bore aluminium cylinder (shell/water side) with flanged ends and gasket seals (Figure 5.6). The inlet and exit of the condenser were fitted with thermocouples and pressure gauges. A liquid receiver was attached at the coil (working fluid) exit of the condenser, to collect the condensate from the condenser before being fed to the metering pump, this serves as a buffer tank to minimise pressure fluctuations in the condenser and to avoid bubbles of vapour getting into the pump. Additionally, to avoid temperature build up (over time) in the liquid receiver, 2 turns of 10 mm copper tube coil (with 70 mm coil diameter) was provided in the receiver, such that, if necessary, the cooling water will be passed through the coil in the receiver before being fed to the water side of the condenser. On the other hand, the working fluid metering pump was adapted (similar as described in the previous chapters) from a 50 mm bore, double acting cylinder pump, fitted with non-return valves, and a three way solenoid valve for pneumatic control.

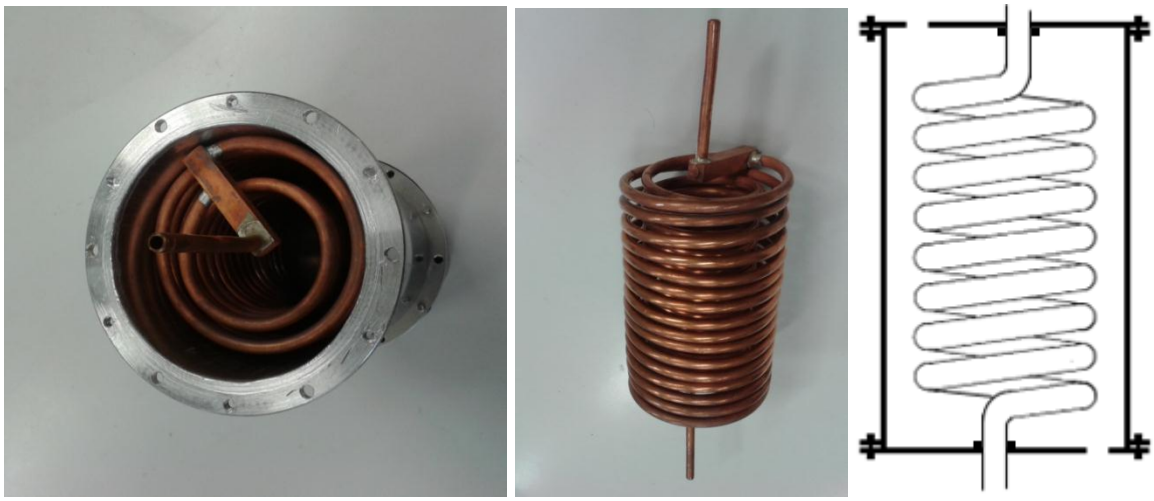

Figure 5.6: Different views of the condenser

5.3.3 Instrumentation

The test rig was instrumented by pressure, temperature, flow rate, conductivity, and displacement measuring devices to enable the collection of the appropriate data, with which to analyse the performance of the desalination system. These measuring devices will be described as follows.

All thermocouples utilized in the measurements were K-type thermocouples (accuracy 2.5^{o}C). 1.5 mm diameter stainless steel mineral insulated thermocouples were used for measuring the fluid temperatures at different positions in the test rig, while welded tip thermocouples were used for surface measurements. On the other hand, the pressure transducer utilized were Gems^{TM} sensors with 0.25% accuracy.

Displacement transducers were implemented with linear slide potentiometers (± 10% tolerance) to measure the stroke lengths of the power and water pump pistons, to enable calculations of the swept volumes. To improve the accuracy of the conversion of voltage signals to displacement values, the voltage output signals were processed in the data acquisition system in such a way that zero error correction was automatically effected at the start of operation. However, position sensing at various points of end of movement on the rig were implemented with magnetic proximity, and micro limit switches.

5.3.4 Data acquisition

The control architecture and data acquisition of the rig was based on LabVIEW® software from National Instruments (NI). The control design provided a user interface on the computer screen for real time visual supervision of the parameters and operating status of the rig. A mixed signal data acquisition system was implemented with a range of NI data acquisition packages, and a computer. NI-9174 chassis DAQ (data acquisition) with four slots, was used to accommodate different signal input modules for the temperature, pressure, conductivity and flow measurements. The thermocouples were connected to NI-9213 thermocouple input module, which occupied one of the four slots in the chassis. The NI-9213 module is a 16-channel input module, thus all the thermocouples required for the text rig were accommodated without taking too many slots. However, the pressure transducers and the conductivity cell were connected to NI-9203 analogue current input module, which was also inserted on another slot of the chassis. The flow sensors were connected to NI-9421 on the third slot of the chassis. On the other hand, for the displacement sensing, the slide potentiometers were connected to the analogue voltage side of NI USB-6008 DAQ; conversely, the proximity sensors were connected to the digital voltage side of the DAQ.

5.4 ORC DesaLink experiment

The description of the integrated isothermal ORC DesaLink experimental procedure and results are presented in this section. The performance of the ORC loop is characterised by the achieved pressure level in the power cylinder, the work output, and the thermal cycle efficiency of the ORC loop; in addition, the performance of the cylinder base is also presented. On the other hand, the performance of the RO loop is characterised by the average desalting rate (i.e. the volume of water produced in relation to the time of operation per cycle); while the overall performance of the integrated system is characterised by the ensuing mechanical and thermal SECs.

5.4.1 Test procedure

Upon setting up the test rig, the saline water loop was first flushed with de-chlorinated tap water with 2 ppm sodium-metabisulphate solution, in order to protect the RO membrane from oxidation due to chlorine attack [183]. After which the feed saline water was prepared from sodium chloride (Nacl) solution, to the appropriate concentration (4000 ppm). The saline feed water was also flushed through the system to get a uniform salinity through the pipe work, and to bleed off pockets of trapped air. The heating system was activated and the temperature was set to 95^{o}C and allowed sufficient time for the system temperature to stabilise and achieve steady state, whilst the thermal fluid was circulated through the cylinder base. The pump stroke was set to correspond to the desired liquid volume, afterwards the start operation was activated, and a metered volume of the working fluid liquid was injected into the cylinder base; and the measurement data profiles were viewed on the PC screen (Figure 5.7) as they are been recorded by the DAQ (after a number of initial test runs to achieve a smooth operation).

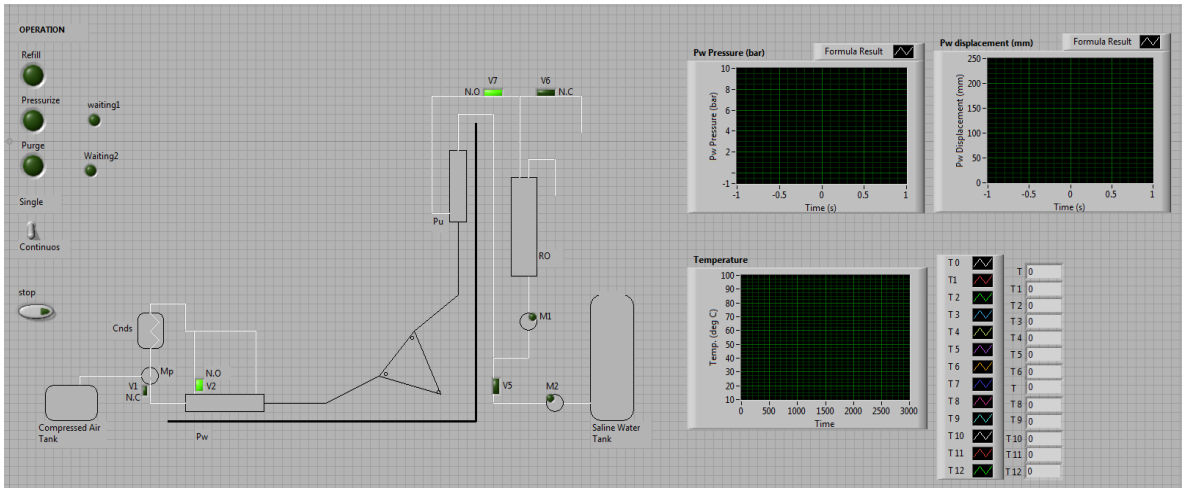

Figure 5.7: DesaLink control panel (LabVIEW)

5.4.2 Results

The cylinder base wall (internal) temperature profile achieving steady state condition is shown in Figure 5.8. With a thermal fluid temperature set-point of 95^{o}C, a heat source power set at 1.5 kW, and a fluid flow rate of 50 ltr/min, the set-point temperature was achieved in about half hour; however, it took more than one hour for the temperatures to be fairly stabilized. The outlet temperatures very closely match those of the inlet, with a maximum temperature drop (from inlet to exit) of 0.5^{o}C observed during the rising gradient, and about 0.15^{o}C during the stable regime. On the other hand, the temperature at the wall was about 3^{o}C less than the inlet temperature, while that at the wall's cladded copper plate was about 5^{o}C less.

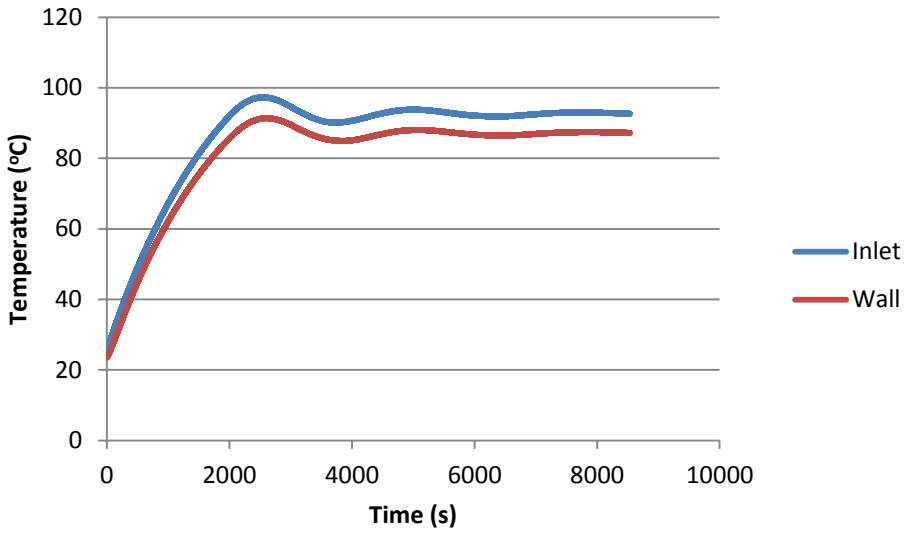

Figure 5.8: Thermal fluid and cylinder base wall temperature profiles

The performance of the ORC cycle can be accessed with the aid of the p-V characteristics of the power cylinder, as be shown in Figure 5.9. Upon injection, the liquid evaporated at an average pressure (gauge) of 7.5 bar, which reduced to 2.5 bar at the end of the expansion, and was blown down to the condenser pressure of 1.6 bar at the release of the exhaust valve. The work output computed directly from the p-V diagram represents the indicated/reversible work; however the actual work is obtained by subtracting the losses due to friction at the cylinder seals. For low friction pneumatic cylinders (without cushion), the minimum pressure required to overcome the friction at the piston seal could be as low as 0.05 bar for large bore cylinders (>125 mm), however during operation, the pressure equivalent of the seal's sliding resistance varies linearly with the operating pressure at a gradient of less than 1% of the operating pressure [184].

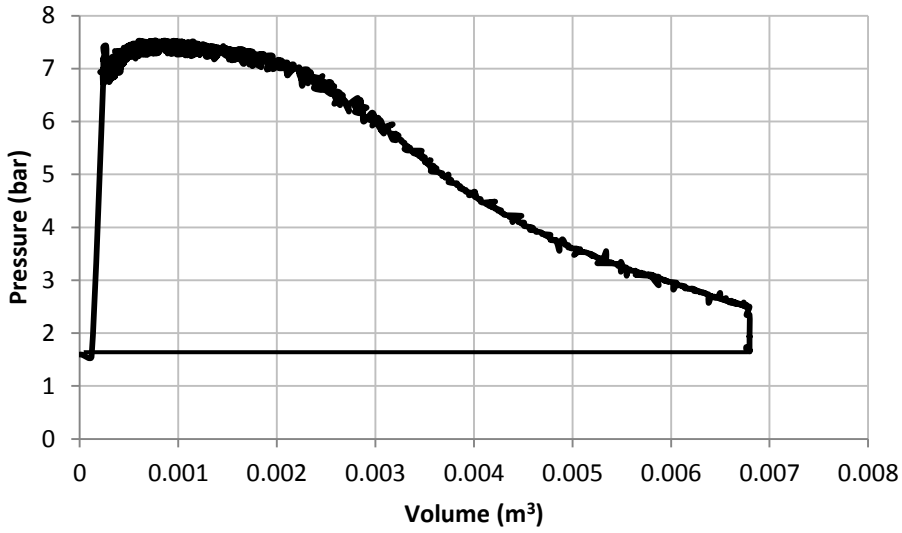

Figure 5.9: Pressure volume (p-V) diagram of the ORC subunit

The profiles of the R245fa pressure in the power cylinder and the water pressure in the RO loop are shown in Figure 5.10. As the R245fa evaporates fairly uniformly at 7.5 bar in the power cylinder, the saline water pressure in the pump cylinder increases gradually (due to the increasing mechanical advantage from the linkage system) until the end of evaporation; from whence the pressure transits and declines, as the R245fa pressure decreases upon expansion. Here, the gains from the rising mechanical advantage is not sufficient to overcome the decrease from the expanding power pressure, thus, there is a net decline in the water pressure (nevertheless, it remains higher than the power pressure). However, resetting the linkage system for a slightly higher mechanical advantage (by slightly increasing the starting angular position of the triangular crank), slightly increases the operating pressures in water cylinder, minimises the decline in the water pressure during the expansion stage and results to increased pressure towards the end of the stroke, which eventually reduced the operating cycle time from 1170 s to 810 s as shown in Figure 5.11a.

Awkwardly, the improved operating cycle time is seen to be almost twice that observed in the original version of the machine reported by Qiu (using compressed air) [182]. This unfortunate situation can be attributed to the fact that the achieved net driving pressure is significantly less than would be ideal. Since the piston rod side of the cylinder was connected to the condenser as mention earlier, the evaporating pressure of 7.5 bar less the condenser pressure of 1.5 bar gives a net driving pressure of 6 bar, which is less than the 8 bar driving pressure that would be ideally required (as in Qiu's work). To alleviate this issue, a further improvement in the cycle time was achieved by reducing the condenser pressure (to 0.7 bar), thus, slightly increasing the net driving pressure; and consequently reducing the cycle time by more than 120 s (Figure 5.11b). The net work done (with friction considered) is obtained as 2.85 kJ, while the efficiency is 7.7%, and isothermality is 0.85.

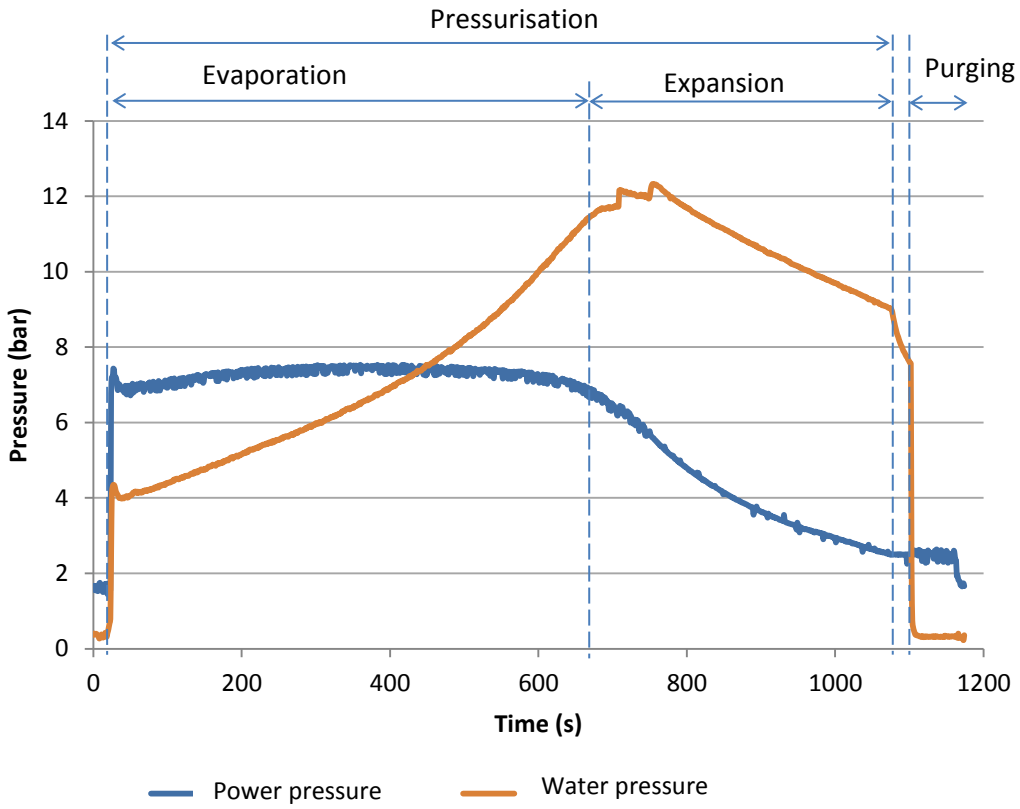

Figure 5.10: Pressure profiles of power and water cylinders

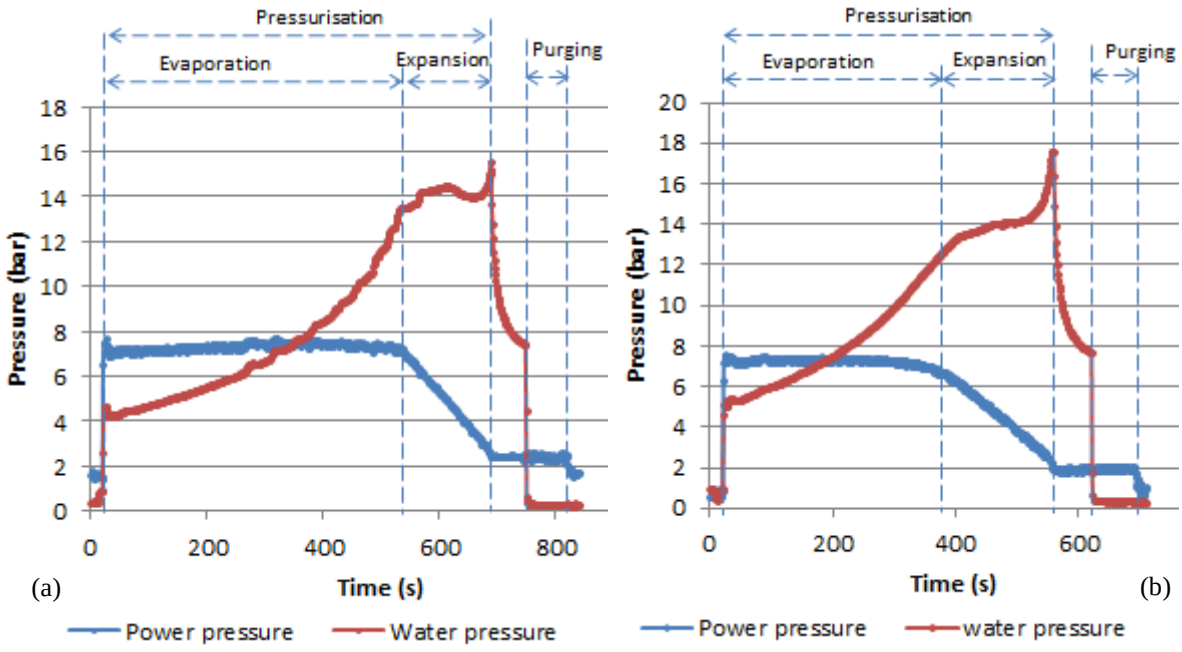

Figure 5.11: The improved pressure (gauge) profiles in the power and water cylinders; (a) with 1.5 bar condenser pressure (b) improved cycle time, with lower condenser pressure of 0.7 bar

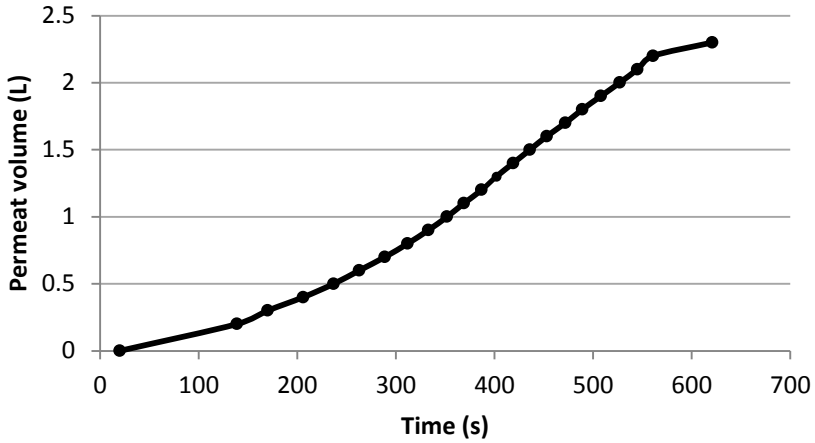

Figure 5.12: Profile of the volume of fresh water production

The evaporation phase together with the expansion phase of the R245fa constitutes the pressurisation phase of the saline water, during which, fresh water is continuously permeated out from the RO module. At the end of the pressurisation phase, a waiting time of 60 seconds was set to allow further permeate to drip out the module, because the water pressure at the end of the expanding stage (9 - 17 bar) was significantly higher than the osmotic pressure of the bulk solution (about 3 bar); as a result, the pressure difference was sufficient to drive additional fresh water through the membrane. During this waiting time, the water pressure decreased sharply, as freshwater is removed from the system with no further external pressure applied. The cumulative volume of the permeated fresh water is shown in Figure 5.12, the volume increased uniformly at a rate that depends on the water pressure; and a total of about 2.3 ltr of fresh water (of about 500 ppm) was obtained. At the end of the water production of the waiting time, the purging process commenced, with new saline water (about 1 ltr) pumped through the RO module to wash out the accumulated brine from the membrane. After the purging, the power cylinder's exhaust valve was released (and the power pressure drops down to the condenser pressure) to enable it for the return stroke; then the next batch of feed saline water refilled the water cylinder, ideally forcing both pistons to return to their initial positions with the aid of the weight of the triangular crank. However, here, some external force was manually applied just to overcome the initial limiting friction of the system, after which the return stroke continued on its own, followed by the start of next cycle.

Based on the results, for each cycle of operation, about 2.85 kJ of work was performed by the power cylinder per cycle to produce 2.3 ltr of fresh water from the RO module. This equates to a mechanical specific energy consumption of 0.34 kWh/m^3 (1.24 kJ/ltr). In terms of thermal energy, about 37 kJ of heat was consumed to evaporate the R245fa in the power cylinder to perform the work which produced the 2.3 ltr permeate; thus equating to a thermal SEC of 4.4 kWh/m^3 (16

kJ/ltr). The mechanical energy consumption performance achieved with the ORC-DesaLink system can be presented in comparison to those of the reported practical performances for conventional ORC-RO desalination systems as depicted in Figure 5.13; while an overview of the general performances is given in Table 5.1. In comparison, it can be seen that the ORC-DesaLink consumes about 35 to 51% of the mechanical energy consumed by conventional ORC-RO systems to desalinate a unit volume of water, despite the fact that these systems operated at significantly lower feed water salinity and recovery ratio. However, it worth mentioning that due to the slow speed of the DesaLink machine, the fresh water production capacity per unit plant area occupied by the machine is relatively low compared to the conventional systems.

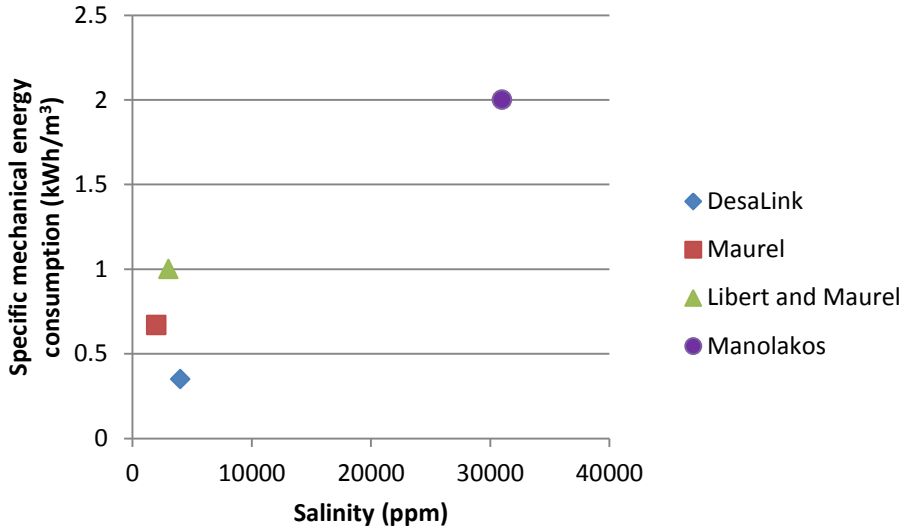

Figure 5.13: The achieved specific mechanical energy consumption of the ORC-DesaLink, in comparison with conventional ORC-RO systems by Maurel [65], Libert and Maurel [64] and Manolakos et.al [66].

Table 5.1: Overview of the performance of the ORC-RO DesaLink system in comparison to conventional ORC-RO systems

Study	Temp. (^{o}C)	η_{ORC} (%)	Feed water (ppm)	SEC_{mech} (kWh/m^3)	$SEC_{thermal}$ (kWh/m^3)	Recovery ratio
ORC-DesaLink (experimental)	80	7.7	4000 (BW)	0.34	4.4	0.69
Maurel [65] (experimental)			2000 (BW)	0.68		0.5
Libert and Maurel [64] (experimental)	92		(3000) BW	1		
Manolakos et al [66] (experimental)	60	3.5-5	31000 (SW)	2-3	80-110	0.2

5.6 Chapter Summary

An integrated isothermal ORC unit has been built and coupled to drive the batch desalination machine, DesaLink. Experimental work carried out to access the performance of the integrated ORC-DesaLink system showed that at 7.9% ORC efficiency, 2.3 ltr of fresh water was produced from 4000 ppm saline feed water, at a specific mechanical energy consumption of 0.35 kWh/m^3 (which is about a half of the energy requirement of conventional ORC-RO desalination systems). Based on the obtained results, the ORC-DesaLink can be expected to produce an output of about 12 ltr of fresh water per hour.

However, the achieved cycle time for each batch of operation was undesirably slow, as a result of low net driving pressure. Efforts employed to increase the net driving pressure, and thus improve the cycle time included: increasing the mechanical advantage of the linkage system, and reducing the condenser pressure. Recommendations for further improvement would require increasing the heating temperature of the power cylinder base, to increase the evaporating pressure, and of course, a corresponding higher pneumatic pressure supply to the metering pump to enable injection of the working fluid at a higher pressure into the power cylinder.

Nevertheless, having proved the feasibility of the ORC-DesaLink system, the following chapters will proceed to developing models to describe/characterize the operation of the integrated system and using the models to analyse the potential performance of the system in real live scenarios, as case studies.

Chapter 6 System modelling

This chapter presents a description of the theoretical models adopted to describe (characterise and predict) the behaviour/performance of the integrated ORC-DesaLink system. Models for the sub-units of the integrated system were first developed and validated (with experimental data) and then integrated into a complete system model.

6.1 Introduction

The integrated ORC DesaLink system has been shown practicable in the experimental work carried out in the previous chapter. However, the operational behaviour and performance of the system in different operating conditions can be further investigated. As such, here, it is sought to develop models to characterize the integrated system.

The modelling of the ORC DesaLink system can be realized from a group of sub models – the ORC sub-model, the linkage mechanism sub-model and the RO sub-model. The RO sub-model has been comprehensively studied (alongside a compressed air based driving power model) by Qiu in a MATLAB/Simulink environment [182]. However, here, the relevant models will be modified to represent the current system design; most especially, the compressed air based power sub-model will be replaced with the ORC cycle sub-model that will be presented shortly in this chapter. The ORC cycle sub-model is a further development on the cycle models previously presented in Chapter 4.

The structure of the ORC DesaLink model is presented in Figure 6.1, the integrated system model is built by developing and interconnecting a set of semi-empirical sub models of the different sub systems. The sub models are initially developed based on the appropriate underling theories, and where necessary, model parameters, efficiency terms or correction factors are utilised and calibrated with experimental data, as the final model is validated with measurements from additional experiments. The models are developed in the Engineering Equation Solver (EES) environment. This environment has been chosen because of its comprehensive library of thermodynamic fluid properties, as already utilised in Chapter 4.

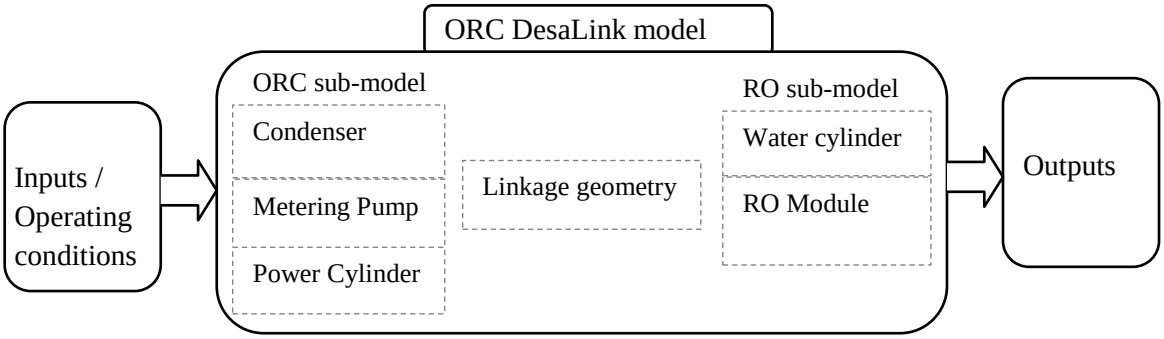

Figure 6.1: Structure of the ORC DesaLink model

6.2 ORC sub model

The ORC sub model can be developed by interconnecting the sub-models of the different subcomponents of the cycle (condenser, metering pump and heated power cylinder); thus here, emphasis is placed on characterising the behaviour of the ORC subcomponents based on thermodynamic principles and heat transfer correlations.

6.2.1 Condenser

As described in the previous chapter, the condenser was fabricated as helical coil in tube, with the vapour inlet piped from the power cylinder; and a liquid receiver affixed to the outlet (Figure 6.2), by extension, the liquid receiver can be considered as part of the condenser.

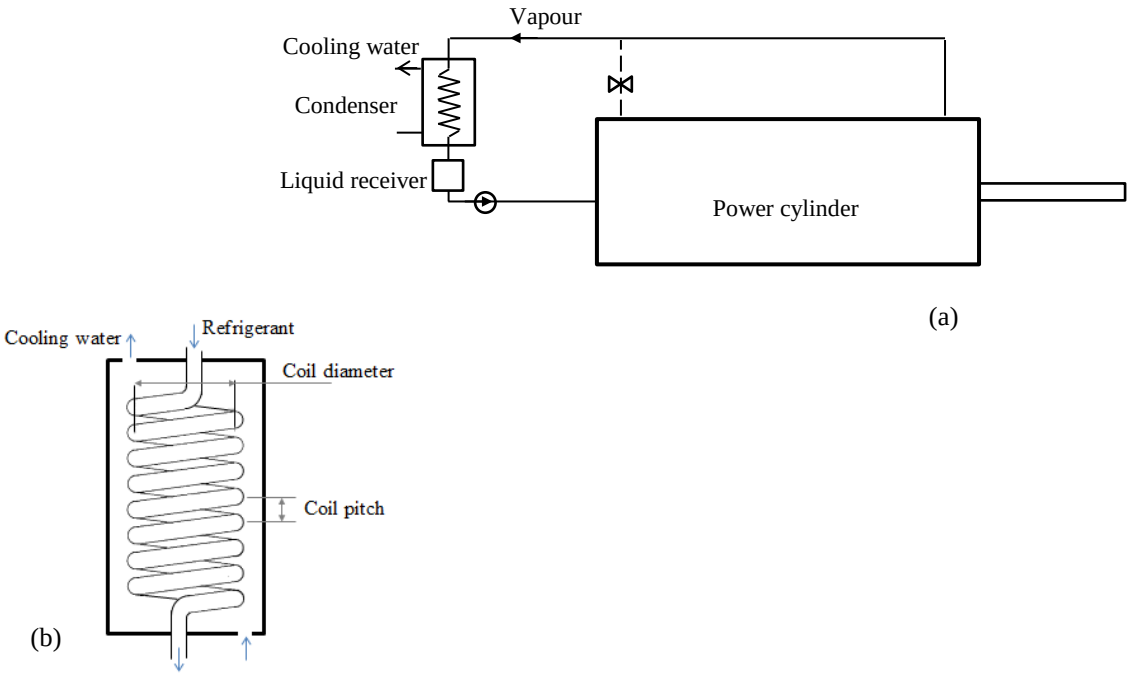

Figure 6.2: (a) ORC and (b) condenser setup

The prevailing pressure in the condenser (and by extension, the liquid receiver) is function of the mass of working fluid in the system, the volume of the system (mainly the power cylinder), the average temperature in the cylinder, and the heat transfer characteristics in the condenser. For a given condenser heat transfer coefficient, the pressure becomes mainly dependent on the state of the vapour in the power cylinder. This can be obtained with the aid of an appropriate *equation of state* (example the Peng-Robisson equation of state [185]) using the specific volume, and temperature of the vapour in the power cylinder as the state parameters. However, this can be easily computed directly in the EES software environment; example by using the expression $P = Pressure\left(R245fa, v = v, T = T_{avg}\right)$; where, v and T_{avg} are the specific volume and average temperature of the vapour in the power cylinder, respectively. Based on the system configuration, the volume of power cylinder is much larger than that of the condenser and liquid receiver, thus, on operation, the pressure exerted in the condenser is actually imposed by the conditions of the vapour in the power cylinder.

At the condenser outlet, the condition of the fluid exiting, can be either subcooled, (in which case the pressure remains constant) or two-phase (in which case the pressure is going to increase), depending on the overall effectiveness of the condenser. However, it is desirable for the condenser to maintain a constant pressure despite having an increasing vapour temperature at the inlet. To achieve this, the heat transfer coefficient must be sufficient to ensure that the heat rejected by the vapour is completely evacuated by the cooling water.

Hence, the condenser can be modelled based on the coefficient of heat transfer between the refrigerant and the cooling water. The heat exchange in the condenser can ideally be subdivided into three zones namely: superheated vapour zone, two phase zone and subcooled liquid zone.

Since the helical coil is enveloped by the cooling water, and if there is only an insignificant temperature difference between the condenser and the ambient, it can be assumed that the condensation sensible heat (of the single phase zones) and latent heat (of the two phase zone) of the refrigerant are effectively transferred into the water, and we can neglect heat loss, while also neglecting fouling effect. Also, if the level of superheat and sub cooling in the single phase zones are minimal, there effect could be neglected since majority of the heat transfer is due to the condensation latent heat.

The cooling load (heat) absorbed by the water from the refrigerant can be calculated as:

$$\dot{Q} = \dot{V}_{\text{w}}\, \rho_{\text{w}}\, C_{p,\text{w}}\left(T_{\text{w},o} - T_{\text{w},i}\right) \tag{6.1}$$

However, based on Newton's cooling law, the heat transferred can be given as

$$\dot{Q} = U_o \, A \, \Delta T_{LMTD} \tag{6.2}$$

Thus, based on energy balance, the overall heat transfer coefficient, U_o, between the water side and the refrigerant side can be determined as

$$U_o = \frac{\dot{V}_w \rho_w C_{P,w} (T_{w,o} - T_{w,i})}{A \, \Delta T_{LMTD}} \tag{6.3}$$

where, $\dot{V}_w$, ρ_w, and $C_{P,w}$ are the volumetric flow rate, density and specific heat of the coolant water respectively; $T_{w,i}$ and $T_{w,o}$ are respectively, the water inlet and exit temperatures; and ΔT_{LMTD} is the log mean temperature differential defined as

$$\Delta T_{LMTD} = \frac{(T_{r,o} - T_{w,i}) - (T_{r,i} - T_{w,o})}{\ln[(T_{r,o} - T_{w,i})/(T_{r,i} - T_{w,o})]} \tag{6.4}$$

where, $T_{w,i}$ and $T_{w,o}$ are the inlet and outlet coolant water temperatures respectively; $T_{r,i}$ and $T_{r,o}$ are the temperatures of the refrigerant at the inlet and outlet respectively. If the single phase zones are considered, the ΔT_{LMTD} can be applied for each zone; in this case, the intermediary coolant water temperatures (corresponding to the saturation temperature at the zone boundaries) can be identified with the aid of energy balance for each zone.

Furthermore, the heat transfer coefficient between the refrigerant and water sides can be related to the convective heat transfer coefficient, α, and the other heat transfer resistances encountered along the heat path, as:

$$\frac{1}{U_o} = \frac{A_o}{A_i \alpha_{ci}} + \frac{A_o ln(d_o/d_i)}{2\pi k L} + \frac{1}{\alpha_o} \tag{6.5}$$

where, A_o, A_i, d_o, d_i are the surface areas and diameters of the outer and inner sides of the tube respectively, while k and L are respectively the thermal conductivity and length of the tube; α_o is the water side (outside) convective heat transfer coefficient; and α_{ci} is the convective/condensation heat transfer coefficient of the refrigerant side (inside).

The convective heat transfer coefficient of the refrigerant side can be given in terms of the dimensionless parameter Nusselt number, *Nu*, and the thermal conductivity of the refrigerant k_i as:

$$\alpha_{ci} = \frac{Nu_i k_i}{d_i} \tag{6.6}$$

For the two phase zone, the Nusselt number of the flow in the helical tube can be obtained from the correlation developed by Kang et al. [186].

$$Nu_i = 2.3\, \dot{Re_i}^{0.94}\, Pr^{0.4} \tag{6.7}$$

$$\dot{Re_i} = \frac{\acute{m} x d_i}{\mu_f \sqrt{\rho_f / \rho_g}} \tag{6.8}$$

$$(1100 < \dot{Re_i} < 2500)$$

where, *Pr*, $\acute{m}$ and *x* are respectively the Prandtl number, mass flux and average vapour quality from inlet to exit; while ρ_f and ρ_g, the densities of the liquid and vapour state respectively.

However if the single phase zones are to be considered, their heat transfer coefficients can be calculated with the Nusselt number correlation for laminar flow (Re <1500) as [187]

$$Nu_{lam} = \left[\left(4.364 + \frac{4.636}{x3}\right) + 1.816\left(\frac{Dn}{x4}\right)^{3/2}\right]^{1/3} \tag{6.9}$$

$$x3 = \left(1 + \frac{1342}{Dn^2 Pr}\right)^2 \;;\; x4 = \left(1 + \frac{1.15}{Pr}\right) \;;\; Dn = Re\left(\frac{d_i}{d_{coil}}\right)^{1/2} \tag{6.10}$$

Or, in the case of turbulent flow (1500<Re>20000), as [187]

$$Nu_{turb} = Nu_{straight}\left[1 + 3.4\frac{d_i}{d_{coil}}\right] \tag{6.11}$$

$$Nu_{straight} = \frac{f_{straight}}{8}(Re - 1000)/\left[1.07 + 12.7\left(f_{straight}\right)^{0.5}\left(Pr^{2/3} - 1\right)\right] \tag{6.12}$$

$$f_{straight} = (0.79\ln(Re) - 1.64)^{-2} \tag{6.13}$$

On the other hand, for the water side convective heat transfer coefficient, the correlation developed by Salimpour [188] and modified by Elsayed [189] (for small diameter tubes) is used

$$Nu_o = 24.55\, Re_o^{0.513} Pr_o^{0.129} \text{y}^{0.938} \tag{6.14}$$

Then, the water side heat transfer coefficient is

$$\alpha_o = \frac{Nu_o k_w}{Đ} \tag{6.15}$$

$$Re_o = \frac{\rho V_o Đ}{\mu} \tag{6.16}$$

$$Đ = \frac{d_{shell}^2 - \pi d_{coil} d_o^2 \gamma^{-1}}{d_{shell} + \pi d_{coil} d_o \gamma^{-1}} \tag{6.17}$$

$$\gamma = \frac{\delta_{coil}}{\pi d_{coil}} \tag{6.18}$$

where, V_o, δ_{coil}, Đ, are the average velocity, coil pitch and the hydraulic/effective diameter of the shell side respectively.

To validate the aforesaid models, the condensing pressure and temperature were assessed for varying inlet vapour temperatures and mass flow rates. For the range of inlet vapour temperatures considered, the predicted constant pressure was in agreement with the measured pressure (Figure 6.3). Thus affirming the earlier assertion made regarding the constancy of the pressure for a given sufficient overall heat transfer characteristics. To validate the heat transfer model, the refrigerant exit temperature from the condenser was assessed for a range of vapor mass flow rates (0.07 – 0.43 g/s) and corresponding inlet temperatures of (30 – 40^{o}C). For the vapor conditions considered, the heat transfer model predicted the refrigerant exit temperatures with a relative error of within $\pm$10% (Figure 6.4).

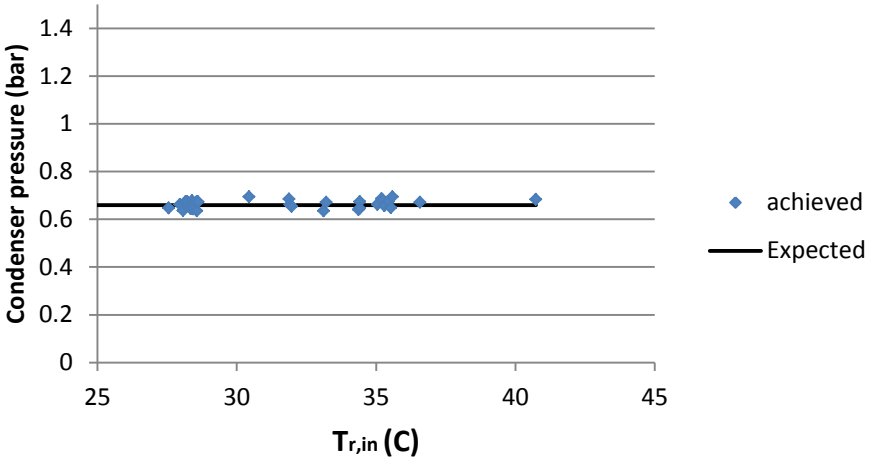

Figure 6.3: Predicted and measured condensing pressure for varying condenser inlet temperatures

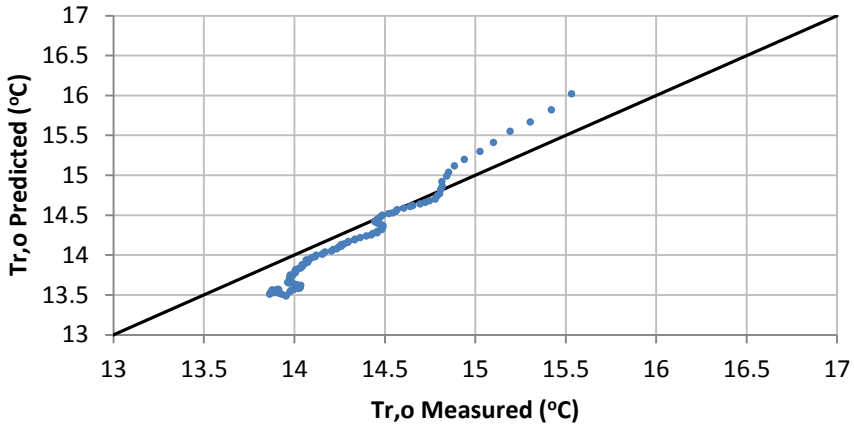

Figure 6.4: Predicted vs measured refrigerant temperatures at condenser outlet

6.2.2 Metering Pump

The reciprocating piston pump is characterised by its swept volume (based on the piston diameter and stroke length) and efficiency. The reciprocating pump efficiency can be viewed in two aspects – volumetric efficiency and mechanical efficiency.

For a given swept volume, the volumetric efficiency enables the actual volume of fluid discharged into the power cylinder to be determined, based on the fluid properties and operating pressure. The volumetric efficiency can be given as:

$$\eta_{VE} = 1 - \left((\Delta P \ \beta \ \varphi) + \forall_{slip} + \forall_{vap}\right) \tag{6.19}$$

Thus, the volume of fluid that eventually gets pumped can be given as:

$$V_{liq} = A_{pm} S_{pm} \ \eta_{VE} \tag{6.20}$$

where, ΔP is the differential pressure between the discharge and suction; β is the compressibility (inverse of bulk modulus) of the liquid at the pumping pressure/temperature; φ is the ratio between the volume of the total pumping chamber (including the void volume at the valve ports) to the pump piston displacement volume (area, A_{pm}, x stroke length, S_{pm}); $\forall_{slip}$ is the losses due to fluid slippage back past the pump valves before full closure, typically about 1 to 5% based on valve design and pumping speed; $\forall_{vap}$ is the fractional volume losses due to vaporisation of the liquid along the discharge duct (into the heated cylinder) and cavitation in the pump chamber [190]. The effect of this reduced metered liquid volume is that, the resulting vaporisation length and stroke end pressure in the power cylinder will be less than anticipated (this will be better appreciated later in section – 6.2.3.2).

On the other hand, the pump efficiency takes care of other internal irreversibility of the pump, which ultimately results to pressure losses across the pump, and thus, a reduced discharge pressure into the power cylinder. The pressure of the pumped fluid, P_o, can be cast as a fraction of the driving pressure, P_i, as

$$P_o = P_i - P_{loss} = P_i - (\Delta P_{nv} + f_p A_{pm} + \Delta P_{hyd}) \tag{6.21}$$

$$P_o = \eta_{pm} P_i \tag{6.22}$$

where, P_{loss} is the pressure loss in the pump system. The pressure loss include a combination of various losses such as the minimum pressure required to open the non-return valve (P_{nv}), the pressure loss due to the friction (f_p) at the piston seal and the cylinder wall, and other pressure drops due to hydraulic losses along the flow path, including acceleration pressure drop and losses due to sudden expansion of pipe chamber. The seal friction (both break-out and running) could be difficult to quantify, since it involves a lot of parameters that cannot be easily measured. The amount of break-out friction which an O-ring seal will develop depends on the length of time the surfaces of the rubber and the metal have been in contact. This is more significant at the initial start of operation, and diminishes with subsequent strokes; as such the break out friction could be ignored from operational analysis.

To validate the above model, an experiment was carried out, wherein, different driving pressures where applied and the achieved output pressures in the power cylinder where recorded. For a range of injection pressures (5 to 9 bar), a pump efficiency of about 0.79 was found to yield the best prediction of the measured output pressure values, within $\pm$ 6.6% relative error (Figure 6.5).

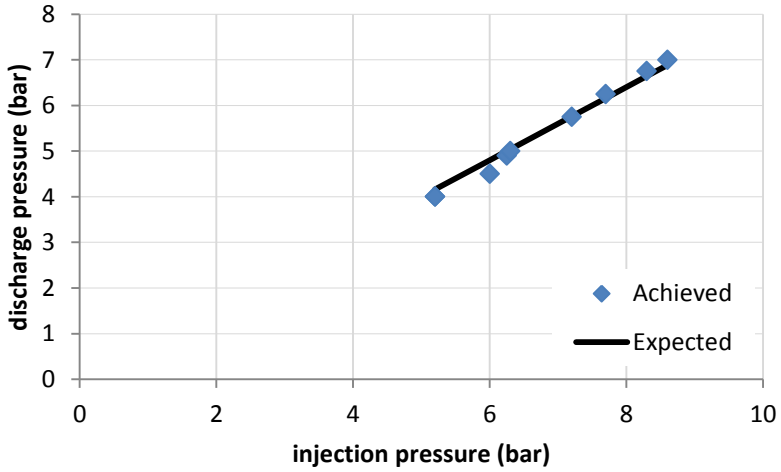

Figure 6.5: Measured and model pumped pressures for varying driving pressures

6.2.3 Heated Expander (Power Cylinder)

The heated expander model can be sub-divided into the evaporator and expansion sub-models. The evaporator model will treat the heat transfer characteristics from the thermal fluid into the cylinder base interior surface (which serves as the heating surface to evaporate the working fluid), while the expander model will consider the expansion behaviour of working fluid vapour during the expansion process.

6.2.3.1 Evaporator (heated cylinder base) model

The cylinder base model is based on the surface temperature profile. The model of the cylinder base surface temperature can be developed from the models generally used in the analysis of rectangular fin heat sinks with high aspect ratio (channel width, ω << height, H) [191].

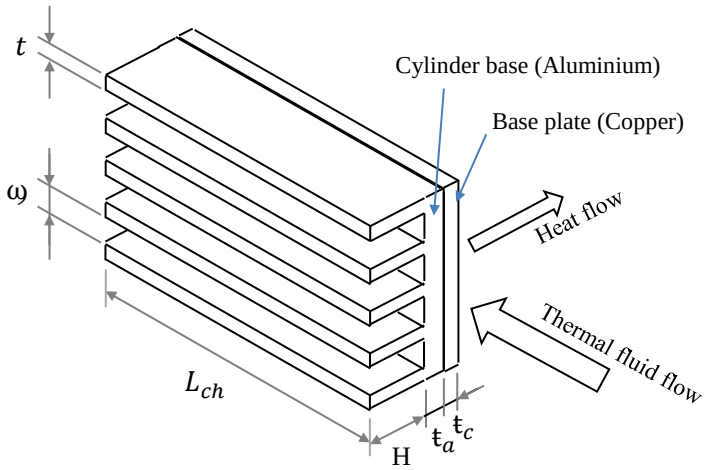

Figure 6.6: Schematic of fin cylinder base

At steady state condition, the heat supplied by the heat transfer fluid can be obtained as

$$\dot{Q}_{HTF} = \rho \ \dot{V} \ c_p \ (T_{HTF,in} - T_{HTF,out}) \tag{6.23}$$

The heat received at the cylinder base internal wall surface can be expressed as a fraction of the heat supplied

$$\dot{Q}_{base} = \eta_{HTF} Q_{HTF} \tag{6.24}$$

where, η_{HTF} expresses the heat received at the internal wall as a fraction of the heat supplied by the fluid. Some of the heat provided is conducted to other parts of the assembly and lost to the ambient. Given the complexity of the machine geometry, as it involves many number of mating surfaces, it is

difficult to calculate the heat loss directly. However, the heat loss fraction can be estimated by taking a heat balance between the supplied and received heat values which are calculated based on a set of reference measured temperatures of the fluid flow and base wall.

The heat received at the cylinder base wall surface can be calculated as:

$$\dot{Q}_{base} = U\, A_{fb}(T_{HTF} - T_{base}) \tag{6.25}$$

where, T_{HTF} is the average temperature of the thermal fluid given as $(T_{HTF,in} + T_{HTF,out})/2$; T_{base} is the average temperature of the cylinder base, U is the overall heat transfer coefficient between the fluid and the cylinder base; A_{fb} is the total area of heat transfer surface (including the fin).

Then the cylinder base surface temperature T_{base} can be predicted as

$$T_{base} = T_{HTF} - \left(\frac{Q_{base}}{UA_{fb}}\right) \tag{6.26}$$

$$T_{base} = T_{HTF} - \left(\frac{\eta_{HTF}\, \rho\, \dot{V}\, c_p\, (T_{HTF,in} - T_{HTF,out})}{U\, A_{fb}}\right) \tag{6.27}$$

wherein, $1/UA_{fb}$ is the overall thermal resistance to heat flow along the path of flow. For the cylinder base under consideration, the thermal resistance can be expressed as:

$$R_{th} = \frac{1}{UA} = \frac{1}{\alpha_{HTF,f}\, A_{fb}} + \frac{\mathfrak{t}_a}{k_a\, A_a} + \frac{TCR}{A_{cj}} + \frac{\mathfrak{t}_{cj}}{k_c\, A_{cj}} + \frac{\mathfrak{t}_c}{k_c\, A_c} \tag{6.28}$$

where, $\mathfrak{t}_a, k_a, A_a,$ are the thickness, thermal conductivity and area of the aluminium cylinder base respectively; $\mathfrak{t}_c, k_c, A_c,$ are respectively the thickness, thermal conductivity and area of the copper base plate; while $\mathfrak{t}_{cj}\ and\ A_{cj}$ are the thickness and area of the copper surface contacting the aluminium. The first two terms of the summation represents the thermal resistance from the thermal fluid to the base wall surface, whereas the entire summation represents the resistance from the fluid up to the cladding copper base plate. The term TCR represents the thermal contact resistance between the mating surfaces (of aluminium base and copper plate). Although this can depend on a number factors including contact pressure, surface roughness, void fill, etc., experimental studies have shown values in the range of 0.00012 – 0.0004 and 0.00016 – 0.0003 (m^2.K/W) for aluminium/aluminium interface and copper/copper interface respectively for contact pressures below 2 MPa [192, 193]. The term $\alpha_{HTF,f}$, is the convective heat transfer coefficient between the fluid and the fin, and can be obtained as

$$\alpha_{HTF,f} = Nu_b \frac{k_{HTF}}{Đ} \tag{6.29}$$

here, k_{HTF} is the thermal conductivity of the fluid; Đ is the hydraulic diameter of the channel, defined as $Đ = 4(crossectional\ area/perimeter)$; and Nu_b, the Nusselt number can be obtained from correlations (for rectangular ducts), assuming a fully developed laminar flow along the channel length, as is the case for most liquids with high Prandtl number and low flow Reynolds number [194-196]:

$$Nu_b = 8.235(1 - 1.88ϒ + 3.767ϒ^2 - 5.814ϒ^3 + 5.361ϒ^4) \tag{6.30}$$

$$\text{For: } (\mathcal{L}/ĐRe_bPr) \geq 0.1 \quad \text{and} \quad Re_b \leq 2100$$

$$Re_b = \frac{VρĐ}{\mu} \tag{6.31}$$

where, $ϒ$ is the aspect ratio (= channel width/height), $\mathcal{L}$ is the distance from the entrance of the channel, along the channel length, ($0 \leq \mathcal{L} \leq L_{ch}$), and V the mean uniform velocity through the channels.

The validation of the above described model for the cylinder base surface temperature is presented in Figure 6.7. For a given thermal fluid supply temperature (in the range of 70 to 95°C), the model predicts the cylinder base surface temperature with a relative error of less than ±3%. The heat transfer efficiency, η_{HTF}, from the thermal fluid to the base surface was found to be about 45%.

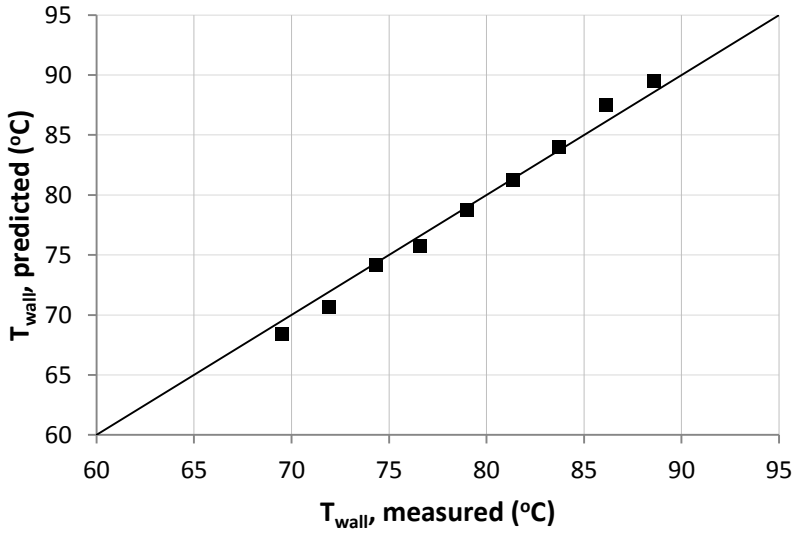

Figure 6.7: Predicted vs measured cylinder base surface temperature

6.2.3.2 Evaporation and Expansion model

Upon injection into the heated cylinder base, the liquid working fluid initially evaporates at the pump pressure. For a given operating conditions, ideally, a given load at the piston would maintain equilibrium with the fluid to vaporise at constant pressure, such that the rate of vaporisation balances the displacement of the piston/load; and the piston stroke volume of the vaporisation phase, V_{vap}, would be a function of the actual volume of pumped liquid and the dead volume present in the expansion chamber of the power cylinder (as indicated in chapter 3)

$$V_{vap} = \left(v_g\ \rho_{liq}\ V_{liq}\right) - V_d = V_{g,sat} - \ V_d \tag{6.32}$$

$$V_{vap'} = \frac{V_{liq}}{V_d}\ V_{g,sat} \tag{6.33}$$

where, V_{liq} is the actual volume of liquid injected (with the volumetric efficiency taken into consideration as in the previous section – 6.2.2), ρ_{liq} is the density of the injected liquid; V_d is the dead volume, while v_g is the specific volume of the saturated vapour at the evaporating pressure, and $V_{g,sat}$ is the actual volume of the dry saturated vapour.

However, in the present DesaLink configuration, this constant pressure vaporisation phase gets truncated by virtue of the apparent decreasing load, due to the increasing mechanical advantage ($M.A$) introduced by the linkage mechanism. Here it is worth mentioning that, although there is also an apparent increasing load due to increasing osmotic pressure, P_{osm}, in the saline water cylinder, the effect of the magnitude of the $M.A$ sufficiently exceeds that of the osmotic pressure, thus resulting to the net apparent decrease in load. As such the expansion phase appears to commence while the vaporisation is still ongoing.

Thus, with considerations of the aforementioned effects of $M.A$ and P_{osm}, the evaporating pressure can be given as:

$$P_2 = \ P_1\left(1 - a\ \ M.A\ \ \frac{P_1}{P_{osm}}\right) \tag{6.34}$$

Meanwhile, the pressure of the vapour can be approximated from the general polytropic process equation (albeit with different polytropic index, *n*, for the different phases of vaporisation, transition and expansion).

$$P_2 = P_1\left(\frac{V_1}{V_2}\right)^n \tag{6.35}$$

Hence, the combined evaporation-expansion pressure equation can be given as:

$$P_{p2} = P_{p1}\left(\frac{V_{p1}}{V_{p2}}\right)^{n}\left(1 - a\ M.A\ \frac{P_{p1}}{P_{osm}}\right)^{y} \tag{6.36}$$

wherein,

$$n = 0\ ;\ \ y = 1 \qquad \{for\ Vaporisation\ phase\ (\ V_p \leq V_{vap'})\} \tag{6.37}$$

$$n = \acute{n}(x)^2 = \acute{n}\left(\frac{V_p}{V_{g,sat}}\right)^2 \qquad \{for\ Transition\ phase\ (V_{vap'} > V_p < V_{g,sat})\} \tag{6.38}$$

$$n \approx 1\ ;\ \ y = 0 \qquad \{for\ Expansion\ phase\ (V_p \geq V_{g,sat})\} \tag{6.39}$$

where, V_p is the instantaneous volume of the vapour in the cylinder at any point in time, P_{p1}, V_{p1} and P_{p2}, V_{p2} are respectively the pressure and volume at any two successive points along the process path; x $(= V_p/V_{g,sat})$ is a representative dryness fraction of the vapour (a measure of the extent of vaporisation), coefficients a and $\acute{n}$ are constants; exponents *n* and *y* are respectively 0 and 1 during the early stage of the vaporisation phase; the value of the index n is zero during the early vaporisation phase, however, during the transition phase it increases rapidly as a power function of the vapour dryness fraction; and is approximately unity for the rest of the actual expansion phase when the volume is more than the dry saturated vapour volume (i.e. when all the liquid must have vaporized).

Based on the experimental results, coefficients a and $\acute{n}$ values of 0.0045 and 0.7 respectively, were found to yield the best correlation between the model and the achieved pressure profile (Figure 6.8).

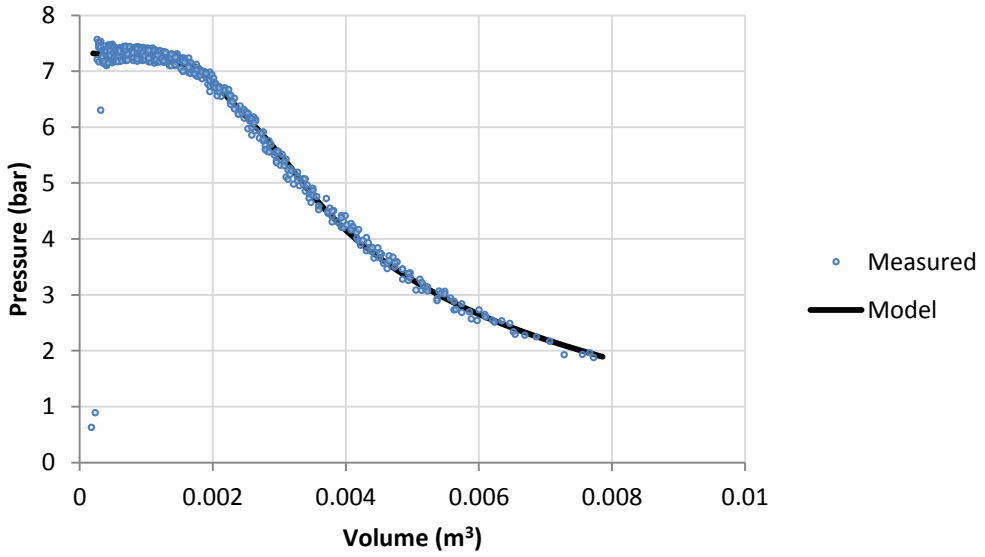

Figure 6.8: Measured and model power pressure variation with power stroke volume

6.3 Linkage system model

The displacements of the pistons and the transfer of pressure force from the power piston to the water piston is characterised by the geometry of the linkage system. Details of this are as given in Figure 6.9 and Table 6.1.

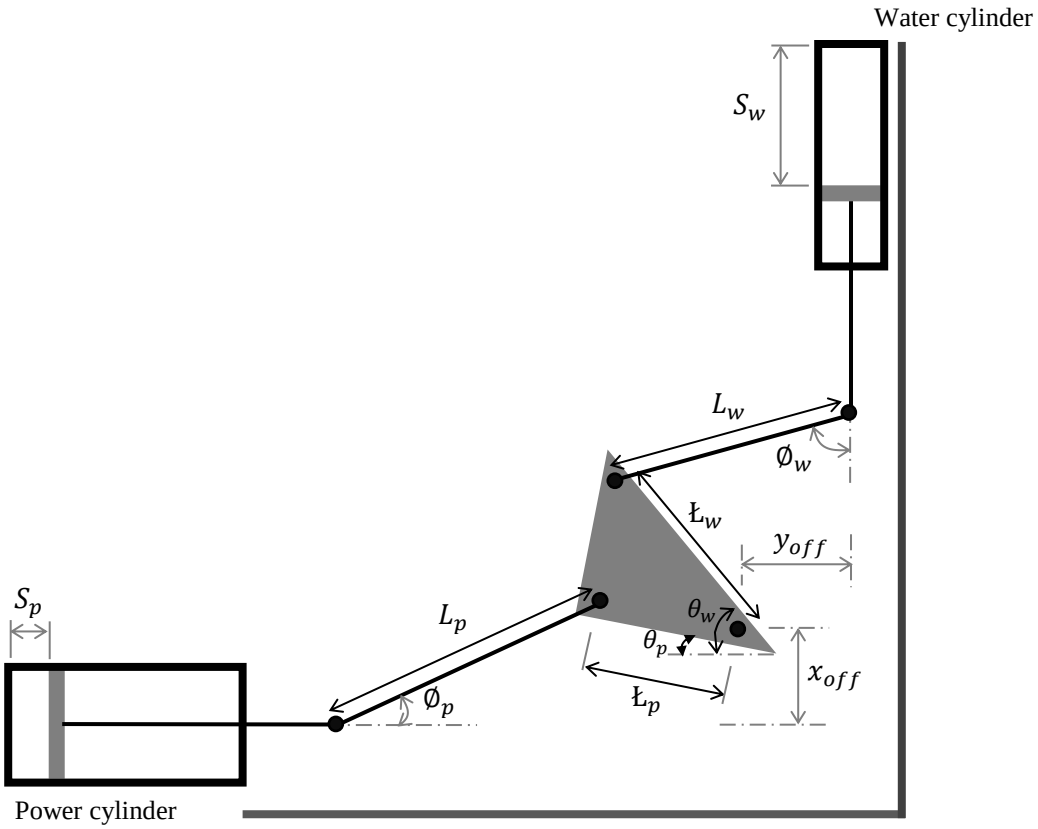

Figure 6.9: Schematic of the DesaLink linkage geometry

Table 6.1: DesaLink geometric details

Power cylinder		Water cylinder	
L_p(m)	0.76	L_w(m)	0.5
Ł$_p$(m)	0.25	Ł$_w$(m)	0.35
x_{off}(m)	0.28	y_{off}(m)	0.2
θ_p(°)	3 – 55	θ_w(°)	48 – 100
$\emptyset_p$(°)	22 – 40	$\emptyset_w$ (°)	64 – 16

Based on the trigonometric relations of the pistons and the linkage mechanism, the power piston displacement (S_p) and that of water piston (S_w) can be determined with respect to the angular positions of the crank (θ_p) within the operating min – max range.

$$\theta_w = \theta_p + 45^{\circ} \tag{6.40}$$

$$\emptyset_p = \sin^{-1}\left(\left(Ł_p \sin\theta_p + x_{off}\right)/L_p\right) \tag{6.41}$$

$$\emptyset_w = \sin^{-1}\left(\left(Ł_w \cos\theta_w + y_{off}\right)/L_w\right) \tag{6.42}$$

$$S_p = \left(Ł_p \cos\theta_{p,min} + L_p \cos\emptyset_{p,min}\right) - \left(Ł_p \cos\theta_p + L_p \cos\emptyset_p\right) \tag{6.43}$$

$$S_w = \left(Ł_w \sin\theta_{w,max} + L_w \cos\emptyset_{w,max}\right) - \left(Ł_w \sin\theta_w + L_w \cos\emptyset_w\right) \tag{6.44}$$

On the other hand, the mechanical advantage of the linkage mechanism can be determined from the forces acting on the pistons and linkages. Given that the forces at the power and water pistons are F_p and F_w respectively, the mechanical advatnage can be given as $M.A = {F_w}/{F_p}$

But, the total driving torque (moment of the force about the crank pivot), $\mathcal{T}$, from the power linkage is

$$\mathcal{T}_p = F_p\, Ł_p\, sin\theta_p + (F_p\, tan\alpha_p\ Ł_p\, cos\theta_p) \tag{6.45}$$

Similarly, at the water linkage, the torque is

$$\mathcal{T}_w = F_w\, Ł_w\, cos\theta_w + (F_w\, tan\alpha_w\ Ł_w\, sin\theta_w) \tag{6.46}$$

However at equilibrium, $\mathcal{T}_p = \mathcal{T}_w$

Thus,

$$\frac{F_w}{F_p} = \frac{(Ł_p\, sin\theta_p + Ł_p\, cos\theta_p tan\emptyset_p)}{(Ł_w\, cos\theta_w + Ł_w\, sin\theta_w tan\emptyset_w)} \tag{6.47}$$

Hence, the mechanical advantage is

$$M.A = \frac{(Ł_p\, sin\theta_p + Ł_p\, cos\theta_p tan\emptyset_p)}{(Ł_w\, cos\theta_w + Ł_w\, sin\theta_w tan\emptyset_w)}$$

6.4 RO subsystem model

The major components of the RO subsystem are the pressurised water cylinder and the RO module. Thus the main parameters of emphasis of the RO sub model are the water pressure, the volumetric flow rate and concentration of the permeate.

6.4.1 Water pressure

The pressure transmitted to the water cylinder piston can be determined from the force available at the power piston and the effect of the mechanical advantage based on the linkage geometry.

The pressure force available from the power piston is

$$F_p = (P_p - P_{cnds})\ A_p \tag{6.48}$$

While the force delivered to the water piston is

$$F_w = F_p\ M.A \tag{6.49}$$

Though the ideal water pressure $P_{w.ideal}$ can be simply obtained as $P_{w.ideal} = F_w/A_w$; the actual water pressure P_w can be expressed as:

$$P_w = \mathfrak{c}\ F_w/A_w \tag{6.50}$$

wherein,

$$\mathfrak{c} = 1 - \mathfrak{k}\ M.A\frac{P_{w.ideal}}{P_{osm}} \tag{6.51}$$

$$P_{osm} = P_{osm,ini}\left(\frac{V_{w,ini} + V_{RO}}{V_w + V_{RO}}\right) \tag{6.52}$$

The initial osmotic pressure of the feed water solution can be obtained as [197]

$$P_{osm,ini} = i\emptyset MR_{gas}T = i\ \emptyset\ \frac{C_{f,ini}}{Mm\ 1000}\ R_{gas}\ T_f \tag{6.53}$$

where, $\mathfrak{c}$ is a correction factor introduced to take into consideration the effects of losses in the linkage mechanism and the changing mechanical advantage and osmotic pressure of the saline water; in which $\mathfrak{k}$ is a constant; $P_{osm,ini}$, is the ideal initial osmotic pressure (due to the

concentration of the initial feed water $C_{f,ini}$); P_{osm}, represents the increasing osmotic pressure with respect to the relative volume displacement of the water loop; $V_{w,ini}$ is the initial volume of the feed water (at maximum water piston displacement); $V_{w,}$ is the water volume at any displacement; V_{RO} is the volume of the spaces in the RO module and pipe work (taken as 0.0011 m^3 for the present configuration); i is the number of ions produced during dissociation of the solute; $\emptyset$ is a coefficient to account for the random pairing of some of the dissociated ions in the solution; $C_{f,ini}$ is the initial concentration/salinity (mg/L) of the feed water; Mm is the molar mass of the solute (g/mol); R_{gas} is the gas constant, equal to 0.08314 L·bar/mol·K; T_f is the feed water temperature (K).

The value of constant ƙ can be adjusted to achieve good fit between the model predicted and measured pressures. In accessing the water pressure profile relative to the piston displacement, ƙ = 0.038 was found to yield the optimum fit (Figure 6.10), wherein, the calculated water pressure described the measured values with very good accuracy.

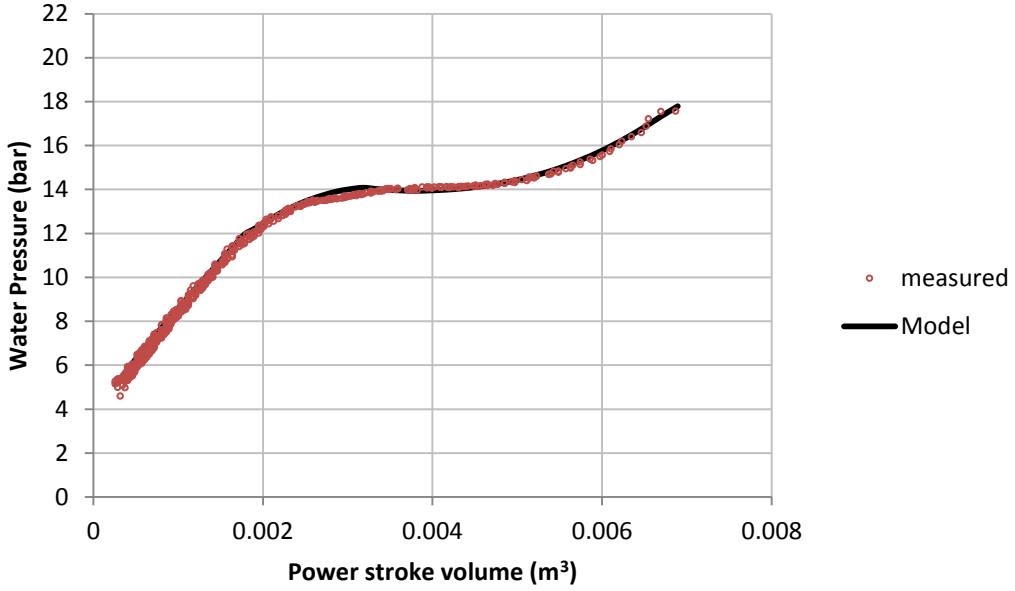

Figure 6.10: Model predicted and measured water pressures

6.4.2 Permeate flow rate

The rate of fresh water production, i.e., permeate flow rate is dependent on the net driving pressure across the RO membrane, which is basically the difference between the water pressure and the osmotic pressure across the membrane. Thus, the permeate flow rate can be given in terms of the net driving pressure and the membrane characteristics as:

$$\dot{V}_{\mathcal{p}} = Imp \ \ A_{\text{mem}} \ (P_w - \sigma R P_{osm}) \ \ \mathfrak{c}_{\dot{V}\mathcal{p}} \tag{6.54}$$

However, the water permeability through the RO membrane can be affected by some factors of the operating conditions such as the operating temperature and pressure of the water, and fouling of the membrane [183]. These effects can be reflected by the correction term $\mathfrak{c}_{\dot{V}\mathcal{p}}$

$$\mathfrak{c}_{\dot{V}\mathcal{p}} = TCF \ \ FF \ \left(\frac{P_{osm}}{P_w}\right) \tag{6.55}$$

where, A_{mem}, Imp and Rr are respectively the active membrane area, intrinsic membrane water permeability and salt rejection fraction of the RO module; for the RO module used in this study (Dow® FilmTec® BW30-2540), the membrane area, permeability and salt rejection are taken as 2.6 m^2, 9.14x10^{-12} $m \cdot s^{-1} \cdot Pa^{-1}$ and 0.995 respectively [182]; σ is reflection coefficient (it's is a measure of the membranes ability to perfectly reject solute/salt passage) which generally approaches unity for high solute rejection membranes [198]; TCF is temperature correction factor, which varies exponentially with the water temperature, and is 0.84 for 20°C water [183]; FF is flow/fouling factor, which is ideally unity when there is no fouling, and is taken as 0.92 here.

Figure 6.11 shows a comparison between measured and predicted flow rates; it can be seen that the model estimated the measured values with good agreement (within a relative error of about ±25%).

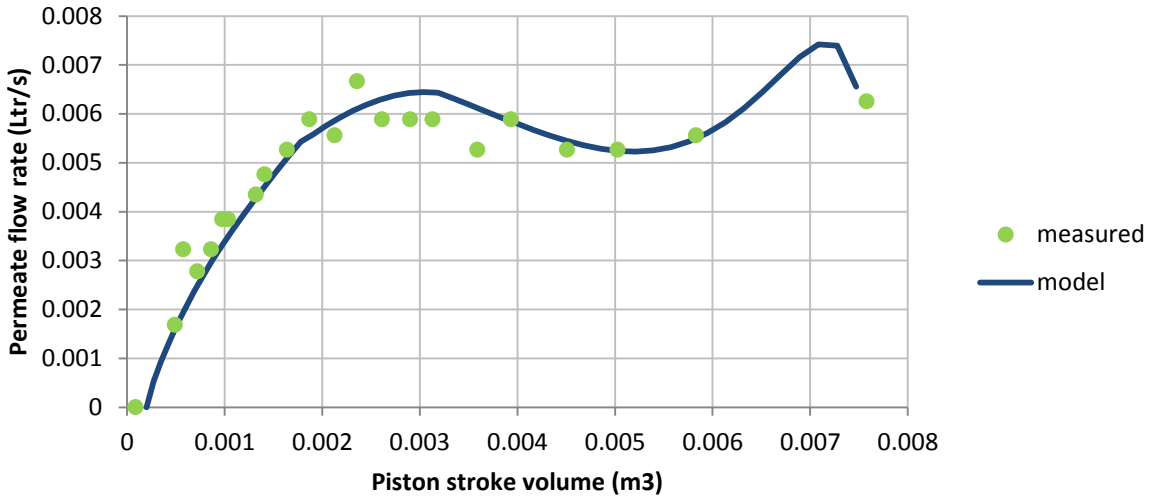

Figure 6.11: Measured and model permeate flow rates

6.4.3 Time of operation

The time of operation is dependent on the net driving pressure and concentration of the feed solution. However, these parameters translates to the permeate flow rate, thus, the operation time can be obtained from the permeate flow rate in relation to the water volume. Since the flow rate is not constant over the duration of the operation, the total time of operation can be obtained as the integral of the flow rate, or simply the summation of the elemental time between two successive points along the operation.

$$Time = \int \frac{1}{\dot{V}_p} dV_w \tag{6.56}$$

Or

$$Time = \sum \frac{\left(V_{w,2} - V_{w,1}\right)}{0.5\ (\dot{V}_{p,1} + \dot{V}_{p,2})} \tag{6.57}$$

where, $V_{w,1}$ and $V_{w,2}$ are the volume of the water cylinder at two successive step points; while, $\dot{V}_{p,1}$ and $\dot{V}_{p,2}$ are the corresponding flow rates determined. Although, ideally, the water cylinder volume ought to equal the permeate volume, in reality, the actual permeate volume is slightly less (it is largely a function of the speed of operation, amongst other factors), thus this phenomena is represented by the constant, $\mathfrak{c}_v$, the value of which approaches 1 for slow speed (found to be about 0.9 for the present study).

6.4.4 Permeate concentration

The permeate flow concentration can generally be obtained as the rate of salt passage through the membrane relative to the permeate water flow rate. However, in this batch configuration, the bulk salinity of the permeate can be taken as the ratio of the total mass of salt transported, to the volume of water produced.

$$C_p = \frac{\int \mathcal{B}\ \ CPF\ \ C_f\ \ A_{mem}}{V_{w,ini}} \tag{6.58}$$

$$C_f = C_{f,ini}\left(V_{w,ini} + V_{RO}\right)/(V_w + V_{RO}) \tag{6.59}$$

where, $\mathcal{B}$ and CPF are respectively the membrane salt permeability coefficient and concentration polarisation factor, taken as 1.18 x 10^{-7} m/s and 1.2 respectively for the DesaLink system [182]; while C_f is the feed concentration.

6.5. Integrated DesaLink Model

Having developed the individual models describing the different subsystems of the ORC-DesaLink system, an integrated model is built by interconnecting the sub models of the different sub-systems, as depicted in Figure 6.12.

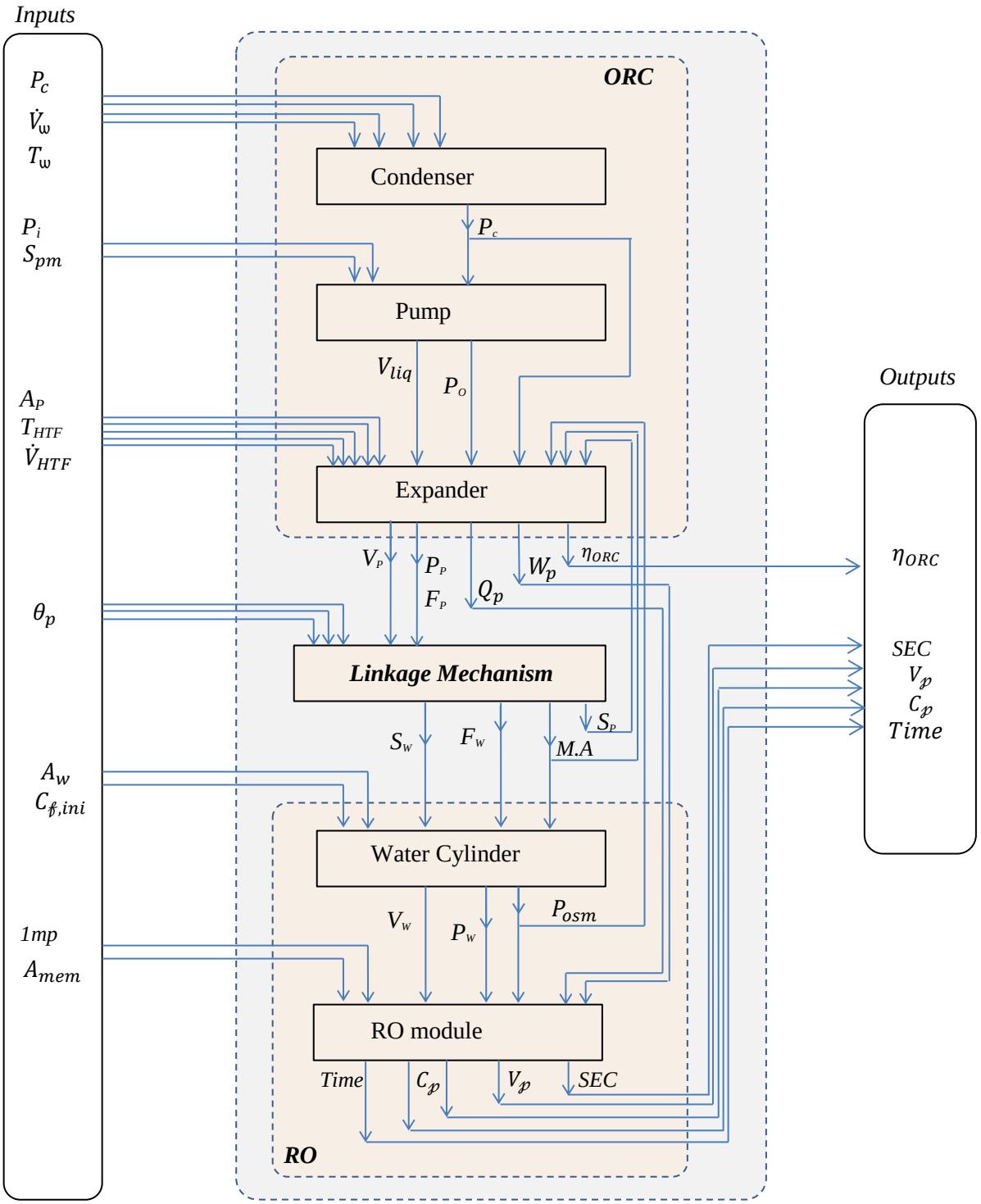

Figure 6.12: The integrated model

In the figure, each sub component represents a set of the underlying sub models. The different sub models can simultaneously receive some independent input variables / operating parameters; however relevant input/output variables of dependent sub components are appropriately linked together. On operation, the interconnection is such that from a given set of operating parameters, the condenser pressure is set and impressed into the pump and the power cylinder. Input variable information such as pneumatic driving pressure and metering stroke, is used by pump to deliver a corresponding volume of the working fluid to the power cylinder, and imposes the evaporation pressure therein. However, the power cylinder calculates the instantaneous power pressure, which is fed (together with piston displacement information) to the linkage mechanism sub-model (which uses additional operating geometric information) to determine the mechanical advantage, with which the water pressure is calculated. The water pressure is subsequently used (together with the membrane characteristics) by the RO sub model to calculate the permeate flow rate, concentration and the cycle time. And finally, the SEC, together with the ORC efficiency are determined and presented as the system outputs.

6.6 Chapter Summary

The proposed ORC driven batch-RO desalination system have been studied and characterised by developing models to represent the behaviour, to aid prediction of the performance of the system.

The model of the integrated system was obtained by developing and interconnecting sub-models of the individual components, using engineering equation solver software (the model EES code is appended in Appendix 5). The realisation of the developed individual subsystem models were based on underlying physical principles and use of non-dimensional factors (in linear or non-linear form) to adjust for deviation from ideal conditions. Key underlying system parameters that influence the outcome of subsequent dependent parameters were first modelled and validated with a set of experimental results from a range of working conditions; in most cases, the models were able to accurately correlate the experimental results with less than 10% error.

Chapter 7 Case Study

This chapter illustrates how the models developed previously can be used to predict the performance of the isothermal ORC-DesaLink desalination system. For this purpose, two case studies, based on two different geographic locations with two different thermal sources (solar thermal and waste heat recovery) have been performed to illustrate the feasibility and performance of the ORC-RO system. The studies showed that multiple units of DesaLink can be employed to produce substantial quantity of fresh water from minimal thermal energy consumption.

7.1 Introduction

The previous chapters have presented the performance (from laboratory experiments) of the isothermal ORC engine in driving DesaLink batch desalination system; model(s) describing the operation of the integrated system have also been presented. Following this, case studies can be carried out in this chapter, to gain insights on the potential on-site performance of the integrated system. The thermal energy source in the laboratory experiments was provided by electrical heaters, however, as introduced in chapter 1, solar thermal and waste heat are two attractive thermal energy sources that will be considered in this study. The solar thermal is especially attractive for remote or arid and semi-arid regions of the world where conventional power supply is unavailable or unreliable or with prohibitive cost; while, the waste heat is especially attractive where it is abundantly available. For this purpose, the case study site locations can be considered in India and USA, respectively for solar thermal and waste heat sources, owing to their available energy resources and considerable ground water salinity.

For both cases of the thermal energy source, the relevant governing equations will be appended to the already developed DesaLink model; such that the potential desalination capacity (volume of fresh produced per day) can be calculated based on the thermal energy input or the availability of the resource, alternatively, where a target water production capacity is specified, the size of the thermal source system can be obtained based on the intended water production capacity. Hence for the thermal system of the solar case, emphasis will be placed on using the meteorological data of the location to determine the thermal energy that can be captured by a given solar collector; whereas, for the waste heat case, the emphasis will be on selecting an appropriating industrial scale waste heat source and determining the available energy that can be recovered via heat exchanger.

7.2 Case study 1 – Solar

In India, salinity in ground water is prevalent mainly in the arid and semi-arid regions of the states of Rajasthan, Haryana, Punjab, Gujarat, Uttar Pradesh, Delhi, Andhra Pradesh, Maharashtra, Karnataka and Tamil Nadu [199]; with Rajasthan and Gujarat having the more affected land mass and population [200]. Of these states, Gujarat has been noted to be very active in setting up desalination plants [201]. Ground water salinity of more than 1500 ppm can be found in parts of several districts and villages of the state. Kadachhala (in Savil Taluka of Vadodara district) is one such village with salinity of about 4000 ppm [202]. Located towards the north east of the state, the area receives abundant solar radiation annually, thus making it well suited for a case study to predict the real life performance of our DesaLink system when driven by solar thermal energy. For this case, a nominal daily water production capacity of 1000 litres is targeted.

The performance of solar thermal plants is generally dependent on the weather conditions (ambient temperature and solar irradiance) of the location; as such the meteorological data on the case study site is required in order to predict realistic results. The case study site – Kadachhala village – is located on Longitude 73.58^{o}E and Latitude 22.17^{o}N on the globe, at an altitude of 168 m. The variation of the monthly average ambient temperatures of the study area in a typical year is depicted in Figure 7.1, as can be seen from the figure, the average temperature increases from January, with the highest temperature (36^{o}C) experienced in May. The valley in average temperature profile corresponds to the high precipitation (rainfall) experienced during the monsoon rainy season (June, July and August). The temperature peaks again, and then drops during the winter months. The solar irradiance on horizontal surface follows a similar profile, the maximum values of the mean irradiance are 620 and 860 W/m^{2} for the typical winter and summer day; however, the insolation drops during the monsoon rainy season, as the sun is often occluded. Such high solar irradiances, especially in the summer, give rise to a big advantage of utilizing solar thermal technologies in this area.

The high solar irradiance and ambient temperatures are desirable for better performance of the thermal collector (and thus, enhanced freshwater production). Although the seasonal drops in the weather conditions would result to seasonal drops in freshwater outputs, however, this effect is likely to be compensated for by the fact that freshwater requirements by the inhabitants during this seasons is likely to be less, compared to the hot summer months.

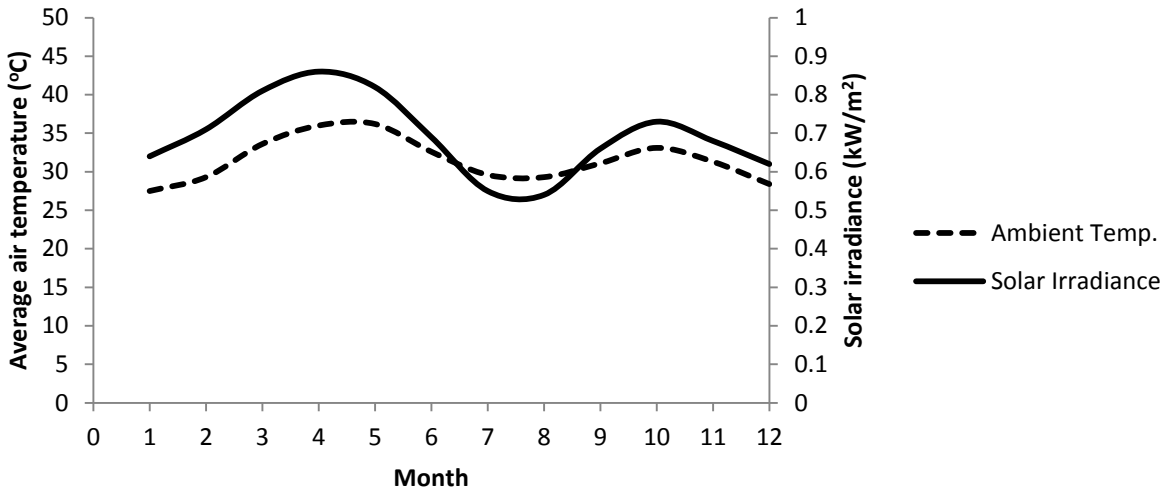

Figure 7.1: Monthly average ambient temperature variation for Savli taluka. *Generated from NASA Atmospheric Science Data Centre* [203]

7.2.1 Solar thermal field

There are different types of solar thermal collectors that could be coupled to ORC system; reviews are available in literature [204, 205]. Low – medium temperature collector types include Flat plate collector (FPC), evacuated tube collector (ETC), parabolic trough collector (PTC), Linear Fresnel reflector (LFR), etc. In this study, the criteria for choosing the collector type for consideration includes, ease of commercial availability and operating temperature range. Thus, the collectors for consideration should be capable to exceed the 75^{o}C evaporating temperature of the R245fa working fluid at the 7 bar driving pressure for DesaLink, as mentioned earlier in Chapter 5. As such, FPC (up to 90^{o}C) and ETC (up to 150^{o}C) are considered (details of the collectors are available in the datasheet as provided in Appendix 6).

The solar thermal energy captured, Q_{sol}, by the collector can be given in terms of the solar irradiance (I_{solar}) and collector area (A_{sol}). Thus the solar collector area required for the DesaLink system can be obtained by balancing the captured solar thermal energy and thermal power required for the desalination.

$$Q_{sol} = A_{sol}\, I_{solar}\, \eta_{solar} \tag{7.1}$$

Where, η_{solar} is the solar collector efficiency, and can be determined from the collector's performance characteristic curve, expressed as [61]

$$\eta_{solar} = \eta_0 - a_1\left(\frac{T_{htf} - T_{amb}}{I_{solar}}\right) - a_2\left(\frac{T_{htf} - T_{amb}}{I_{solar}}\right)^2 I_{solar} \tag{7.2}$$

where η_0, a_1 and a_2 are the efficiency parameters (Table 7.1), decided by the collector efficiency curves of the solar collector, T_{htf} (ºC) and T_{amb} (ºC) are temperatures of the heat transfer fluid at the outlet of the solar collector and the ambient temperature respectively.

Table 7.1: Technical parameters of the solar collectors [61]

Parameters	Flate plate collector (Sonnenkraft SK500)	Evacuated tube collector (Sydney SK-6)
η_0	0.768	0.665
$a_1\ (W/m^2K)$	2.9	0.59
$a_2\ (W/m^2K^2)$	0.0108	0.0019
Aperture area (m^2)	2.307	1.088

7.2.2 Results and discussion

To analyse the DesaLink performance in this case study application, the aforementioned solar field governing equations and parameters were appended to the DesaLink model presented in the previous chapter. The appended model is such that: for the given feed water condition at the study site, the thermal energy required (with efficiency of the cylinder base heat exchange system taken into consideration) is calculated (so also the desalted water volume and operating cycle time); while the solar thermal energy captured by the solar collector (with consideration of the solar efficiency) is calculated based on the meteorological data of same study site.

For the simulation, the meteorological data (solar irradiance, temperature, and hours of sunshine) of the study site's geographical location is generated from Meteonorm 7.1 software and uploaded into a parametric table, as input parameters in the DesaLink model in Engineering Equation Solver, to calculate the solar energy captured by the collector. To obtain optimal annual solar irradiation the collectors were assumed to be arranged in a true south orientation (0^oAzimuth, and 25^o tilt angle). The simulation is carried out for daily monthly average, for the whole year. The main result is the average daily desalted water volume per unit solar collector area.

Figure 7.2, shows the daily average quantity of fresh water produced per square meter of solar collector area (for both collectors) in a typical day of the months of the year. As would be expected The ETC yields more freshwater per square meter of collector area, mainly due to its superior efficiency. For the required heat transfer fluid temperature of 95^oC, the ETC collector showed an average efficiency of around 57%, while that for FPC was around 35%.

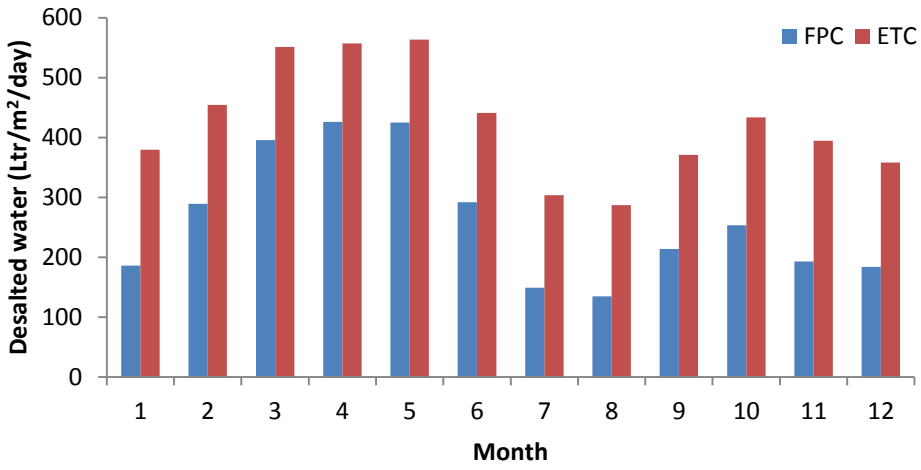

Figure 7.2: Simulated average daily water production for the months of a year

On the average, the ORC-RO DesaLink unit can desalinate about 100 litres per 8 h day; thus, from Figure 7.2, it can be seen that a square meter of solar field can power multiple units of DesaLink to produce over 400 litres daily, during the peak summer month. The criterion for eventually determining the size of solar field area can be based on the available solar field area space restriction or the desired water production capacity. For the desired production of 1000 litres of freshwater daily, the solar field area was determined, based on the least favourable weather season's solar radiation (i.e., 480 W/m^2) so as to ensure adequate production throughout the year. The result indicates a solar field area of about 7.5m^2 for the FPC collectors, thus requiring 3 units of the FPC collectors (since the aperture area is 2.3 m^2). While in the case of the ETC collectors, the solar field area is about 3.5 m^2, thus similarly requiring 3 units of the collector (since the ETC aperture area is 1.1m^2). Figure 7.3 shows the potential desalination capacity for the ETC collector field, while an overview of the results for both collectors is presented in Table 7.2.

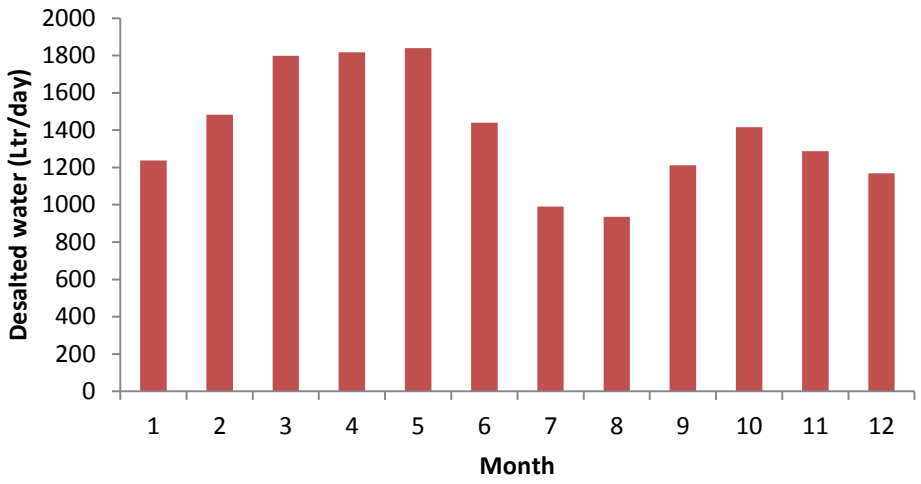

Figure 7.3: Potential water production from multiple units of DesaLink systems driven by a solar field of 3 units of ETC

Table 7.2: Results overview for solar ORC DesaLink system

	FPC	ETC
Solar field Area (m^2)	7.5	3.5
Number of collectors	3	3
Average collector efficiency (%)	35	57
Nominal desalted water production (litre/day)	1000	1000
Nominal Number of DesaLink units	10	10
Maximum water production (litre/day)	2900	1800
Maximum number of DesaLink units	29	18

7.3 Case study 2 – Waste heat recovery (WHR)

In the United States, brackish groundwater resource is vastly available in the southern states like Texas, New Mexico, Oklahoma, California [206]. However, New Mexico is one of the states where the phenomenon is most acute, as approximately 75 percent of its ground water is too saline for most use, without treatment [207]. Although, the salinity of the groundwater varies across the state, salinity of about 4000 ppm has been reported in Alamogordo town, in Otero County, in the south central of the state [208].

Although, the city's historical water supply mainly comes from surface water, in recent years, the available water from the surface sources has diminished severely, due to prevailing drought conditions. Consequently, adequate surface water is not available to meet the city's increasing demands, and there is no adequate water supply to provide the inhabitants with an acceptable level of typical water use needs. This causes the city to explore the desalination of the brackish groundwater, to meet its water needs [209]. Information available at the town's chamber of commerce portal [210] indicated that though there are reasonable business activities, especially goods and services, there are only a handful of manufacturing and process industries. One notable of such industries is a bakery – Western Baking Corporation. In the bakery industry, baking is as energy intensive process, and generally loses significant amounts of heat to the environment. Thus it would be quite interesting to explore opportunities within the bakery to capture portions of the heat that would otherwise be wasted, to power desalination system in producing fresh water from the brackish ground water resource in the locality of the bakery.

7.3.1 Site description

Western Baking Corporation [211] is a large (225,000 Square Feet) commercial bakery facility, located on a 28-acre land parcel in Alamogordo, New Mexico; and specialized in the production of a wide range of cookies and crackers. The facility has several high-end bakery equipment including five Baker Perkins' 300 ft (100 m) 7-zone direct gas fired ovens. Direct gas fired ovens are widely used in baking industries. The baking chamber is heated directly with gas burners, with baking temperatures often exceeding 200^{o}C; flue gas from the combustion (together with water vapour, traces of fat and particulates from the baking) gets ducted from the different zones and exhausted through chimney/stack, with typical flue gas temperature exceeding 120^{o}C [212]. In the production of cookies and crackers, the baking process represents about 78% of the total energy requirement [213], while studies have also shown that, for a typical direct fired gas oven baking, about 20% of the gas energy is wasted in the exhaust [214, 215]; thus signifying a substantial potential for exhaust waste heat recovery.

The bakery facility, on operation, bakes about 3000 to 4000 pounds (1360 to 1814 kg) of product per hour, with a total heat consumption rate of about 2625 – 6125 x10^{3}Btu/hr (769 – 1795 kW) (depending on the product baked); thus signifying a bakery specific gas energy consumption of 1.53 – 4.75 MJ per kg of baked product. The ovens are generally operated for about 20 to 24 hours daily.

To harness energy from the flue gas, appropriate waste heat recovery systems such as gas-to-liquid heat pipe heat exchanger (HPHE) could be installed on the oven exhaust stacks to capture the flue gas energy (as depicted in Figure 7.4). Here, changeover dampers are employed to divert the flue gas through the heat exchanger, where the flue heat is transferred to the thermal fluid (ethylene glycol) which is circulated through the evaporator (finned cylinder base) of the ORC DesaLink system, to provide the needed heat in driving the system to desalinate batches of brackish water. In waste heat recovery heat exchanger (WHRX) applications, the heat pipe heat exchangers are really of particular choice when the flue gas contains substances and particles that could lead to fouling and clogging which could consequently hamper heat exchanger effectiveness. The construction of the heat exchanger allows the heat pipe surfaces to be easily accessible and cleaned quickly with very little system down-time; design options with self-cleaning mechanisms are also available. Other advantages include durability, compactness and low pressure drops [216, 217].

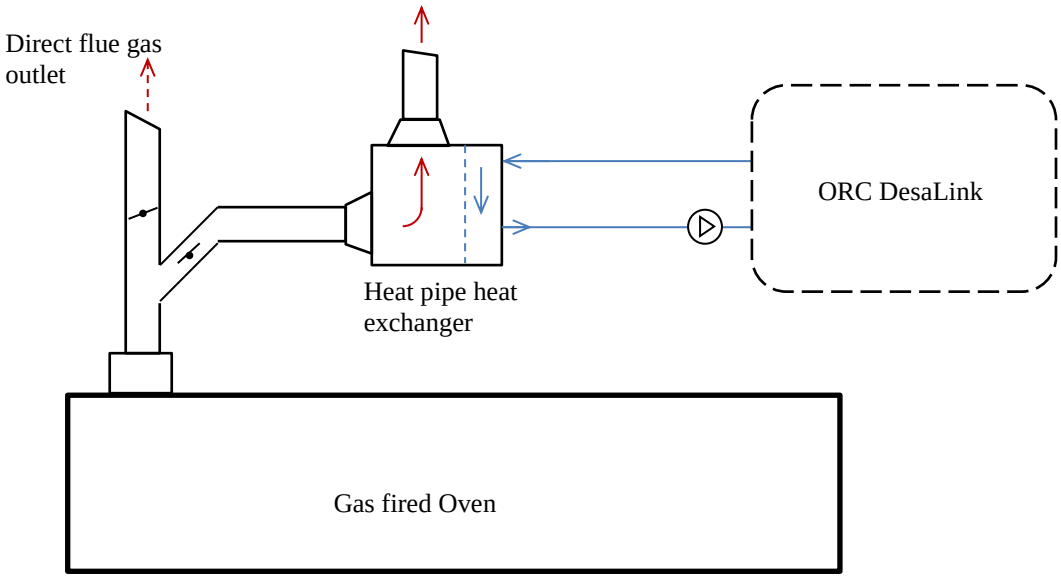

Figure 7.4: Schematic of the bakery waste heat recovery ORC DesaLink

7.3.2 Theory

Although a sizeable portion (about 20%) of the gas energy is contained in the flue gas, in reality not all of this quantity is available for recovery at a given operating condition. The actual quantity of energy recovered by the recovery system strongly depends on the operating conditions, typically, the temperature difference between the flue gas and the thermal fluid.

The actual heat transferred from the flue gas to the thermal fluid can be given by the energy balance

$$Q_{fg} = \rho_{fg}\dot{V}_{fg}c_{p_{fg}}(T_{fg,i} - T_{fg,o}) = \rho_{htf}\dot{V}_{htf}c_{p_{htf}}(T_{htf,o} - T_{htf,i}) \quad (7.3)$$

Where, $\rho_{fg}, \dot{V}_{fg}, c_{p_{fg}}$ and $\rho_{htf}, \dot{V}_{htf}, c_{p_{htf}}$ are the density, volumetric flow rate, heat capacity of the flue gas and the thermal fluid respectively; $T_{fg,i}$, $T_{fg,o}$ and $T_{htf,i}$, $T_{htf,o}$ are the inlet and out temperatures of the flue gas and the thermal fluid respectively entering and leaving the heat exchanger.

As mentioned previously, the thermal fluid is supplied to the power cylinder base evaporator of the ORC DesaLink system at 95^{o}C (inclusive of about 2^{o}C transmission losses); from the experiments (in chapters 5 and 6), at steady state condition, it was observed that the temperature drop across the cylinder base evaporator was only about 0.13^{o}C. Now, taking the power cylinder return line as the inlet to the WHRX, 94.8^{o}C can be assumed as the thermal fluid inlet temperature at the WHRX. On

the other hand, the flue gas inlet temperature at the WHRX is taken as that from the oven's exhaust, while the outlet temperature is assumed to be 10^{o}C above incoming thermal fluid temperature.

The volumetric flow rate of the flue gas is taken as the sum of the natural gas fuel flow rate at the burners (of the oven) and the flow rate of the air required for complete combustion and that of the gases released from the dough during baking. The amount (volume) of air relative to that of the gas fuel used in the combustion can be estimated from the air-fuel ratio, AFR, (The AFR, by volume, for complete combustion of natural gas is 9.4:1 [218]).

Hence, the flue gas volumetric flow rate can be given as:

$$\dot{V}_{fg} = \frac{\dot{Q}_{fuel}}{HV} + \frac{\dot{Q}_{fuel}}{HV} AFR + ₲ \; PR \tag{7.4}$$

Alternatively, the flow rate can also be given in terms of the specific gas energy consumption of baking as

$$\dot{V}_{fg} = \; PR \left[\frac{SEC_{bake}}{HV} + \frac{SEC_{bake}}{HV} AFR + ₲ \right] \tag{7.5}$$

Where, $\dot{Q}_{fuel}$ is the heat level of the ovens' gas burner (kJ/hr); HV is the higher heating value of the natural gas fuel, taken as 40 MJ/m^3; PR is the baking production rate i.e. the total mass of doughs baked per hour (kg/hr); and ₲ is the volume of gases released (from the dough) per unit mass of dough baked, studies have shown this to be about 0.115 m^3/kg for bread baking [215], here same is assumed for cookies and cracker; SEC_{bake} is the average gas energy consumption per unit mass of dough baked, 2.9 MJ/kg$_{dough}$.

The thermo-physical properties (density and specific heat) of the flue gas are estimated based on the composition of the combined gasses from the combustion product and the baked product. Generally, natural gas fuel combustion product consists mainly of nitrogen (75%), carbon dioxide (13%), water vapour (11%) and others (1%); while the baked product gas consists mainly of water vapour (89%), carbon dioxide (5.4%) and others (5.6%) [215]. The combined composition of the flue gas (for the present parameters already defined above) can be shown to be: nitrogen – 65.6%, carbon dioxide – 12%, water vapour – 20.8% and others – 1.6% (details in appendix 7). With the above combined composition, the thermo-physical properties are obtained, using a web based flue gas calculator

tool, FGKH® [219]. The specific heat and the density are obtained as 1.13 kJ/kg^{o}C and 0.91 kg/m^{3} respectively.

7.3.3 Results

With flue gas properties and other relevant parameters defined, the actual quantity of heat transferred from the flue gas to the ORC-RO DesaLink system via the thermal fluid is determined; and then the quantity of desalted water that can be produced, based on the quantity of the recovered heat, is determined (like in the previous case study). As depicted in Figure 7.5, the result shows that, for a typical average baking production rate of 1500 kg/h (with average natural gas energy consumption of 2.9 MJ/kg$_{dough}$ and flue gas temperature of 120^{o}C), about 2.5% of the exhaust heat (21 MJ) is recovered and utilised by multiple units of the ORC DesaLink system to desalinate about 793 litres of water per hour, thus yielding a daily fresh water production of about 15,866 litres/day. It is interesting that such large quantity of fresh water can be produced from a very small fraction of the exhaust heat.

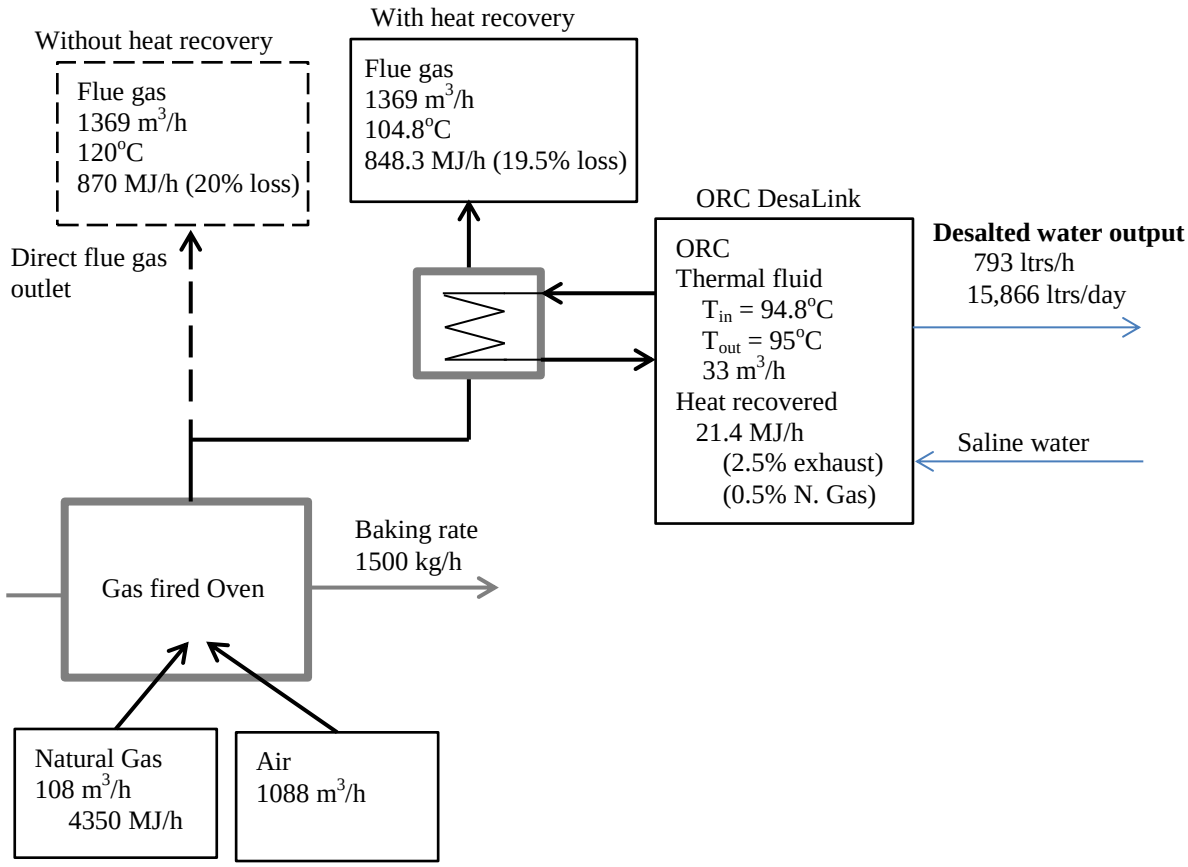

Figure 7.5: Schematic of the systems set up, operating parameters and the results

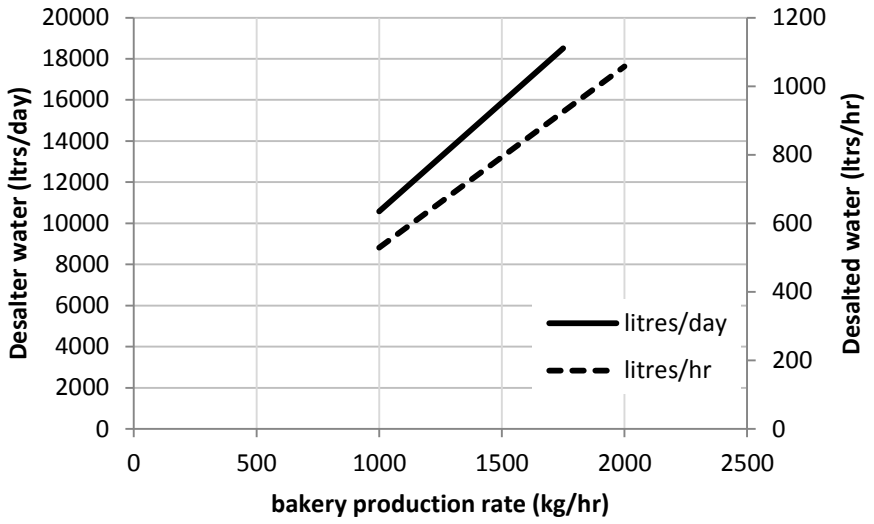

Figure 7.6: Potential fresh water production rate variation with bakery production rate

Figure 7.6 shows the potential desalination hourly and daily fresh water production rates varying linearly with the bakery production rate; indicating that, up to 18,000 litres/day could be desalted with a bakery rate of 1750 kg/hr, for the bakery average specific gas energy consumption of 2.9 MJ/kg_{dough}. However, depending on the type of product baked, given that, the specific gas energy consumed per unit mass of dough baked at the bakery facility varies from 1.53 to 4.75 MJ/kg_{dough}; correspondingly, the water desalted varies linearly from 466 to 1236 litres/hr, i.e., 9,315 – 24,712 litres/day (Figure 7.7).

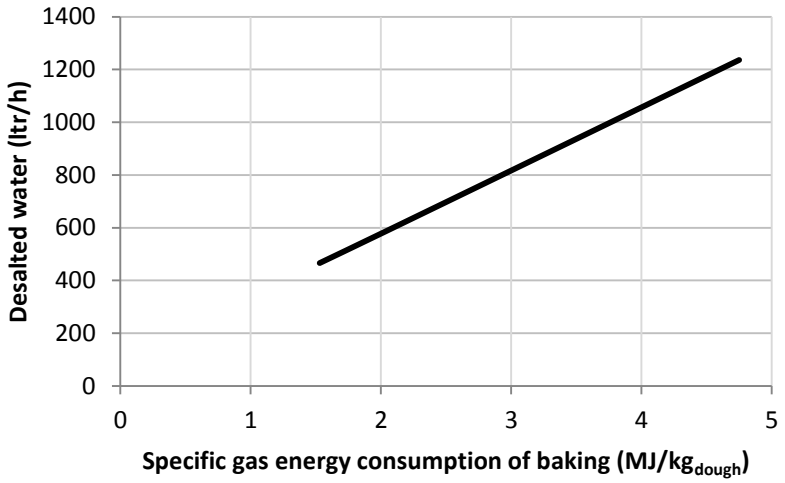

Figure 7.7: potential desalting capacity variation with bakery specific gas energy consumption (MJ per kg of baked dough)

7.4 Chapter Summary

Two case studies have been presented to demonstrate the performance of the ORC-RO DesaLink system in desalinating batches of brackish ground water in practical scenarios, where the required thermal energy to drive the system is provided by two different thermal sources (solar thermal and waste heat recovery). The first case study showed the potential of the system when driven by solar thermal collectors in Kadachhala village (in Savil Taluka of Vadodara district), Gujarat, India. Here, the solar field sizing was based on a nominal fresh water production need of 1,000 litres per day. It was found that 3 units of FPC or ETC (with 7.5 and 3.5 m^2 respectively) collectors could capture enough energy to meet this water needs, in the least favourable weather days; however, production could potentially be doubled in peak summer days. On the other hand, the second case study demonstrated the potential of the system when driven by waste heat recovered from oven exhaust of an industrial bakery facility in Alamogordo, New-Mexico, USA. It was shown that less than 5% of the exhaust heat could be recovered to drive the DesaLink system; and about 15,800 litres of fresh water could be produced daily when the bakery is operating at its average production capacity. From both studies, the ORC DesaLink system has been demonstrated to be potentially attractive in delivery substantial quantities of fresh water at minimal energy requirement.

Chapter 8 Conclusions

The summary of this research thesis and the main contributions are discussed in this final chapter, by responding to the aims and objectives outlined in chapters 1and 2. Recommendations for further work are also proffered.

8.1 Background

Salinity of natural water resources contributes to the global shortfall in available fresh water for drinking. Desalination of the saline water by means of reverse osmosis (RO) membrane is one interesting approach of alleviating/addressing this issue; and batch operating RO systems has been noted for exhibiting better recovery rate and requiring less energy compared to the more common continuously operated systems. The energy needed to drive the RO process could be sourced from renewable energy sources such as solar or waste heat recovery, so as to circumvent the challenges faced also with the conventional global energy supply (cost effective reliable supply and environmental concerns). Generally, heat cycle engines could be employed to convert the renewable thermal energy into mechanical work to drive the RO process; however, where the thermal resource is largely available as low temperature heat, obtainable efficiency will be consequently low. Thus fostering research interests in seeking ways of efficiency improvements; of which isothermal expansion is noted as a potential solution. As such this thesis broadly aimed to investigate the feasibility of applying the isothermal technique to low temperature organic Rankine cycle (ORC) heat engine to drive a batch-RO desalination system. In light of this broad aim, the specific objectives considered and the corresponding work carried out to meet the objectives are summarized in the following sections.

8.1 Responses to objectives

Objective 1: Review the state of the art in low temperature heat cycle engine driven RO desalination; and also review the current methods of achieving thermal cycle efficiency improvements by isothermal expansion, and identify potential or promising solution(s) for further consideration.

This objective originated from the background that, heat cycle engines can be employed to convert thermal energy into mechanical work to drive reverse osmosis (RO) desalination. The review buttressed that the higher the cycle efficiency in thermal to mechanical energy conversion, the

higher the desalinated water output per unit thermal input, thus high thermal efficiency is desirable for improved heat utilisation and water production.

In the heat cycle engine, isothermal expansion – continuous addition of heat to the working fluid in the expansion chamber (of the engine) during the expansion process – has been identified as an effective means of improving the specific work output and thus cycle efficiency of the engine. Various vapour power cycle heat engines with such isothermal or quasi-isothermal (less than ideal) operation include Rankine cycle with continuous heat addition during the expansion process, cryogenic heat engines, and Stirling cycle with a condensable vapour as working fluid (the vapour Stirling cycle exhibits higher specific work output compared to the traditional Stirling engines using gas).

The methods found to be commonly employed to implement quasi-isothermal expansion have generally included liquid flooded expansion and expander surface heating. Liquid flooded expansion was found to approach isothermal behaviour with increasing oil fraction; but at the detriment of increased suction pressure drop and viscous losses that tends to wane the overall performance. On the other hand, the expansion chamber surface heating technique has been shown to achieve significant improvement in performance (over 40% and 20% increase in specific work output and efficiency respectively). Nevertheless, a relatively slower operating speed is required here to enable significant heat transfer during the expansion process, since the expansion chamber (plain cylinder wall, for reciprocating engines) surface area may not be sufficient to deliver the needed heat at a high rate. However, more heat transfer could be expedited by enhancing the expansion chamber with geometries of large surface area such as fins or porous matrix. The later promises very high surface-to-volume ratio (surface area density) and could be deployed with the aid of liquid piston.

As a result of this first objective, the outcome and contributions to knowledge has been a novel review of state of the art in vapor power cycle engines with isothermal expansion. The work contained therein has been published in the journal, *Energy:*

Igobo O.N. and Davies P. A. Review of low-temperature vapour power cycle engines with quasi-isothermal expansion. Energy 70 (2014): 22-34.

Objective 2: Design and build test engine to ascertain the practicability

This objective had the broad aim of experimenting, analysing and selecting the optimum (in terms of performance and practicability) amongst two potential configurations of the heated expansion

chamber (i.e., heated plain wall and heated porous matrix) technique for effecting quasi-isothermal expansion highlighted by the previous objective.

A thermodynamic analysis of the general isothermal cycle was introduced as a basis for theoretical development of these two configurations and subsequent developments in the thesis. The analysis showed that the ideal thermal efficiency of the isothermal Rankine cycle closely approaches the Carnot efficiency limit of the operating temperatures considered.

The proposed versions of both configurations of the isothermal engine generally entailed direct injection of liquid working fluid into a heated expansion chamber, where it vaporises and performs work quasi-isothermally due to further heat addition from the chamber during expansion. The heated plain wall variant simply entailed heating the expander/cylinder surface, while the porous matrix variant was heated via thermal oil (which also acted as the liquid piston). A number of matrix options namely: packed spheres, packed rods, wire mesh and metal foam were analysed, using surface-area-density and porosity as the geometric parameters for matrix selection; and wire mesh was favoured for its reasonable balance between the two parameters, and relative availability.

In preliminary experimental analysis of the two variants for similar operating conditions (250^{o}C heat source temperature, 100 mm cylinder diameter and 100 mm stroke), although the porous matrix variant markedly had higher surface area available for heat transfer, the achieved performance (4.5% efficiency and 293 J work output from 3.5 mL injected water) was substantially poor, relative to that of the plain wall variant (14% efficiency and 378 J work output from 1.6 mL input water). The performance of the porous matrix variant was mired by practicality issues such as foaming of the oil, inadequate oil separation, and vapour condensation in the expansion chamber, which all adversely contributed to reduced specific work output. Attempting to address these practicality issues will require significant amount of optimisation efforts, as such the heated plain wall variant was preferred for its impressive performance with simple practicality.

The contributions to knowledge made under the second objective are:

- A simplified and more straightforward mathematical expression for estimating the obtainable thermal efficiency of isothermal steam Rankine cycle
- Characterisation of the performance of isothermal steam Rankine cycle with respect to volume of injected working fluid
- experimental study highlighting technical constraints in vaporising and expanding water in hot oil expansion chamber

Part of the work has been published in *International Journal of Low-Carbon Technologies*:

Igobo O.N. and Davies P.A. A high-efficiency solar Rankine engine with isothermal expansion. International Journal of Low-Carbon Technologies. 2013;8(suppl 1):i27-i33.

Objective 3: Optimise the engine for low temperature operation

This objective was met in chapter 4. In this objective, firstly, a more complete thermodynamic analysis of the isothermal Rankine cycle was carried out, taking into account the practical effects of blow down, non-ideal isothermal operation and dead volume, which all tend to result in a performance less than the ideal potential indicated in the previous objective.

To adapt the engine for low-temperature operation, organic working fluids were considered. Several organic working fluids were investigated for isothermal operation. The potential candidates were screened based on the fluid properties, engine performance and environmental considerations. The key parameters used were: vapour density, thermal conductivity, evaporating pressure, thermal efficiency and engine size. The analysis showed that, generally, the efficiency increases sharply with evaporation temperature, but the increase diminishes as the temperature approaches the critical temperature of the fluid. The study further showed that, at a reference evaporating temperature of 100^{o}C, R123 offers the highest cycle efficiency amongst the fluids studied, but suffers the disadvantage of large engine swept volume. Ammonia and R245fa also offer high efficiencies, with Ammonia (and R134a) having the most compact engine size but with detrimental high operating pressures and pump requirement.

In experimenting with R245fa, it was observed that, the expansion process approached isothermal behaviour for operating speed < 200 mm/min. The work output increased steadily with increase in the volume of injected liquid; but, the resulting efficiency increase was however truncated due to limited expansion stroke of the piston (in the experimental set up); nevertheless the achieved efficiency was about 8.8%.

Contributions to knowledge arising from this chapter are:

- Comparative characterisation of different organic working fluids for isothermal operation, which contrast to studies available in literature which are based on adiabatic operation.
- The achieved performance can serve as a practical performance reference for R245fa ORC operating in low temperature and low speed isothermal expansion.

The study completed in chapter 4 for the third objective has been published in *Desalination and Water Treatment*:

Igobo O.N. Davies P.A. Low-temperature organic Rankine cycle engine with isothermal expansion for use in desalination. Desalination and Water Treatment. 2015;55(13):3694-703

Objective 4: Further develop the engine and drive a pre-built batch desalination system to produce fresh water, and characterize its behaviour for a range of conditions.

This objective was met in chapters 5 and 6. The previous design of the isothermal ORC system was scaled up by a factor of 10 and coupled to the pre-built batch RO desalination machine 'DesaLink'. The integration of the ORC system with DesaLink entailed replacing the original power cylinder base of the DesaLink system with a bespoke fabricated fin cylinder base that facilitated heat transfer from a circulating thermal fluid, together with associated injection and condenser equipment. Experimental work carried out to access the performance of the integrated ORC-DesaLink system powered by 95^{o}C heat source temperature of 70% ethylene glycol thermal fluid, showed that, with 112 mL of R245fa liquid injected, the ORC achieved thermal efficiency of 7.9%, as the system produced 2.3 litres of fresh water (of approximately 500 ppm) from 4000 ppm saline feed water per cycle, at a specific thermal energy consumption of 4.4 kWh/m^3 or specific mechanical energy consumption of 0.35 kWh/m^3 (which is less than half of the energy requirement of conventional ORC-RO desalination systems); however, at a less than expected production rate of about 12 L of fresh water per hour.

Further, having proved the feasibility of the integrated ORC-DesaLink batch desalination system, the work proceeded to developing integrated model to characterise the operation of the system. The integrated system model was built by developing and interconnecting a set of semi empirical models of the various sub-units/components of the system. In general, the models were able to correlate the experimental results with less than 20% relative error.

The outcome and contributions to knowledge of this objective are:

- Characterisation of the performance of a quasi-isothermal ORC driven batch RO desalination system; since no other author has reported work as regards the present configuration
- Record low SEC compared to state of the art systems by a factor of 2

Objective 5: To access the potential field performance of the system in Case studies

This objective of accessing the potential performance of the ORC-RO DesaLink system in real life scenarios was explored in chapter 7. Here, two case studies were presented to demonstrate the performance of the system, based on two different thermal energy sources (solar thermal and waste heat recovery) at two different geographic locations. For both cases, the appropriate governing equations characterizing the thermal energy source were identified/developed and appended to the ORC-DesaLink model already developed (in the previous objective). The first case, presented the application of the ORC-DesaLink system with a target water production capacity of 1000 litres of fresh water per day when powered by FPC or ETC solar thermal collectors in Gujarat, India. The simulation results indicated that 3 units of the solar collectors (with total area of 7.5 or 3.5 m^2 respectively) will be required to meet the desired water need.

The second case demonstrated the potential of the system in utilizing waste heat recovered from the exhaust/flue gas of a natural gas fired oven of an industrial bakery facility in New-Mexico, USA. The study showed that, the potential water production rate varies linearly with the oven's gas burning rate (per unit mass of baked product). It indicated that, less than 5% of the energy content of the exhaust gas can be recovered to the drive multiple units of the ORC-DesaLink system to produce about 15,000 litres of fresh water daily, when the bakery is operating at its average production capacity. The fresh water can be produced at about 0.5 litres per kg of products backed. From both studies, the ORC DesaLink system has been demonstrated to be potentially attractive in delivering substantial quantities of fresh water at minimal energy requirement.

The outcome and contributions to knowledge arising from this objective are:

- The characterization of the potential performance of an ORC-RO batch desalination system in waste heat recovery application.
- The characterization of desalination water output with respect to bakery oven flue gas and bakery product mass production rate.

8.2 Responses to overall aim

The overall aim of this thesis was to investigate the feasibility of adopting low temperature organic Rankine cycle with isothermal expansion for batch RO desalination.

This aim was successfully achieved through the research outcomes of the aforementioned objectives. The work was accomplished in four phases; the first phase (chapters 1 and 2) provided a

good insight into the background of the field of study, including the state-of-the-art and performance shortcomings; and potential solution techniques were identified. In the second phase (chapters 3 and 4), the decision for which technique to pursue was made, based on comparison of their experimental performance and complexity. As a result, expander wall heating technique was chosen for further consideration. Subsequently, the system was further developed and optimised for low temperature operation, with the appropriate organic working fluid (R245fa). In the third phase (chapter 5), a larger scale rig was developed and integrated to a pre-built batch desalination machine, and the integrated system performance was experimentally accessed. The results showed the isothermal ORC was able to successfully drive the batch RO desalination machine to produce fresh water at a relatively lower energy requirement than conventional RO systems. In the final phase (chapters 6 and 7) the theoretical models for characterising the operation and performance of the integrated system were outlined and used to demonstrate the potential desalting performance of the system in real world application, when powered by two alternative thermal energy sources (solar and waste heat), with superior energy efficiency as compared to state-of-the-art systems using low-grade heat to drive desalination.

8.3 Final remarks and future work

The research work has successfully developed a quasi-isothermal low temperature ORC engine to drive a batch RO desalination system to produce fresh water at relatively modest energy requirement. Although the underlying principles and key components of the system have been thoroughly investigated, there are certain aspects of the system that require further investigations.

One particular of such aspects recommended for further consideration is ‘heat loss’ from the heated cylinder. Although the cylinder wall was largely insulated, further improvement is recommended to minimise both direct and indirect heat losses. Given that there is a number of mating metal parts eventually connecting the heated cylinder to the steel chassis of the system, this inadvertently provides a medium for heat conduction to the ambient, thus it is recommended to investigate appropriate means of providing effective insulation without compromising on the systems’ structural robustness.

Another aspect worth investigating further is the enhancement of the rate of vaporisation of the working fluid at the heated cylinder base and base plate confinement surfaces. Here it is recommended to investigate alternative design configurations (of the cylinder base and base plate) that could facilitate faster vapour evacuation (from the confinement area) without adverse effect on

overall performance. Also vaporisation rate enhancement by means of surface treatment for improved heat transfer could be investigated. However, these enhancements should be sought without seriously compromising the contact surface area between the two metal mating surfaces (so as not to negate the rate of heat transfer to the base plate). Thus, in general, the investigation should seek a balance between the vapour evacuation rate, metal-fluid heat transfer rate and metal-metal heat transfer rate. In addition, it would be interesting to explore the possibility of adopting nanofluids – dispersion of nano-particles in the base organic working fluid – for improvements in the thermal properties of the working fluid.

In a nutshell, the quasi-isothermal ORC DesaLink system described in this thesis is demonstrated as a feasible and promising technology that may be worth commercialising, albeit with some further development. The study has been primarily focused on the technical rather than commercial prospects of the system. As such, an assessment of the cost (both capital and operating) of the technology will be worthwhile, to eventually assess whether it will be a commercially viable option compared to the conventional methods of utilising low grade thermal energy sources in driving RO desalination systems to produce fresh water, in the face of the global water and energy challenges.

References

[1] United Nations. The Millennium Development Goal Report, 2013. http://www.undp.org/content/dam/undp/library/MDG/english/mdg-report-2013-english.pdf; ; accessed February 2014.

[2] El-Sadek A. Water desalination: An imperative measure for water security in Egypt. Desalination. 2010;250(3):876-84.

[3] Zotalis K, Dialynas EG, Mamassis N, Angelakis AN. Desalination Technologies: Hellenic Experience. Water. 2014;6(5):1134-50.

[4] Lattemann S, Kennedy MD, Schippers JC, Amy G. Chapter 2 Global Desalination Situation. In: Isabel CE, Andrea IS, editors. Sustainability Science and Engineering: Elsevier; 2010. p. 7-39.

[5] Watson IC, Morin O, Henthorne L. Desalting handbook for planners. Desalination Research and Development Program Report2003.

[6] Water desalination report. http://www.desalination.com/; accessed 1/12/2014.

[7] International Energy Agency (IEA). Key World Energy Statistics. 2013 ed. Paris, France: OECD/IEA; 2013.

[8] Shafiee S, Topal E. When will fossil fuel reserves be diminished? Energy Policy. 2009;37(1):181-9.

[9] International Energy Agency (IEA). Key world energy statistics. 2010 ed2010.

[10] International Atomic Energy Agency (IAEA). Tackling the Global Energy Crisis. IAEA Bulletin; 2008.

[11] Amor MB, Lesage P, Pineau P-O, Samson R. Can distributed generation offer substantial benefits in a Northeastern American context? A case study of small-scale renewable technologies using a life cycle methodology. Renewable and Sustainable Energy Reviews. 2010;14(9):2885-95.

[12] International Energy Agency (IEA). Key world energy statistics. 2012 ed. Paris, France: OECD/IEA; 2012.

[13] Internal Energy Agency (IEA). World energy outlook, Executive summary. 2012 ed. Paris, France: OECD/IEA; 2012.

[14] KPMG International. Taxes and incentives for renewable energy. Toronto, Canada: KPMG; June 2012.

[15] International Energy Agency (IEA). Insights series: Policies for renewable heat, an integrated approach
Paris, France: OECD/IEA; 2012.

[16] Department of Energy and Climate Change (DECC). Renewable Heat Incentive (RHI). https://www.gov.uk/government/policies/increasing-the-use-of-low-carbon-technologies/supporting-pages/renewable-heat-incentive-rhi; accessed 1/6/2013.

[17] Resch G, Held A, Faber T, Panzer C, Toro F, Haas R. Potentials and prospects for renewable energies at global scale. Energy Policy. 2008;36(11):4048-56.

[18] Jacobson MZ, Delucchi MA. Providing all global energy with wind, water, and solar power, Part I: Technologies, energy resources, quantities and areas of infrastructure, and materials. Energy Policy. 2011;39(3):1154-69.

[19] Hoogwijk M, Faaij A, van den Broek R, Berndes G, Gielen D, Turkenburg W. Exploration of the ranges of the global potential of biomass for energy. Biomass and bioenergy. 2003;25(2):119-33.

[20] Rayegan R, Tao Y. A procedure to select working fluids for Solar Organic Rankine Cycles (ORCs). Renewable Energy. 2011;36(2):659-70.

[21] Wang J, Dai Y, Gao L. Exergy analyses and parametric optimizations for different cogeneration power plants in cement industry. Applied Energy. 2009;86(6):941-8.

[22] Hung T, Shai T, Wang S. A review of organic Rankine cycles (ORCs) for the recovery of low-grade waste heat. Energy. 1997;22(7):661-7.

[23] Engin T, Ari V. Energy auditing and recovery for dry type cement rotary kiln systems—A case study. Energy Conversion and Management. 2005;46(4):551-62.

[24] BCS Inc. Waste heat recovery: technologies and opportunities in U.S. industry. US Dept. of Energy (DOE) 2008.

[25] Novatec Biosol. http://www.novatecsolar.com/; Accessed 24/09/2014.

[26] National Renewable Energy Laboratory (NREL). http://www.nrel.gov/csp/troughnet/power_plant_data.html; Accessed 27/09/2014.

[27] Echogen power systems. http://www.echogen.com/our-solution/product-series/eps100/; Accessed 22/09/2012.

[28] Obernberger I, Thonhofer P, Reisenhofer E. Description and evaluation of the new 1000 kWel Organic Rankine Cycle process integrated in the biomass CHP plant in Lienz, Austria. Euroheat & Power. 2002;10:1-17.

[29] BIOMASS Energy Centre. UK biomass power stations, current and planned. http://www.biomassenergycentre.org.uk/; Accessed 27/09/2014.

[30] Bao J, Zhao L. A review of working fluid and expander selections for organic Rankine cycle. Renewable and Sustainable Energy Reviews. 2013;24(0):325-42.

[31] Quoilin S, Broek MVD, Declaye S, Dewallef P, Lemort V. Techno-economic survey of Organic Rankine Cycle (ORC) systems. Renewable and Sustainable Energy Reviews. 2013;22:168-86.

[32] Mathioulakis E, Belessiotis V, Delyannis E. Desalination by using alternative energy: Review and state-of-the-art. Desalination. 2007;203(1):346-65.

[33] Sharon H, Reddy KS. A review of solar energy driven desalination technologies. Renewable and Sustainable Energy Reviews. 2015;41(0):1080-118.

[34] Ghaffour N, Bundschuh J, Mahmoudi H, Goosen MFA. Renewable energy-driven desalination technologies: A comprehensive review on challenges and potential applications of integrated systems. Desalination. 2015;356(0):94-114.

[35] Davies PA. A solar-powered reverse osmosis system for high recovery of freshwater from saline groundwater. Desalination. 2011;271(1):72-9.

[36] Qiu T, Davies P. The scope to improve the efficiency of solar-powered reverse osmosis. Desalination and water treatment. 2011;35(1-3):14-32.

[37] Clarke DP, Al-Abdeli YM, Kothapalli G. The effects of including intricacies in the modelling of a small-scale solar-PV reverse osmosis desalination system. Desalination. 2013;311:127-36.

[38] Ghermandi A, Messalem R. Solar-driven desalination with reverse osmosis: the state of the art. Desalination and water treatment. 2009;7(1-3):285-96.

[39] Organization WH. Total Dissolved Solids in Drinking-water. Background Document for preparation of WHO Guidelines for Drinking-water Quality. World Health Organization (WHO/SDE/WSH/0304/16). 2003.

[40] Elimelech M, Phillip WA. The future of seawater desalination: energy, technology, and the environment. Science. 2011;333(6043):712-7.

[41] Efraty A, Barak RN, Gal Z. Closed circuit desalination—A new low energy high recovery technology without energy recovery. Desalination and Water Treatment. 2011;31(1-3):95-101.

[42] Efraty A. Apparatus for continuous closed circuit desalination under variable pressure with a single container. Google Patents; 2009.

[43] Qiu T, Igobo O, Davies P. DesaLink: solar powered desalination of brackish groundwater giving high output and high recovery. Desalination and water treatment. 2013;51(4-6):1279-89.

[44] Igobo ON, Davies PA. Review of low-temperature vapour power cycle engines with quasi-isothermal expansion. Energy. 2014;70:22-34.

[45] Peñate B, García-Rodríguez L. Current trends and future prospects in the design of seawater reverse osmosis desalination technology. Desalination. 2012;284:1-8.

[46] Li C, Goswami Y, Stefanakos E. Solar assisted sea water desalination: A review. Renewable and Sustainable Energy Reviews. 2013;19:136-63.

[47] Delgado-Torres AM, García-Rodríguez L. Design recommendations for solar organic Rankine cycle (ORC)–powered reverse osmosis (RO) desalination. Renewable and Sustainable Energy Reviews. 2012;16(1):44-53.

[48] Manolakos D, Papadakis G, Mohamed ES, Kyritsis S, Bouzianas K. Design of an autonomous low-temperature solar Rankine cycle system for reverse osmosis desalination. Desalination. 2005;183(1):73-80.

[49] Peñate B, de la Fuente JA, Barreto M. Operation of the RO Kinetic® energy recovery system: Description and real experiences. Desalination. 2010;252(1–3):179-85.

[50] Delgado-Torres AM, García-Rodríguez L. Preliminary design of seawater and brackish water reverse osmosis desalination systems driven by low-temperature solar organic Rankine cycles (ORC). Energy Conversion and Management. 2010;51(12):2913-20.

[51] El-Nashar AM, Husseiny AA. Design aspects of a solar assisted reverse osmosis desalting unit for urban communities. Desalination. 1980;32:239-56.

[52] Childs WD, Dabiri AE, Al-Hinai HA, Abdullah HA. VARI-RO solar-powered desalting technology. Desalination. 1999;125(1–3):155-66.

[53] Childs WD, Dabiri AE. VARI-RO™ "low energy" desalting for the San Diego region. Desalination. 1995;103(1–2):49-58.

[54] Bowman TE, El-Nashar AM, Thrasher BH, Husseiny AA, Unione AJ. Design of a small solar-powered desalination system. Desalination. 1981;39(0):71-81.

[55] Charcosset C. A review of membrane processes and renewable energies for desalination. Desalination. 2009;245(1–3):214-31.

[56] Attia AAA. Thermal analysis for system uses solar energy as a pressure source for reverse osmosis (RO) water desalination. Solar Energy. 2012;86(9):2486-93.

[57] Nafey A, Sharaf M. Combined solar organic Rankine cycle with reverse osmosis desalination process: Energy, exergy, and cost evaluations. Renewable Energy. 2010;35(11):2571-80.

[58] Delgado-Torres AM, García-Rodríguez L. Preliminary assessment of solar organic Rankine cycles for driving a desalination system. Desalination. 2007;216(1):252-75.

[59] Delgado-Torres AM, García-Rodríguez L, Romero-Ternero VJ. Preliminary design of a solar thermal-powered seawater reverse osmosis system. Desalination. 2007;216(1–3):292-305.

[60] Karellas S, Terzis K, Manolakos D. Investigation of an autonomous hybrid solar thermal ORC–PV RO desalination system. The Chalki island case. Renewable Energy. 2011;36(2):583-90.

[61] Bruno JC, Lopez-Villada J, Letelier E, Romera S, Coronas A. Modelling and optimisation of solar organic rankine cycle engines for reverse osmosis desalination. Applied Thermal Engineering. 2008;28(17):2212-26.

[62] Manolakos D, Kosmadakis G, Kyritsis S, Papadakis G. On site experimental evaluation of a low-temperature solar organic Rankine cycle system for RO desalination. Solar Energy. 2009;83(5):646-56.

[63] Kosmadakis G, Manolakos D, Kyritsis S, Papadakis G. Simulation of an autonomous, two-stage solar organic Rankine cycle system for reverse osmosis desalination. Desalination and Water Treatment. 2009;1(1-3):114-27.

[64] Libert J, Maurel A. Desalination and renewable energies-a few recent developments. Desalination. 1981;39:363-72.

[65] Maurel A. Dessalement et energies nouvelles. Desalination. 1979;31(1–3):489-99.

[66] Manolakos D, Kosmadakis G, Kyritsis S, Papadakis G. Identification of behaviour and evaluation of performance of small scale, low-temperature Organic Rankine Cycle system coupled with a RO desalination unit. Energy. 2009;34(6):767-74.

[67] Campos MC, Vargas JVC, Ordonez JC. Thermodynamic optimization of a Stirling engine. Energy. 2012;44(1):902-10.

[68] Park Jk, Ro PI, Lim SD, Mazzoleni AP, Quinlan B. Analysis and optimization of a quasi-isothermal compression and expansion cycle for ocean compressed air energy storage (OCAES). Oceans, 2012: IEEE; 2012. p. 1-8.

[69] Redderson RH. Vapor stirling heat machine. US Patents; 1989.

[70] Alanne K, Saari K, Kuosa M, Jokisalo J, Martin AR. Thermo-economic analysis of a micro-cogeneration system based on a rotary steam engine (RSE). Applied Thermal Engineering. 2012;44(0):11-20.

[71] Markides CN. The role of pumped and waste heat technologies in a high-efficiency sustainable energy future for the UK. Applied Thermal Engineering. 2012;53:197-209.

[72] Bianchi M, De Pascale A. Bottoming cycles for electric energy generation: Parametric investigation of available and innovative solutions for the exploitation of low and medium temperature heat sources. Applied Energy. 2011;88(5):1500-9.

[73] Cengel YA, Boles MA. Thermodynamics, an engineering approach. 7th ed. NewYork, USA: McGraw-Hill, 2011.

[74] Cengel YA, Cimbala JM, Turner RH, Kanoglu M. Fundamentals of thermal-fluid sciences. 4th ed. NewYork, USA: McGraw-Hill, 2012.

[75] Rajput RK. Engineering thermodynamics. 3rd ed. Massachusetts, USA: Jones and Bartlett, 2010.

[76] O'Kelly P. Computer Simulation of Thermal Plant Operations. New York, USA: Springer; 2012.

[77] NIST Standard Reference Database. Thermophysical Properties of Fluid Systems. webbook.nist.gov; accessed 1/11/2013.

[78] Moran MJ, Shapiro HN, Boettner DD, Bailey M. Fundamentals of engineering thermodynamics. 7th ed. New Jersey, USA: John Wiley & Sons, 2010.

[79] Chen H, Ding Y, Li Y, Zhang X, Tan C. Air fuelled zero emission road transportation: A comparative study. Applied Energy. 2011;88(1):337-42.

[80] Bell IH, Lemort V, Groll EA, Braun JE, King GB, Horton WT. Liquid flooded compression and expansion in scroll machines–Part II: Experimental testing and model validation. International Journal of Refrigeration. 2012;35(7):1890-900.

[81] Woodland BJ, Groll EA, Braun JE, Horton WT. Performance benefits for organic Rankine cycles with flooded expansion and internal regeneration. International refrigeration and air conditioning conference. Purdue University: Paper 1134; 2010.

[82] Lemort V, Declaye S, Quoilin S. Experimental characterization of a hermetic scroll expander for use in a micro-scale Rankine cycle. Proceedings of the Institution of Mechanical Engineers, Part A: Journal of Power and Energy. 2012;226(1):126-36.

[83] Kim YM, Shin D, Lee J. A scroll expander with heating structure and their systems. International compressor engineering conference , Purdue: paper 1635; 2004.

[84] Igobo ON, Davies PA. A high-efficiency solar Rankine engine with isothermal expansion. International Journal of Low-Carbon Technologies. 2013;8(suppl 1):i27-i33.

[85] The Dearman Engine Company. www.dearmanengine.com/cms/liquid-air/; accessed 22/6/2013.

[86] Wen D, Chen H, Ding Y, Dearman P. Liquid nitrogen injection into water: pressure build-up and heat transfer. Cryogenics. 2006;46(10):740-8.

[87] Knowlen C, Williams J, Mattick A, Deparis H, Hertzberg A. Quasi-isothermal expansion engines for liquid nitrogen automotive propulsion. SAE paper 972649. 1997.

[88] West CD. Two-phase, two-component Stirling engine with controlled evaporation. Oak Ridge National Lab., Tennesse, USA; 1982.

[89] Isshiki N, KOJiMA H, Ushiyama I, Isshiki S. Report on the developments of steam super Stirling engine. Energy Conversion Engineering Conference and Exhibit, 2000(IECEC) 35th Intersociety: IEEE; 2000. p. 111-9.

[90] Couper JR, Penney WR, Fair JR, Walas SM. 8 - Heat Transfer and Heat Exchangers. In: Couper JR, Penney WR, Fair JR, Walas SM, editors. Chemical Process Equipment (Third Edition). Boston, USA: Butterworth-Heinemann; 2012. p. 161-221.

[91] Cheng C-H, Yang H-S, Keong L. Theoretical and experimental study of a 300-W beta-type Stirling engine. Energy. 2013;59:590-9.

[92] Cicconardi S, Jannelli E, Perna A, Spazzafumo G. A steam cycle with an isothermal expansion: the effect of flowvariation. International journal of hydrogen energy. 1999;24(1):53-7.

[93] Stosic N, Milutinovic L, Hanjalic K, Kovacevic A. Experimental investigation of the influence of oil injection upon the screw compressor working process. International Compressor Engineering Conference. Purdue University: paper 687; 1990.

[94] Sakuda A, Sawai K, Iida N, Hiwata A, Morimoto T, Ishii N. Performance improvement of scroll compressor with new sealing-oil supply mechanism. International Conference on Compressors and their Systems: No. C591/019; 2001.

[95] Hugenroth J, Braun J, Groll E, King G. Liquid-flooded Ericsson cycle cooler: Part 1– Thermodynamic analysis. International Refrigeration and Air conditioning Conference. Purdue University: Paper 823; 2006.

[96] Wang W, Wu Y-t, Ma C-f, Xia G-d, Wang J-f. Experimental study on the performance of single screw expanders by gap adjustment. Energy. 2013;62(0):379-84.

[97] Declaye S, Quoilin S, Guillaume L, Lemort V. Experimental study on an open-drive scroll expander integrated into an ORC (Organic Rankine Cycle) system with R245fa as working fluid. Energy. 2013;55:173-83.

[98] Hugenroth J, Braun J, Groll E, King G. Thermodynamic analysis of a liquid-flooded Ericsson cycle cooler. International Journal of Refrigeration. 2007;30(7):1176-86.

[99] Hugenroth J, Braun J, Groll E, King G. Experimental investigation of a liquid-flooded Ericsson cycle cooler. International Journal of Refrigeration. 2008;31(7):1241-52.

[100] Bell IH, Lemort V, Groll EA, Braun JE, King GB, Horton WT. Liquid-flooded compression and expansion in scroll machines – Part I: Model development. International Journal of Refrigeration. 2012;35(7):1878-89.

[101] Bell IH, Groll EA, Braun JE, King GB, Horton WT. Optimization of a scroll compressor for liquid flooding. International Journal of Refrigeration. 2012;35(7):1901-13.

[102] Halm NP. Mathematical modeling of scroll compressors [Master Thesis]. Indiana, USA: Purdue University, 1997.

[103] Chen Y, Braun JE, Groll EA. Modeling of hermetic scroll compressors: model development. HVAC&R Research. 2004;10(2):129-52.

[104] Lemort V, Bell I, Groll EA, Braun J. Analysis of liquid-flooded expansion using a scroll expander. International compressor engineering conference at Purdue: Paper 1323; 2008.

[105] Williams JD. Design of a liquid nitrogen vaporization system for automotive propulsion [PhD Thesis]. Washington, USA: University of Washington 1997.

[106] Cicconardi S, Jannelli E, Perna A, Spazzafumo G. Parametric analysis of a steam cycle with a quasi-isothermal expansion. International journal of hydrogen energy. 2001;26(3):275-9.

[107] Woodland BJ, Braun JE, Groll EA, Horton WT. Organic Rankine cycle with flooded expansion and internal regeneration. US Patents; 2011.

[108] Woodland BJ, Krishna A, Groll E, Braun JE. Thermodynamic comparison of organic Rankine cycles employing liquid-flooded expansion or a solution circuit. Applied Thermal Engineering. 2013;61(2):859–65.

[109] Bell I, Groll E, Braun J, Horton WT. Experimental testing of an oil-flooded hermetic scroll compressor. International Journal of Refrigeration. 2013;36(7):1866–73.

[110] Kim Y-M, Shin D-G, Lee S-Y, Favrat D. Isothermal transcritical CO< sub> 2</sub> cycles with TES (thermal energy storage) for electricity storage. Energy. 2013;49:484-501.

[111] Rogers GFC, Mayhew YR. Engineering thermodynamics work and heat transfer. London, UK: Longmans, 1965.

[112] Clark DK. The Steam engine: A treaties on steam engines and boilers. London, UK: Blackie and Sons limited, 1890.

[113] Cho S-Y, Cho C-H, Ahn K-Y, Lee YD. A study of the optimal operating conditions in the organic Rankine cycle using a turbo-expander for fluctuations of the available thermal energy. Energy 2013;64:900-11.

[114] Ordonez C, Plummer M. Cold thermal storage and cryogenic heat engines for energy storage applications. Energy Sources. 1997;19(4):389-96.

[115] Li Y, Chen H, Ding Y. Fundamentals and applications of cryogen as a thermal energy carrier: A critical assessment. International Journal of Thermal Sciences. 2010;49(6):941-9.

[116] Dong H, Zhao L, Zhang S, Wang A, Cai J. Using cryogenic exergy of liquefied natural gas for electricity production with the Stirling cycle. Energy. 2013;63:10-8.

[117] Zhu HM, Liu HW, Sun H. Exergy Analysis of Cascade Ethylene-Propane Rankine Cycle with Cold Energy Recovery of LNG. Applied Mechanics and Materials. 2012;170:2489-93.

[118] Xia G, Sun Q, Cao X, Wang J, Yu Y, Wang L. Thermodynamic analysis and optimization of a solar-powered transcritical CO2 (carbon dioxide) power cycle for reverse osmosis desalination based on the recovery of cryogenic energy of LNG (liquefied natural gas). Energy. 2014;66:643-53.

[119] Li Y, Wang X, Jin Y, Ding Y. An integrated solar-cryogen hybrid power system. Renewable Energy. 2012;37(1):76-81.

[120] Castle W. Air separation and liquefaction: recent developments and prospects for the beginning of the new millennium. International Journal of Refrigeration. 2002;25(1):158-72.

[121] Dooley J, Hammond R. Concept evaluation of automotive propulsion using liquid air/nitrogen. Final report. R and D Associates, Marina del Rey, California, USA; 1982.

[122] Tian CZ, Yuan GJ, Chen GJ. Cylinder Flow Simulation of Liquid Nitrogen Engine Based on STAR-CD. Applied Mechanics and Materials. 2013;344:31-6.

[123] Plummer M, Koehler C, Flanders D, Reidy R, Ordonez C. Cryogenic heat engine experiment. Advances in cryogenic engineering. 1998;43:1245-52.

[124] Williams J. Cryogenic automobile propulsion: heat exchanger design and performance issues. Proceedings of AIAA 19th IECEC. CA, US: AIAA 97-0017; 1997.

[125] Amrit J, Douay C, Dubois F, Defresne G. Cryogenic heat exchanger with turbulent flows. European Journal of Physics. 2012;33(1):189.

[126] Knowlen C, Hertzberg A, Mattick A. Cryogenic automotive propulsion. AIAA 94-4224; 1994.

[127] Knowlen C, Mattick A, Bruckner AP, Hertzberg A. High efficiency energy conversion systems for liquid nitrogen automobiles. SAE paper 981898. 1998.

[128] Yuanwei L, Hongchang Y, Chongfang M. Analysis and optimization of the power cycle based on the cold energy of liquefied natural gas. Measuring Technology and Mechatronics Automation (ICMTMA), 2011 Third International Conference on: IEEE; 2011. p. 455-8.

[129] Choi I-H, Lee S, Seo Y, Chang D. Analysis and optimization of cascade Rankine cycle for liquefied natural gas cold energy recovery. Energy. 2013;61:179-95.

[130] Liu Y, Guo K. A novel cryogenic power cycle for LNG cold energy recovery. Energy. 2011;36(5):2828-33.

[131] Ameel B, T'Joen C, De Kerpel K, De Jaeger P, Huisseune H, Van Belleghem M, et al. Thermodynamic analysis of energy storage with a liquid air Rankine cycle. Applied Thermal Engineering. 2012;52:130-40.

[132] Dearman's liquid air engine could rival battery systems. Professional Engineering; Feb 2012. p. 9.

[133] Morse TL, Kytömaa HK. The effect of turbulence on the rate of evaporation of LNG on water. Journal of Loss Prevention in the Process Industries. 2011;24(6):791-7.

[134] Esteves AS, Reis Parise JA. Mathematical modeling of cryogenic spills onto quiescent sea waters followed by pool fires of liquefied natural gas (LNG). Applied Thermal Engineering. 2013;59(1):587-98.

[135] Aceves SM, Petitpas G, Espinosa-Loza F, Matthews MJ, Ledesma-Orozco E. Safe, long range, inexpensive and rapidly refuelable hydrogen vehicles with cryogenic pressure vessels. International Journal of Hydrogen Energy. 2012;38(5):2480-9.

[136] Sripakagorn A, Srikam C. Design and performance of a moderate temperature difference Stirling engine. Renewable Energy. 2011;36(6):1728-33.

[137] Huang D, Wu F. Research of Refrigerant Phase-Change Stirling-Cycle Heat Engines. International conference on Measuring Technology and Mechatronics Automation (ICMTMA). Shangshai: IEEE; 2011. p. 1088-91.

[138] West CD. Liquid-piston Stirling machines. 2nd International Conference on Stirling Engines. Shanghai, China1984. p. 1-10.

[139] Stevens JW. Low Capital Cost Renewable Energy Conversion With Liquid Piston Stirling Engines. ASME 2010 4th International Conference on Energy Sustainability: American Society of Mechanical Engineers; 2010. p. 479-84.

[140] West CD. Stirling engines and irrigation pumping. Tennessee, USA: Oak Ridge national laboratory; 1987.

[141] Mauran S, Martins M, Stitou D, Semmari H. A novel process for engines or heat pumps based on thermal-hydraulic conversion. Applied Thermal Engineering. 2012;37(0):249-57.

[142] Van de Ven J, Gaffuri P, Mies B, Cole G. Developments towards a liquid piston Stirling engine. International Energy Conversion Engineering Conference, Cleveland, Ohio: Paper 5635; 2008.

[143] Van de Ven JD. Mobile hydraulic power supply: Liquid piston Stirling engine pump. Renewable Energy. 2009;34(11):2317-22.

[144] Davoud JG, Burke Jr JA. Condensing vapor heat engine with two-phase compression and constant volume superheating. US Patents; 1977.

[145] Burke Jr JA, Davoud JG. Condensing vapor heat engine with constant volume superheating and evaporating. US Patents; 1978.

[146] Çinar C, Aksoy F, Erol D. The effect of displacer material on the performance of a low temperature differential Stirling engine. International Journal of Energy Research. 2012;36(8):911-7.

[147] Tian J, Kim T, Lu T, Hodson H, Queheillalt D, Sypeck D, et al. The effects of topology upon fluid-flow and heat-transfer within cellular copper structures. International Journal of Heat and Mass Transfer. 2004;47(14):3171-86.

[148] Mahjoob S, Vafai K. A synthesis of fluid and thermal transport models for metal foam heat exchangers. International Journal of Heat and Mass Transfer. 2008;51(15):3701-11.

[149] Prasad SB, Saini JS, Singh KM. Investigation of heat transfer and friction characteristics of packed bed solar air heater using wire mesh as packing material. Solar Energy. 2009;83(5):773-83.

[150] Abduljalil AS, Yu Z, Jaworski AJ. Selection and experimental evaluation of low-cost porous materials for regenerator applications in thermoacoustic engines. Materials & Design. 2011;32(1):217-28.

[151] Costa S, Barrutia H, Esnaola JA, Tutar M. Numerical study of the pressure drop phenomena in wound woven wire matrix of a Stirling regenerator. Energy Conversion and Management. 2013;67:57-65.

[152] Trevizoli P, Liu Y, Tura A, Rowe A, Barbosa Jr J. Experimental assessment of the thermal–hydraulic performance of packed-sphere oscillating-flow regenerators using water. Experimental Thermal and Fluid Science. 2014;57(0):324-34.

[153] Lounici MS, Loubar K, Balistrou M, Tazerout M. Investigation on heat transfer evaluation for a more efficient two-zone combustion model in the case of natural gas SI engines. Applied Thermal Engineering. 2011;31(2):319-28.

[154] Zhang C, Wu Y, Xu L, Liu D, Chen Y. Connecting hose's operating characteristics and its effect on the cooling performance of an 80 K Oxford split-Stirling-cycle cryocooler. Cryogenics. 2003;43(6):335-44.

[155] Sanli A, Ozsezen AN, Kilicaslan I, Canakci M. The influence of engine speed and load on the heat transfer between gases and in-cylinder walls at fired and motored conditions of an IDI diesel engine. Applied thermal engineering. 2008;28(11):1395-404.

[156] Demuynck J, De Paepe M, Huisseune H, Sierens R, Vancoillie J, Verhelst S. On the applicability of empirical heat transfer models for hydrogen combustion engines. International Journal of Hydrogen Energy. 2011;36(1):975-84.

[157] Rao V, Bardon M. Convective heat transfer in reciprocating engines. Proceedings of the Institution of Mechanical Engineers, Part D: Journal of Automobile Engineering. 1985;199(3):221-6.

[158] Costea M, Petrescu S, Harman C. The effect of irreversibilities on solar Stirling engine cycle performance. Energy conversion and management. 1999;40(15):1723-31.

[159] Kongtragool B, Wongwises S. Optimum absorber temperature of a once-reflecting full conical concentrator of a low temperature differential Stirling engine. Renewable Energy. 2005;30(11):1671-87.

[160] Chen Y, Luo E, Dai W. Heat transfer characteristics of oscillating flow regenerator filled with circular tubes or parallel plates. Cryogenics. 2007;47(1):40-8.

[161] Brouwers H. Particle-size distribution and packing fraction of geometric random packings. Physical review E. 2006;74(3):031309.

[162] Chemieingenieurwesen V-GVu, Gesellschaft V. VDI Heat Atlas. Berlin, Germany: Springer, 2010.

[163] Bear J. Dynamics of fluids in porous media: Courier Dover Publications, 2013.

[164] Zhang W, Thompson KE, Reed AH, Beenken L. Relationship between packing structure and porosity in fixed beds of equilateral cylindrical particles. Chemical Engineering Science. 2006;61(24):8060-74.

[165] Tian J, Lu T, Hodson H, Queheillalt D, Wadley H. Cross flow heat exchange of textile cellular metal core sandwich panels. International journal of heat and mass transfer. 2007;50(13):2521-36.

[166] Bai M, Chung J. Analytical and numerical prediction of heat transfer and pressure drop in open-cell metal foams. International Journal of Thermal Sciences. 2011;50(6):869-80.

[167] Duocel® Aluminum Foam. http://www.ergaerospace.com/; accessed 14/09/2014.

[168] Igobo ON, Davies PA. Low-temperature organic Rankine cycle engine with isothermal expansion for use in desalination. Desalination and Water Treatment. 2015;55(13):3694-703.

[169] Badami M, Mura M. Preliminary design and controlling strategies of a small-scale wood waste Rankine Cycle (RC) with a reciprocating steam engine (SE). Energy. 2009;34(9):1315-24.

[170] Tchanche BF, Lambrinos G, Frangoudakis A, Papadakis G. Low-grade heat conversion into power using organic Rankine cycles–a review of various applications. Renewable and Sustainable Energy Reviews. 2011;15(8):3963-79.

[171] Liu B-T, Chien K-H, Wang C-C. Effect of working fluids on organic Rankine cycle for waste heat recovery. Energy. 2004;29(8):1207-17.

[172] Angelino G, Colonna di Paliano P. Multicomponent working fluids for organic Rankine cycles (ORCs). Energy. 1998;23(6):449-63.

[173] Saleh B, Koglbauer G, Wendland M, Fischer J. Working fluids for low-temperature organic Rankine cycles. Energy. 2007;32(7):1210-21.

[174] Maraver D, Uche J, Royo J. Assessment of high temperature organic Rankine cycle engine for polygeneration with MED desalination: A preliminary approach. Energy Conversion and Management. 2012;53(1):108-17.

[175] Quoilin S, Orosz M, Hemond H, Lemort V. Performance and design optimization of a low-cost solar organic Rankine cycle for remote power generation. Solar Energy. 2011;85(5):955-66.

[176] Jradi M, Li J, Liu H, Riffat S. Micro-scale ORC-based combined heat and power system using a novel scroll expander. International Journal of Low-Carbon Technologies. 2014:ctu012.

[177] Pei G, Li J, Li Y, Wang D, Ji J. Construction and dynamic test of a small-scale organic rankine cycle. Energy. 2011;36(5):3215-23.

[178] Wang J, Zhao L, Wang X. An experimental study on the recuperative low temperature solar Rankine cycle using R245fa. Applied Energy. 2012;94:34-40.

[179] Tchanche BF, Papadakis G, Lambrinos G, Frangoudakis A. Fluid selection for a low-temperature solar organic Rankine cycle. Applied Thermal Engineering. 2009;29(11):2468-76.

[180] Klein S. Engineering Equation Solver (EES), F-Chart Software. 2014.

[181] Kang SH. Design and experimental study of ORC (organic Rankine cycle) and radial turbine using R245fa working fluid. Energy. 2012;41(1):514-24.

[182] Qiu T. Desalination of Brackish Water by a Batch Reverse Osmosis DesaLink System for use with Solar Thermal Energy [PhD Thesis]. Birmingham, UK: Aston University, 2013.

[183] FILMTEC Reverse Osmosis Membranes: Technical manual. http://msdssearch.dow.com/PublishedLiteratureDOWCOM/dh_08db/0901b803808db77d.pdf?filepath=liquidseps/pdfs/noreg/609-00071.pdf&fromPage=GetDoc; accessed 10/12/2015.

[184] SMC: Smooth Cylinder/Low Speed Cylinder. http://content2.smcetech.com/pdf/smoothcylinder.pdf; accessed 24/12/2015.

[185] Luján JM, Serrano JR, Dolz V, Sánchez J. Model of the expansion process for R245fa in an Organic Rankine Cycle (ORC). Applied Thermal Engineering. 2012;40:248-57.

[186] Kang H, Lin C-X, Ebadian M. Condensation of R134a flowing inside helicoidal pipe. International journal of heat and mass transfer. 2000;43(14):2553-64.

[187] Kakac S, Liu H. Heat exchangers: selection, rating, and thermal design. 2 ed. Florida: CRC press, 2002.

[188] Salimpour M. Heat transfer coefficients of shell and coiled tube heat exchangers. Experimental thermal and fluid science. 2009;33(2):203-7.

[189] Elsayed AM. Heat Transfer in Helically Coiled Small Diameter Tubes for Miniature Cooling Systems [PhD Thesis]. Birmingham, UK: University of Birmingham, 2011.

[190] Bloch HP. Practical Machinery Management for Process Plants: Volume 1: Improving Machinery Reliability: Gulf Professional Publishing, 1998.

[191] Teertstra P, Yovanovich M, Culham J, Lemczyk T. Analytical forced convection modeling of plate fin heat sinks. Conference Analytical forced convection modeling of plate fin heat sinks. IEEE, p. 34-41.

[192] Salgon J-J, Robbe-Valloire F, Blouet J, Bransier J. A mechanical and geometrical approach to thermal contact resistance. International journal of heat and mass transfer. 1997;40(5):1121-9.

[193] Rao V, Bapurao K, Nagaraju J, Murthy MK. Instrumentation to measure thermal contact resistance. Measurement Science and Technology. 2004;15(1):275.

[194] Tuckerman DB, Pease R. High-performance heat sinking for VLSI. Electron Device Letters, IEEE. 1981;2(5):126-9.

[195] Harms TM, Kazmierczak MJ, Gerner FM. Developing convective heat transfer in deep rectangular microchannels. International Journal of Heat and Fluid Flow. 1999;20(2):149-57.

[196] Agarwal G, Moharana MK, Khandekar S. Thermo-hydrodynamics of developing flow in a rectangular mini-channel array. Conference Thermo-hydrodynamics of developing flow in a rectangular mini-channel array. p. 1342-9.

[197] Lenntech Water Treatment Solutions: Osmotic pressure calculator. http://www.lenntech.com/calculators/osmotic/osmotic-pressure.htm; accessed 10/12/2015.

[198] Zhu A, Christofides PD, Cohen Y. Effect of thermodynamic restriction on energy cost optimization of RO membrane water desalination. Industrial & Engineering Chemistry Research. 2008;48(13):6010-21.

[199] Central Ground Water Board (CGWB). Ministry of water resources, India: http://www.cgwb.gov.in/; accessed 6/12/2014.

[200] Central Soil Salinity Research Institute. Indian Council of Agricultural Research, Ministry of Agriculture, India: http://www.cssri.org/; accessed 6/12/2014.

[201] Abraham T, Luthra A. Socio-economic & technical assessment of photovoltaic powered membrane desalination processes for India. Desalination. 2011;268(1–3):238-48.

[202] Sumit D, Bindu B, Janak J, Sharma N. Assessment and Spatial Distribution of Quality of Groundwater in Mahi-Narmada Inter Stream Region Gujarat India using Water Quality Index (WQI). International Journal of Geology, Earth & Environmental Sciences. 2014;4(1): 184-95.

[203] Atmospheric Science Data Center. NASA Langley Research Center: https://eosweb.larc.nasa.gov/; accessed 7/12/2014.

[204] Kalogirou SA. Solar thermal collectors and applications. Progress in Energy and Combustion Science. 2004;30(3):231-95.

[205] Mills D. Advances in solar thermal electricity technology. Solar Energy. 2004;76(1–3):19-31.

[206] National Brackish Groundwater Assessment. U.S Geological Survey (USGS), USA: http://www.usgs.gov/water/; accessed 6/8/2015.

[207] U.S Geological Survey (USGS). Desalination of Ground Water: Earth Science Perspectives. USGS Fact Sheet 075-03. Virginia, USA October 2003.

[208] Desalination of saline and brackish water is becoming more affordable. Membrane Technology. 2009;2009(7):8-10.

[209] Alamogordo regional water supply project draft environmental impact statement. US Department of Interiaor, Bureau of Land Management, USA. August 2010.

[210] Alamogordo chamber of commerce. Alamogordo, New Mixico, USA: http://www.alamogordo.com/; accessed 1/5/2015.

[211] Western Baking Corporation. http://www.westernbaking.com/; accessed 2/5/2015.

[212] Industrial Energy Efficiency Accelerator - Guide to the industrial bakery sector. London, UK: The Carbon Trust.

[213] Therkelsen P, Masanet E, Worrell E. Energy efficiency opportunities in the US commercial baking industry. Journal of Food Engineering. 2014;130:14-22.

[214] Stear CA. Control Technology and Energy Recovery. Handbook of Breadmaking Technology: Springer; 1990. p. 620-37.

[215] Carbon Trust. Improving the efficiency of bakery ovens - Case study. London, UK: The Carbon Trust; April, 2015.

[216] Danielewicz J, Sayegh MA, Śniechowska B, Szulgowska-Zgrzywa M, Jouhara H. Experimental and analytical performance investigation of air to air two phase closed thermosyphon based heat exchangers. Energy. 2014;77:82-7.

[217] Energy recovery from exhaust gases using Heat Pipe technology. http://www.spiraxsarco.com/Documents/Energy_recovery_from_exhaust_gases_using_Heat_Pipe_technology-Sales%20Brochure.pdf; accessed 6/8/2015.

[218] Huang Z, Wang J, Liu B, Zeng K, Yu J, Jiang D. Combustion characteristics of a direct-injection engine fueled with natural gas–hydrogen blends under different ignition timings. Fuel. 2007;86(3):381-7.

[219] FGKH. Flue Gas Know How. http://fluegasknowhow.com/flue-gas-properties/ accessed 5/7/2015.

Appendices

Appendix 1: Thermal fluid properties

Table A.1: Thermo-physical properties of Globaltherm™ Syntec thermal fluid

Temperature (°C)	Density (Kg/m^3)	Vapour Pressure (mbar)	Kinematic Viscosity (mm^2/s)	Specific Heat (KJ/(KG.K))	Thermal Conductivity (W/(m.K)
20 °C	1008		100	1.6	0.120
40 °C	994		26.2	1.67	0.119
60 °C	980		11.5	1.74	0.118
80 °C	966		6	1.8	0.117
100 °C	953	0.2	3.7	1.88	0.115
120 °C	940	0.6	2.4	1.95	0.114
140 °C	926	1.9	1.8	2.02	0.112
160 °C	912	4.7	1.4	2.09	0.111
180 °C	899	10.8	1.1	2.16	0.109
200 °C	885	25	0.99	2.22	0.107
220 °C	872	44	0.8	2.3	0.105
240 °C	858	80	0.7	2.37	0.103
260 °C	844	137	0.63	2.44	0.101
280 °C	831	224	0.57	2.51	0.099
300 °C	818	340	0.53	2.58	0.096
320 °C	804	531	0.48	2.65	0.094
340 °C	790	777	0.45	2.72	0.091
360 °C	776	1105	0.42	2.79	0.088

Appendix 2: Specific Surface Area of metal foam

The specific surface area of foam is the amount of surface area within a given volume of foam. The Specific surface area increases with the foam pore density (defined as pores per inch (PPI)) and relative density. The graph below shows the variation of the specific surface area as a function of both of these key foam parameters.

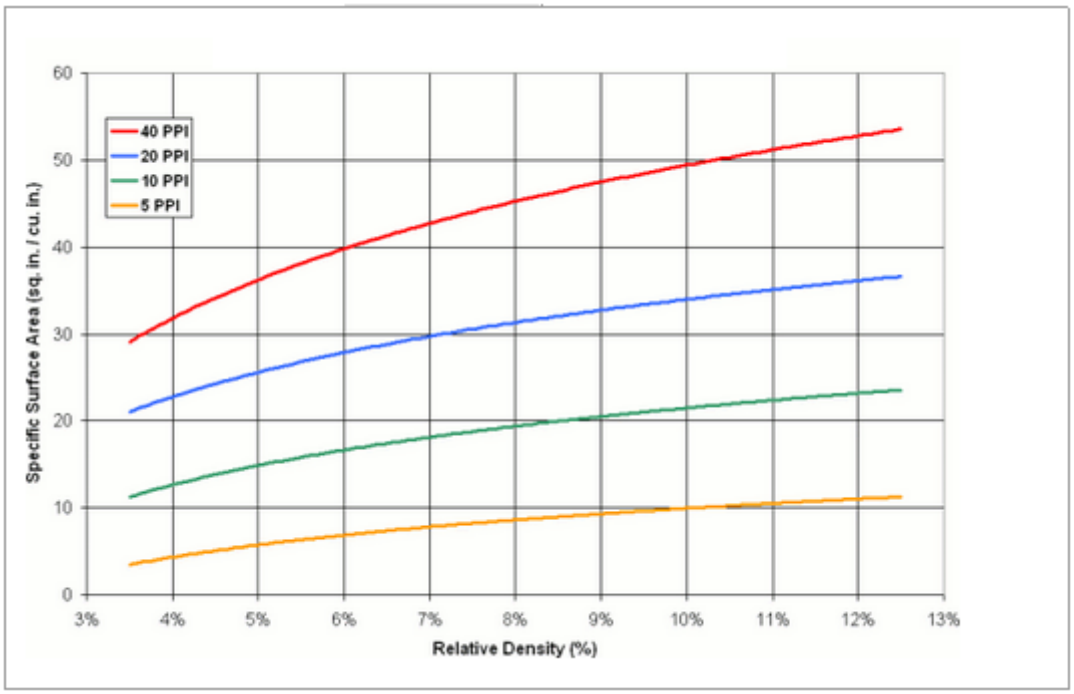

Figure A.1: Specific Surface Area of ERG Duocel® metal foams

Appendix 3: R245fa data sheet

Conforms to 91/155/EEC - 2001/58/EC - United Kingdom (UK)

SAFETY DATA SHEET

Honeywell

Enovate® 3000 (HFC-245fa)

Identification of the substance/preparation and of the company/undertaking

Identification of the substance or preparation

Product name	:	Enovate® 3000
Chemical name	:	1,1,1,3,3-pentafluoropropane. (HFC-245fa)
Synonyms	:	HFC-245fa.
Chemical formula	:	$CHF_2CH_2CF_3$
Use of the substance/preparation	:	Foam blowing agent.

Company/undertaking identification

Supplier : Honeywell Fluorine
Products Europe B.V.
Kempenweg 90
6002 SX Weert, The Netherlands
Tel: +31-495-514200
Fax: +31-495-518259

Emergency telephone number : (32) 16 391 391

Composition/information on ingredients

Substance/Preparation : Substance

Ingredient Name	CAS number	%	EC Number	Classification
United Kingdom (UK) 1,1,1,3,3-pentafluoropropane. (HFC-245fa) **See Section 16 for the full text of the R Phrases declared above**	460-73-1	100	419-170-6	

*** Occupational Exposure Limit(s), if available, are listed in Section 8**

Hazards identification

The substance is not classified as dangerous according to Directive 67/548/EEC and its amendments.

Additional Hazards : High vapour concentrations can cause headaches, dizziness, drowsiness, and nausea, and may lead to unconsciousness. Heartbeat irregularity (arrhythmia). Causes damage to the following organs: cardiovascular system, upper respiratory tract.

Ecological information

Ecotoxicity Data

Ingredient Name	Species	Period	Result
1,1,1,3,3-pentafluoropropane. (HFC-245fa)	Daphnia (EC50)	48 hour(s)	>97.9 mg/l
	Rainbow trout (LC50)	96 hour(s)	>81.8 mg/l

Other Ecological Information

Ingredient Name	Persistence/degradability						Bioaccumulative potential		
	BOD_5	COD	ThOD	Aquatic Half-life	Photolysis	Biodegradability	$LogP_{ow}$	BCF	Potential
1,1,1,3,3-pentafluoropropane. (HFC-245fa)							1.35		low

Ozone Depleting Potential (ODP) (R-11 = 1) : 0

Global Warming Potential (GWP) : 950

Mobility : Practically non-toxic to aquatic organisms.

Physical and chemical properties

General information

Appearance

Physical state : Gas. (Liquefied gas.)

Colour : Colourless.

Odour : Slight.

Molecular Weight : 134.03 g/mole

Important health, safety and environmental information

Boiling point : 15.3°C (59.5°F)

Melting point : -103°C (-153.4°F)

Flash point : Not applicable.

Relative density : 1.32 g/cm^3

Solubility : Partially soluble in methanol, diethyl ether.
Water: 0.013 g/100 ml.

Octanol/water partition coefficient : The product is more soluble in octanol; log(octanol/water) = 1.35

Vapour density : 4.6 (Air = 1)

Evaporation rate : <1 compared to Ether (anhydrous).
> 1compared to CCl_4 .

Other information

Auto-ignition temperature : 412°C (773.6°F)

Decomposition Temperature : >250°C (482°F)

Stability and reactivity

Stability : The product is stable. Hazardous Polymerisation : Will not occur.

Conditions to Avoid : In a fire or if heated, a pressure increase will occur and the container may burst. Pressurised container: protect from sunlight and do not expose to temperature exceeding 50°C. Do not pierce or burn, even after use.

Decomposition Temperature : >250°C (482°F)

Materials to avoid : Strong oxidising materials. Incompatible with magnesium, zinc, sodium, potassium and aluminium.
Incompatibility is more severe if the metal is present as dust or powder or has freshly exposed surfaces.

Hazardous Decomposition Products : These products are halogenated compounds, hydrogen fluoride, carbon oxides (CO, CO_2), carbonyl halides.

Toxicological information

Potential Acute Health Effects

Inhalation : Heartbeat irregularity (arrhythmia).

Ingestion : No specific hazard.

Skin Contact : Slightly irritating to the skin.

Eye contact : Slightly irritating to the eyes.

Acute toxicity

Ingredient Name	Test	Result	Route	Species
1,1,1,3,3-pentafluoropropane. (HFC-245fa)	LD50	>2000 mg/kg	Dermal	Rat
	LC50	>200000 ppm (4 hour(s))	Inhalation	Rat
	LC50	>100000 ppm (4 hour(s))	Inhalation	Mouse

Subchronic exposure, no-observed-effect level (NOEL) : 500 ppm (Rat/Mouse).

Appendix 4: Cylinder base engineering drawing

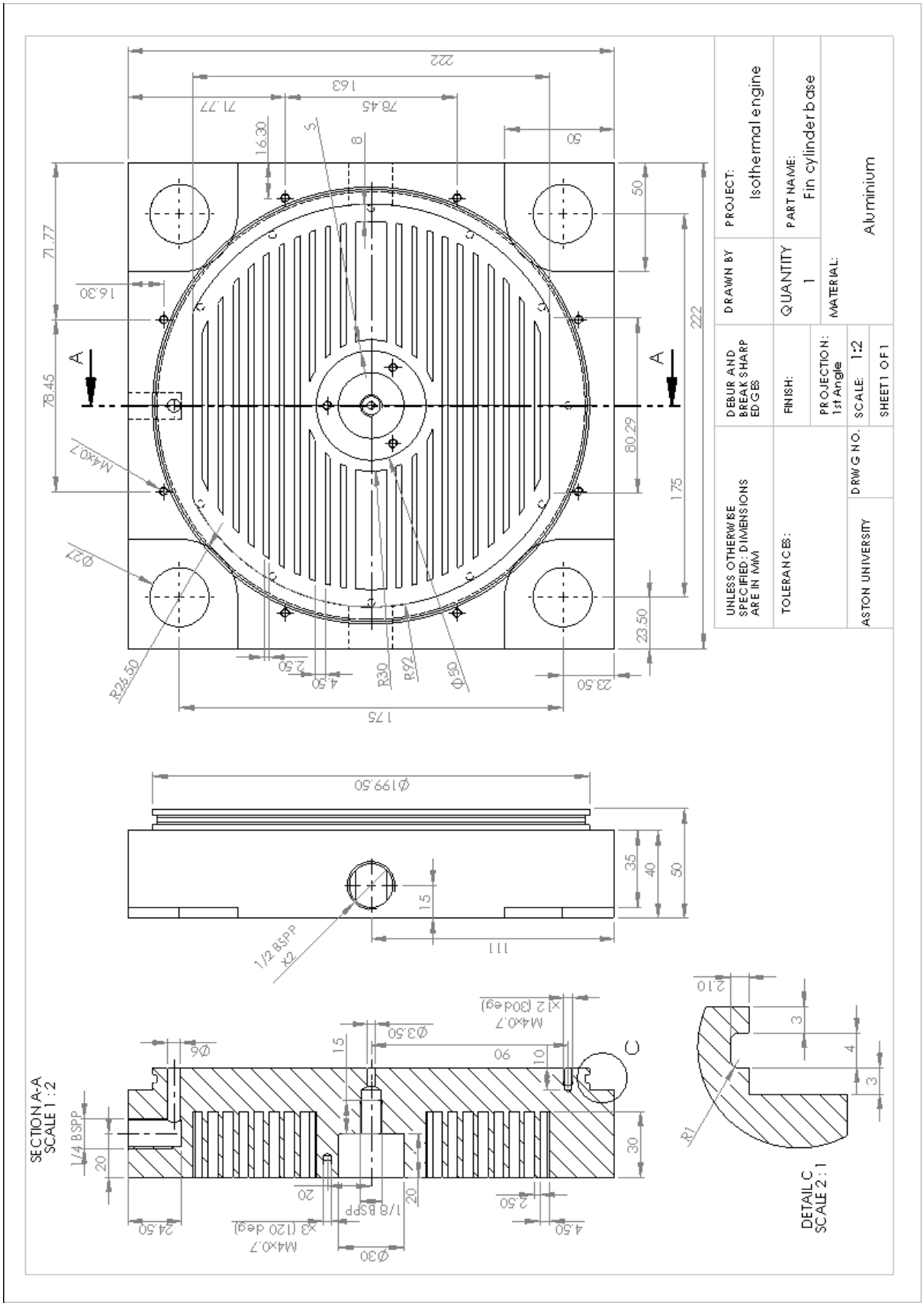

Figure A.2: Engineering drawing of the power cylinder base

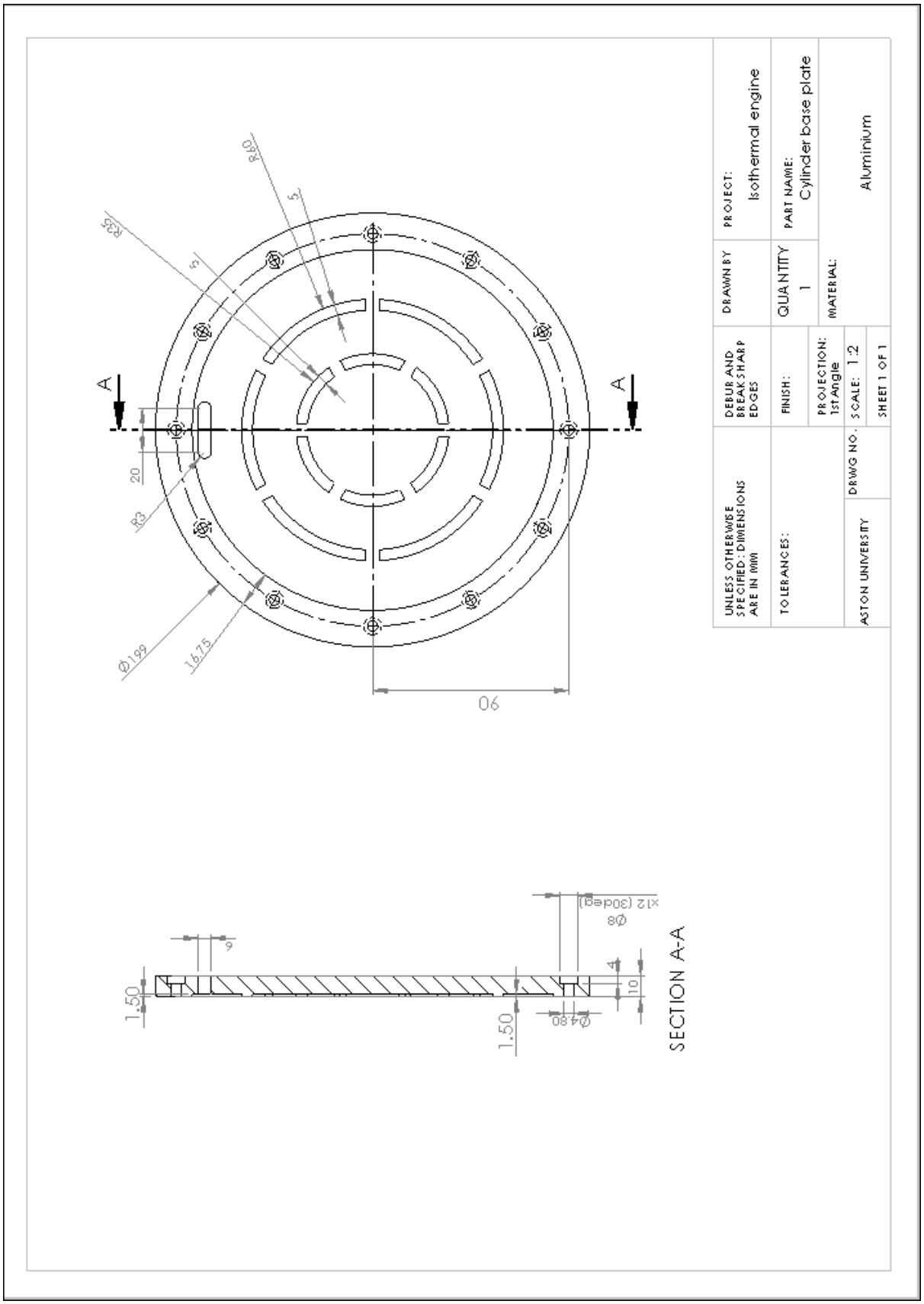

Figure A.3: Cylinder base plate

Cross-sectional view of the cylinder base assembly of the power cylinder

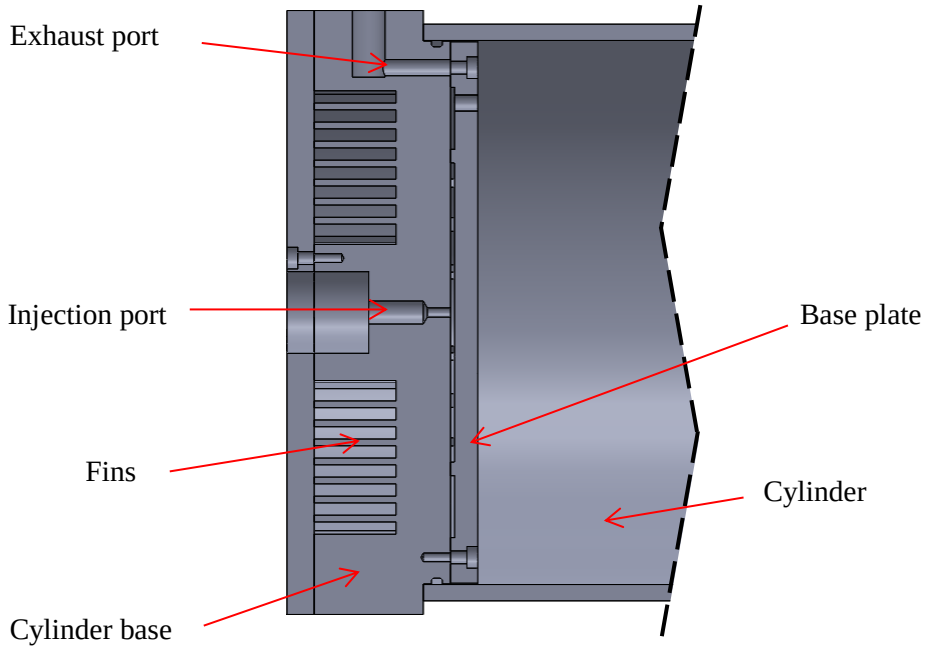

Figure A.4: Cross-sectional view of the power cylinder base assembly

Heat transfer Surface Areas of the fin cylinder base

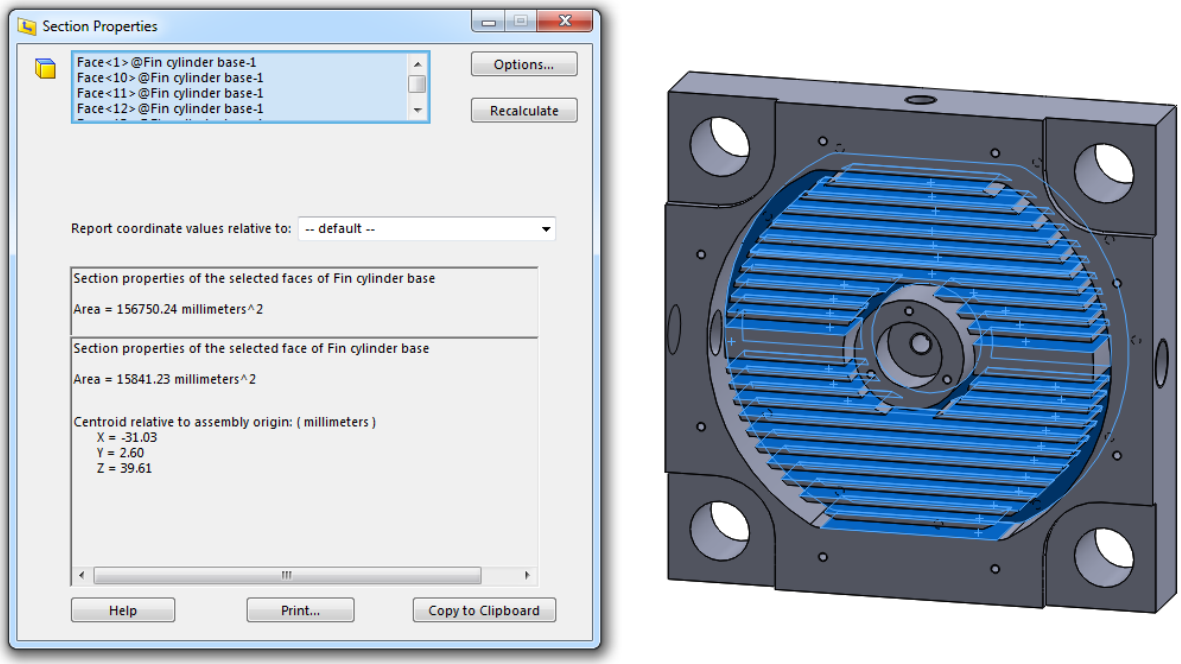

Figure A.5: Surface area of the cylinder base fins

The planer surfaces of the sides of the fins and the base area are determined directly from SolidWorks, while the non-planer surfaces are calculated separately and added, to obtain the total heat transfer surface area (A_{fb}) as 0.197 m^2.

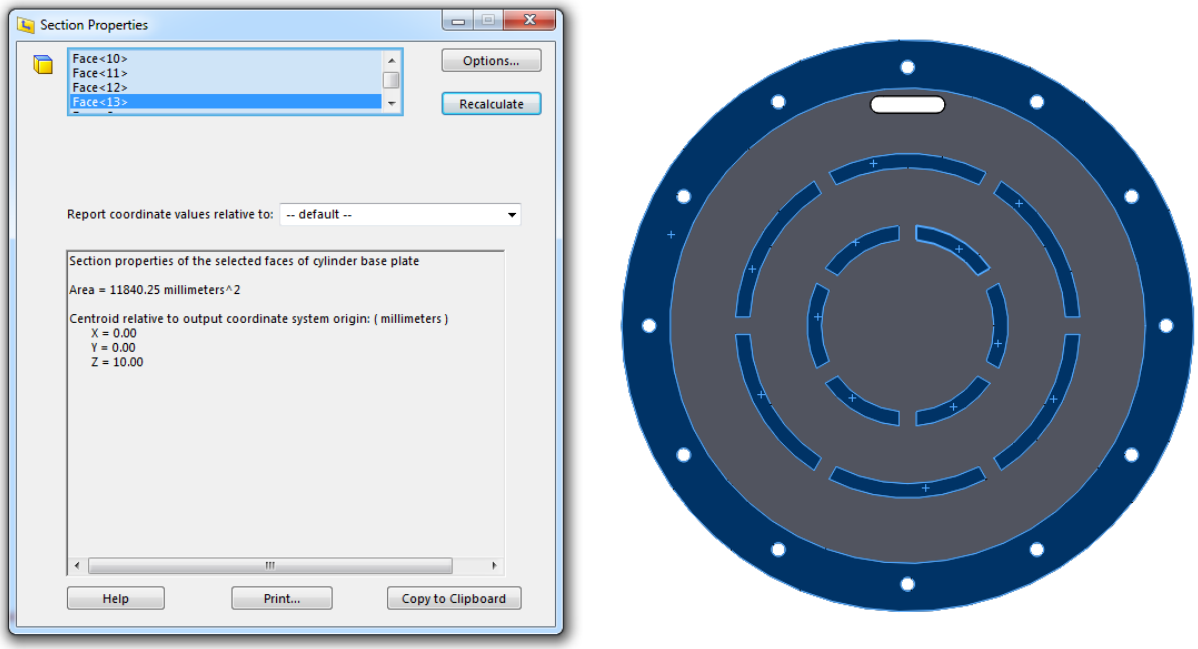

Figure A.6: Surface area of the cylinder base plate

The surface area of the base plate that makes direct contact with the cylinder base (A_{cj}) is 0.0118 m^2.

Appendix 5: Engineering Equation Solver (EES) code

```
PROCEDURE index(Vp,Vvap,Vvapp,ny:n,y)
    if (Vp<Vvap) Then
      m:=0
      z:=1
    Endif
      if (Vp>Vvap) Then
        m:=0.85
        z:=0
      Endif
    if (Vp>Vvap) and (Vp<Vvapp)  Then
      m:=ny
      z:=0
    Endif
    n:=m
    y:=z
End
```

"SYSTEM PARAMETRS"

"Power cylinder gemometry"
D=0.21[m] "diameter"; A_p = 3.142*D^2/4 "Area" ; Ls=0.2188[m] "stroke"; {Vs=0.0007855[m^3];}
{Vs=3.142*D^2/4*Ls }; vd=0.0002[m^3] "dead volume" ;

"Water clinder geometry"
D_w = 0.1[m] ; A_w = 3.142*D_w^2/4 ;   V_ro = 0.0011[m^3] "minimum void volume in RO"

" Feed water condition"
C_nacl = 4[kg/m^3] "Feed water salinity/concentration. 4000 ppm = 4000mg/L = 4kg/m^3" ;
T_nacl = 25[C] "feed water temperature" ; P_atm = 1[bar]

Posm_ini = i*q*(C_nacl/Mm_nacl)*R#*T "initial osmotic pressure" ; P_osm.ini=P_atm
+Posm_ini*convert(kPa,bar) ;   Mm_nacl = 58.44[kg/kmol] "molar mass of nacl";

T=convertTemp(C,K,T_nacl); i = 2 " no of ions, 2 for NACL"; q = 0.92 "dissociation and random
pairing coefficient" ; "R# is universal gas constant"

//.....
.....

"LINKAGE MECHANISM"

{Ap = 0.03464[m^2] }
Vp = S_p * A_p + vd

L_p = 0.765[m]
L_w = 0.5[m]
x_off = 0.28[m]
y_off = 0.205[m]
R_p = 0.25[m]
R_w = 0.35[m]

theta_p_min = 3[Deg]
theta_p_max = 54.5[Deg]

```
theta_w_min = theta_p_min + 45[Deg]
theta_w_max =  theta_p_max + 45[Deg]

alpha_p_min = arcsin((R_p * sin(theta_p_min) + x_off)/L_p)
alpha_p_max = arcsin((R_p * sin(theta_p_max) + x_off)/L_p )
alpha_w_min = arcsin((R_w * cos(theta_w_min) + y_off)/L_w)
alpha_w_max =arcsin((R_w * cos(theta_w_max) + y_off)/L_w)

{ theta_p=3[Deg] }    ;    theta_w=theta_p + 45[Deg]    ;    x=sin(theta_p)

alpha_p =arcsin((R_p * sin(theta_p) + x_off)/L_p)
alpha_w =arcsin((R_w * cos(theta_w) + y_off)/L_w)

        "power piston displacement"
 S_p = (R_p * cos(theta_p_min) + L_p * cos(alpha_p_min)) - (R_p * cos(theta_p) +
L_p*cos(alpha_p))
        "water piston displacement"
 S_w = (R_w * sin(theta_w_max) + L_w * cos(alpha_w_max)) - (R_w * sin(theta_w) +
L_w*cos(alpha_w))
          "initial or maximum water displacement at start"
 S_w_ini = (R_w * sin(theta_w_max) + L_w * cos(alpha_w_max)) - (R_w * sin(theta_w_min) +
L_w*cos(alpha_w_min))
 S_w2 = (R_w * sin(theta_w_min) + L_w * cos(alpha_w_min)) - (R_w * sin(theta_w) +
L_w*cos(alpha_w))
        "mechanical advantage"
 M.A = ( R_p*sin(theta_p) + R_p*cos(theta_p)*tan(alpha_p) ) / ( R_w*cos(theta_w) +
R_w*sin(theta_w)*tan(alpha_w) )
        "initial M.A at the start"
 M.A_initial = ( R_p*sin(theta_p_min) + R_p*cos(theta_p_min)*tan(alpha_p_min) ) / (
R_w*cos(theta_w_min) + R_w*sin(theta_w_min)*tan(alpha_w_min) )

S_p_min = 0[m] ;    S_p_max = 0.218[m]  ;                S_w_min =0[m] ;    S_w_max =  0.35[m]

theta_p_unit = theta_p / 1[Deg]

Row=theta_p_unit -2          "Table Row number"          "Only required when solving Table"
//Vp_old=tablevalue(Row-1,#Vp)        "Previous value in the table"  "Only required when solving
Table"


//
.....
.....

                                "CONDENSER"

P_c=1.65[bar]   "condenser pressure";
T_c=T_sat(R245fa,P=P_c);   "Temperature"
rho_cnds=Density(R245fa,P=P_c, x=0)   "Density"

//
    .....
.....
                                "PUMP"

 "Pump diameter : "  Dp=0.050[m];  "stroke : " LpA= 0.061[m] ;    "stroke volume : " VpA=
3.142*Dp^2 /4 *LpA;
"void vol in the injection tube : " vb=3.142*vdd^2/4*vbl;    vdd=0.0042[m] "tube i.d";    vbl = 0.080[m]
"length of void in tube" ;
```

```
"volume of pumped liquid"; V_liq = VpA * Eff_vol ;
 "mass of pumped liquid";   m_liq =  rho_cnds * V_liq

Eff_vol = 1 - ((dp_p * Zz * r) + v_slip + (vb/VpA) )      "volumetric efficiency of the pump" ;

      Zz = 1/(rho_cnds*SS^2) "Compressibility" ;
            SS=SoundSpeed(R245fa,P=P_c,x=0)  ; "compressibility = 1/modulus, but
ss=(modulus/density)^0.5"
      dp_p = (P_o - P_c)*convert(bar,Pa)              "differential pressure between the outlet and inlet"
      r =  (vd_p +VpA)/ VpA                    "ratio of the total pumping chamber volume (including void
volume at the ports) to piston displacement volume" ;
         vd_p = 0.00001[m^3]  "estimated as 0.0000038+0.0000039+0.00000157";
      v_slip = 0.05       "loss due to fluid slippage back the valve before full closure - typical about 1
to 5 %"

P_o = P_i * Eff_p    "output pressure from the pump" ;
        Eff_p = 0.8 "pump mech efficiency" ;
        P_i = 10.4[bar] "pump pneumatic driving pressure"

// ..........................................................................................................

                                    "HEATED POWER CYLINDER"

"Properties of 70% ethylene glycol heat transfer fluid, HTF, @ about 90 degC" ;

C_htf = 0.7   "concentration";   Mu_htf = 0.00098[kg/m·s] "dynamic viscosity" ;
Rho_htf = 950[kg/m^3] "density" ; cp_htf = 3.34[kJ/kg·K]  ;
k_htf = 0.34[W/m·K] "thermal conductivity"
//cp_htf2=Cp(EG,T=T_htf,C=C_htf) ; mu_htf2=Viscosity(EG,T=T_htf,C=C_htf);
rho_htf2=Density(EG,T=T_htf,C=C_htf) ;k_htf2=Conductivity(EG,T=T_htf,C=C_htf);
Pr_htf2=Prandtl(EG,T=T_htf,C=C_htf)


"Fin cylinder base geometrics"
"Fin : "  b = 0.004[m] "channel width" ;  H= 0.025[m] "channel height" ;  no=26 "no. of channels" ;
A_ch = b*H*no "total flow area from channels" ; L_ch = 0.122[m] "average channel length" ; Dh =
2*b*H/(b+H) "Hydraulic diameter" ; A_fb = 0.197[m^2] "Total heat transfer area"
"Aluminium base : "  k_a = 210[W/m·K] "thermal condtvty"; th_a = 0.025[m] "thickness"; LB =
0.222[m] "length of sides"; A_a = LB*LB "Area";
"Copper Clad : "      k_c = 400[W/m·K] ; th_c = 0.01[m] ; D_c =0.199[m] ; A_c = 3.142*D_c^2 /4 ;
th_cj = 0.002[m] "copper junction thickness"; A_cj =0.0106[m^2] "copper junction Area";
"Other parameters"
     F_dot_htf =0.00094[m^3/s] "flow rate of HTF"; T_htf = 95[C]  "inlet Temp for HTF";   DT =
0.1175[K]  "average temp difference of HTF btw inlet and out, at steady state condition" ;  Eff_htf =
0.45 "collector efficiency of cylinder base, at steady state condition"
"                    "
    Um_htf = F_dot_htf / A_ch "mean velocity";  Re_htf = Rho_htf*Um_htf *Dh/Mu_htf  "Reynold
number"; Pr_htf = (Mu_htf *cp_htf / k_htf)*convert(kJ/s,W)  "Prandtle number"; L_dot_ch =
L_ch/(Dh*Re_htf*Pr_htf) "dimensionless channel length from the inlet"

"the base wall temperature"
T_w=T_htf - Eff_htf * (Q_htf*convert(kJ/s,W)) * Rth ; Q_htf = Rho_htf * F_dot_htf *cp_htf * DT;
              " Rth (= 1/UA) is the thermal resistance : "
Rth = 1/(h_htf * A_fb) + th_a/(k_a*A_a) + TCR/A_cj + th_cj/(k_c*A_cj) + th_c/(k_c*A_c)  ;
   TCR = 0.00012[m^2·K/W] "thermal contact resistance" ;   h_htf = Nu_b*k_htf/Dh ;
 Nu_b = 8.235*(1-1.88*a+3.767*a^2 - 5.814*a^3 + 5.361*a^4) "Nusselt number";  a = b/H "aspect
ratio"

                                    "EVAPORATION AND EXPANSION"
```

```
 Vvapp = (v_g * rho_cnds * V_liq)   " Volume length of vaporisation phase"  ;
       v_g = Volume(R245fa,P=P_o,x=1) ;    V_vap = (v_g * rho_cnds * V_liq) - vd ;
      Vr = (V_liq/vd) ;  Vvap = (V_liq/vd)* (v_g * rho_cnds * V_liq)

ny = 0.7*(Vp/Vvapp)^2

CALL index(Vp,Vvap,Vvapp,ny:n,y)


Pp = P1 * (Vp_1/Vp_2)^nn *MA.Posmt  "pressure"

     MA.Posmt = 1 - g * M.A * (P1)/P_osmt   ;   g=0.004;

     nn=n; yy=y                                                    ;

Vp_1 = tablevalue(Row-1,#Vp) ;  P1 = tablevalue(Row-1,#P_p)  ; P2=P_p
Vp_2 = Vp

                                "WATER PRESSURE"

P_osmt = P_osm.ini * V_w.ini/V_w   ;   P_osm = P_osm.ini * (1 + ((V_w.ini - V_w)/V_w.ini))   ;

        V_w = A_w*S_w +V_ro  ;  V_w.ini=A_w*S_w_ini +V_ro  "Water volume"


P_w = ci* F_w / A_w
      ci =  1 - 0.038 * M.A * (Pw_ideal)/P_osmt ;
            Pw_ideal = F_w/A_w
      F_w = F_p * M.A     "force delivered to the water piston"   ;
     F_p = (Pp - P_c) * A_p   " force transmited from power piston"



                                "Permeate Flow Rate"

F_dot_w = imp * A_mem * ((P_w - P_osmt)*(convert(bar,kPa))) *zet_w.flo

    imp = 9.14E-09 [m^3/m^2·s·kPa]    "intrinsic membrane permeability" ;
   A_mem = 2.6[m^2]  "active memrane area"  ;
   zet_w.flo = 0.35+ 0.175 * M.A - 0.00*M.A^2


                                "Permeat Concentration"

C_perm = B_salt * (CPF*C_f - 0)*A_mem / F_dot_w    "permemat contration"

       B_salt = 1.18E-07[m/s] "salt permeability coefficient";
      CPF =1.2  "concentration polarisation factor";
      C_f = C_nacl * V_w.ini/V_w  "concentration at RO feed side"

C_perm2 = m_salt.Tot / (V_w.ini - V_ro)  ;

     m_salt = 0.5* (m_dot_salt1 + m_dot_salt)* T_oprtn  ;
          m_dot_salt = B_salt * (CPF*C_f - 0)*A_mem     "salt mass transfer rate";
          m_dot_salt1=tablevalue(Row-1,#m_dot_salt) ;
     m_salt.Tot =  m_salt+tablevalue(Row-1,#m_salt.Tot)

     CPF2=EXP(Jv/B_salt);  Jv=imp * ((P_w - P_osmt)*(convert(bar,kPa)))
```

"Time of Operation"

T_oprtn = 0.9 * (V_w1 - V_w) / (0.5*(F_dot_w1 + F_dot_w)) "duration";

Time=T_oprtn+tablevalue(Row-1,#Time) "Time elasped"

V_w1=tablevalue(Row-1,#V_w) "Previous value in the table. For solving tables only"
F_dot_w1=tablevalue(Row-1,#F_dot_w)

V_w_min = A_w*S_w_min; V_w_max = A_w*S_w_max

"WORKDONE and EFFICIENCY"

//T_w=87[C] "cylinder base wall temperature"

P_3 = P_o ;
P_4 = tablevalue(Row-1,#P_p) ;
Vp_4 = tablevalue(Row-1,#Vp)

P_1=P_c; "after metering, @injection @expansion";
P_ce=P_c "residual pressure in the cylinder" ; v_cge=Volume(R245fa,P=P_ce,x=1);

T_cc=21[C] ; {T_c=T_sat(R245fa,P=P_c)}

s_1=Entropy(R245fa,P=P_c,T=T_cc); h_5=Enthalpy(R245fa,P=P_c,x=1) ;

v_cf=Volume(R245fa,P=P_c,x=0); v_cg=Volume(R245fa,P=P_c,x=1);

md=vd/v_cge ;{m_d=Vs/v_cg}

v_3g = v_g ; Vs=Vp_4 ; m_inA = m_liq

"start"
{ P_3=8.4[bar] } ;
{ v_3g=Volume(R245fa,P=P_3,x=1) }; v_3f=Volume(R245fa,P=P_3,x=0);
   T_3=T_sat(R245fa,P=P_3);
   s_3=Entropy(R245fa,P=P_3,x=1);

    h_2=Enthalpy(R245fa,s=s_1,P=P_3);
   h_3=Enthalpy(R245fa,P=P_3,x=1);
   u_3=IntEnergy(R245fa,P=P_3,x=1);
  q_vapA=h_3 - h_2;

"finish"
{ P_4=3.657[bar] } ; T_4=T_sat(R245fa,P=P_4);
v_4A=(Vp_4+vd)/(m_inA+md);
 T_4A=Temperature(R245fa,P=P_4,v=v_4A);
 s_4A=Entropy(R245fa,P=P_4,v=v_4A);
q_34A = ConvertTemp(C,K,(0.5*(T_3+T_4A))) * (s_4A - s_3);

```
"isothermal finish with same mass"
 P_4isoA = Pressure(R245fa,T=T_3,v=v_4A);
 {v_4iso=v_4A}
 {T_4iso=T_3}
 s_4isoA=Entropy(R245fa,T=T_3,v=v_4A);
q_34isoA=ConvertTemp(C,K,T_3)*(s_4isoA - s_3);
 h_4=Enthalpy(R245fa,T=T_3,v=v_4A);
 u_4=IntEnergy(R245fa,T=T_3,v=v_4A);

"heat input"
QvapA = (q_vapA + (q_34isoA*0.5)) * m_inA ;
Q_vap =(q_vapA + q_34A)*m_inA

"Workdone"
W_totA=(w_2a3A+w_34A)*m_inA       "ideal work done";
 w_2a3A= P_3*(v_3g - v_3f)*convert(bar,kpa);                    w_34A=q_34isoA - (u_4 - u_3);

W_p = 0.5 * (P1+P2)*convert(bar,kPa)* (Vp_2 - Vp_1) ; W_out =W_p + tablevalue(Row-1,#W_out)
;  W_outA = W_out  ;   "Practical work out"

 w_puA=v_cf *((P_o-P_c)*convert(bar,kpa))   "pump work";
W_exh=P_c*(Vp)*convert(bar,kpa)    "exhaust work";

     gamma_WA =  W_outA/W_totA      "Isothermicity";

"Efficiency"
      eff_A=(W_totA -W_exh- w_puA*m_inA)/((q_vapA + q_34isoA)*m_liq);  "Ideal "   ;
       eff_rA=(W_outA - W_exh- w_puA*m_inA) /((q_vapA + q_34A)*m_inA)   "Actual"
      eff_rA2=(W_outA - W_exh- w_puA*m_inA) /((q_vapA + q_34isoA)*m_inA);
      eff_rA3=(W_outA - W_exh- w_puA*m_inA) /((q_vapA + (q_34isoA*0.5))*m_inA)
```

Appendix 6: Solar collector data sheet

Appendix 7: Flue gas composition

Operating parameters

Specific energy consumption SEC = 2.9 MJ/kg

Heat value HV = 40 MJ/m3

Air-to-fuel ratio AFR = 10

₲ = 0.115 m3/kg

Production rate PR = 1500 kg/hr

Flow rates

Combustion product $\dot{V}_{cg} = PR\left[\frac{SEC_{bake}}{HV} + \frac{SEC_{bake}}{HV}AFR\right] = 1196\ m3/hr$

Baked product flow rate $\dot{V}_{bg} = PR * ₲ = 172\ m3/hr$

Flue gas flow rate $\dot{V}_{fg} = \dot{V}_{cg} + \dot{V}_{bg} = 1368\ m3/hr$

Natural Gas flow rate $\dot{V}_{NG} = PR\ \frac{SEC_{bake}}{HV} = 108.75\ m3/hr$

Air flow rate $\dot{V}_{Air} = AFR\ \dot{V}_{NG} = 1087.5\ m^3/hr$

Compositions

Using the regular natural gas combustion products composition (%) from literature, the corresponding combustion product elements flow rates can be obtained as (% $\dot{V}_{cg}$). Similarly, using the baked product gas composition (%) from literature, the corresponding baked product elements flow rates can be obtained as (% $\dot{V}_{bg}$). While the flue gas (combined products) elements flow rates is obtained as the sum of both elements flows. Thus the composition of the flue gas can be obtained from the fraction of the total flow.

Table 0.2: Estimated composition of the bakery oven flue gas

	Combustion product		Baked product		**Flue gas** Combined products	
	%	m^3/hr	%	m^3/hr	m^3/hr	**%**
N_2	75	897.1875	0	0	897.1875	**65.5**
CO_2	13	155.5125	5.4	9.315	164.8275	**12.0**
H_2O	11	131.5875	89	153.525	285.1125	**20.8**
others	1	11.9625	5.6	9.66	21.6225	**1.6**
Total					1344.825	